Offshore grid control of voltage source converters for integrating offshore wind power plants

Muhammad Raza

Departament d'Enginyeria Elèctrica

UNIVERSITAT POLITÈCNICA DE CATALUNYA

Doctoral Thesis

Offshore Grid Control of Voltage Source Converters for Integrating Offshore Wind Power Plants

Muhammad Raza

Thesis Supervisor:
Prof. Dr. Oriol Gomis Bellmunt

Barcelona, Spain
September 9th, 2017

Offshore Grid Control of Voltage Source Converters for Integrating Offshore Wind Power Plants

by Muhammad Raza

Academic Years: 2014-2017

This thesis is submitted to Departament d'Enginyeria Elèctrica of Escola Tècnica Superior d'Enginyeria Industrial de Barcelona in partial fulfillment of the requirements for the degree Doctor of Philosophy in Electrical Engineering at the Universitat Politècnica de Catalunya (UPC-BarcelonaTech) Barcelona Spain.

Examination Committee:

Prof. Dr. Dirk Van Hertem, University of Leuven, Belgium
Prof. Dr. Andreas Sumper, Universitat Politècnica de Catalunya, Spain
Prof. Dr. Adriano da Silva Carvalho, University of Porto, Portugal

This page is intentionally left blank.

To My Little Angel
Hawra-e-Zahra...

Acknowledgements

Thanks to Almighty God who gave me an insight and strength to learn and implement the mysteries of technology.

I would like to express my sincere gratitude to my research supervisor, Prof. Dr. Oriol Gomis Bellmunt, for his guidance, unwavering support, and collegiality. I highly admire his valuable comments and discussion as well as for the financial support to execute this research. I must thank him for providing me a great opportunity to be involved in the momentous EU project 'MEDOW' that would set the foundation of future offshore grid.

I am obliged to European Commission for initiating MEDOW project which was a great platform to express own ideas as well as to meet with the experts of offshore wind energy research society.

I am highly obliged to the members of MEDOW team for their guidance and knowledge sharing during the execution of the project. Specially, I am thankful to the team of GE Renewable Energy Offshore Wind Barcelona Spain for paving the ways for my professional growth and giving me the technological insight.

I must pay thanks to all my research colleagues at Centre d'Innovació Tecnològica en Convertidors Estàtics i Accionaments of Universitat Politècnica de Catalunya for their cooperation and encouragement.

I must thank the captivating beauty at Spain which was my real inspiration during my stay.

In addition to all above, I owe to my family for their prayers and love that drive me always to achieve my goals.

Summary

The offshore grid in North and Baltic Sea can help Europe to achieve 2020 and 2030 renewable energy target to counter climate changes. The formation of offshore grid requires the interconnection between several offshore wind power plants with multiple onshore grids. A voltage source converter based high voltage direct current transmission system is suitable to operate such an integrated offshore network. The offshore grid will enhance the trade between countries, provide better infrastructure for offshore wind power plants integration, and improve the energy market.

This thesis presents the control system design of voltage source converter to operate an offshore grid. The offshore grid is built gradually, starting from the integration of a single offshore wind power plant till combined offshore AC and DC network in order to perform the power system analysis associated with the networks such as steady-state power flow, dynamic behavior, network stability, and short circuit response. The research presents the method of determining control parameters with respect of power distribution and network stability requirements.

The research presents the frequency and voltage droop schemes to enhance the grid forming mode of voltage source converter to operate in parallel in the offshore grid. A multi-objectives optimal power flow algorithm is proposed to determine the frequency and voltage droop gains in order to control the active and reactive power distribution among converters. Later, the impact of these droop gains on network dynamics and stability are analyzed. The study shows that the converter performance influences the offshore AC network stability in conjunction with the droops control loop.

Furthermore, a short circuit and frequency coordinated control schemes are presented for both offshore wind generation units and grid forming converters. The frequency coordinated control scheme reduces the wind

power up to the maximum available export capacity after the disturbance in the offshore grid. It is suggested that the coordination control must have both frequency and over voltage control for improved transient response.

In the end, converter control of multiterminal DC network and its integration with the offshore AC network has been presented. The research demonstrate the converter ability to control the distribution of power among the transmission system while ensuring the network stability. The finding of the research can be applied to derive the information and recommendation for the future wind power plant projects.

Resumen

Las redes eléctricas marítimas en el Norte y en el Mar Báltico pueden ayudar a Europa a conseguir los objetivos para 2020 y 2030 de combatir el cambio climático. La formación de la red eléctrica marítima requiere la interconexión entre varios parques eólicos marinos con múltiples redes eléctricas en tierra. Un convertidor de la fuente de voltaje basado en el sistema de transmisión de corriente directa de alto voltaje es el apropiado para poder operar una red marítima integrada. Las redes eléctricas marítimas aumentarán el comercio entre países, proveerán una mejor infraestructura para la integración de los parques eólicos marinos y mejorarán el mercado energético.

Esta tesis presenta el diseño del sistema de control del convertidor de las fuentes de voltaje para operar una red eléctrica marítima. La red eléctrica marítima se construye gradualmente, empezando por la integración de un solo parque eólico marino hasta la combinación de redes eléctricas marítimas en CA y CD, esto para mejorar el análisis del sistema de potencia asociado con las redes, tales como el flujo de potencia en estado estacionario, el comportamiento dinámico, la estabilidad de la red y la respuesta en corto circuito. La investigación presenta el método de determinación de parámetros de control con respecto a la distribución de potencia y los requerimientos de estabilidad de la red.

La investigación presenta los esquemas de frecuencia y la caída de voltaje para mejorar el método de formación de red del convertidor de la fuente de voltaje y operar en paralelo con la red eléctrica marítima. Se propone un algoritmo de múltiples objetivos para lograr un flujo de potencia óptimo, determinar las ganancias en la frecuencia y en la caída de voltaje y así lograr controlar la distribución de potencia activa y reactiva entre los convertidores. Después, se analiza el impacto de estas ganancias en la dinámica y estabilidad de la red. El estudio nos muestra que el desempeño del convertidor influencía

la estabilidad de la red eléctrica marítima en CA en conjunto con el lazo de control de la caída.

Así mismo, se presentan los esquemas de control coordinado de frecuencia y corto circuito, aplicados para las unidades de generación eólica marítima y los convertidores en red. El esquema de control coordinado de frecuencia reduce la potencia eólica hasta la máxima capacidad de exportación disponible después de las perturbaciones en la red eléctrica marítima. Se sugiere que la coordinación del control debe de tener control sobre la frecuencia y el sobre voltaje para mejorar la respuesta en transitorios.

Por último, se presenta el control del convertidor de las multiterminales en la red CD y su integración con la red eléctrica marítima en CA. La investigación demuestra la habilidad que posee el convertidor para controlar la distribución de potencia, junto con el sistema de transmisión, mientras se asegura la estabilidad de la red. Los hallazgos de esta investigación pueden ser aplicados para obtener información y recomendaciones en los futuros proyectos de parques eólicos.

Contents

List of Figures

List of Tables

1 Introduction

This chapter explains the background of the thesis and the challenges that future offshore wind power integration may face. The aim and contribution of the thesis are also described in this chapter.

1.1 The Emergence of Offshore Wind Energy

The current era requires attention to unprecedented issues of security and sustainability of energy generation. A threat of global warming is also added in the existing challenges of diminishing fossil resources and increasing world population [1]. The world must escape from the dependency of pollutant technologies of energy generation, and move towards a clean and sustainable source of generation to meet the future energy demand [2].

Renewable resources have made the biggest transition in the global energy sector compared to fossil fuels. Among all the new power generation installation in EU in 2015, the share of renewable energy is 77 % whereas more energy was from conventional power sources decommission compare to their new install [3]. In Europe alone, 224 GW of renewables was added over the last decade, of which 122 GW is produced by new installation of wind power plants during 2005-2016 [3, 4]. Whereas, every year generation from fossil fuels is reduced with an average of 10 GW installed capacity [3]. Wind energy is the fastest growing technology among other renewables. In 2016, wind energy with the capacity of 12.5 GW was installed in the European Union which amounts to 51 % of all new installation [4]. Of the total installed capacity in 2016, 10.923 GW was installed onshore and 1.567 GW offshore [4]. The annual growth of onshore and offshore wind power is shown in Figure 1.1. By the end of 2016, the EU-28 countries installed 153.7 GW wind power capacity, out of which 141.1 GW is onshore
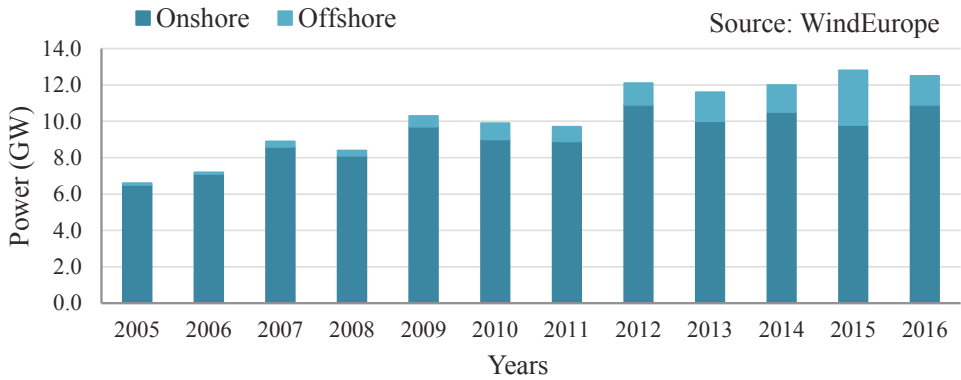
Figure 1.1: Annual onshore and offshore wind power in the EU.

and 12.6 GW offshore. Germany is the leading country with the highest number of installed wind power capacity, followed by Spain, UK, and France [4]. During 2016, Germany has installed four wind power plants having total number of 155 fully grid connected wind turbines with the total installed power of 813 MW [5]. Until now, Germany has installed up to 50.0 GW of cumulative onshore and offshore wind energy. Whereas, Spain has 23.1 GW and UK has 14.5 GW of cumulative installed wind energy. This trend of connecting wind energy into European grid will be continued in order to achieved the target of EU 2030 climate and energy framework. The framework set three main targets i.e reduction in greenhouse gas emissions up to 40 % since 1990 level, increase in renewable energy share of at least 27 % of EU energy consumption, and at least 27 % improvement in the energy efficiency [6].

Wind industry has emerged as a proven technology for the clean and affordable energy in order to fulfill the ambitious energy policies of EU. The wind energy resources are huge in Europe. However, the cost-effective development is the key challenge. Onshore, high wind energy potential is available in the industrial and agricultural areas. The environmental and social constraints associated with land acquisition for onshore wind power plant development are the main limiting factors in utilizing the wind potential to its full extent. Also, the environmental and social constraints such as Natura 2000 areas, shipping lane, and military areas leave up to

4 % of offshore area within the 10 km of the EEA countries coast to build wind power plants. This has reduced the offshore wind utilization potential by more than 85 % of total available wind power near coast (2800 TWh of 25000 TWh in 2020) [7]. These onshore and near to coast limitations for wind power plants installation are forcing to go deeper into the Sea. As illustrated in Figure 1.2, many offshore wind power plants are under construction and consented for future installation far from the shore [8]. Future wind power plants are expected to be installed as far as 100 km and as deep as 50 m. Around, 100 GW of offshore wind energy projects have already been proposed in North and Baltic Sea. The grid integration of such huge offshore energy requires an unique infrastructure. European Wind Energy Association (EWEA) have proposed a 20 year offshore network development plan which provides gradual approach to plan offshore grid in the North and Baltic Seas. The future offshore grid will not only be a national grid but it will become an European backbone for electricity trade. The future transnational offshore grid will provide benefit to European countries such as access to offshore wind energy, enhance the ability to trade electricity, and smooth the wind energy variability in the markets [9]. The concept of integrated network is not limited to Europe only but it is being given importance worldwide [10]. Some of the initiatives that are taken worldwide to construct international electrical grid are list below:

- **Friends of SuperGrid:** The Friends of Supergrid (FOSG) is a group of companies and organizations who are promoting the concept of Supergrid in Europe. According to them a SuperGrid is 'a pan-European transmission network facilitating the integration of large-scale renewable energy and the balancing and the transportation of electricity'. The FOSG proposed the SuperGrid technology roadmap that provides a comprehensive overview on the energy transmission technology evolution for interconnections between European countries until 2050. The roadmap also propose EU level regulatory framework which will accelerate the Supergrid projects.

- **Offshore Grid:** It is an European project which will set the offshore grid regulatory framework considering economic, technical, policy and
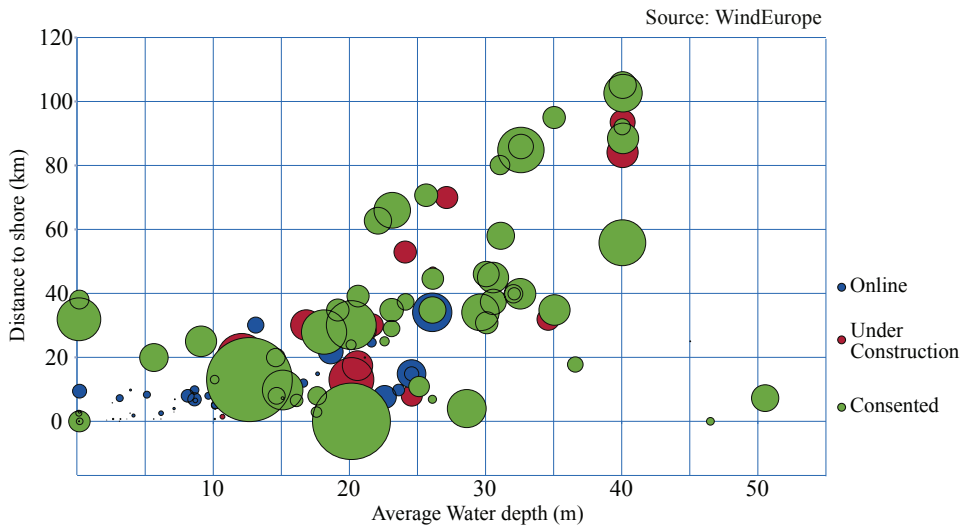
Figure 1.2: Average water depth and distance to shore of offshore wind power plants (bubble size indicates the installed size).

regulatory aspects. In the first phase, the project focuses on the regions of North Sea, Baltic Sea, the English Channel, and the Irish Sea. In the second phase, the results will be applied for the Mediterranean projects.

- **Atlantic Wind Connection:** This project will construct an offshore electrical transmission system around the mid-Atlantic region. It will be built in three phases over the period of ten years. In the first phase, New Jersey Energy Link will be built which will connect the South Jersey electrical network with North Jersey electrical grid. The DelMARVA Energ Link will be built in the second phase in which wind power plants more than 16.1 km off the coast of Delaware, Maryland and Virginia will create three offshore hubs to connect with the onshore grids. In the third phase, the Bay Link will be developed that will complete the interconnection between the New Jersey Energy Link and the Delmarva Energy Link forming the north-south offshore backbone.

- **Medgrid:** It is an Euro-Mediterranean electricity network planned to build for providing inexpensive renewable electricity in North Africa
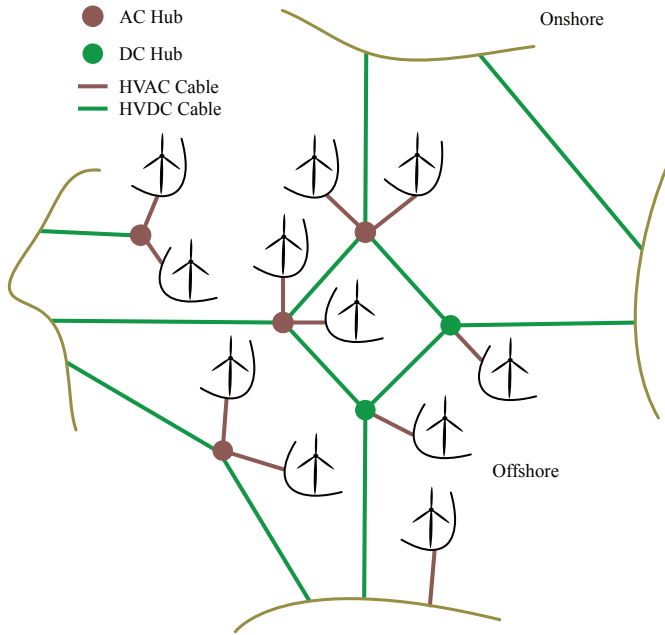
Figure 1.3: Future Offshore Grid: different scenarios of interconnecting wind power plants, offshore and onshore nodes.

and Europe. This transmission infrastructure will have capacity of around 20 GW from which 5 GW is planned to export to Europe.

- **Asian Super Grid:** It is an idea to build the transnational electrical grid between China, South Korea, Russia, and Japan. The electrical transmission infrastructure will interconnect the renewable energy build at the location where it can produce best with the region where it needed the most. The network will be the combination of both AC and DC transmission system, and it will have the overall transmission capacity of 10 GW.

The future integrated European offshore grid will consist of both multiterminal (MT) high voltage direct current (HVDC) transmission system and offshore AC network. Several scenarios to interconnect wind power plants, offshore hubs, and onshore grids together are illustrated in Figure 1.3. For the transnational grid, several offshore wind power plants will be connected together to form the offshore hubs. The offshore hub can be based on alter-

nating current (AC) and/or direct current (DC) technology. These offshore hubs will act as the mediator between wind power plants and different countries. The net power from these hubs will be transferred where it is needed hereby enhances trade and improves competition in the European energy market. This will improve the connection between load centers around the North and Baltic Sea, and develop more interconnection between countries which avoid the bottleneck on the existing international inter-connectors [11]. Although the transactional grid have several economical benefits, it requires further research to address technical challenges associated with it. Such as what is the control and operational principle of an offshore AC or DC hub; how to ensure the offshore grid stability; how power is distributed through the AC or DC hub; what would be the behavior of the wind turbines and transmission system during short circuit at offshore grid etc. In this context, this thesis focus on the following key points:

- Control and operation of the HVDC transmission system for offshore hubs

- Control of the active and reactive power flow within the offshore grids

- Integration of the offshore AC and DC hubs

1.2 MEDOW: A Solution to Global Warming

The threat of global warming has risen to an alarming level in last two decades. There is an urgent need of reducing greenhouses gases, such as carbon dioxide, to restrain the fast changes of climate. The energy generation by burning fossil fuels, such as coal, oil, and natural gas, has highest impact on the atmosphere than any other human activity. Globally, power generation is adding almost 700 tonnes of CO_2 emission every second and 23 billion tonnes every year [12]. To reduce climate risks, the CO_2 emissions must be cut by deploying green power sources like wind energy. European Union (EU) has taken several steps toward the clean energy generation prominently from wind. Many research projects are ongoing to study the feasibility of wind generation and its integration with the existing grid especially for offshore

wind power plants. One of these project is MEDOW: Multi-tErminal Dc grid for Offshore Wind [13].

MEDOW is a Marie Curie Initial Training Network (ITN) which consists of five universities and six industrial organizations. The objective of the project is to find the solutions to the issues of offshore grid for integrating wind energy. The overall objectives of the project are divided into four work packages (WP) i.e connection of offshore wind power to DC grids (WP-1), investigation of voltage source converters for DC grids (WP- 2), relaying protection (WP-3), and interactive AC/DC grids (WP-4). The achievements from the project will contribute in the technological development for integrating offshore wind power with the onshore grids in European countries. The project has suggested that the DC grid will be the key technology in realizing the future European offshore 'SuperGrid'. In addition, the project has also offered a development path to researchers across Europe in the area of DC grids.

The presented thesis is the part of the MEDOW research work. The thesis has contributed to achieve the following milestones and deliverables of WP-1:

- Design of converter control and its operational mode characteristics.

- Evaluation of AC and DC grid configuration for offshore wind power plants.

- Development of optimum power flow algorithm for offshore grids.

- Method of reducing wind power during disturbance.

During the execution of the thesis, the collaboration with MEDOW partners have been done on varies aspect of the thesis research area.

1.3 State of the Art

A voltage source converter (VSC) based high voltage direct current (HVDC) transmission system is getting preference over line commutated converter (LCC) based HVDC transmission system due to its operational principle. Although the LCC technology is well developed and available for high power

Table 1.1: Salient feature of voltage source and line commutated converter based HVDC transmission system

Voltage Source Converter (VSC)	Line Commutated Converter (LCC)
- Available in low power rating - Black start capability: create AC grid - Less harmonic generation - Compact site area; $50 - 60\%$ of LCC site area - Individual active and reactive power control - DC voltage polarity does not change - Multiterminal DC network operation is quite straightforward - Newly emerged technology especially for offshore wind power plant application	- Available in high power rating - Requires strong AC grid connection - Significant amount of harmonics: AC and DC harmonic filter require - Large site area, dominated by harmonic filters - Consumes significant amount of reactive power from the grid - DC current polarity does not change - Lower losses - proven technology

ratings, the ability of the VSC to control the active and reactive power independently and its capability to perform the black start of network makes it highly suitable for offshore applications [14]. The salient features of these two technologies are listed in Table 1.1. Thyristors are the main switching device in LCC technology and the inductor in the DC network provides natural ability to withstand short circuit. The basic structures of LCC and VSC technology are illustrated in Figure 1.4. In the VSC, insulated gate bipolar transistors (IGBTs) are the main switching devices which require the DC capacitor. The protection scheme in VSC based HVDC system is more challenging since the application of DC capacitor results in high DC voltage and current during fault. This requires the advance protection method and equipment such as hybrid circuit breakers [15, 16]. This was one of the main concern that lead less installation of VSC based HVDC system.

There are four main variants of DC cables connection between two converters typically known as monopole, bipolar, homopole, and symmetrical monopole. In monopole, the power is transmitted via only one conducting wire with respect of ground or metallic return wire. This connection is usu-
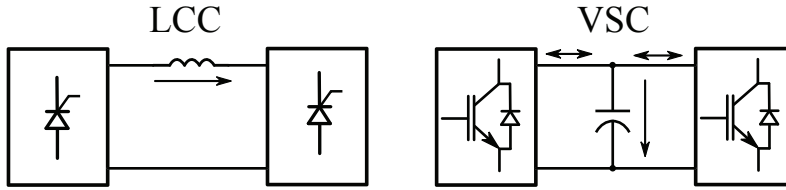
Figure 1.4: Basic setup of VSC and LCC based transmission system.

ally used to reduce the cost. In bipolar connection, the power is transmitted over two opposite polarities conducting wire with respect to the ground or metallic return wire. Typically, two converters are connected at each end of the DC cable forming the two monopoles configuration having the same ground or return wire. In the normal operation, the current in the return wire is zero and the same amount of power flows through each conducting wire. In case of failure in one conducting wire, the system can still be operated with half of the rated power via only one conducting wire as like monopole connection. In homopole connection, the power is transmitted via more than one conducting wires having same polarity with respect of ground. Typically, negative polarity is preferable since the corona effects in the DC cable is less compared to positive polarity [14]. In symmetrical monopole, two opposite polarities conducting wire are used to transfer power like the bipolar connection however it contains only one converter at each end of the DC cable with mid-point grounded. Also, whole power transmission will be interrupted in case of one DC conducting wire failure. This arrangement is very common in VSC compare to LCC based HVDC transmission system [17].

The most common application of HVDC system for power transmission has evolved the DC connection into three topologies i.e back-to-back, point-to-point, and multiterminal. In back-to-back topology, the two converters are connected together with very short cables and they are located at same converter station or area. This topology is mainly applied for connecting two asynchronous AC systems. The more recent application of this configuration is being used in wind power generation system commonly known as Type IV wind turbine, where the power from the wind generator is passed through

Table 1.2: List of VSC based HVDC system projects

Name	Commissioned Year	Power (MW)	DC Voltage (kV)	AC Voltage (kV)	DC Cable Length (km)
East-West Link, UK-Ireland	2013	500	±200	400	261
Mackinac, USA	2014	200	±71	138	Back-To-Back
BorWin1, Germany	2015	400	±150	380/170	200
HelWin1, Germany	2015	576	±250	155/400	130
DolWin1, Germany	2015	800	±320	155/380	165
NordBalt, Sweden-Lithuania	2016/17	700	±300	330/400	450

the back-to-back converters before injecting into the grids. By this, the fluctuation in the power due to wind variation is reduced. The point-to-point topology is applied between two converters that are located far from each other. This is an effective way of transferring power between two grids located at long distance from each other. In multiterminal topology, more than two converters at different geographical location are connected using DC cables. This topology enables the power transfer to multiple locations. It is expected that this topology will play a major role in forming the future offshore grid in the North and Baltic Sea for integrating offshore wind energy [14].

In recent years, several VSC based HVDC transmission systems have been developed. Some of the projects are listed in Table 1.2 [18]. The ability of VSC to create an AC grid is the decisive factor in the installation of high capacity wind power plants at offshore. Based on this ability, a recent concept of 'hub and spoke' transmission system for the interconnected North Sea is proposed by TenneT. In this concept, an artificial island called 'hub' will be built in center of different offshore wind power plants that are far from the shore. Offshore wind power plants and onshore grids will be connected with export system called as 'spoke'. For wind power plant connections with the hub, the export system will be high voltage alternating current (HVAC) cables system since the distance will be short and the installation is simple and cheap. For onshore connection with the hub, the export system will be VSC-HVDC transmission system as the distances of countries from the island are longer. Once built, up to 100 GW or more of offshore wind energy is expected to be connected via this island [19, 20].
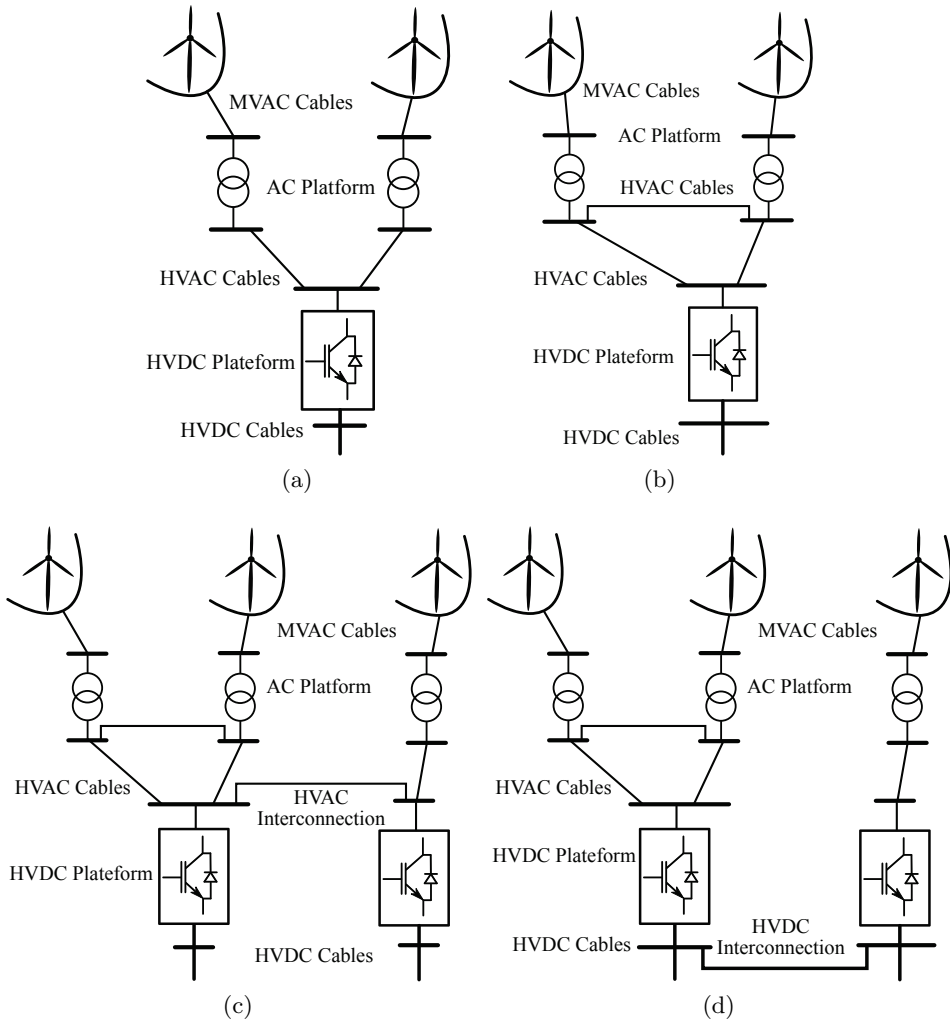
Figure 1.5: Variants of offshore AC collector system for offshore wind power plants integration with the onshore grids.

The vision of the offshore grid has opened up the new possibilities of designing offshore AC collector system. An offshore AC collector system is the way of receiving energy produced at different wind power plants at the centralized location in the Sea. Some of the offshore AC collector system variants are shown in Figure 1.5. In the most common and basic configuration of offshore AC collector system, the wind power is received

at the offshore AC platform using MVAC cables. Typically, these MVAC cables are the arrays of offshore wind power plant in radial or radial-ring configuration. The offshore AC platform is then connected to an offshore HVDC platform via HVAC cables, there the collected power is transferred to the onshore grid using HVDC transmission system. The number of offshore AC platforms depends on the wind power plant layout and capacity [21]. These AC platforms can belong to the same or different wind power plants. By this, combined energy from wind power plants that are far from shore can be transferred economically via single HVDC transmission system. In order to increase the redundancy in the AC network, the offshore AC platforms can be connected together as well using HVAC cable. Normally, the voltage of the cables in the wind power plant array is in the range of $30 - 36$ kV. And the HVAC cables have the typical voltage rating of 132, 150 or 220 kV. The number of interconnected offshore wind power plants are limited by the total power transfer capability of the offshore converter, also the power is only transmitted to a single onshore grid in this configuration. In order to increase the trade and overall capability of energy export, more than one HVDC platform can be built and interconnected with each other either using HVAC or HVDC cable depending on distance between them [22].

Nowadays, the export system between onshore grid and offshore wind power plant is the main focus of the transmission system operators (TSOs). Although the studies have highlighted the advantages of HVDC transmission system over HVAC system, there are more offshore wind power plants currently installed at North Sea using HVAC cables. This is due to the simple installation procedure and the vast experience of the industries with it. The reactive power flow through the offshore HVAC cables is the main barrier in applying this technology for high capacity wind power plants, especially for long distance [23]. The reactive power compensation increases the overall cost of the system. The HVAC export system is usually applied for offshore wind power plant distance less than 60 km from shore [24]. In literature, there are some suggestion to use the non-standard frequencies to reduce the over all cost of the system [25–27]. At higher frequencies, the size of the transformer significantly reduces however the number of cable connections increases as well as the cables charging current for longer distance. Lower

frequencies, such as 16.7 Hz, enable the high power transmission over long distance. This may reduce the total number of cables and compensation equipments. But, the low frequency AC (LFAC) system produces more oscillation in the voltage transient, increased amount of low order harmonics, increase in transformer cost, and high short circuit current in the network. The feasibility study of using the non-standard frequencies for the offshore network is at preliminary level, and it particularly requires a mechanism to integrate existing offshore infrastructure with the future developments to encompass the 'SuperGrid' concept. On the other hand, VSC based multiterminal HVDC transmission systems provide more features and ease in operational control such as control of power flow direction in the DC network, independent active and reactive power control in the AC network, frequency support etc.

With the introduction of modular multi-level converter (MMC) technology, the overall system efficiency vs cost has been increased. The MMC generates the AC output signal in hundreds of small steps and contain low harmonics contents hereby require fewer AC filters. Due to the control structure of MMC, all the semiconductors are not switched simultaneously and the average switching frequency is between 100 to 200 HZ. This has reduced the total converter losses down to 1 % [28]. Moreover, the converter is designed in modular way which means that each arm is constructed by connecting individual sub-modules in series. Each sub-module contains its own DC capacitor which eliminates the need of additional DC capacitor at the DC link. The output voltage level is then the function of the number of sub-modules in each arm. By this design, the power rating of the converter can just be increased by increasing the stack of the sub-modules [29–31].

With the increase of power electronics devices such as VSCs in the network, the inertia in the system is reduced which affects the overall system dynamics, and the VSCs must also ensure the system stability [32]. The interaction of VSC with network for offshore wind power plant integration is happened at three levels i.e at onshore grid connection point, in the DC network, and in the offshore AC network. Typically, the VSC connected with the onshore network is synchronized with grid frequency and controls the power flow either by direct or vector control method [33]. The direct control

method does not have the current limiting capability and its bandwidth is limited due to AC resonance frequencies. On the other hand, the vector control manipulates the current to control the power flow in the rotating reference frame. The vector control method enables the decouple control of active and reactive power flow, however the transformation of signals into $dq0$ rotating frame introduces the 2ω cross-couple oscillation produced by positive and negative sequence current injection under unbalanced grid voltage condition [34]. This oscillation can be damped by employing active and passive filtration methods [35–38]. There are different variants of passive filters such as L, LC, LCL etc. Passive filter are required particularly in two or three level PWM converters [39–42]. It is suggested that the LCL filter are more cost-effective compared to L-filters since a smaller inductor can be applied to achieve the same reduction in the switching harmonics [43]. For MMC based converter, a simple L-filter can provide the necessary harmonic reduction in the system.

Usually, onshore grids are operated at their maximum level to fully utilized infrastructure. In this situation, the transient behavior of the system has uttermost importance in order to prevent operational limits violations and instability. The TSOs define the required characteristics in their grid codes for the generation units (for example VSCs and wind turbines), which includes both short circuit and normal operation such as voltage support, fault-ride through, frequency support etc [44–46]. Among the grid code requirements, fault-ride through (FRT) is the most critical and important requirement that need to be fulfilled at the point of common coupling (PCC). In FRT support, it is required that the generation units must not be disconnected after few millisecond (approximately 150 ms) during a fault [47, 48]. In VSCs, such a characteristic is achieved by employing a DC chopper [49]. During fault period, the power is dissipated through DC chopper to maintain the DC voltage within the operational limits. Furthermore, VSCs are required to inject only reactive current to support the grid voltage during grid fault.

The stability of the DC network highly depends on the control of the DC voltage [50]. In the VSC-HVDC system for integrating offshore wind energy, the onshore converter has the main responsibility to control the DC voltage regardless whether the DC network is a point-to-point link or

MTDC. In the point-to-point configuration, the onshore converter has the sole responsibility to maintain the DC voltage which is typically achieved by applying proportional-plus-integral (PI) control system [51]. For the MTDC network, there are several voltage control strategies proposed in the literature such as centralized DC slack bus control, voltage margin control, and distributed voltage droop control [52]. Using droop control, the responsibility to balance the DC voltage is distributed among several onshore VSC in the MTDC system without communication signals. The voltage droop control provide robust performance as well as power sharing among converters [53, 54]. The voltage droop control is either based on current or power feedback signal. The distribution of the net power in a MTDC network among converters can be made by selecting appropriate droop slopes, however the droop characteristic increases the complexity in power flow. The power infeed into the onshore AC grids are of fluctuating nature due to wind power variation. Furthermore, it is difficult to steer power between converters with droop schemes. In order to compensate these limitations, the enhancements in the droop control scheme have been proposed such as dead-band droop control, ratio control, priority control etc [55–58]. Generally, the control of the DC network regulate the DC voltage that varies the power flows in the cables. Although the power losses in the DC cable is less than the AC cable, an optimal power flow (OPF) algorithm of the combined AC and DC network is required to achieve the desire steady-state operating points [59–62]. Additionally, the OPF algorithm provides the control parameters considering criteria such as minimizing losses, cost function, voltage deviation etc.

The protection of the MTDC network is one of the important issue nowadays [63, 64]. The DC circuit breaker is still a new technology which has relatively high cost. There are several types of DC circuit break technologies exist such as mechanical circuit breaker with passive or active resonance circuit, hybrid technology which is the combination of mechanical and controllable solid-state devices, and pure solid-state circuit breaker. The performance of the DC circuit breaker is related to its interruption time, power losses, and availability in different voltage and current rating. The DC fault requires fast interruption time compared to AC fault. The mechanical

circuit breaker can interrupt up to 60 ms whereas pure semiconductor based circuit breaker interruption time can be achieved less than 1.0 ms. The mechanical circuit breaker has the lowest power losses due to lower voltage drop across the metallic contact of the main circuit breaker connected in the normal conduction path. The power loss during normal operation is less than 0.001 % in the mechanical circuit breaker, and the power loss up to 0.1 % may occur in the hybrid circuit breaker. Pure semiconductor based circuit breaker has the highest power loss due to the presence of several switching devices in the main current conduction path. The mechanical circuit breaker is available in high voltage and current rating i.e up to 550 kV and 8.0 kA. The hybrid circuit breaker has comparatively lower voltage rating i.e 120 kV. However, its theoretical current rating can goes up to 16 kA. Pure semiconductor circuit breakers are mainly available for medium voltage level applications. The DC network protection scheme greatly depends on the MTDC topologies (such as ring, star, star with central switching ring, wind power plant ring, substation ring) based on the criteria of redundancy, flexibility and need of communication [16, 65].

The offshore AC network connected with main land AC grid via only VSC based HVDC transmission system is like an island network. The offshore converters of VSC-HVDC transmission system needs to be operated in the grid forming mode in order to operate offshore AC network. In grid forming mode, VSCs impose the frequency and voltage on the offshore AC network. Unlike the onshore grid, this isolated offshore network does not have any natural inertia when the wind power plant is equipped with Type IV wind turbines. The performance of VSC voltage and current control is predominant against any disturbance in the network and they must ensure the network stability [66]. In the grid forming mode, there is no direct relationship between frequency and active power in the network. In order to operate the offshore AC network similar to the principle of a network having convention synchronous machines, frequency and voltage droop schemes can be applied for parallel connected grid forming VSCs [67–71]. The active power sharing among the grid forming converters can be controlled using frequency droop control. And the reactive power contribution by each grid forming VSCs is controlled through voltage droop control [72, 73].
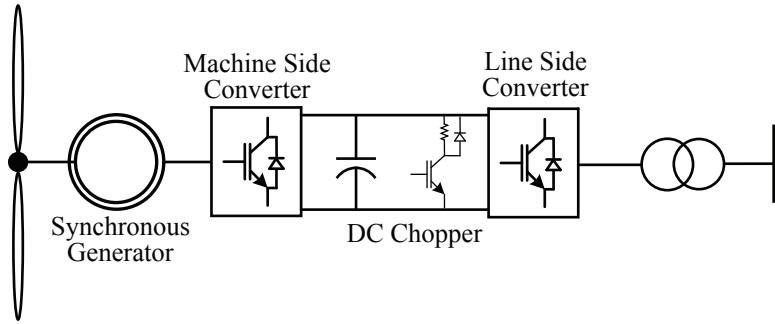
Figure 1.6: Permanent magnet synchronous machine with full rated power
converter.

With the increase of wind energy penetration into the main grid and the
reduction in conventional generation units such as nuclear power plants, the
TSOs requires that the large offshore wind power plants also participate in
the primary frequency regulation. The frequency support to the main land
AC grid by wind generation units is achieved by traversing the frequency
variation over the DC link [74–76]. The variation on the DC link can then
be reflected on the VSC imposed frequency in order to reduce the wind
generation units power output [77]. Nowadays, the TSOs demand that the
wind generation units must have the performance similar like a conventional
synchronous machine [47, 78–80]. A permanent magnet synchronous machine
with full rated power converter is the most favorable wind generation unit
in order to fulfill the TSOs requirements. The direct-driven wind turbine
configuration is shown in Figure 1.6. In this configuration, the rotor axis
is connected without gearbox with the synchronous machine. Due to the
permanent magnet, no additional power is needed for field excitation. The
produced power is injected into the connected network through back-to-
back converters. The machine side converter (MSC) is operated at variable
frequency to track the turbine characteristics i.e rotor speed corresponding to
the power at each wind speed. The line side converter (LSC) is synchronized
with the grid frequency and injects received power into the grid. The
converters size must be equal to the rated power of the generator which
is a disadvantage. Typically, a DC chopper is installed between MSC and
LSC converters to dissipate the excess power during grid faults [81–86]. The

main advantage of this configuration is the independent control of active and reactive power by LSC. By this, the wind generation units can fully participate in the optimization procedure to optimally flow the power in the network [87–89].

1.4 Offshore Grid Challenges

The offshore grid is inevitable for the integration of offshore wind energy either it is trade driven or trade unconstrained [90]. There are various technical challenges associated with the formation of offshore grids that has to be addressed and solved. The three challenges which are identified in this section are analyzed in this thesis. They arise because of no direct AC connection exists between the offshore grid and the main onshore AC grids and the governing principle of operational control do not apply directly as on the onshore AC network.

System Integration and Power Flow Control: The future offshore grid will not serve a single purpose. It will cover several application such as integration of offshore wind energy, provides interconnections for power balancing, international trade, bootstraps etc [10]. However, the unique offshore grid infrastructure cannot be built at once rather it will grow organically with time from simple initial phase to fully functional integrated network. The main challenge is to adopt the approach of building the system that can be expanded with minimum modification both from the prospective of control and network infrastructure. The future offshore grid must evolve from the network currently exists in the North and Baltic sea.

After the definition of a suitable network architecture, the next step is to establish a mechanism of power flow control for the integrated AC and DC network. Although the power electronics devices provide the flexibility and sufficient control over the power flow, suitable control schemes and optimization algorithms are required for both AC and DC network operation especially considering the power sharing constraints of TSOs and long term network stability.

Dynamics and Stability: The dynamics and stability of the network are the major issues on which the successful operation of the offshore grid highly rely. The offshore AC network control analogue to onshore network requires the operation of inverters in parallel. The control schemes for inverters connected in parallel have been introduced but so far is applied for small scale micro-grid or island network [69]. The principle of controlling offshore AC grid using frequency and voltage droop scheme in inverters makes power balancing phenomena similar to the network with synchronous machines [71]. However, the dynamic response of the offshore AC grid is different as compared to onshore grid due to the absence of inertia and fast response of power electronics. The droop gain analysis along with the inverter voltage and current control performance is the key aspect that needs to be address for the control design of offshore AC grids.

The main difference between island network and offshore AC grid is the cable capacitive effects. The micro-grid or island network is assumed more resistive while the offshore AC grid is more capacitive. The inverters in the offshore AC grids are acting like reference machines or slack sources which absorb the network power by controlling voltages. The rise in the voltage set-point due to voltage droop scheme as the function of absorb reactive power creates a chain reaction between network reactive power and voltages. This effect is significant in offshore AC grid due to the high cable capacitance which could produce the long term voltage instability [91, 92]. Thus, it is crucial to determine the criteria for the selection of voltage droop gain to keep system stable while keeping the characteristic of reactive power distribution by the VSCs.

Fault Behavior: The large wind energy generation must not be disconnected to ensure the onshore grid stability. It is desirable to have the same characteristics for the future offshore grid as for onshore grid regarding reliability and availability. The use of DC circuit breaker is imperative to ensure the selectivity in the MTDC network [65]. The DC circuit breaker technology is at an early stage of development however it is expected to be available at the final stage of offshore grid development.

The fault protection scheme can be developed using AC circuit breaker

for the offshore AC network that are either connected to a single or multiple onshore grids using point-to-point VSC-HVDC system. Although the VSC capability will not be the constraint of short circuit current level within the offshore AC network due to the contribution of fault by the multiple wind power plants, the short circuit current control characteristic of the inverters is the main concern for the successful operation of the network. The offshore inverter must also have current control to ensure the fast response against faults and to be able to manipulate the short circuit current characteristic directly [22]. Although the wind power curtailment requirements due to the over frequency in the network could be derived from the onshore grid codes, the offshore AC network frequency behavior and its operational characteristics still must to be analyzed as the inertia is very low as compared to onshore network [77]. A well coordinated frequency control system is still needed considering the dynamic and stability limitation imposed by offshore inverters.

1.5 Objective and Research Questions

Based on the offshore grid challenges identified, the aim of this research is drafted around the operational principle of the network shown in Figure 1.3. The main objective of the thesis is:

> *to design and analyze the control system of voltage source converter in the offshore grid to interconnect offshore wind power plants with multiple onshore grids*

The above mentioned objective is achieved by formulating the research questions and addressing each of them in the subsequent chapters. These questions are given as follows:

1. *What is the control architecture of voltage source converter that can be extended to fulfill different operational modes necessary by the offshore grid without changing its fundamental structure?*

2. *How can an offshore AC network consisting of multiple grid forming*

voltage source converters be operated?

3. *What is the impact of frequency and voltage droop control of the voltage source converter on the offshore AC network dynamic and stability?*

4. *Which are the onshore and offshore AC fault management schemes of the voltage source converter, and how can power reduction coordination be established between wind generation units and offshore voltage source converters?*

5. *How an offshore AC network can be integrated with a multiterminal DC network?*

1.6 Contributions and Innovation

The results of the thesis contribute in the aspects of modeling, power flow control, short circuit control, dynamic, and stability analysis of the voltage source converter for the offshore grid application. The main contributions are listed as follows:

- A method of modeling the voltage source converter is proposed from the prospective of its control operation, and its integration with the offshore AC network. The linearized models are developed in order to apply the linear control theory for dynamic and stability analysis.

- An enhancement in the voltage decoupling scheme has been proposed for the grid forming control of VSC to improve the transient voltage response.

- A method of performing stability analysis for VSC current, voltage, and power control is proposed which provides the stability criteria of each control loop. The VSC controller parameters are tuned based on this method.

- The frequency and voltage droop scheme is developed for an offshore AC network control by multiple grid forming VSC. The research presents a method of selecting droop gains according to power sharing

criteria. Also, a criteria to select voltage droop gain is proposed to ensure long term voltage stability.

- A multi-objective optimal power flow algorithm is developed for an offshore AC network having multiple grid forming VSC to minimize active power losses and voltage deviation.

- A method of small-signal analysis for an offshore AC network is proposed to determine the impacts of frequency and voltage control on the network stability. The developed model includes the dynamics of the VSC voltage and current control loop in conjunction with the droop loop in order to consider the complete performance of the VSC in the overall system response.

- A method of performing short circuit analysis is proposed for an offshore AC network which integrates wind power plants with different onshore grids. Based on the analysis, short circuit control for offshore VSCs and wind generation units is developed.

- A coordinated frequency control is proposed for offshore VSCs and wind generation units. The control scheme allows the reduction in wind power generation without using communication signals in case of over frequency. The control scheme provides the remedy of over voltages during disturbance period that appears due to low inertia in the network.

- An optimal DC power flow algorithm is developed to determine the VSC DC voltage controller gains for an offshore multiterminal DC network according to the power sharing criteria.

- Based on several case studies, the research presents a gradual approach to build an integrated offshore AC and DC hub.

2 Voltage Source Converter Control System

In this chapter, a voltage source converter dynamic modeling and stability analysis have been presented. Five operational modes of the VSC are explained and linear control theory is applied to design the controller. The architecture of the VSC control is configured in a cascaded form, thus a sequential approach has been adopted for designing controller gains. The VSC control has two main control loops that are referred as an inner and outer control loops. The inner control loop is always a current feedback system. And, the outer control loop depends upon the operational mode of the VSC i.e. reactive power control, active power control etc. At the end of the chapter, the controller design methodology has been validated by performing nonlinear simulations using MATLAB/SIMULINK[1].

2.1 Introduction

The dynamics of any physical system can be understood by defining its behavior using differential equations. Often, the derived mathematical model of the system is nonlinear. However, the model may behave linearly within a certain operating range of the equilibrium point. A linear model of the system enables the application of the linear control theory and the design procedure of the control system is rather simple.

Generally, a nonlinear system can be approximated to a linear system by

---

[1]This chapter is based on the following publication:

M. Raza, and O. Gomis-Bellmunt, "Dynamic modeling and implementation of VSC-HVDC system: A grid connected offshore wind farm application" in Proceedings of the 3rd International Conference on Smart Grids and Green IT Systems, (Barcelona, Spain), pp. 53-62, apr 2014.

(a) V-canonical form   (b) P-canonical form
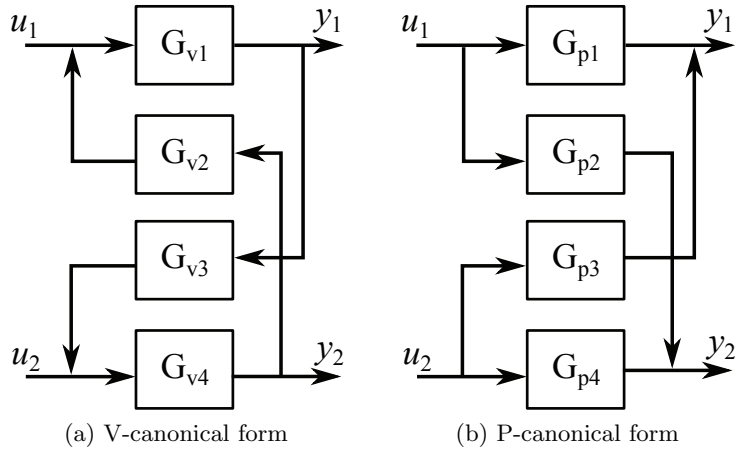
Figure 2.1: MIMO structures of two input two output system.

using first order Taylor series expansion about the operating point. Such as, a nonlinear function $f(x, u)$ can be linearly represented as (2.1).

$$\dot{x} = f(x, u)$$

$$f(x, u) \approx f(x_0, u_0) + \left.\frac{\partial f}{\partial x}\right|_{\{x_0, u_0\}} (x - x_0) + \left.\frac{\partial f}{\partial u}\right|_{\{x_0, u_0\}} (u - u_0) \tag{2.1}$$

Dynamic equation describes the state of a system through a set of state variables. These state variables determine the future behavior of the system with respect to the present states and the input signals. The dynamics of the linear time invariant (LTI) system can be expressed by its differential equation in a state-space representation using (2.2).

$$\dot{x} = Ax + Bu$$
$$y = Cx + Du \tag{2.2}$$

Here, x is the state vector, A is a system matrix, B is the input matrix, u is a vector of input signals, C is the output matrix, D is the disturbance matrix, and y is the vector of output signals.

A system is said to be a single-input single-output (SISO) system, if one

output is controlled by a single manipulated variable. However, most of the systems do not exhibit such a simple control configuration. A system may contain more than one output and being influenced by multiple input signals. Such a control configuration is known as multi-input multi-output (MIMO) system. In any MIMO system, there exist at least two or more control loops and quit often these loops may act against each other in order to achieve their respective objectives. Such an interaction between control loops can cause the instability in the system. Several methods exist to design control system for MIMO system such as singular value analysis, pairing of controlled and manipulated variables, tuning of multi-loop PID control systems, decoupling control strategies etc. A selection of a reliable control technique depends on the structure of a linear system model in order to ensure the control scheme resembles the dynamics of the system. The two most common model representations of MIMO system are the V- and P-canonical as illustrated in Figure 2.1. In the P-canonical form, the loop interaction has the form of feed-forward coupling and in V-canonical form it is feedback coupling. Contrary to P-canonical form, a change in one input in V-canonical form will not only affect all outputs but it will also influence the input signals. There is no explicit rule which model form is more useful. However, any model form must represent the actual system dynamics and should be able to give necessary data for the control system design.

In the dynamics of the power system components, the state variables are voltage, current, power, and frequency. An instantaneous three phase balanced voltage in an electrical network is a nonlinear time variant function as expressed by (2.3). A time variant system explicitly depends on time and is not stationary. A control system design is relatively complex for a time variant system.

$$
\begin{aligned}
u_a(t) &= Um \sin\left(\omega t + \delta\right) \\
u_b(t) &= Um \sin\left(\omega t - 2\pi/3 + \delta\right) \\
u_c(t) &= Um \sin\left(\omega t + 2\pi/3 + \delta\right)
\end{aligned}
\tag{2.3}
$$

Often, it is of interest for power system studies to analyze the change in the network state variables with respect to the disturbances and the

(a) Axis orientation

(b) Three Phase AC Voltage

(c) Voltage transformation into
$\alpha\beta\gamma$ components

(d) Voltage transformation into
$dq0$ components
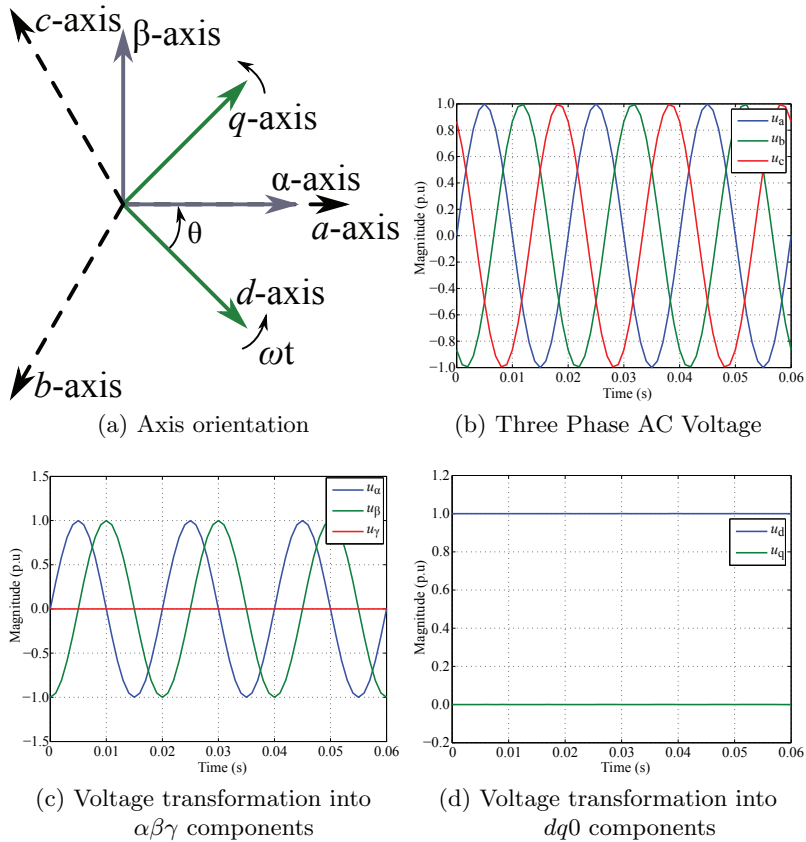
Figure 2.2: Axis transformation from abc to dq0 frame.

control signals rather than time. By using Clarke and Park transformation theory, measured time variant signal can be transformed into $dq0$ rotating coordinate frame from the three phase stationary coordinate frame. This transformation theory is a mathematical tool formulated to simplify the solution of the system equation by transforming from one coordinate into another coordinate system. The transformation method applies two steps: firstly, a transformation from the three phase stationary coordinates system to the two-phase, so-called $\alpha\beta\gamma$ stationary coordinate system, and secondly, a transformation from the $\alpha\beta\gamma$ coordinate system to the $dq0$ rotating coordinate system. The axis transformation principle is illustrated in Figure 2.2. A three phase balanced voltage is transformed into two orthogonal component

using (2.4). The α component is aligned with phase-a of the voltage signal. The β component has a phase shift of $-\pi/2$ with respect to α, and the γ component is always zero for a balanced system. Thus, voltage α and β component can be expressed in complex form as (2.5).

$$\begin{bmatrix} u_\alpha(t) \\ u_\beta(t) \\ u_\gamma(t) \end{bmatrix} = \frac{2}{3} \begin{bmatrix} 1 & -\frac{1}{2} & -\frac{1}{2} \\ 0 & \frac{\sqrt{3}}{2} & -\frac{\sqrt{3}}{2} \\ \frac{1}{2} & \frac{1}{2} & \frac{1}{2} \end{bmatrix} \begin{bmatrix} u_a(t) \\ u_b(t) \\ u_c(t) \end{bmatrix} \tag{2.4}$$

$$\underline{u}_{\alpha\beta} = u_\alpha + ju_\beta = U_m e^{j(\delta(t)-\pi/2)} \quad \because \delta(t) = \omega t + \delta \tag{2.5}$$

By rotating the coordinate frame with the angular frequency of the reference system, the two stationary orthogonal components can be transformed into rotating components. Furthermore, if the rotating frame is aligned with the measured busbar voltage, then the busbar is referred as reference bus and the voltage d-component is U_m, and the q-component is zero as expressed by (2.6).

$$\underline{u}_{dq} = u_d + ju_q = \underline{u}_{\alpha\beta} e^{-j(\delta(t)-\pi/2)} = U_m + j0 \tag{2.6}$$

Here, $e^{-j(\delta(t)-\pi/2)}$ is the reference bus synchronization factor. Now, the same approach is used to transform the measured current of a branch into $\alpha\beta$ components as expressed in (2.7).

$$\underline{i}_{\alpha\beta} = I_m e^{j(\psi(t)-\pi/2)} \quad \because \psi(t) = \omega t + \psi \tag{2.7}$$

The current is then transformed into voltage synchronous rotating frame by multiplying with the synchronization factor as given in (2.8). It is clear that the current in the dq rotating frame is the function of current and load angle.

$$\begin{aligned} \underline{i}_{dq} &= I_m e^{j(\psi(t)-\pi/2)} \cdot e^{-j(\delta(t)-\pi/2)} \\ &= I_m e^{-j(\delta-\psi)} \\ i_d + ji_q &= I_m \left\{ \cos(\delta-\psi) - j\sin(\delta-\psi) \right\} \end{aligned} \tag{2.8}$$

The $dq0$ transformation matrix is orthogonal and it posses the property

$T(\omega t) \cdot T^{-1}(\omega t) = I$. By applying inverse transformation, the signals can be transformed from $dq0$ frame to abc frame i.e.

$$u_{abc}(t) = T^{-1}(\delta(t))u_{dq0}$$

$$\begin{bmatrix} u_a\,(t) \\ u_b\,(t) \\ u_c\,(t) \end{bmatrix} = \begin{bmatrix} \sin(\omega t) & \cos(\omega t) & \frac{1}{2} \\ \sin(\omega t - 2\pi/3) & \cos(\omega t - 2\pi/3) & \frac{1}{2} \\ \sin(\omega t + 2\pi/3) & \cos(\omega t + 2\pi/3) & \frac{1}{2} \end{bmatrix} \begin{bmatrix} u_d \\ u_q \\ u_0 \end{bmatrix} \tag{2.9}$$

2.2 Voltage Source Converter Averaged Model

For the future offshore wind power plants development, it may be desired for the application of HVDC system to have two main characteristics i.e an ability to have bi-directional power flow (from AC to DC network, and vice versa) without changing the voltage polarity, and the ability to create an electrical grid. With the advancements in semiconductor devices such as the insulated-gate bipolar transistor (IGBT), voltage source converters (VSC) are gaining preference over line commutated converters (LCC). A two-level converter is the simplest type of voltage source converter. As the name implies, a two-level converter switches the output voltage between two levels i.e $+U_{dc}/2$ and $-U_{dc}/2$, however it produces relatively more harmonics compared to other types. Several pulse-width-modulation (PWM) techniques are being developed to control the fundamental signal magnitude and to reduce the harmonic in the output voltage. The most common modulation strategies are selective harmonic elimination (SHE), sinusoidal pulse width modulation (SPWM), and space vector modulation (SVM). In the PWM technique, IGBTs are operated at a high frequency consequently converter produces higher switching losses approx 2 to 3 %. Also, the step change in the output voltage due to switching is large which limits the development of high capacity converters.

In 2003, a new converter topology was developed, commonly known as modular multilevel converter (MMC). The topology of a MMC-VSC is illustrated in Figure 2.3. Each leg of the MMC is split into two arms (upper and lower), and each arm consist of a series reactor and several identical sub-modules connected in series. The sub-modules are individually
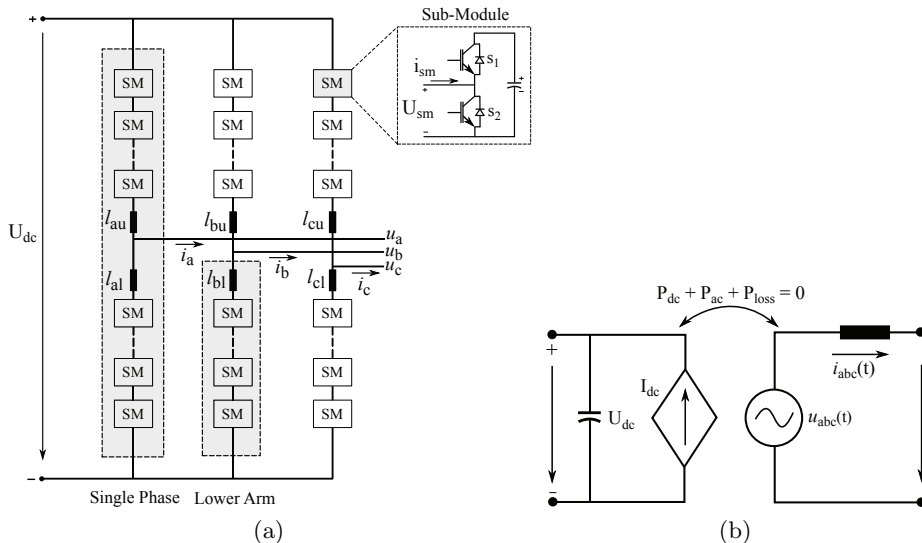
Figure 2.3: MMC VSC converter and an equivalent averaged model.

controllable and each have their own capacitive storage. There are different sub-modules variants according to the semiconductor configuration, but the most common one is a two level half bridge converter. In the two-level half bridge variant, each sub-modules can produce two voltage levels i.e U_{sm} or zero. By connecting the sub-modules in series, the converter is able to generate output voltage in high number of small discrete steps. The converter output voltage can be generated very close to a sine-wave by synthesizing the step voltages which can have very low harmonics content.

The use of voltage source converters has a large impact on the power system and an appropriate model is required for the system analysis. The detailed MMC-VSC model contains large number of switching devices which slow down the simulation process due to the small simulation time steps. The use of detailed models is restricted to component level and fault studies. An averaged model which can reproduce the dynamic performance accurately is sufficient for the study of slow dynamic stability phenomena and performance analysis within a large scale AC network [93]. The averaged model of the voltage source converter is given in Figure 2.3b. The ability of the VSC to generate AC output voltage depends on the DC voltage level. Thus in the
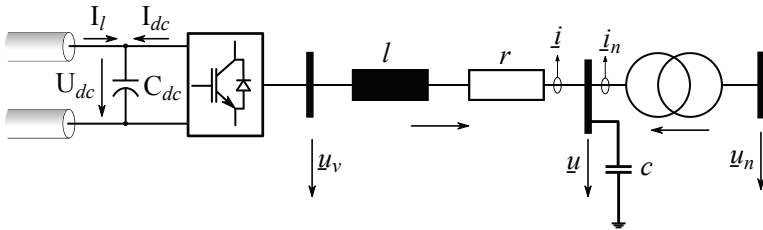
Figure 2.4: Voltage source converter substation configuration.

average model, the AC side is modeled as a DC voltage controlled three phase AC voltage source and DC side as a controlled current source. In a balanced system, the AC power is equal to the DC power including converter losses. The three phase AC output voltage has only fundamental frequency signal and can be expressed using (2.3). The balanced three phase voltage magnitude and angle are defined as (2.10).

$$U_m = m \cdot U_{dc} \cdot \sqrt{u_{v\_d}^2 + u_{v\_q}^2}, \qquad \delta = \tan^{-1}\left(\frac{u_{v\_q}}{u_{v\_d}}\right) \qquad (2.10)$$

Here, m is the modulation index, u_{v_d} and u_{v_q} are the control signals in p.u generated by the VSC controller in $dq0$ frame. A typical configuration of a voltage source converter (VSC) substation is shown in Figure 2.4. It consists of a VSC and its control unit, AC filter capacitor, series reactor, DC filter capacitor, and transformer. In the average model of the VSC, the voltage at the busbar connecting with the VSC can be considered as applied converter controlled voltage. The series reactor is designated as the arm inductance and/or additional inductance for smoothing current. Further, it also limits the short circuit current as well as enables the power flow control. The AC filter capacitor is installed to filter out the harmonics and to provide reactive power support to the network. The dynamic of the DC capacitors connected in the converter can be characterized by referring them with equivalent capacitance at DC side connecting in parallel with the current source. The transformer steps up the voltages and connects the VSC system with the network of different voltage levels. The grid connection point is usually established at the transformer busbar and the operational mode of the converter depends on the type of the connection such as; grid
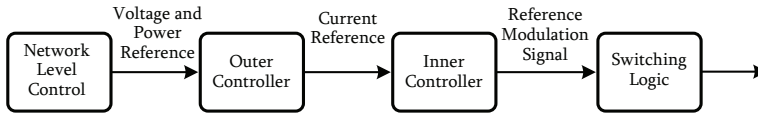
Figure 2.5: Overview of cascaded voltage source converter control.

synchronous mode or grid forming mode.

Vector control is a well known method that is being applied for the design of VSC control system. In this method, a $dq0$ transformation theory is utilized to transform the signal into voltage synchronous rotating frame. The reference voltage rotating angle is measured across the AC capacitor busbar. In $dq0$ rotating frame, the measurement and the control signals can be considered as phasor quantity for the control system design. For a balanced system, the d-component of the variables can be designated as real component on the complex plane and q-component as imaginary, whereas the third component is always zero.

An overview of the VSC control scheme is illustrated in Figure 2.5. A reference modulation signal for the switching logic is generated by inner controller which is typically a current control closed loop system. The reference current command is generated from the outer controller. The outer controller could be based on voltage or power closed loop control depending on the required operational mode. The inner and outer controller are local control system. A network level control system could be a part of a local or centralized control system. The network level control system usually defines the reference command for outer controller according to the whole network requirement e.g to optimize losses in the network, to provide frequency support, enable import and export etc. The control loops in the converter control system are implemented in cascaded form and can be designed sequentially.

2.3 Grid Synchronous Control of VSC

In this operational mode, the VSC is synchronized with the grid and injects power at the grid frequency. The reference rotating angle is obtained
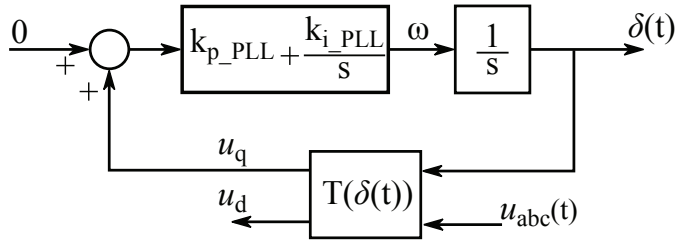
Figure 2.6: Phase-locked loop control system for converter grid synchronization.

using a phase-locked loop (PLL). The VSC explicitly controls the current through the series reactor which consequently controls power flow. By utilizing a decoupled scheme, active and reactive current can be controlled independently. The reference current set-points are defined with respect to voltage and power set-points. There are four operational controls in this mode i.e active power control, reactive power control, AC voltage control, and DC voltage control.

2.3.1 Phase-Locked Loop for Grid Synchronization

A control system that generates an output signal that has the same phase as of input signal is called as phase-locked loop (PLL) system. The PLL provides a rotating angle for $dq0$ transformation in order to synchronize the VSC control system with the grid frequency. A PLL scheme similar to the one presented in [94], is adopted for the grid synchronization. The PLL control system is illustrated in Figure 2.6. The measured voltage signal is transformed into $dq0$ rotating frame using (2.11). The rotating angle is the feedback signal of the PLL output.

$$
\begin{bmatrix} u_d & u_q & u_0 \end{bmatrix}^T = T(\delta(t)) \begin{bmatrix} u_a(t) & u_b(t) & u_c(t) \end{bmatrix}^T
$$

$$
T(\delta(t)) = \begin{bmatrix} \sin(\omega t) & \sin(\omega t - 2\pi/3) & \sin(\omega t + 2\pi/3) \\ \cos(\omega t) & \cos(\omega t - 2\pi/3) & \cos(\omega t + 2\pi/3) \\ \frac{1}{2} & \frac{1}{2} & \frac{1}{2} \end{bmatrix} \tag{2.11}
$$

The transformation is applied in p.u system and the orientation of the

dq frame is aligned such that at synchronization the *d*-component would be 1.0 p.u, and the *q*-component is zero. The proportional-plus-integral (PI) control scheme is applied to acquire the desired performance and to ensure system stability. By applying Laplace transformation, the PLL closed loop control can be represented with the second order transfer function and the selection of the controller gains can be made using (2.12).

$$
G(s) = \frac{k_{p\_PLL} \cdot s + k_{i\_PLL}}{s^2 + k_{p\_PLL} \cdot s + k_{i\_PLL}}
$$
$$
k_{p\_PLL} = 2\omega_n \zeta, \quad k_{i\_PLL} = \frac{1}{\omega_n^2}
$$

$$(2.12)$$

Here, k_{p_PLL}, and k_{i_PLL} are the proportional and integral gains, ω_n is the natural frequency, and ζ is the damping factor. Further detail is given in [94]. This type of PLL is the simplest and widely applied in different power system applications. It is also known as 'Synchronous Frame PLL (SF-PLL)'. There are other advanced methods of phase detection such as PQ-PLL based on instantaneous real and imaginary power theory, double synchronous frame PLL (DSF-PLL), sinusoidal signal integrator PLL (SSI-PLL), double second order generalized integrator PLL (DSOGI-PLL), three phase magnitude PLL (3M-PLL), enhanced PLL (EPLL), etc. The SF-PLL with high bandwidth provides fast and precise phase detection of the non distorted input signal. The SF-PLL can still exhibit sufficient performance with the input signal having high order harmonics on the cost of PLL response speed. Furthermore, SF-PLL scheme cannot be applied straightforward to single phase system and it provides the average information of phase, frequency, and magnitude rather than individual phases. In [95], it is highlighted that the SF-PLL may fail to synchronize in some adverse conditions during start-up. It may achieved the stable operational point in the presence of harmonics synchronized with the subharmonic frequency. The PQ-PLL usually provides remedy to this issue. Another scheme such as DSF-PLL, also cover the limitation of SF-PLL by detecting the phase angle using both positive and negative sequence components of the input signal. There are many more PLL schemes however the selection of the suitable scheme depends on the specific requirements and applications [96].
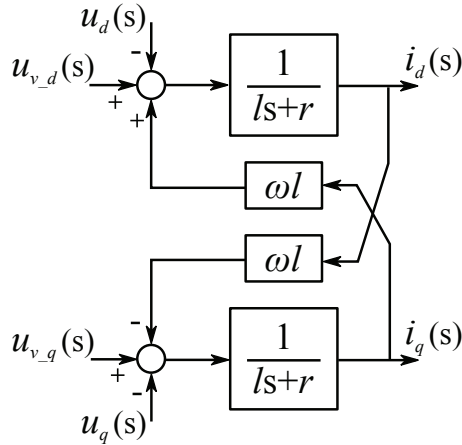
Figure 2.7: Converter current open loop model.

2.3.2 Current Control

The inner controller controls the current through a series reactor. According to the laws of Kirchhoff, the current flow through the reactor is proportional to the difference of the converter and the filter bus voltages. The differential equation of the reactor current can be written as (2.13).

$$l\frac{d\underline{i}}{dt} + r\underline{i} + j\omega l\underline{i} = \underline{u}_v - \underline{u} \tag{2.13}$$

Here, l and r are the inductance and resistance of the series reactor, $\underline{i}$ is the current flowing through the reactor, ω is the network frequency, $\underline{u}_v$ is the voltage applied by the VSC, and $\underline{u}$ the voltage at the filter bus. Further, the reactor current is a nonlinear function and can be expressed using state-space representation in the $dq0$ coordinates as (2.14).

$$\begin{bmatrix} \dot{i}_d \\ \dot{i}_q \end{bmatrix} = \begin{bmatrix} -\frac{r}{l} & \omega \\ -\omega & -\frac{r1}{l} \end{bmatrix} \begin{bmatrix} i_d \\ i_q \end{bmatrix} + \begin{bmatrix} \frac{1}{l} & 0 \\ 0 & \frac{1}{l} \end{bmatrix} \begin{bmatrix} u_{v\_d} - u_d \\ u_{v\_q} - u_q \end{bmatrix} \tag{2.14}$$

The stability of the system is determined by the roots of its characteristic equation and they must lie on the left hand side of the complex plane. In a state-space model, roots of the system can be directly calculated by performing eigenvalues analysis. The Eigenvalues of the open loop current
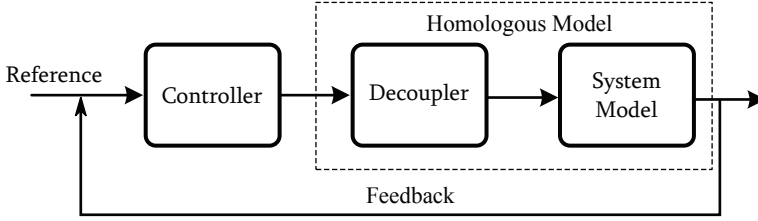
Figure 2.8: A generalized closed loop control structure including state de-
coupling scheme.

model are given in (2.15). The Eigenvalues express that the system response
is under-damped having natural frequency of ω and the damping factor is
equal to $r/\omega l$.

$$s_{1,2} = -\frac{r}{l} \pm j\omega \tag{2.15}$$

Further, it can be noticed from the converter current open loop model
(Figure 2.7) that the d-component and q-component of the current are
coupled. The open loop model is a MIMO system in V-canonical form and
it has current d- and q- control loop interactions. The decoupling control
scheme is a most common approach for linear MIMO system to eliminate
the effects of loop interaction. A generalized closed loop control including
state decoupling scheme is shown in Figure 2.8.

Consider the same V-canonical form as of the system model for designing
the decoupling control scheme as shown in Figure 2.9. The input and output
relationship of the system shown in Figure 2.9 is given in (2.16). It is clear
that the control model is a MIMO system with no elements in the cross
diagonal input matrix, but with non-zero elements in the cross diagonal of
the output feedback matrix.

$$
\begin{bmatrix} y_1 \\ y_2 \end{bmatrix} = \begin{bmatrix} G_1 & 0 \\ 0 & G_4 \end{bmatrix} \begin{bmatrix} u_1 \\ u_2 \end{bmatrix} + \begin{bmatrix} G_1 G_5 & 0 \\ 0 & G_4 G_8 \end{bmatrix} \begin{bmatrix} u_3 \\ u_4 \end{bmatrix} + \begin{bmatrix} G_1 G_5 & 0 \\ 0 & G_4 G_8 \end{bmatrix} \begin{bmatrix} u_{c\_d} \\ u_{c\_q} \end{bmatrix}
$$
$$
+ \begin{bmatrix} 0 & G_1 \left(G_2 + G_5 G_6 \right) \\ G_4 \left(G_3 + G_8 G_7 \right) & 0 \end{bmatrix} \begin{bmatrix} y_1 \\ y_2 \end{bmatrix} \tag{2.16}
$$

In order to converter into a SISO system and to control each converter
current component through only one control signal i.e u_{c_d} and u_{c_q}, the
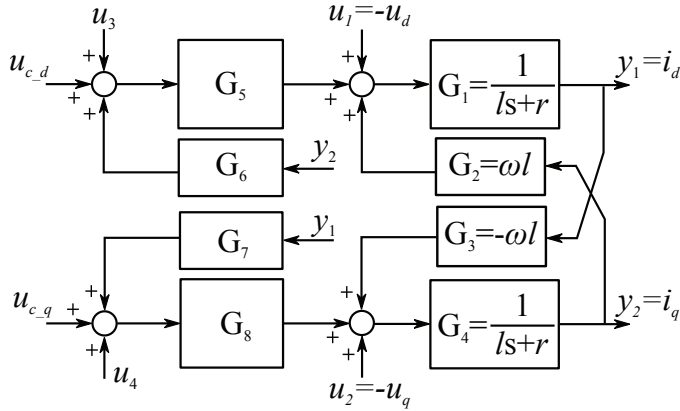
Figure 2.9: Open loop current model including decoupling scheme.

condition given in (2.17) can be applied.

$$G_5 = G_8 = 1$$
$$u_3 = -u_1 \quad \because u_3 \neq u_{c\_d}$$
$$u_4 = -u_2 \quad \because u_4 \neq u_{c\_q}$$

(2.17)

The decoupling between the output signals is achieved by applying the condition given in (2.18).

$$G_6 = -G_2 \quad \because G_1 \neq 0$$
$$G_7 = -G_3 \quad \because G_4 \neq 0$$

(2.18)

By incorporating decoupled control equations in the converter voltage reference signal as expressed by (2.19), d- and q- components of the current can be controlled independently. Thus, the open loop current model with converter control signal can be defined as (2.20).

$$u_{v\_d} = u_d - \omega l i_q + u_{c\_d}$$
$$u_{v\_q} = u_q + \omega l i_d + u_{c\_q}$$

(2.19)

$$\begin{bmatrix} \dot{i}_d \\ \dot{i}_q \end{bmatrix} = \begin{bmatrix} -\frac{r}{l} & 0 \\ 0 & -\frac{r}{l} \end{bmatrix} \begin{bmatrix} i_d \\ i_q \end{bmatrix} + \begin{bmatrix} \frac{1}{l} & 0 \\ 0 & \frac{1}{l} \end{bmatrix} \begin{bmatrix} u_{c\_d} \\ u_{c\_q} \end{bmatrix}$$

(2.20)

(a) Stability analysis model

(b) Converter control implementation model
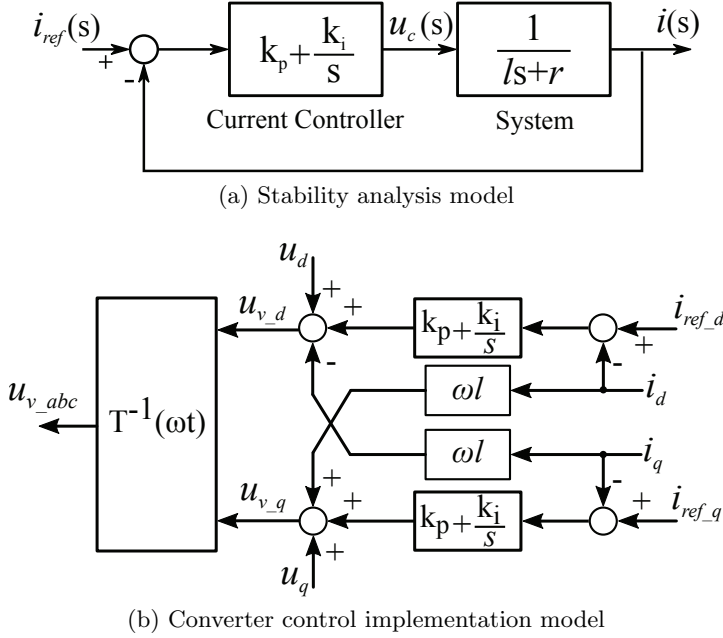
Figure 2.10: Closed loop feedback control system for current.

Now, the converter current model becomes a single-input-single-output (SISO) system, and the linear control theory can be applied to design the controller for i_d and i_q separately. The open loop system is stable and its poles lie on the left half of complex plane as given in (2.21). It is clear that there are two poles in a system; one for i_d and other is for i_q. These two states are decouple from each other and they are influenced by only one input each. Thus the control scheme can be designed using one signal and replicate it for the other.

$$s_{1,2} = -\frac{r}{l} \tag{2.21}$$

A closed loop control block diagram for the VSC current control is shown in Figure 2.10. A proportional-plus-integral (PI) control system is selected for zero steady state error. Closed-loop transfer function of the converter current with PI controller is given in (2.22).

$$\frac{i(s)}{i_{ref}(s)} = \frac{(k_i + k_p s)/l}{s^2 + (r + k_p)s/l + k_i/l} \tag{2.22}$$

(a) if $-k_i/k_p < -r/l$ (b) if $-k_i/k_p > -r/l$
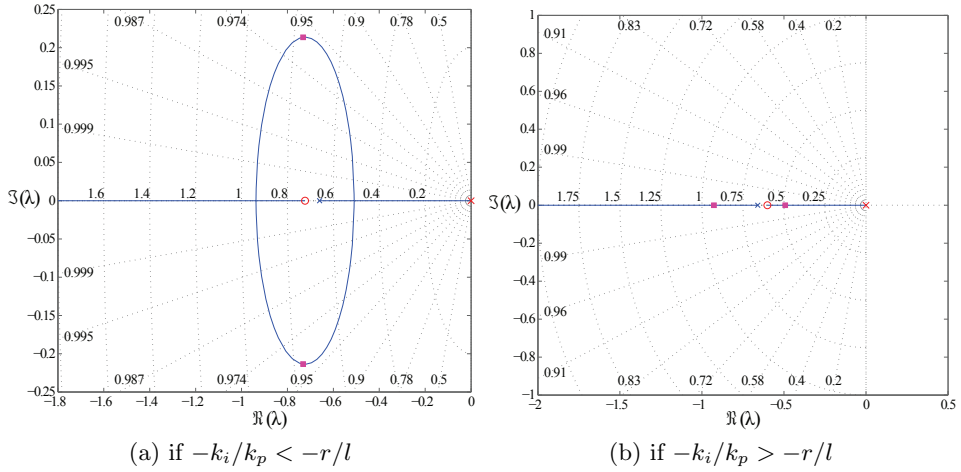
Figure 2.11: Root locus analysis of closed loop current control of the VSC HVDC system.

The closed loop system has one zero and two poles as expressed by (2.23). The root locus analysis of the current closed loop is demonstrated in Figure 2.11. The response shows that the system performance varies with respect to the location of the zero.

$$s_z = -\frac{k_i}{k_p}$$

$$s_{p\_1,2} = \frac{1}{2} \left\{ -\frac{r + k_p}{l} \pm \sqrt{\left(\frac{r + k_p}{l^2} \right)^2 - \frac{4k_i}{l}} \right\} \tag{2.23}$$

The system will exhibit damped response at all gain values if $s_z > -r/l$. However, the damping in the system varies depending how far zero is located from the system poles, when $s_z < -r/l$. Synthesis of optimum dynamic response by trial and error method is not a straightforward approach. Instead, the Integral-Time-Absolute-Error (ITAE) performance index can be applied to determine the controller gains for the optimum transient response analytically. The ITAE performance criteria are the indexes of 2nd order to 8th order normalized transfer function coefficients to minimize the error for a step input [97]. For the selection of VSC current controller gains, ITAE

(a) $\xi = 0.7, w_n = 286$ rad/s

(b) Step response: $T_s = 20$ ms
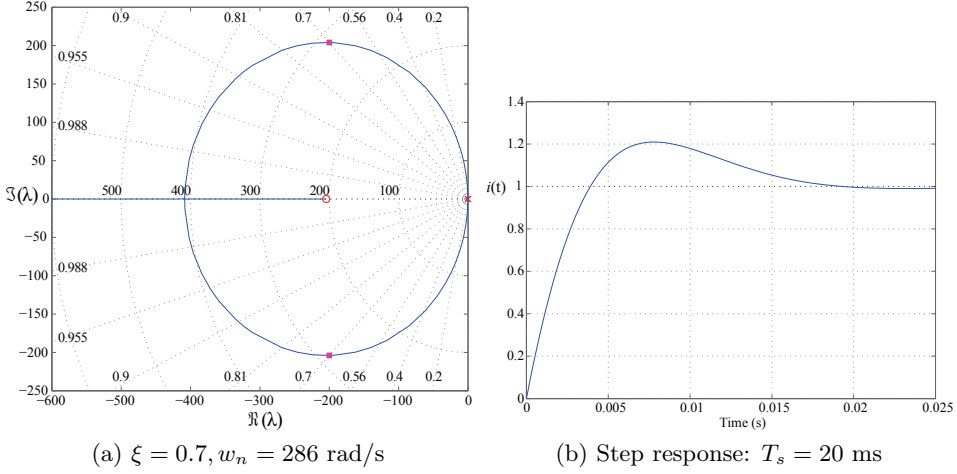
Figure 2.12: Under-damped performance analysis of the closed loop current control.

criteria is applied by using (2.24) for zero-displacement error.

$$s^2 + 1.4\omega_n s + \omega_n^2 = s^2 + (r + k_p)s/l + k_i/l$$
$$k_p = 1.4\omega_n l - r, \quad k_i = \omega_n^2 l \tag{2.24}$$
$$T_s = \frac{4}{0.7\omega_n} \quad \because \xi = 0.7$$

Here, T_s is the settling time, and ω_n is the natural frequency of the closed loop. It is to be noticed that the standard ITAE criteria is provided for the transfer function without finite zeros. This criteria can also be applied up to $\xi < 0.8$ for the transfer function that has one zero. The current closed loop performance is shown in Figure 2.12 for the under-damped condition. The overshoot in the current response can be observed in this condition. The damping in the response is increased when zeros move toward the poles. The zeros of the closed loop system influence the transient response significantly when they are located near to the dominant poles.

The influence of the zero on the current closed loop system can be analyzed by placing the zero at the dominate pole as expressed in (2.25). By substituting the value of k_i in (2.23), the current closed loop transfer function can be derived from the zeros and poles of the system as given by (2.26).

$$s_z = -k_i/k_p = -r/l,$$
$$k_i = rk_p/l \tag{2.25}$$

$$G_i(s) = \frac{i(s)}{i_{ref}(s)} = \frac{k_p/l\,(s + r/l)}{(s + r/l)\,(s + k_p/l)} = \frac{1}{l/k_p s + 1} \tag{2.26}$$

It is clear that the current closed loop will behave as a first order system by placing the zero at the dominant pole. The time constant (τ_i) of the current response can be controlled by varying proportional gain of the PI controller. The system is stable for $k_p > 0$. The calculation of the PI current controller gains using (2.27) ensure that the current response do not have overshoot during transient period and the thermal limits of IGBTs remains in the operating range.

$$k_p = l/\tau_i, \ \ k_i = r/\tau_i$$
$$G_i(s) = \frac{1}{\tau_i s + 1} \tag{2.27}$$

It is well known that any system is subjected to a changing environment and optimal model parameters are not accurately predictable. The error in estimating model parameters affects the controller performance and may not be as designed. The dynamic performance and system stability is greatly affected if designing controller gains using model parameters such as using (2.27). The main ability of closed loop feedback control system is to reduce the overall system sensitivity. However, it is important to find the system sensitivity of the current control with respect to the inductance (l) and resistance (r). In general, system sensitivity can be defined as a ratio of the change in the system transfer function to the change of system parameter for a small incremental change. The sensitivity of feedback system can be calculated using (2.28).

$$S_a^T = \frac{\partial T}{\partial a} \cdot \frac{a}{T} \tag{2.28}$$

Here, T is referred as closed loop transfer function, and a is the parameter of the system model for which system sensitivity is determined. Thus, by applying (2.28) on (2.22), sensitivity with respect of l, and r can be
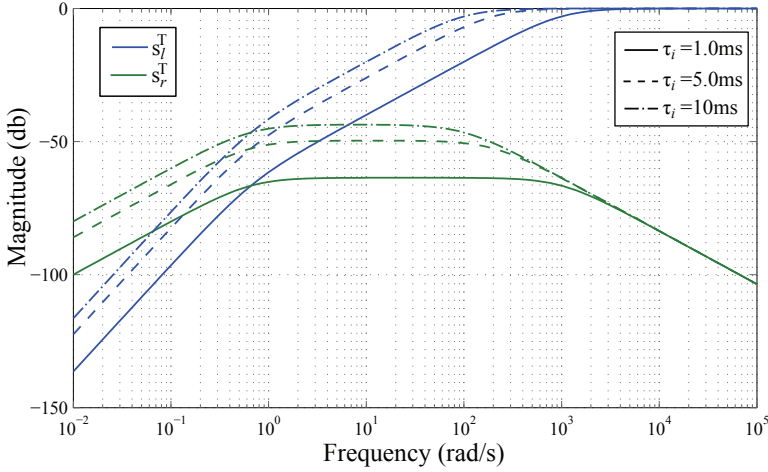
Figure 2.13: Bode plot for analyzing parametric sensitivity of VSC current closed loop control.

calculated as (2.29).

$$S_l^T = \frac{-ls^2}{ls^2 + (r + k_p)s + k_i}, \quad S_r^T = \frac{-rs}{ls^2 + (r + k_p)s + k_i} \qquad (2.29)$$

Using bode analysis, sensitivity function can be evaluated at varies frequencies as illustrated in Figure 2.13. The analysis has been made for different time constant (τ_i) of current response using (2.27). For robust performance, it is required to have low sensitivity at all frequencies. The sensitivity function on the bode plot indicate the error in the process caused by the model parameter. It is clear from the analysis that the controller has robust performance against resistive parameter. On the other hand, the sensitivity is high for inductive parameter at higher frequency and low for lower frequency. The low sensitivity at lower frequency indicates that the steady state error is zero. However, the performance of the control system is affected during transient period depending on the time constant. In the frequency domain analysis, the natural frequency (ω_n) is an indicator to determine the frequency region in which both sensitivity and system stability satisfy. Consider 6 % error is allowed during transient period (i.e -24 db sensitivity), then the sensitivity at the closed loop natural frequency

(a) Active current step response

(b) Reactive current step response

(c) Active current response at 20 % parametric change

(d) Reactive current response at 20 % parametric change
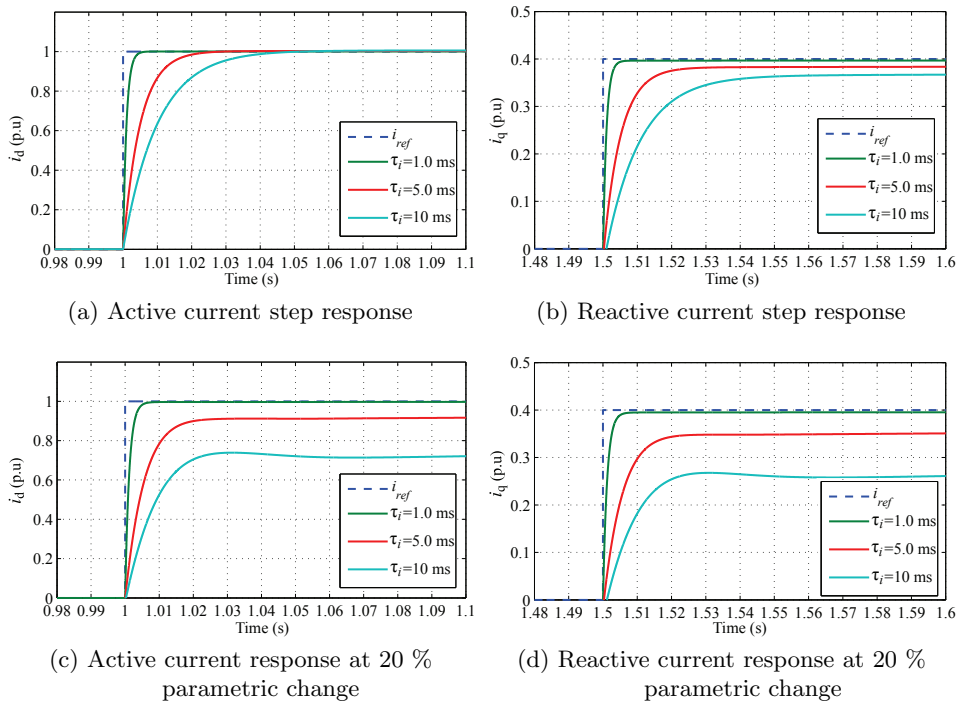
Figure 2.14: Current step response analysis for system sensitivity and decoupled scheme verification.

for 10 ms current time constant is higher than the limits i.e -21.6 db at $\omega_n = 8.41$ rad/s. Although the stability is ensured, the system does not exhibit a robust response. The natural frequency for 5 ms current time constant is 11.5 rad/s and the sensitivity is -24.8 db which satisfy the design criteria. The VSC current control system will exhibit robust performance for the time constant $\tau_i \leq 5$ ms.

The current control system design has been verified by performing non-linear simulation in simulink environment using simscape power systems block set. The responses of the current subjected to step input change are shown in Figure 2.14. For the analysis, a step change in active current is applied at 1.0 s, and at 1.5 s in reactive current. The simulation results validate the developed control scheme, and it is possible to control both current components independently. Furthermore, the system performance
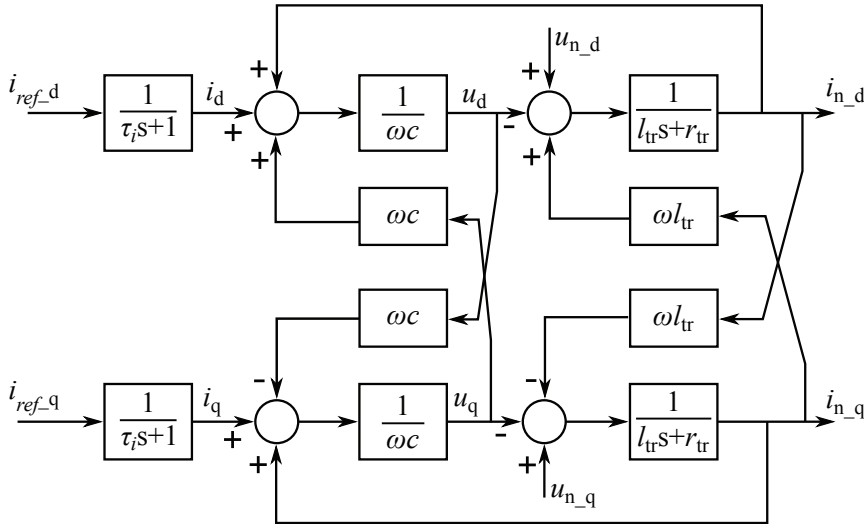
Figure 2.15: Grid connected VSC open loop control block diagram with respect to the outer controller.

is more robust for less than 5 ms current time constant. The parametric sensitivity is analyzed by changing the series reactor value by 20 %. It is clear that the current transient response for time constant greater than 5 ms is significantly influenced, and the steady state reaches very late. At slower current controller, the transient decoupling between the current component may also not be achieved properly.

2.3.3 Power-Voltage Control

The operational principle of the VSC in grid synchronous mode is defined by the outer control mode which depends on the feedback signal employed in the outer controller. The outer controller regulates the current reference signal according to the measured voltage or power signal. The dynamics of the outer controller depends on the network elements that are being involved in the feedback signal. Typically, a VSC substation is connected with the network at the transformer bus, but the outer controller perform the voltage control either at the filter bus or the power control through the series reactor. In this regard, the open loop dynamic model can be developed for outer controller performance analysis by defining filter bus voltage and

transformer current differential equations as (2.30). Note that the simplified transformer modeled is used which is represented by series resistance and reactance. Other linear models of transformer can also be applied using their linear differential equations. The impedance and network voltages are referred to the converter side.

$$c\frac{d\underline{u}}{dt} + j\omega c\underline{u} = \underline{i} + \underline{i}_n$$

$$l_{tr}\frac{d\underline{i}_n}{dt} + r_{tr}\underline{i} + j\omega l_{tr}\underline{i}_n = \underline{u}_n - \underline{u}$$

(2.30)

Here, l_{tr} and r_{tr} are the inductance and resistance of the transformer, c is the capacitance of AC filter, $\underline{i}_n$ is the current flowing through the transformer, and $\underline{u}_n$ is the network voltage.

The open loop control block diagram with respect of outer controller is shown in Figure 2.15. Since, the current component is decoupled and can be controlled independently therefore the current closed loop transfer function can be modeled with the first order transfer function as given in (2.27). The open loop model can be represented in state-space form as (2.31).

$$
\begin{bmatrix} \dot{i}_d \\ \dot{i}_q \\ \dot{u}_d \\ \dot{u}_q \\ \dot{i}_{n\_d} \\ \dot{i}_{n\_q} \end{bmatrix}
=
\begin{bmatrix}
-\frac{1}{\tau_i} & 0 & 0 & 0 & 0 & 0 \\
0 & -\frac{1}{\tau_i} & 0 & 0 & 0 & 0 \\
\frac{1}{c} & 0 & 0 & \omega & \frac{1}{c} & 0 \\
0 & \frac{1}{c} & -\omega & 0 & 0 & \frac{1}{c} \\
0 & 0 & -\frac{1}{l_{tr}} & 0 & -\frac{r_{tr}}{l_{tr}} & \omega \\
0 & 0 & 0 & -\frac{1}{l_{tr}} & -\omega & -\frac{r_{tr}}{l_{tr}}
\end{bmatrix}
\begin{bmatrix} i_d \\ i_q \\ u_d \\ u_q \\ i_{n\_d} \\ i_{n\_q} \end{bmatrix}
+
$$

$$
\begin{bmatrix}
0 & 0 & \frac{1}{\tau_i} & 0 \\
0 & 0 & 0 & \frac{1}{\tau_i} \\
0 & 0 & 0 & 0 \\
0 & 0 & 0 & 0 \\
\frac{1}{l_{tr}} & 0 & 0 & 0 \\
0 & \frac{1}{l_{tr}} & 0 & 0
\end{bmatrix}
\begin{bmatrix} u_{n\_d} \\ u_{n\_q} \\ i_{ref\_d} \\ i_{ref\_q} \end{bmatrix}
$$

(2.31)

The open loop model have network voltage and reference current command as the input. In grid synchronous mode, the network voltage is energized by

other synchronous machines in the network rather than VSC, therefore the network voltage is considered as a disturbance or an external signal (i.e an uncontrolled signal). Thus, the power and the voltage control can only be achieved by manipulating reference current command. The stability of the system can be determined using an eigenvalues analysis. The eigenvalues of the open loop model is given in (2.32) which gives the roots of the system characteristic equation. It can be noticed that the real part of all the roots exist on the left side on the complex plan which implies that the open loop system is stable.

$$
\begin{aligned}
s_{1,2} &= -\frac{1}{\tau_i} \\
s_{3,4,5,6} &= \frac{-c \cdot r_{tr} \pm \sqrt{(r_{tr} \cdot c)^2 - (2\omega c \cdot l_{tr})^2 - 4c \cdot l_{tr} \pm 4c \cdot l_{tr} \cdot h}}{2c \cdot l_{tr}} \\
\because h &= \sqrt{-(\omega c \cdot r_{tr})^2 + 4\omega^2 c \cdot l_{tr}}
\end{aligned}
\tag{2.32}
$$

The power injected by the VSC into the filter bus can be calculated using (2.33). In the $dq0$ voltage synchronous frame, the voltage at the reference bus would be $u_d = 1.0$ p.u, and $u_q = 0.0$, thus it can be stated that the active power is proportional to current d-component and the reactive power is proportional to current q-component.

$$
\begin{aligned}
S &= p + jq = \underline{u}_{dq} \cdot \underline{i}_{dq}^* \\
p &= u_d i_d + u_q i_q \approx i_d \\
q &= u_q i_d - u_d i_q \approx -i_q
\end{aligned}
\tag{2.33}
$$

For active and reactive power control system analysis, the simplification given in (2.33) can be applied to formulate the closed loop feedback system. The closed loop feedback diagram for power control system design is shown in Figure 2.16. Here τ_i is the time constant of current closed loop response. Note that the VSC control system is implemented in p.u system. A proportional-plus-integral controller is selected for the zero steady-state error for power control. The characteristic equation of the VSC power closed loop transfer function as given in (2.34) exhibits a second order response. The system

(a) Power model for stability analysis

(b) Active power control implementation

(c) Reactive power control implementation
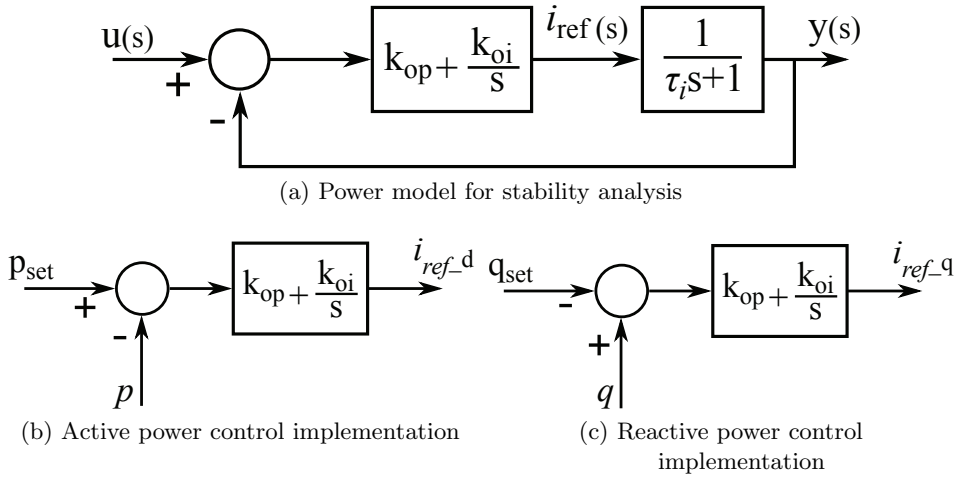
Figure 2.16: Closed loop feedback diagram for power controller design in grid synchronous mode.

response varies from over-damped to under-damped response according to the location of zeros. The frequency and dynamic response of power control for over-damped system is shown in Figure 2.17.

$$\frac{y(s)}{u(s)} = \frac{k_{op}\left(s + k_{oi}/k_{op}\right)}{\tau_i s^2 + \left(k_{op} + 1\right)s + k_{oi}}$$

$$1/\tau_i > k_{oi}/k_{op}, \qquad k_{op} > 0$$

(2.34)

Yet again, it is desirable to not to have overshoot during transient period in the power to avoid stress on the IGBT. Therefore, the zero of the closed loop transfer function must be placed according to the condition given in (2.34). A nonlinear step analysis for over-damped system response is shown in Figure 2.17c. For the analysis, a step change in active and reactive power is applied at 1.0 s, and 1.5 s respectively. It can be seen that active and reactive power are controlled individually and they are decoupled from each other. Moreover, the bandwidth of power closed loop response is less than the current response. The rise time of 100 ms is considered as a design condition. Faster rise time may introduce transient coupling between active and reactive power due to weak grid voltage.

Typically, active power control mode is set for performing import and

(a) Root locus of VSC power control

(b) Bode plot of VSC power control

(c) Nonlinear dynamic response
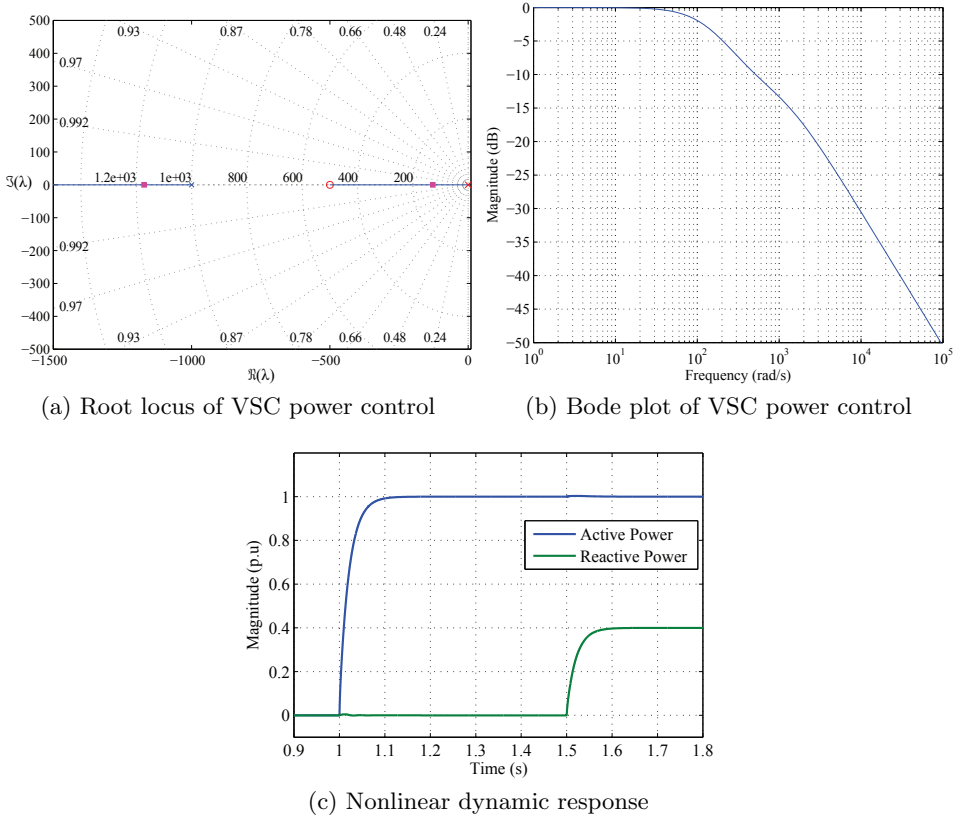
Figure 2.17: Active and reactive power control analysis of VSC in grid synchronous mode.

export of energy from one country to another via VSC-HVDC transmission system. In this mode, converter behaves as constant power source in the DC network. In order to balance the power, one of the converter must control the DC voltage in the DC network. A converter controlling the DC voltage is considered as a slack source in the DC network. In the DC voltage control mode, the converter controls the DC voltage across the DC capacitor at the given set-point. The dynamics of the DC voltage can be analyzed by defining the differential equation of the DC capacitor voltage as (2.35).

$$C_{dc}\frac{dU_{dc}}{dt} = I_l + I_{dc} \tag{2.35}$$

(a) Stability model of DC voltage control

(b) DC voltage control implementation
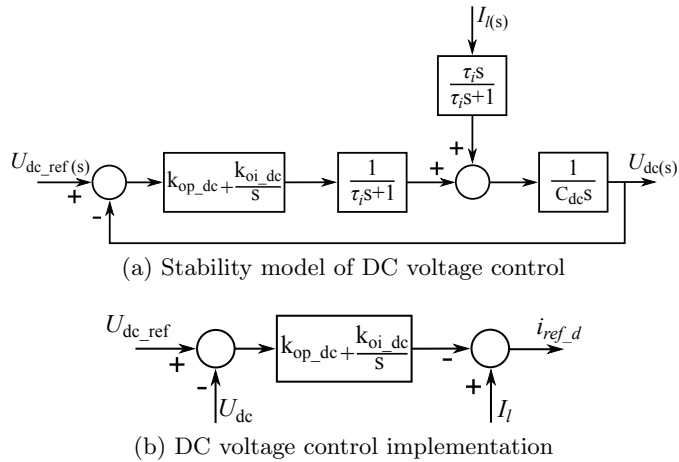
Figure 2.18: Closed loop block diagram of VSC DC voltage control.

Here, U_{dc} is the voltage across DC capacitor, C_{dc} is the DC capacitor value, I_l is the current injected by the DC network, and I_{dc} is the DC current of the VSC. In the lossless converter, AC active power is equal to DC active power thus DC current can be approximated to d-axis of the AC current as expressed by (2.36).

$$p_{ac} = p_{dc} \Rightarrow u_d i_d = U_{dc} I_{dc}$$
$$i_d \approx I_{dc}$$

$$(2.36)$$

The DC voltage control closed loop stability model and its implementation for nonlinear simulation is illustrated in Figure 2.18. Note that in the nonlinear control implementation $I_{dc} = -i_d$ to maintain the sign convention. A proportional-plus-integral control scheme is applied for zero steady state error. The dynamics of the DC voltage is the function of two inputs i.e the network DC current and reference DC voltage set-point. The closed loop transfer functions with respect of both inputs are given in (2.37).

$$T_u(s) = \frac{U_{dc}(s)}{U_{dc\_ref}(s)} = \frac{k_{op\_dc}s + k_{oi\_dc}}{\tau_i C_{dc}s^3 + C_{dc}s^2 + k_{op\_dc}s + k_{oi\_dc}}$$

$$T_i(s) = \frac{U_{dc}(s)}{I_l(s)} = \frac{\tau_i s^2}{\tau_i C_{dc}s^3 + C_{dc}s^2 + k_{op\_dc}s + k_{oi\_dc}}$$

$$(2.37)$$

(a) Bode plot analysis

(b) Nonlinear simulation result
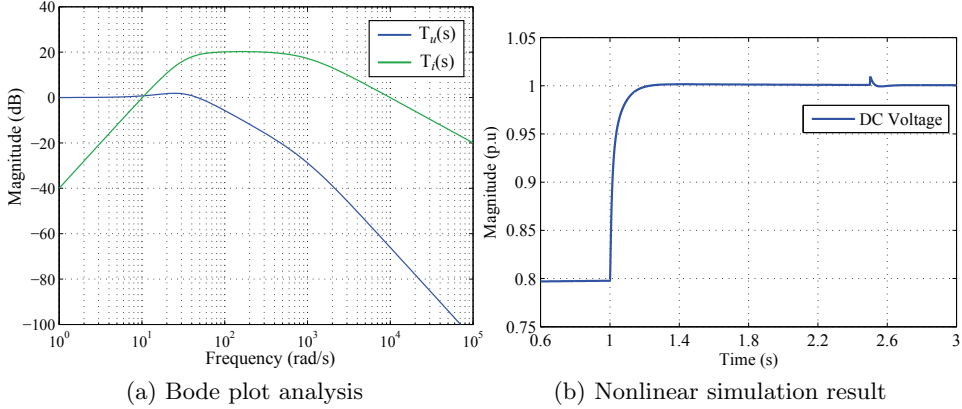
Figure 2.19: Frequency response analysis and nonlinear time domain simulation results of VSC DC voltage control.

The system can be analyzed against both inputs in frequency domain using bode plot as shown in Figure 2.19a. The gain of the transfer function $T_u(s)$ at the lower frequency is equal to 1.0 p.u, which means that the DC output voltage is tracking the reference voltage set-point. For higher frequencies, $T_u(s)$ must have low gains for low overshoot and damped response. The response shows that the peak gain of $T_u(s)$ is 1.87 db at frequency 25.4 rad/s. On the other hand, the gains of the system should be very low at all frequencies for the network DC current input. It can be seen that the transfer function $T_i(s)$ gain is not zero at all frequencies. The analysis shows that the gain of $T_i(s)$ is higher than -3 db for the frequencies $8.55 < \omega < 14.1 \times 10^3$ rad/s. The gain of the system can be reduced by increasing the size of the DC capacitor. Further, the response of the controller can be made faster by increasing the value of k_{op_dc}. This will reduce the closed loop bandwidth of $T_i(s)$ but increase the bandwidth of $T_u(s)$. The increase in the bandwidth of $T_u(s)$ will produce the high frequency oscillation while tracking the reference voltage set-point. Thus, a trade off is needed in the dynamic performance with respect of both inputs while tuning controller gains.

Nonlinear simulation result of the DC voltage control is shown in Figure 2.19b. For the analysis, a step signal in DC voltage set-point is applied from 0.8 p.u to 1.0 p.u at 1.0 s, and at 2.5 s a current of magnitude 1.0 p.u
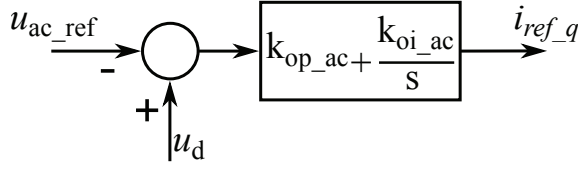
Figure 2.20: AC voltage nonlinear control implementation of VSC in grid synchronous mode.

is injected by the DC network. It can be seen that DC voltage transient is minimum with respect of current injection and the transient is damped out at steady state. The transient peak voltage is approximately 1.01 p.u.

The VSC can control reactive current individual in order to support the onshore grid voltage. This can be achieved either by defining reactive power set-point as explained previously or with respect of network AC voltage feedback signal. In the AC voltage control of VSC, a proportional-plus-integral control scheme is employed to track the reference AC voltage by injecting reactive current in the reference bus. The voltage feedback signal is measured at the AC filter bus. The nonlinear control scheme is illustrated in Figure 2.20. The system will have the multiple control loops with the addition of u_d as the feedback signal, and it becomes a MIMO system having coupling between the states. Onshore side network model including closed loop AC voltage control in state space representation is given in (2.38).

$$\dot{x} = Ax + Bu$$

$$x = \begin{bmatrix} i_d & i_q & u_d & u_q & i_{n\_d} & i_{n\_q} & e_{ac} \end{bmatrix}^T \tag{2.38}$$

$$u = \begin{bmatrix} u_{n\_d} & u_{n\_q} & i_{ref\_d} & u_{ac\_ref} \end{bmatrix}^T$$

$$A = \begin{bmatrix} -\frac{1}{\tau_i} & 0 & 0 & 0 & 0 & 0 & 0 \\ 0 & -\frac{1}{\tau_i} & \frac{k_{op\_ac}}{\tau_i} & 0 & 0 & 0 & \frac{1}{\tau_i} \\ \frac{1}{c} & 0 & 0 & \omega & \frac{1}{c} & 0 & 0 \\ 0 & \frac{1}{c} & -\omega & 0 & 0 & \frac{1}{c} & 0 \\ 0 & 0 & -\frac{1}{l_{tr}} & 0 & -\frac{r_{tr}}{l_{tr}} & \omega & 0 \\ 0 & 0 & 0 & -\frac{1}{l_{tr}} & -\omega & -\frac{r_{tr}}{l_{tr}} & 0 \\ 0 & 0 & k_{oi\_ac} & 0 & 0 & 0 & 0 \end{bmatrix}, \quad B = \begin{bmatrix} 0 & 0 & \frac{1}{\tau_i} & 0 \\ 0 & 0 & 0 & -\frac{k_{op\_ac}}{\tau_i} \\ 0 & 0 & 0 & 0 \\ 0 & 0 & 0 & 0 \\ \frac{1}{l_{tr}} & 0 & 0 & 0 \\ 0 & \frac{1}{l_{tr}} & 0 & 0 \\ 0 & 0 & 0 & -k_{oi\_ac} \end{bmatrix} \tag{2.39}$$

(a) Nonlinear voltage response

(b) Nonlinear reactive power response

(c) Pole Maps
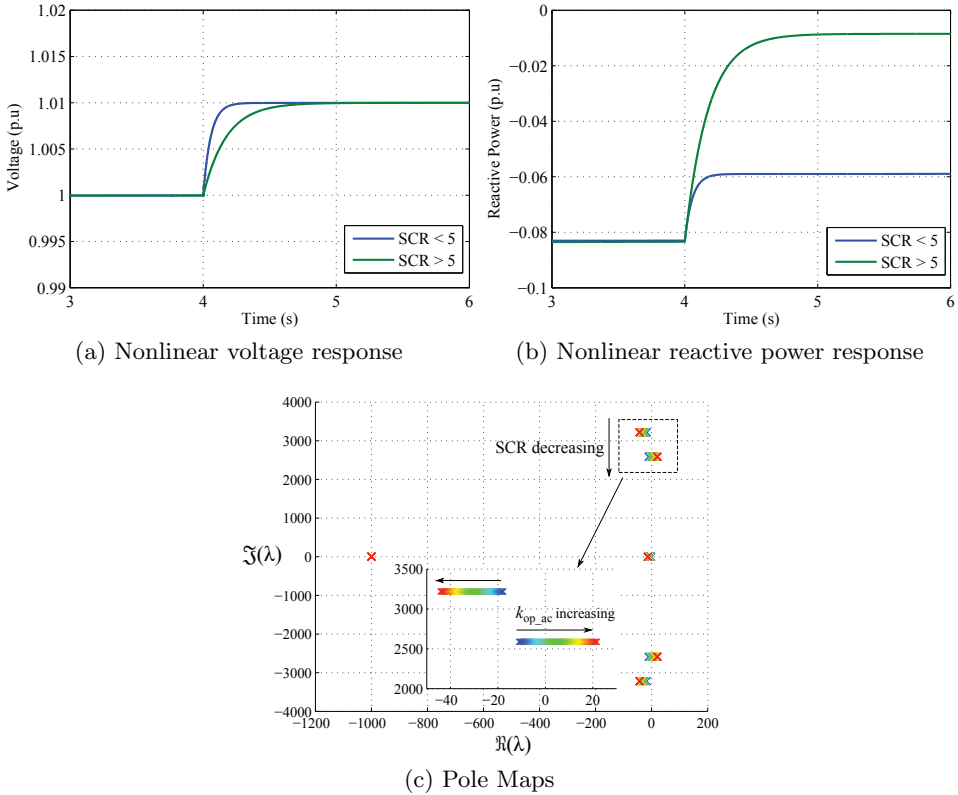
Figure 2.21: Dynamic and stability analysis of VSC AC voltage control in grid synchronous mode.

Here, A, and B are the state matrix and input matrix respectively. The stability of the system can be determined by calculating eigenvalue of the state matrix.

Poles map and nonlinear dynamic analysis for VSC AC voltage control in grid synchronous mode are shown in Figure 2.21. The trajectory of the poles are plotted by changing proportional gains of the controller. The poles that are located at the real axis scale of -1000 are mainly influenced by the integral gains, and the poles near -20 real axis scale are affected by proportional gain. The instability in the system mainly occurs due to proportional gain therefore it should be set small. Furthermore, the strength of the onshore grid also influences the system dynamics. The comparison in

the VSC controller response for weak and strong grid can be made from the voltage response shown in Figure 2.21a. For the weak grid, VSC control is dominant and the steady-state reaches faster. The negative sign represents a inductive reactive power in the power plots. On the other hand, the network voltages are stiff due to strong grid and requires more reactive power injection by the VSC to achieve the same voltage set-points. Moreover, the sets of poles near to imaginary axis move further toward the real axis by reducing short circuit ratio (SCR) which increases the damping in the system.

2.4 Grid Forming Control of VSC

The voltage source converter in the grid forming mode imposes the frequency on the network and energizes the network by controlling the voltage. In grid forming mode, the converter does not require a PLL since it imposes frequency on the network and the rotating angle for $dq0$ transformation is calculated by using (2.40).

$$\frac{d\delta}{dt} = \omega_r \tag{2.40}$$

Here, ω_r is the reference frequency imposed by the VSC on the network, and δ is the voltage angle at the controlling bus.

In the grid forming control, the outer controller controls the reference voltage by defining the reference current command for the current controller. The procedure of designing current controller is same as explained previously. In this mode, the VSC behaves as a controlled voltage source and act like a slack source in the network. The VSC balances the power in the network according to the network demand. The outer controller can be designed by analyzing the dynamic of the filter bus which is referred as reference bus. In the $dq0$ rotating frame, the voltage differential equation of the filter bus can be written as (2.41).

$$
\begin{aligned}
c\frac{du_d}{dt} &= i_d + i_{n\_d} + \omega c u_q \\
c\frac{du_q}{dt} &= i_q + i_{n\_q} - \omega c u_d
\end{aligned}
\tag{2.41}
$$

The dynamic equations show that the voltage d- and q- axis can be controlled individually through current d- and q- component however, each voltage
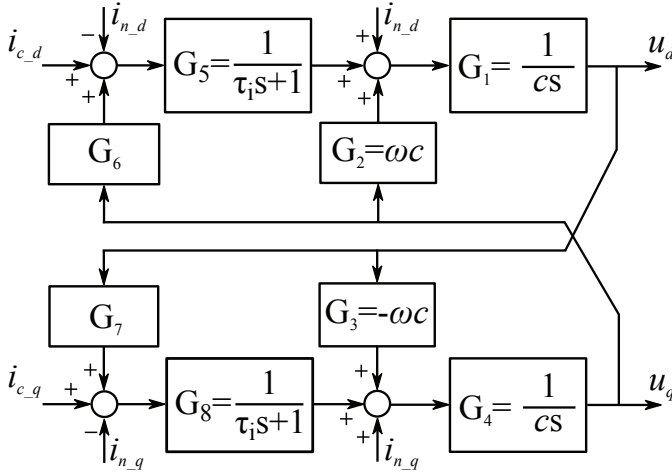
Figure 2.22: Block diagram of voltage $d-$ and $q-$ component decoupling for grid forming control.

component are cross coupled in V-canonical form. The voltage component can be decoupled by applying decoupling scheme using V-canonical form as illustrated in Figure 2.22. It can be noticed that the output voltage is a function of converter control signal (i_{c_d}, i_{c_q}) which is generated by the outer controller and the network current (i_{n_d}, i_{n_q}). The relationship between input and output of the system can be expressed in the matrix form as (2.42).

$$
\begin{bmatrix} u_d \\ u_q \end{bmatrix} = \frac{1}{1 - G_x G_y} \left\{ \begin{bmatrix} G_1 G_5 & G_x G_4 G_8 \\ G_y G_1 G_5 & G_4 G_8 \end{bmatrix} \begin{bmatrix} i_{c\_d} \\ i_{c\_q} \end{bmatrix} \right.
$$
$$
\left. + \begin{bmatrix} G_1 - G_1 G_5 & G_x (G_4 - G_4 G_8) \\ G_y (G_1 - G_1 G_5) & G_4 - G_4 G_8 \end{bmatrix} \begin{bmatrix} i_{n\_d} \\ i_{n\_q} \end{bmatrix} \right\} \tag{2.42}
$$

Here; $G_x = G_1 G_2 + G_1 G_5 G_6$, $G_y = G_3 G_4 + G_4 G_7 G_8$. It can be concluded from (2.42) that the d-component of the voltage can be controlled by d-component of currents only, if $G_x = 0$. Similarly, q-component of the voltage can be controlled by q-component of currents only, if $G_y = 0$. Thus, decouple transfer functions are determined using (2.43).

(a) Stability model

(b) Nonlinear implementation model
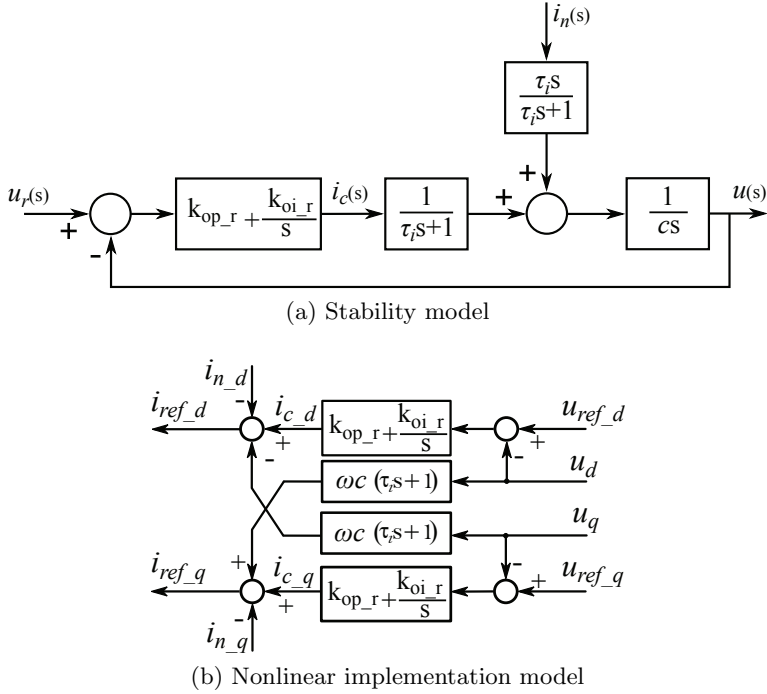
Figure 2.23: VSC Closed loop block diagram of grid forming control.

$$G_6 = \frac{-G_2}{G_5} = -w \cdot c_1 \cdot (\tau_i s + 1)$$

$$G_7 = \frac{-G_3}{G_8} = w \cdot c_1 \cdot (\tau_i s + 1)$$

$$(2.43)$$

Open loop voltage model including decouple transfer function in state-space representation is given in (2.44).

$$
\begin{bmatrix} \dot{i}_d \\ \dot{i}_q \\ \dot{u}_d \\ \dot{u}_q \end{bmatrix} =
\begin{bmatrix}
-\frac{1}{\tau_i} & -\omega & \omega^2 c & -\frac{\omega c}{\tau_i} \\
\omega & -\frac{1}{\tau_i} & \frac{\omega c}{\tau_i} & \omega^2 c \\
\frac{1}{c} & 0 & 0 & \omega \\
0 & \frac{1}{c} & -\omega & 0
\end{bmatrix}
\begin{bmatrix} i_d \\ i_q \\ u_d \\ u_q \end{bmatrix} +
\begin{bmatrix}
\frac{1}{\tau_i} & 0 & -\frac{1}{\tau_i} & -\omega \\
0 & \frac{1}{\tau_i} & \omega & -\frac{1}{\tau_i} \\
0 & 0 & \frac{1}{c} & 0 \\
0 & 0 & 0 & \frac{1}{c}
\end{bmatrix}
\begin{bmatrix} i_{c\_d} \\ i_{c\_q} \\ i_{n\_d} \\ i_{n\_q} \end{bmatrix} \quad (2.44)
$$

Eigenvalues of the state matrix are calculated to determine the poles of the system. From (2.45), it can be seen that the system has four poles, two
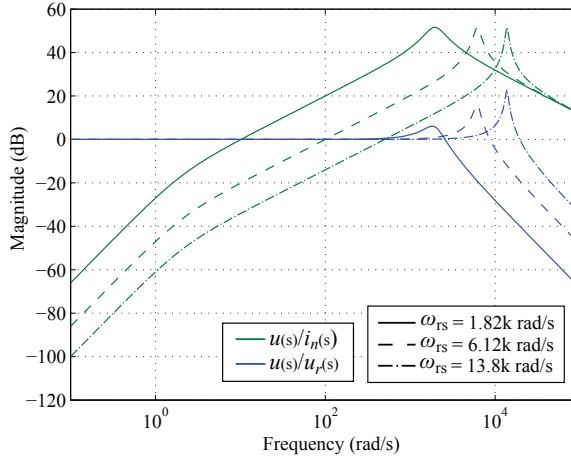
Figure 2.24: Bode analysis of VSC grid forming voltage control.

for each d- and q- components, and the characteristics equation of both components become independent of each other. Thus, the control system of d- and q- components of the voltage can be designed separately.

$$s_{1,2} = -\frac{1}{\tau_i}, s_{3,4} = 0 \tag{2.45}$$

The VSC grid forming voltage control stability model and its nonlinear control implementation are shown in Figure 2.23. A proportional-plus-integral control scheme is applied for zero steady-state error. The closed loop transfer function of the system can be defined as (2.46).

$$u(s) = \frac{\left(k_{op\_r}s + k_{oi\_r}\right)u_r(s) + \left(\tau_i s^2\right)i_n(s)}{\tau_i c s^3 + c s^2 + k_{op\_r}s + k_{oi\_r}} \tag{2.46}$$

The stability of the system depends on the roots of the characteristic equation. The system stability condition has been found as (2.47) by applying Routh-Hurwitz criterion.

$$0 < k_{oi\_r} \quad \text{and} \quad \tau_i k_{oi\_r} < k_{op\_r} \tag{2.47}$$

(a) Voltage set-point changed

(b) Network current changed
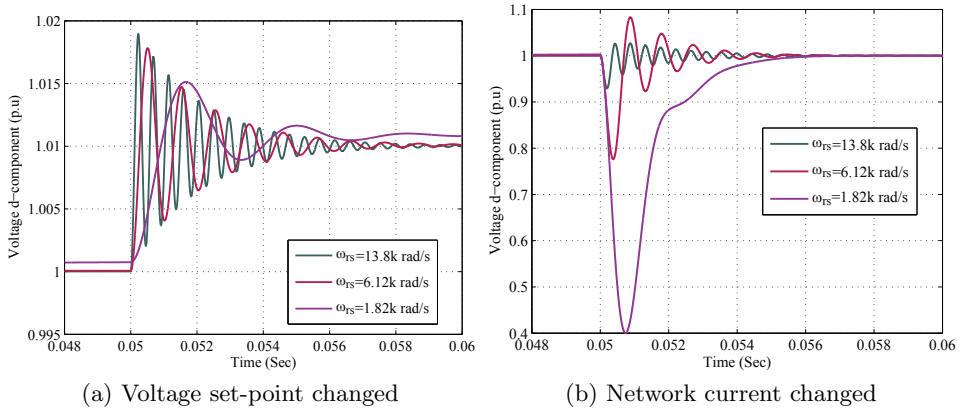
Figure 2.25: Nonlinear simulation results of VSC grid forming voltage control.

The converter output voltage is the function of two inputs i.e the set-point and the network current. The controller gains are required to be tuned with respect of both inputs. The controller performance can be observed using bode analysis given in Figure 2.24. Here, ω_{rs} is the resonant frequency at which the output voltage has its peak magnitude. As a design rule, it is required that the closed loop transfer function must have low gain at all frequencies with respect to the network current input. For voltage set-point input, closed loop gain must be high at low frequencies and low gain at higher frequencies. It can be seen from the bode plot that the output voltage may exhibit damped response with respect of input set-point by reducing the bandwidth of the controller. However, the closed loop system does not reject all the low frequencies with respect to the network current input at slow controller response. The maximum peak in the output voltage with respect to the network current is not affected by the controller speed. The maximum peak can be reduced by increasing current controller bandwidth and increasing the filter capacitance. A trade-off is required in the performance in terms of maximum overshot of the voltage peak with respect to input set-point and the steepness in the frequency response at low frequencies with respect to the network current.

The nonlinear simulation results are shown in Figure 2.25. In the simu-
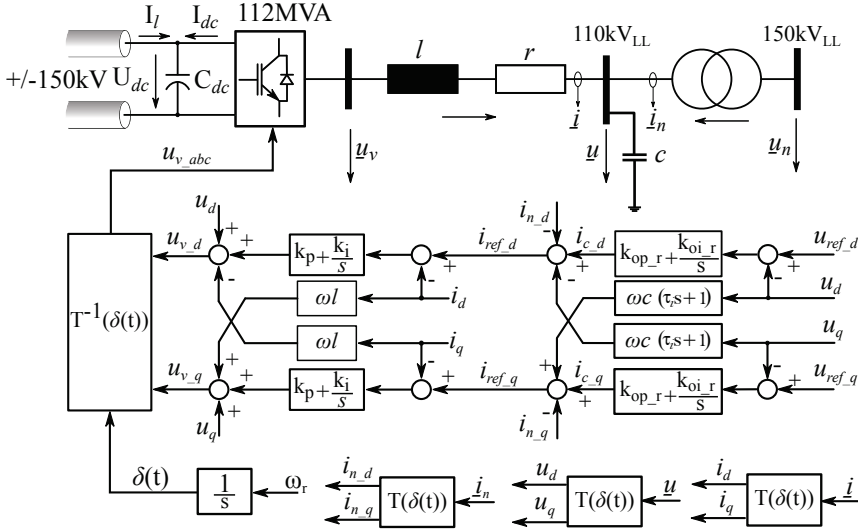
Figure 2.26: Offshore substation configuration of VSC HVDC transmission system.

lation, the network current is changed from zero to 1.0 p.u in active load and the voltage set-point is changed from 1.0 p.u to 1.01 p.u. Note that the performance has been analyzed with respect to both inputs by applying step change one at a time. It is clear from the result that faster controller response increases the peak overshoot and high oscillation in the output voltage while changing input set-point. High controller gain value provide better performance against high rate of change of network current. Further, the offshore grid code may specify the maximum rate of change of power in the offshore network to avoid large voltage deviation during transient.

2.5 VSC Substation Models for System Studies

In this thesis, three voltage source converter based substation configurations are build to perform different case studies. An overview of these configurations are given in this section. The VSC substation network elements value and its control gain settings are also listed. The studies have been performed using these parameters otherwise stated explicitly in each chapter. Further, the control system is designed in p.u system to be able to adapt for

Table 2.1: Offshore VSC HVDC substation network and control parameters

Variables	Value	Unit
Rated Power	112	MVA
Rated AC Voltage	110	kV
Rated DC Voltage	± 150	kV
Transformer	150/110	kV
Transformer Resistance	0.12	%
Transformer Inductance	2	%
AC Filter Capacitance	2.631	μF
DC Filter Capacitance	100	μF
Reactor Resistance	0.0363	Ω
Reactor Inductance	55.0	mH
Current PI Controller gains	$0.51 + 0.34/s$	p.u
Voltage PI Controller gains	$10.8 + 21.6/s$	p.u
Network Frequency	314.16	rad/s

any desired power rating with ease. The details of the network and control parameters conversion in per unit system are given in Appendix B. Here, the models are given without operational limits and short circuit control which are discussed in Chapter 5.

Offshore VSC-HVDC Configuration: An offshore VSC substation configuration of a HVDC transmission system is shown in Figure 2.26. The converter is operated in grid forming mode i.e the VSC energizes the offshore network and imposes the network frequency. The network and control parameters of an offshore VSC substation are given in Table 2.1. In the model, the power flow is considered positive in the direction of arrow. Symmetrical monopolar connection is considered on the DC side. The modulation index of the converter (m) is approximately 0.6. In the offshore network having only one grid forming VSC, the network frequency is equal to the frequency imposed by the VSC i.e ω_r, and the voltage set-points are $u_{ref\_d} = 1.0$ p.u, and $u_{ref\_q} = 0.0$ p.u. The current closed loop time constant is 1.0 ms. The resonant frequency of the outer voltage control loop is set to 6.12x10^3 rad/s. The AC voltage settling time is approximately 40 ms. The time domain voltage responses with respect to voltage set-point and network current
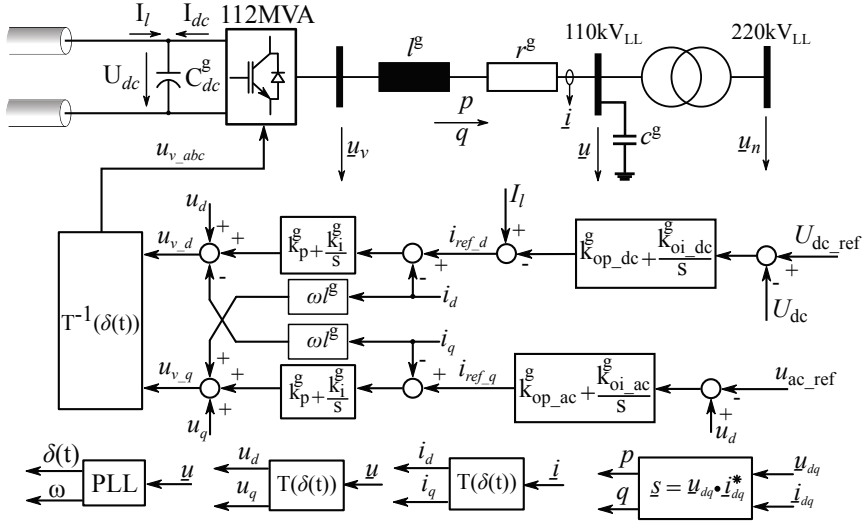
Figure 2.27: Onshore substation configuration of VSC HVDC transmission system.

infeed are shown in previous section. According to the analysis, a voltage dip up to 0.8 p.u will occur when the step change in the network current is applied from zero to rated value.

The grid forming control is further extended in the next chapter for the offshore AC network control interconnecting several grid forming VSCs.

Onshore VSC-HVDC Configuration: The configuration of an onshore VSC substation of a HVDC transmission system is shown in Figure 2.27. The VSC is synchronized with the grid frequency thus requires a PLL. The outer controller operates in the DC voltage and AC voltage control mode. The onshore converter is controlling the DC voltage to balance the DC link. In the point-to-point configuration of HVDC transmission system, the DC voltage control is based on PI regulator as explained in previous section. While the DC voltage control has proportional regulator in multiterminal HVDC transmission system which is explained in Chapter 6. Also, an AC voltage control mode is set in order to support the onshore AC grid voltages. The set-points for AC and DC voltages are $u_{ac\_ref} = 1.0$ p.u and $U_{dc\_ref} = 1.0$ p.u respectively. The network and control parameters are given

Table 2.2: Onshore VSC HVDC substation network and control parameters

Variables	Value	Unit
Rated Power	112	MVA
Rated AC Voltage	110	kV
Rated DC Voltage	± 150	kV
Transformer	220/110	kV
Transformer Resistance	0.6	%
Transformer Inductance	4	%
AC Filter Capacitance	2.631	μF
DC Filter Capacitance	100	μF
Reactor Resistance	0.0363	Ω
Reactor Inductance	55.0	mH
Current PI Controller gains	$0.51 + 0.34/s$	p.u
DC Voltage PI Controller gains	$4.02 + 80.36/s$	p.u
AC Voltage PI Controller gains	$0.043 + 0.432/s$	p.u
Network Frequency	314.16	rad/s

in Table 2.2. According to the control parameters, the time constant of the current closed loop is 1.0 ms. And the DC voltage closed loop rise time is approximately 24 ms. The AC voltage closed loop time constant depends on the strength of the onshore grid. The grid short circuit power of $10,000$ MVA is considered in simulation. Typically, a DC chopper is installed on the DC link at onshore side converter to maintain the DC voltage during fault. The detail of the short circuit control for onshore fault is discussed in Chapter 5.

Wind Generation System: Nowadays, most offshore wind generation system consist of a permanent magnet synchronous generator and fully rated back-to-back converters. The machine side converter is operated in variable frequency control mode which converts the received AC power into DC power, another converter connected at the network side converts back this DC power into AC. The network side converter is synchronized with the grid frequency and able to control active and reactive power independently. The network side converter requires to balance the DC power to be able to infeed all the wind energy into the network. The DC link isolates the generator dynamics and its influence on the network. Further, the detail wind turbine model and its mechanic is not the focus of this thesis, therefore, the wind
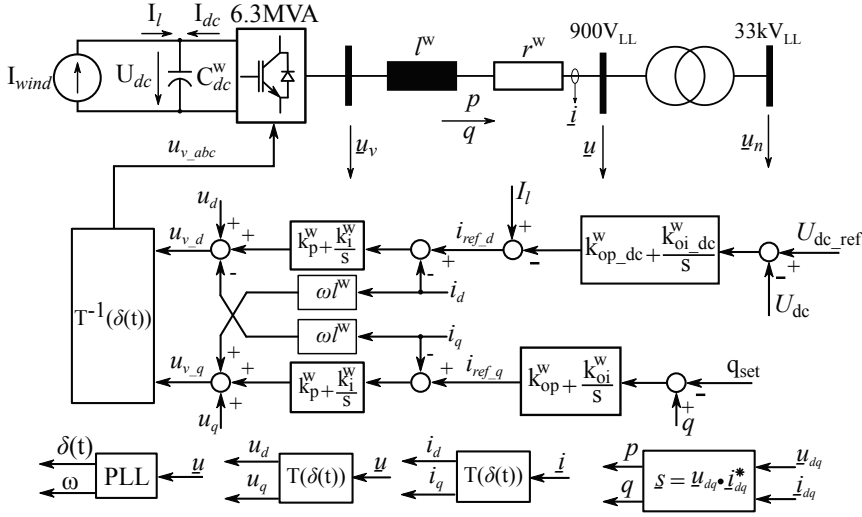
Figure 2.28: Grid side wind turbine VSC substation configuration.

generation system contains only network side converter in the study cases. The wind generation substation configuration is shown in Figure 2.28.

The network and control parameters for the wind generation system are given in Table 2.3. A step-up transformer is installed to connect the wind model with the offshore wind power plant array. Typically, the wind power plant array consist of medium voltage cables of 33 kV level. The converter is set to control the DC voltage and the reactive power. According to the control system design, the rise time of the DC voltage control loop is approximately 24 ms, and the DC voltage set-point is defined as $U_{dc\_ref} = 1.0$ p.u. The time constant of the reactive power control loop is approximately 20 ms. Moreover, the reactive power set-point can be defined according the reactive power support required by the network. The current closed loop time constant is also set to 1.0 ms.

The wind energy infeed by the wind turbine is modeled as constant current source. The wind energy variation can be incorporated in the network study by using wind power to speed profile. Again, a DC chopper is required on the DC link to control the voltage during fault. The detail of the chopper control is explained in the Chapter 5.

Table 2.3: Wind generation unit network and control parameters

Variables	Value	Unit
Rated Power	6.3	MVA
Rated AC Voltage	900	V
Rated DC Voltage	2.0	kV
Transformer	33/900	kV
Transformer Resistance	0.8	%
Transformer Inductance	6	%
DC Filter Capacitance	200	μF
Reactor Resistance	0.1	mΩ
Reactor Inductance	0.02	mH
Current PI Controller gains	$0.156 + 0.778/s$	p.u
DC Voltage PI Controller gains	$0.0032 + 0.0635/s$	p.u
Reactive Power PI Controller gains	$0.1 + 50/s$	p.u
Network Frequency	314.16	rad/s

2.6 Summary

The basic architecture of voltage source converter operation is presented for both high voltage direct current transmission system and offshore wind generation applications. The voltage source converter has ability to operate as constant current source by synchronizing with the connected network, or work as a constant voltage source by imposing network frequency on the network. In both operational characteristics, the control system has current closed loop to improve the system stability as well as to be able to limit the VSC current during short circuit which is particularly difficult in VSC direct voltage control method for grid forming operation.

Moreover, the method of selecting controller gains have been proposed by applying small signal stability analysis. The condition of stability according to each control loop is derived and controller are tuned for desired performance by graphical methods such as bode or root locus analysis. Although the electrical network is a nonlinear system, the derive linearized model sufficiently demonstrate the VSC dynamic behavior and enables the application of linear control theory for control system design. The control structure presented in this chapter is applied in the further extension of VSC control system in next chapters.

3 Offshore Network having Grid Forming VSC-HVDC System

In this chapter, a concept of an offshore grid is introduced to interconnect several offshore wind power plants with different onshore grids using VSC-HVDC transmission system. The VSC grid forming control presented in previous chapter has been extended to form an offshore AC network. Frequency and voltage droop schemes have been implemented to control the sharing of active and reactive power among VSC-HVDC transmission systems. Furthermore, the voltage droop control provides additional degree of freedom to manage the reactive power in the offshore AC network. Later in the chapter, an optimization algorithm is developed to optimize the reactive power flow in order to minimize the losses in the network[2,3].

3.1 Introduction

Renewable energy is becoming a universally adopted primary source of energy. A breakthrough in advanced power transmission system technologies, specially in the power electronics devices, have enabled the installation of renewable generation units at remote location. Wind energy among other renewable sources has been a main focus in the last decade, particularly offshore. Up to the mid of 2016, 3344 offshore wind turbines with a combined power of 11.54 GW are installed in European waters [98].

---

[2]This chapter is based on the following publications:

M. Raza, K. Schoenleber, and O. Gomis-Bellmunt, "Droop control design of multi-VSC system for offshore network to integrate wind energy". Energies (MDPI), 9(10):826, oct 2016, doi: 10.3390/en9100826.

[3]M. Raza, C. Collados, and O. Gomis-Bellmunt, "Reactive power management in an offshore ac network having multiple voltage source converters". Applied Energy (Elseiver), 206:793-803, nov 2017. ISSN 0306-2619. doi: 10.1016/j.apenergy.2017.08.182.

The most common export system of an offshore wind power plant is the high voltage alternating current (HVAC) cables link with an onshore grid, typically at the voltage level of 150 kV. The HVAC export system is well established technology as well as it provides grid forming interconnection to offshore network. However, the HVAC cables have high effective capacitance that limits the transmission of large active power over the long distance through Sea, typically limited up to 90 km for 100 MW [21]. The voltage source converter (VSC) based high voltage direct current (HVDC) transmission system eliminate the power export limitation due to the cable capacitive effect and it has an ability to form the offshore network. However, the current rating of the switching devices (IGBTs) restrains the power transfer capacity.

Many experts are foreseeing the need of having offshore grid for better trade and integration of large offshore wind energy generation. In [99], the impact of an offshore grid on the European energy market has been studied considering several technical concepts for grid connection. One of the concept in the offshore grid is to create a multiterminal (MT) HVDC system to connect the several offshore wind power plants and integrate them with different onshore grids. However, the DC circuit breaker based protection scheme in the MTDC system increases the overall development cost [60, 65]. On the contrary, an offshore AC network formed by connecting wind power plants using HVAC cables and then using several VSC-HVDC systems in a point-to-point configuration to link with different onshore grids provides advantage to not to employee DC circuit breaker and the protection scheme can be applied similar to conventional AC system. An offshore AC network act as a mediator among several wind power plants and different countries grids. In [22], several options of forming offshore AC network are considered by connecting wind power plants center collection points with each other using medium or high voltage AC cable (normally, at 150 kV). This offshore AC network is then connected with the main grids of neighboring countries via VSC-HVDC system. Offshore wind power plants that are far from shore and are within the vicinity of 20 km from each other are economically suitable to form an offshore AC network [100].

In a stand alone network such as an offshore AC network, the VSC-HVDC
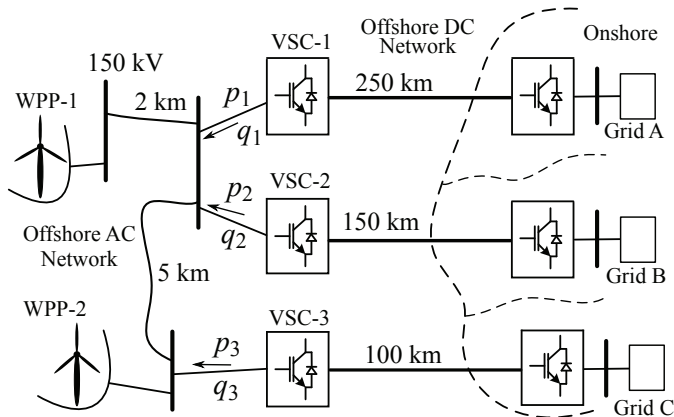
Figure 3.1: Configuration of an offshore AC network to integrate wind power plants using VSC HVDC transmission system with several onshore grids.

system form the grid and behave as a slack source [69, 70]. The voltage and frequency droop schemes are suitable for an offshore AC network having multiple VSC-HVDC systems. The advantage of droop scheme is to have multiple slack sources in the network, and the communication between VSC-HVDC transmission system is not required for power sharing during normal operation as well as in the failure of any transmission system. Further, the droop gains also offer an additional degree of freedom to control the reactive power in the offshore AC network.

3.2 Offshore AC Network Control and Operation

The offshore AC network integrated with onshore grid using VSC-HVDC transmission system is required to be formed by the VSCs. An example of an offshore AC network is shown in Figure 3.1. The VSC-HVDC transmission systems are in point-to-point configuration in which onshore side converter are set to operate in the DC voltage control as explained in Section 2.3. The offshore converters are operating in grid forming mode and they have the same control structure as explained in Section 2.4. Furthermore, the offshore VSC control system is extended by implementing frequency and voltage droop schemes as a network level control in order to operate the offshore
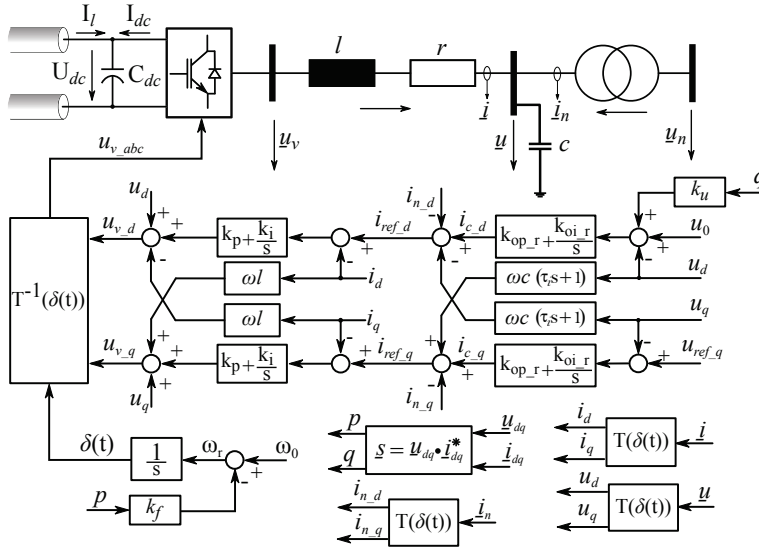
Figure 3.2: The grid forming control of the offshore converter for parallel operation of VSC HVDC transmission systems.

network with multiple VSCs. The network level control is implemented locally in each VSCs control system. The frequency and voltage impose by i^{th} VSC can be defined as (3.1). These droop equations are referred as network level control (see Figure 2.5).

$$\begin{aligned}
\omega_{r\_i} &= \omega_0 + k_{f\_i}\left(p_{0\_i} - p_i\right) \\
u_{r\_i} &= u_0 - k_{u\_i}\left(q_{0\_i} - q_i\right)
\end{aligned} \tag{3.1}$$

Here, ω_{r_i} is the imposed frequency of ith VSC, ω_0 and u_0 are the rated frequency and voltage value, k_{f_i} is the frequency droop gain, k_{u_i} is the voltage droop gains, p_i and q_i are the actual active and reactive power of the ith VSC, u_{r_i} is the imposed voltage of ith VSC, p_{0_i} and q_{0_i} are the initial active and reactive power operating point.

The VSC control system for offshore network including network level control system is illustrated in Figure 3.2. In the control scheme, the initial active and reactive power operating points are set to zero i.e $p_0 = q_0 = 0.0$ p.u. The maximum export power capability of a VSC-HVDC transmission system can be less than the total power present in the offshore network, however the

total power should be equal to the sum of export power capability of all the VSC-HVDC transmission systems. The power sharing can either be done by power set-points or droop gains value. The impact of both techniques on the system is addressed in the next section.

3.2.1 Active Power Control Using Frequency Droop

In the multi-synchronous machine system, the generator inertial system link the network frequency with the active power. The network frequency is not directly controlled by the generator rather it is controlled by balancing mechanical power with the electrical power. The synchronous generator frequency control principle can be understood by its swing equation as given in (3.2). It is clear that any imbalance in electrical and mechanical power cause change in the mechanical speed of the rotor consequently affects the network frequency.

$$
\begin{aligned}
M_m \frac{d\omega_m}{dt} &= p_m - p_e - D_m \omega_m \\
\omega_e &= \frac{P_p}{2} \omega_m, \quad M_m = J\omega_{sm}
\end{aligned}
\tag{3.2}
$$

Here, M_m is the angular momentum of the rotor at the synchronous speed, ω_m is the rotor shaft velocity, D_m is the damping coefficient, p_m is the mechanical power, p_e is the electrical power, ω_e angular electrical frequency, P_p is the number of poles, ω_{sm} is the rotor synchronous speed, and J is the total moment of inertia of the turbine and generator rotor.

On the contrary, offshore AC network such as shown in Figure 3.1 does not have any inertia in the system and contains only static devices. The frequency on the network is directly imposed by the VSCs and using frequency droop scheme $\omega - p$ link is established. The frequencies imposed by all the grid forming VSCs in an offshore AC network must converge at the common equilibrium point for the stable operation. Thus, the condition expressed in (3.3) must be satisfied in steady-state.

$$
\begin{aligned}
\omega_{r\_1} &= \omega_{r\_2} = \cdots = \omega_{r\_i} \\
\omega_0 - \omega_{r\_1} &= \omega_0 - \omega_{r\_2} = \cdots = \omega_0 - \omega_{r\_i} = \Delta\omega
\end{aligned}
\tag{3.3}
$$
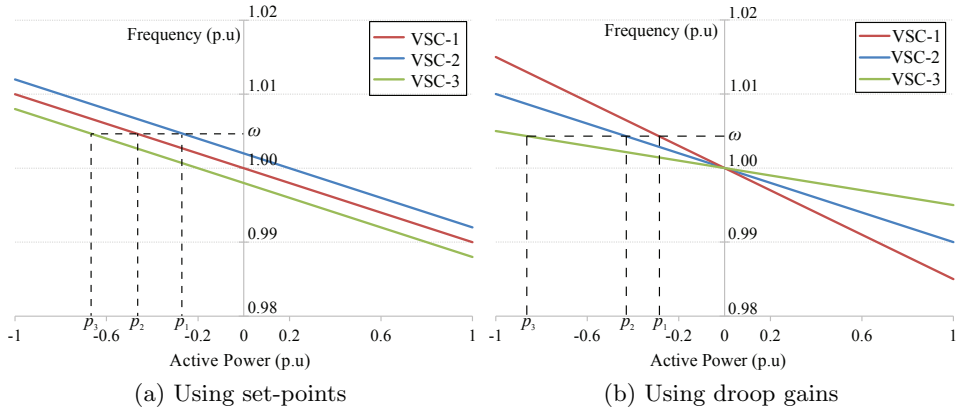
Figure 3.3: Comparison of active power sharing techniques.

Further, the sum of all the grid forming VSCs active power is equal to the total active power (p_s) that is required to export onshore as expressed by (3.4).

$$p_s = p_1 + p_2 + \cdots + p_i$$
$$p_s = \sum_{i=1}^{n} p_i \tag{3.4}$$

Here, n is the total number of grid forming VSCs in the offshore AC network. The change in network frequency can be computed by applying condition (3.3) on frequency droop scheme given in (3.1) and substituting the value of p_i in (3.4).

$$\Delta\omega = \frac{1}{\displaystyle\sum_{i=1}^{n} \frac{1}{k_{f\_i}}} \left(p_s - \sum_{i=1}^{n} p_{0\_i} \right) \tag{3.5}$$

Using (3.5), the active power of ith VSC can be calculated as (3.6).

$$p_i = \frac{\Delta\omega}{k_{f\_i}} + p_{0\_i} \tag{3.6}$$

There are two possibilities to control the sharing of active power between converters i.e by changing the set-points of the active power or by changing

(a) VSCs frequencies

(b) VSCs active powers
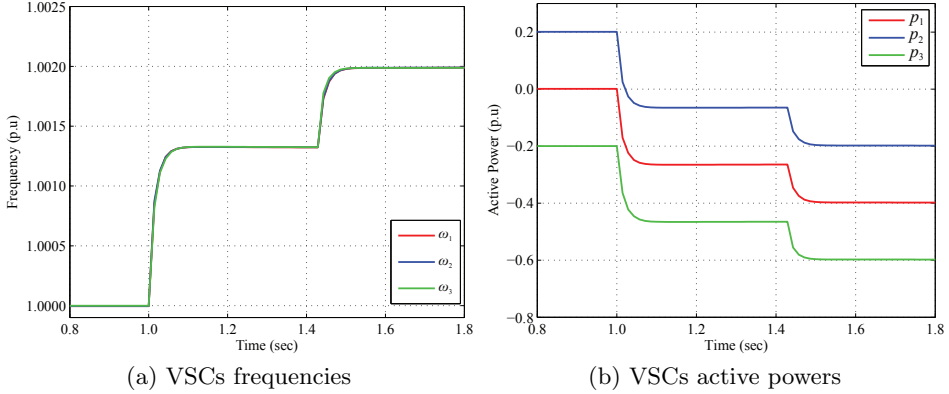
Figure 3.4: Illustration of frequency and active power distribution using set-points.

the droop gains value. The comparison between these two techniques is shown in Figure 3.3.

Active Power Sharing Using Set-points: In the first method, the distribution of the active power among converters is achieved by assigning different active power set-points while keeping droop gains value for all grid forming VSCs equal.

$$
\begin{aligned}
p_{0\_1} \neq p_{0\_2} \neq \cdots \neq p_{0\_i} \\
k_{f\_1} = k_{f\_2} = \cdots = k_{f\_i} = k_f \neq 0
\end{aligned}
\tag{3.7}
$$

Thus, the steady-state change in network frequency and the ith VSC active power can be calculated as (3.8) by applying condition given in (3.7) on (3.5) and (3.6).

$$
\Delta\omega = \frac{k_f}{n}\left(p_s - \sum_{i=1}^{n} p_{0\_i}\right)
$$

$$
p_i = \frac{1}{n}\left(p_s - \sum_{\substack{j=1 \\ j\neq i}}^{n} p_{0\_j}\right) + \left(\frac{n-1}{n}\right) p_{0\_i}
\tag{3.8}
$$

In Figure 3.4, frequency and active power responses of the VSCs are shown of the network illustrated in Figure 3.1. Two steps in the active power infeed into the offshore AC network is applied by the wind power plants i.e 0.8 p.u at 1.0 s in WPP-1 and 0.4 p.u at 1.43 s in WPP-2. It is clear from the result that the change in the frequency does not produce large transient and the rate of change of frequencies is small. Note that prior to 1.0 s no other sources (e.g wind turbines) are injecting active power in the offshore AC network. In this scenario, the active power can be transferred from one onshore grid to another according to the initial set-points via offshore network. However, it will produce losses in offshore converters and offshore AC cables which is not desirable and can be avoided through other export network topology i.e multiterminal HVDC system. Furthermore, the transfer of power from one VSC-HVDC transmission system to another is not constant and it varies according to the wind speed.

Active Power Sharing Using Droop Value: In the second method, the distribution of active power among converters is achieved by assigning different droop values while having the same active power set-points.

$$
\begin{aligned}
p_{0\_1} = p_{0\_2} = \cdots = p_{0\_i} = 0 \\
k_{f\_1} \neq k_{f\_2} \neq \cdots \neq k_{f\_i} \neq 0
\end{aligned}
\tag{3.9}
$$

The change in the network frequency and the active power of ith VSC can be calculated by applying condition given in (3.9) into (3.5) and (3.6).

$$
\Delta\omega = \frac{1}{\displaystyle\sum_{i=1}^{n} \frac{1}{k_{f\_i}}} \cdot p_s
$$

$$
p_i = \frac{1}{k_{f\_i}} \cdot \frac{1}{\displaystyle\sum_{j=1}^{n} \frac{1}{k_{f\_j}}} \cdot p_s
\tag{3.10}
$$

The response of VSCs frequencies and active power using this method is shown in Figure 3.5. The power flow direction through all the VSCs is in same direction which implies that the active power from one VSC-HVDC

(a) VSCs frequencies   (b) VSCs active powers
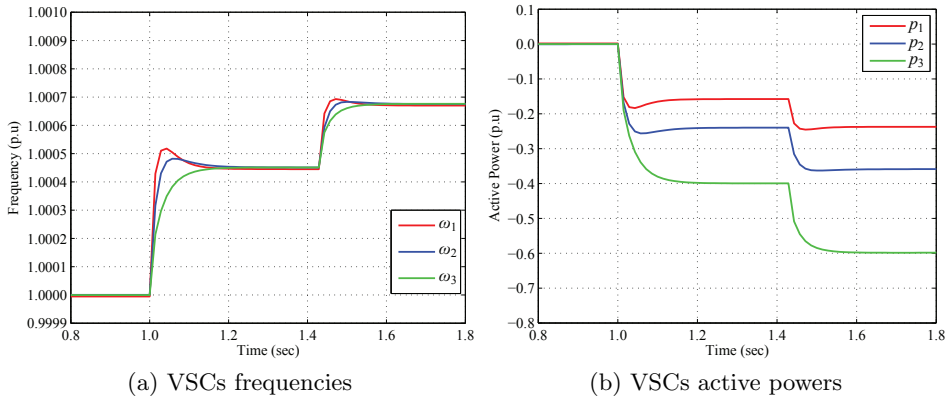
Figure 3.5: Illustration of frequency response and active power distribution using droop gains of an offshore AC network.

transmission system will not be injected to another. Only the active power infeed by the wind power plants will be exported to onshore grids. Such an operation is like the slack source in the electrical network which is desirable for VSCs to be exhibited in the offshore AC network. However, the different droop gains may result in different imposed frequencies transient response which may cause interaction between VSCs. The active power sharing method using droop gain value is applied in rest of the thesis.

3.2.2 Reactive Power Control Using Voltage Droop

Unlike frequency, the VSCs control busbar voltages are not linked with the common bus and each VSCs bus voltage converge to different equilibrium point. Without voltage droop characteristics, VSCs maintain the respective bus voltage level at the predefined value and the power flows through them according to the impedance of the network. It is clear that the VSCs have to balance the reactive power in the offshore AC network which depends on the grid power flow. However, the contribution of reactive power balancing by each VSC can be controlled using voltage droop scheme. Similar to the active power sharing control, the reactive power sharing is controlled using voltage droop gain instead of reactive power set-point as expressed by (3.11). The impact of the voltage droop gains on the steady-state operating
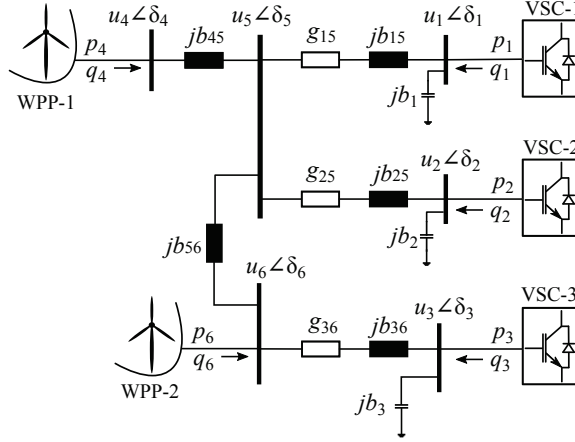
Figure 3.6: An impedance diagram of an offshore AC network for power flow analysis.

points of the network can be understood through power flow analysis on the network given in Figure 3.1.

$$u_{r\_i} = u_0 + k_{u\_i} \cdot q_i \quad \because q_{0\_i} = 0 \tag{3.11}$$

The impedance diagram for power flow analysis is shown in Figure 3.6, and the network impedance's are given in Table 3.1. The power flow in the network can be calculated using (3.12). Note that the VSCs are controlling voltages at their respective filter buses, therefore the substation transformer impedance must also be included in the algorithm. The filter bus voltage of each VSC are defined as slack bus, thus the frequency and voltage droop schemes given in (3.1) are applied at the filter bus.

$$
\begin{aligned}
p_l &= u_l \sum_{m=1}^{z} u_m(g_{lm} \cos(\delta_l - \delta_m) + b_{lm} \sin(\delta_l - \delta_m)) \\
q_l &= u_l \sum_{m=1}^{z} u_m(g_{lm} \sin(\delta_l - \delta_m) - b_{lm} \cos(\delta_l - \delta_m))
\end{aligned}
\tag{3.12}
$$

The response of the active and reactive VSCs power flow with respect to net export energy in the offshore AC network is shown in Figure 3.7. In the analysis, the rated voltage of the offshore network is 150 kV and the

Table 3.1: Offshore AC network impedances for power flow analysis

	Resistance	Inductance	Capacitance
AC Cable	-	0.37 mH/km	0.21 μF/km
Transformer[a]	0.1 Ω	17.2 mH	-
Filter Capacitor[a]	-	-	7.07 μF

[a] refer to 150 kV level.

rated power of each VSC-HVDC transmission system is 500 MVA, and these values are also the base value in the results. The rated active power of both wind power plants is 538.52 MVA with 0.9285 power factor. The VSC active and reactive power with respect to the net export power in the offshore AC network without droop scheme is shown in Figure 3.7a. The net export energy in the lossless network is the sum of WPP-1 (p_4) and WPP-2 (p_6) active power infeed into the offshore AC network. The steady-state power profile is determined by increasing the WPP-1 active power infeed from zero to 1.0 p.u while keeping WPP-2 infeed to zero, and then increasing WPP-2 active power infeed from zero to 1.0 p.u while keeping WPP-1 active power constant to 1.0 p.u, hereby the net active power become twice of a single VSC-HVDC transmission capability. Further, WPP-1 and WPP-2 are not providing any reactive power support to the network i.e $q_4 = q_6 = 0.0$ p.u. The results shows that the VSCs active and reactive powers are according to the impedance of the network without droop scheme and power distribution is not controllable among them.

The impact of the droop scheme on the power flow of the VSCs is shown in Figure 3.7b. The frequency droop gains are set to distributed 20 %, 32 %, and 48 % of the net export power among VSC-1, VSC-2, and VSC-3 respectively. While all the voltage droop gains are set to equal value in order to have same reactive power sharing i.e $k_{u1} = k_{u2} = k_{u3} = 0.08$ p.u. The power flow response indicate that the percentage of active power sharing is consistent among VSCs at each export power operating point. However, the percentage of reactive power sharing is not consistent despite having same voltage droop gains. It shows that the reactive power in the offshore grid depends on two main factors i.e actual active power flow through VSC and the voltage droop gain. The impact of the active power flow on the reactive

(a) Without droop scheme　　　　　(b) With droop scheme
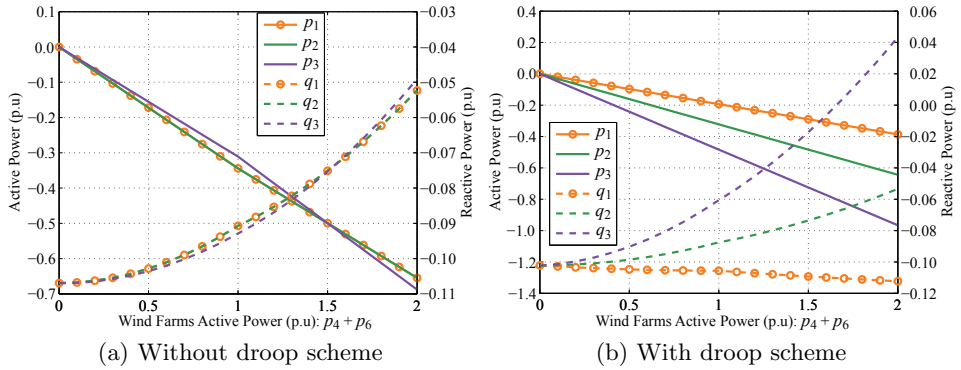
Figure 3.7: The comparison of VSC power flow response with and without droop scheme.

power can be understood from the VSC-1 reactive power expression given in (3.13). It shows that the reactive power varies parabolically with respect to active power.

$$q_1 = u_1 \cdot u_5 \cdot b_{15} \sqrt{1 - \left(\frac{p_1}{u_1 \cdot u_5 \cdot b_{15}}\right)^2} - u_1^2 \cdot (b_1 + b_{15}) \qquad (3.13)$$

In the highly capacitive network such as an offshore AC network, the change in the voltage set-point of the slack bus cause the change in the reactive power generation. According to the voltage droop scheme, the VSC reactive power changes the set-point of its controlling bus voltage consequently affect the reactive power in the grid hereby again change the VSC reactive power ergo creates a chain reaction. This chain reaction can cause voltage collapse in the network. The influence of the VSC control bus voltage on the reactive power can be visualized from Figure 3.7b. It can be seen that the reactive power flow of VSCs start diverging from each other consequently VSC-1 and VSC-2 injecting inductive reactive power and VSC-3 capacitive after net export power of 1.6 p.u. This indicates that the reactive power is circulating among VSCs, thus requires additional droop gains selection criteria to avoid such condition.

3.2.3 Method of Selecting Frequency and Voltage Droop Gains

The selection of frequency and voltage droop gains for the steady-state operation depends on the operational requirement and the long term voltage stability. The main operational requirement is the ability to control the power distribution among the VSC-HVDC transmission systems which could be an operator specification.

It is known that all VSCs active power flow direction would be same while controlling the sharing of active power using droop gains. Thus, the active power of VSC can be expressed as a factor α of the total power (p_s) in the offshore AC grid. The active power of each VSCs can be expressed as (3.14) for n grid forming VSCs.

$$
\begin{aligned}
p_1 &= \alpha_1 \cdot p_s \\
p_2 &= \alpha_2 \cdot p_s \\
&\vdots \\
p_n &= \alpha_n \cdot p_s
\end{aligned}
\tag{3.14}
$$

Also, It is known that the total power must be equal to the sum of the VSCs power, thus (3.14) can be simplified as (3.15).

$$
\begin{aligned}
p_s &= p_1 + p_2 + \cdots + p_n \\
p_s &= \left(\sum_{i=1}^{n} \alpha_i \right) p_s \\
\sum_{i=1}^{n} \alpha_i &= 1 \qquad \forall \alpha \in \Re : 0 \le \alpha \le 1
\end{aligned}
\tag{3.15}
$$

In order to satisfy condition given in (3.15), the nth VSC sharing factor must be defined as (3.16).

$$
\alpha_n = 1 - \sum_{i=1}^{n-1} \alpha_i
\tag{3.16}
$$

The condition of the nth VSC active power can be defined as (3.17) by substituting (3.16) in (3.14).

$$p_n \left(\sum_{i=1}^{n-1} \alpha_i \right) - \left(1 - \sum_{i=1}^{n-1} \alpha_i \right) \sum_{i=1}^{n-1} p_i = 0 \qquad (3.17)$$

For $n - 1$ VSCs, the distribution factor must be defined in order to determine the droop values. This can be achieved by defining the relationship between the distribution factor and the droop values by comparing (3.10) with (3.14). Thus, the distribution factor of any i^{th} VSC can be written as (3.18).

$$\alpha_i = \frac{1}{k_{f\_i}} \cdot \frac{1}{\displaystyle\sum_{j=1}^{n} \frac{1}{k_{f\_j}}} \qquad (3.18)$$

Similarly, consider β as the reactive power distribution factor then the reactive power of each grid forming VSCs in the offshore AC network can be expressed as (3.19).

$$
\begin{aligned}
q_1 &= \beta_1 \cdot q_s \\
q_2 &= \beta_2 \cdot q_s \\
&\vdots \\
q_n &= \beta_n \cdot q_s
\end{aligned}
\qquad (3.19)
$$

Here, q_s is the sum of the reactive power flowing through each grid forming VSCs. Also, the reactive power sharing condition given in (3.20) must be satisfied.

$$
\begin{aligned}
q_s = q_1 + q_2 + \cdots + q_n &= \sum_{i=1}^{n} q_i \\
\sum_{i=1}^{n} \beta_i = 1 \qquad &\forall \beta \in \Re : 0 \leq \beta \leq 1
\end{aligned}
\qquad (3.20)
$$

Unlike frequency droop scheme, the relationship between reactive power sharing factor (β) and the voltage droop gains (k_u) cannot be explicitly defined because of not having a common link between the VSCs control busbars. However, the computation of voltage droop gains can be done with

the common variable i.e reactive power. Thus, the condition for reactive power sharing of ith VSCs can be defined as (3.21) for n grid forming VSCs in the offshore AC network by substituting (3.20) into (3.19).

$$(1 - \beta_i) q_i - \beta_i \sum_{\substack{j=1 \\ j \neq i}}^{n} q_j = 0 \qquad (3.21)$$

Note that $n - 1$ reactive power distribution factor (β) is required to be defined in order to satisfy (3.20), also one system function would be redundant if it is defined by (3.21) for all grid forming VSCs. Furthermore, the busbars voltages are not considered in the selection of droop gains. As explained in previous section that the reactive power flow of the VSCs changes the controlling bus voltage level, and the difference between these bus voltages may generate additional reactive power. The require reactive power sharing can be achieved at high gain as well as at lower, however the interaction between VSCs control busbars would be large at high voltage droop gains. The impact of the voltage droop on the network can be understood by analyzing the change it caused in the reactive power at the load bus.

Consider that a load bus is directly connected with a VSC control bus. The reactive power flow equation of the load bus given in (3.12) can be expanded for the branches that are connected with the VSC control bus (i.e filter bus) as (3.22).

$$q_l - u_l \sum_{\substack{m=1 \\ m \neq i}}^{z-1} u_m \left\{ g_{lm} \sin(\Delta \delta_{lm}) - b_{lm} \cos(\Delta \delta_{lm}) \right\}$$

$$-u_l u_i \left\{ g_{li} \sin(\Delta \delta_{li}) - b_{li} \cos(\Delta \delta_{li}) \right\} = 0 \qquad (3.22)$$

Substitution of the voltage droop equation given in (3.11) into (3.22) yield (3.23).

$$q_l - u_l \sum_{\substack{m=1 \\ m \neq i}}^{z-1} u_m h_{lm} - u_l h_{li} \left(u_0 + k_{u\_i} q_i \right) = 0 \qquad (3.23)$$

$$q_l - u_l \underbrace{\sum_{\substack{m=1 \\ m \neq i}}^{z-1} u_m h_{lm} - u_l u_0 h_{li}}_{k_{u\_i}=0} - \underbrace{u_l k_{u\_i} q_i h_{li}}_{\Delta q_{k\_i}} = 0 \qquad (3.24)$$

Here, z is the total number of AC busbars in the offshore AC network, i is the VSC control busbar index, $h_{lm} = g_{lm}\sin(\Delta\delta_{lm}) - b_{lm}\cos(\Delta\delta_{lm})$, and $h_{li} = g_{li}\sin(\Delta\delta_{li}) - b_{li}\cos(\Delta\delta_{li})$.

The first three terms in (3.24) are the reactive power mismatch without voltage droop scheme at the load bus. The droop gain add the reactive power (Δq_{k_i}) at the load bus as the function of VSC reactive power. In case of one grid forming VSC in the network, this additional reactive power largely impact on the network voltages since there are no sources available other than cable capacitance to absorb it. The voltage droop scheme is not required to be applied for single grid forming VSC in the offshore AC network. However, the multiple grid forming VSCs in the offshore AC network can exchange this additional reactive power (Δq_{k_i}) for balancing and to reduce its impact on the network voltages. To achieve this, the criteria given in (3.25) can be applied to determine the droop gains.

$$\Delta q_{k\_1} + \Delta q_{k\_2} + \cdots + \Delta q_{k\_n} = 0$$
$$\sum_{i=1}^{n} \sum_{l=1}^{y} u_l k_{u\_i} q_i h_{li} = 0 \qquad \forall i, l : i \neq l \qquad (3.25)$$

Here, y is the total number of busbars that is connected with i^{th} VSCs reference bus, n is the total number of grid forming VSCs in the offshore AC network, k_{u_i} and q_i are the voltage droop gain and reactive power of ith VSC.

Steady-State Analysis: The optimum value of droop gains can be calculated using above criteria to achieve desire power sharing among the VSC-HVDC transmission system. To do so, an optimum power flow algorithm is developed using (3.1), (3.10), (3.12), (3.17), (3.18), (3.21), and (3.25) for the network shown in Figure 3.6. The solution is found using MAT-

Table 3.2: Droop gain values according to proposed method

Figure No.	kf_1	kf_2	kf_3	ku_1	ku_2	ku_3
3.8a	0.0076	0.0076	0.0073	-0.0014	-0.0014	0.0026
3.8b	0.0020	0.0031	0.0012	-0.0021	-0.0036	0.0056
3.8c, and 3.8d	0.0012	0.0012	0.0012	-0.0164	-0.0857	0.0442

LAB function 'fmincon'. The detail implementation procedure is explained in next section on the extended network. Here, the analysis is made to focus on the impact of droop gains on the VSCs steady-state power flow with respect to net active and reactive power at different power sharing factors. The droop gains are calculated at the given wind power of $p_4 = 0.4$ p.u, and $q_4 = p_6 = q_6 = 0.0$ p.u using proposed method and their values are given in Table 3.2. The power flow analysis at different power sharing factors is shown in Figure 3.8.

Firstly, the droop gains are determined to have equal active and reactive power flow through all VSC-HVDC transmission systems i.e VSC-1 and VSC-2 are set to flow 33%, and VSC-3 flows 34% of net offshore AC grid active and reactive power. It is clear from Figure 3.8a that the VSCs are sharing active and reactive power according to the defined sharing criteria. Note that both wind power plants are not injecting any reactive power into the offshore AC network. Further, the variation in the reactive power of the VSCs are due to the active power flow in the network. The reactive power sharing among VSCs are consistent and it do not generate circulating power.

Secondly, the power sharing ability of the VSCs at different sharing factors and the effects of active power on reactive power sharing is evaluated. In Figure 3.8b, the response of VSC power flow is shown at the same reactive power sharing factor but different active power sharing factor. The results shows that the active power sharing is according to the setting i.e 30%, 20%, and 50% of net active power flows through VSC-1, VSC-2, and VSC-3 respectively. On the other hand, the reactive power varies significantly despite having same sharing factor. The reactive power sharing is only according to the designed criteria at the operating point at which solution has been found i.e $p_4 = 0.4$ p.u, and $q_4 = p_6 = q_6 = 0.0$ p.u. The change

(a) $\alpha_1 = \alpha_2 = 0.33, \alpha_3 = 0.34, \beta_1 = \beta_2 = 0.33, \beta_3 = 0.34$

(b) $\alpha_1 = 0.3, \alpha_2 = 0.2, \alpha_3 = 0.5, \beta_1 = \beta_2 = 0.33, \beta_3 = 0.34$

(c) $\alpha_1 = \alpha_2 = 0.33, \alpha_3 = 0.34, \beta_1 = 0.3, \beta_2 = 0.2, \beta_3 = 0.5$

(d) $\alpha_1 = \alpha_2 = 0.33, \alpha_3 = 0.34, \beta_1 = 0.3, \beta_2 = 0.2, \beta_3 = 0.5,$
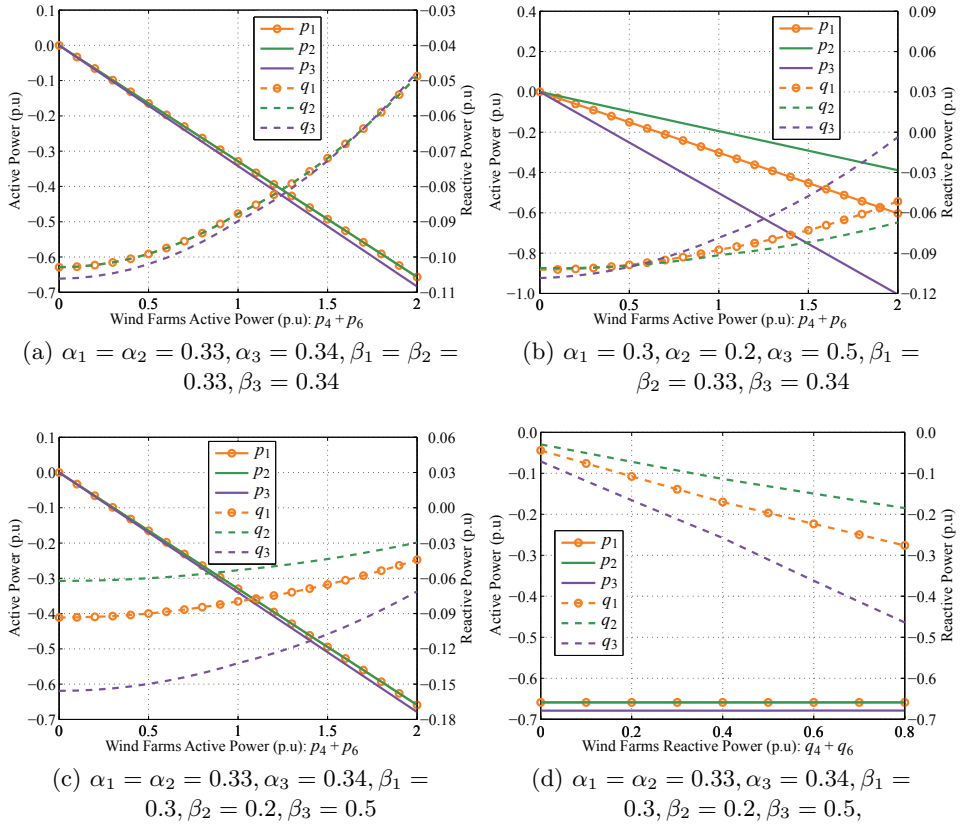
Figure 3.8: Illustration of the frequency and voltage droop effects on the VSC power flow.

in reactive power is due to the difference in active power flow through each VSCs. It is clear that the influence of the active power on reactive power must be taken into account while selecting droop gains. Note that the projection of reactive power of all VSCs is toward the same direction with the application of criteria defined in (3.25). The reactive power profile can be modified by selecting the different operating point in the algorithm for determining droop gains value. The profile can be adjusted over the range of net active power in the offshore AC network. The power responses of VSCs at different reactive power sharing but at same active power sharing are shown in Figure 3.8c. Here, reactive power sharing is constant at the

designed value throughout the variation of net active power in the offshore AC grid. Yet again, the reactive power projection is same in all VSCs which demonstrate that the unnecessary reactive power is not generated in the network.

Thirdly, the analysis of VSCs power response is shown in Figure 3.8d with respect to the net reactive power injection of wind power plants i.e $q_s = q_4 + q_6$. Both wind power plants are injecting maximum active power i.e $p_4 = p_6 = 1.0$ p.u. In the analysis, the active power sharing is set to equal. Here, the reactive power contributions are 30%, 20%, and 50% by VSC-1, VSC-2, and VSC-3 respectively. The power flow profile is created by first changing the power factor of WPP-1 from 1.0 to 0.9285 leading while keeping WPP-1 power factor to 1.0, and then changing WPP-2 power factor from 1.0 to 0.9285 leading. It is evident that the VSCs active power sharing is according to the designed criteria at all operating points and it is not influenced by the reactive power flow. Further, the reactive power sharing is also consistent among the VSCs. Note that the generator oriented sign convention is used in the results.

Time Domain Analysis: The proposed method of selecting frequency and voltage droop gains is validated by performing nonlinear simulation of the network shown in Figure 3.1. The frequency droop gains are set as $k_{f1} = 0.0020$ p.u, $k_{f2} = 0.0031$ p.u, and $k_{f3} = 0.0012$ p.u. The voltage droop gains setting are $k_{u1} = -0.0021$ p.u, $k_{u2} = -0.0036$ p.u, and $k_{u3} = 0.0056$ p.u. The wind power plants reactive power set-points are $q_4 = q_6 = 0.0$ p.u. For the dynamic analysis, the WPP-1 wind active power is changed from zero to 1.0 p.u at 2.0 s, and the WPP-2 active power is changed from zero to 1.0 p.u at 4.0 s. The power and frequency responses of the VSCs are shown in Figure 3.9.

During first step change in power, the VSC-1 is exporting 0.3 p.u active power to onshore whereas VSC-2 and VSC-3 are exporting 0.2 p.u and 0.5 p.u respectively. At the full power infeed by both wind power plants, the VSC-1 reaches its active power export limit. According to the network parameters, the maximum active power sharing factor (α_i) that can be assigned to any VSCs is 0.5 at maximum wind energy infeed. The wind

(a) VSC-1 power response

(b) VSC-2 power response

(c) VSC-3 power response

(d) Frequency response of VSCs
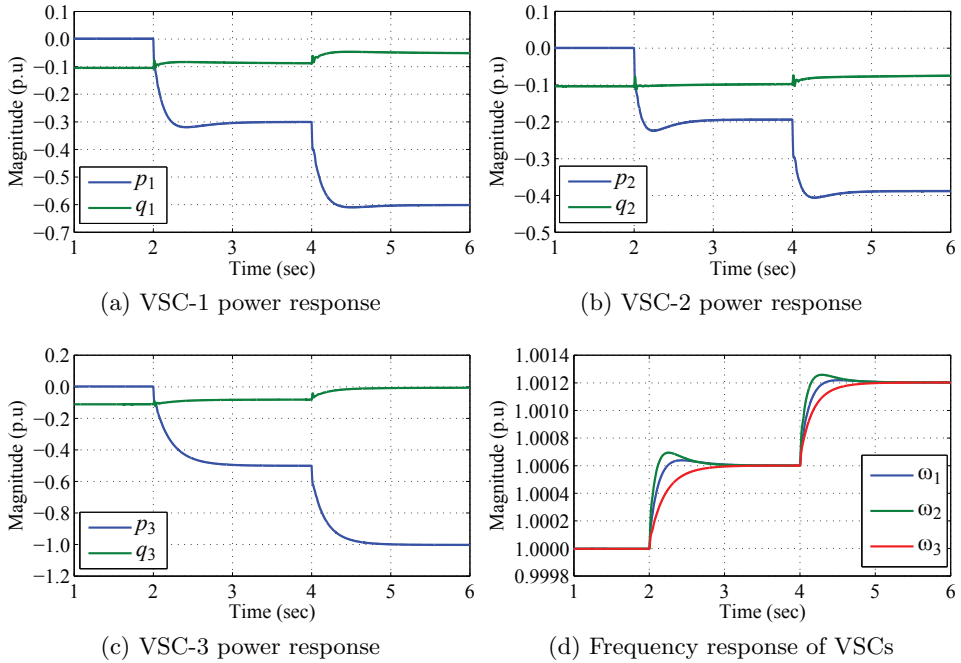
Figure 3.9: Nonlinear simulation result of offshore AC network having multiple grid forming VSC HVDC transmission system.

power plants are not injecting any reactive power into the network. The small variation in the VSCs reactive power corresponds to the influence of active power flow. The steady-state power profile of this dynamic analysis is shown in Figure 3.8b. At steady-state, the dynamic result corresponds to the steady-state analysis i.e the reactive power flow through VSC-1 and VSC-2 is approximately -0.05 p.u, and VSC-3 flows 0.0 p.u. The system is stable and all the VSCs frequencies converge at the same equilibrium value as illustrated in Figure 3.9d. Moreover, the rate of change of frequency imposed by each VSCs is different which depends on the frequency droop gains assigned to each VSCs. The maximum rise in the network frequency is 50.06 Hz at the maximum wind power plant generation. This maximum change in network frequency can be calculated using (3.10).

The response of the voltage at the VSC controlling busbars (filter bus) is shown in Figure 3.10. The influence of the voltage droop gains on the
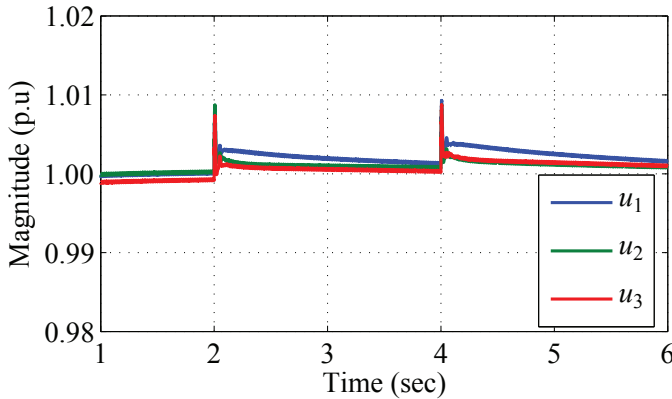
Figure 3.10: The response of voltage d-component of the VSCs controlling busbars.

network voltages are minimum and the small voltage difference between each VSCs reference bus enables the control on the reactive power sharing. The droop gain selection using proposed method shows that the active and reactive power distribution among VSC-HVDC transmission system can be controlled while maintaining system stability.

3.3 Offshore Grid Optimization and Reactive Power Management

Reactive power optimization is an important factor in minimizing losses in the network with respect to the active power dispatch by the wind power plants [86]. Traditionally, reactive power management is addressed as an optimization problem and the solution is found by solving an optimal power flow algorithm (OPF). Multi-objective optimization technique compared to single objective offer advantages in term of providing solution with respect to the weight of multiple loss function criteria in order to operate the network more effectively [87–89, 101]. In this section, a method of reactive power management has been proposed for an offshore AC network using multi-objective optimization technique. The optimization problem is solved using interior point method. The solution of the algorithm provides the reactive power set points of each wind power plant and reactive power contribution
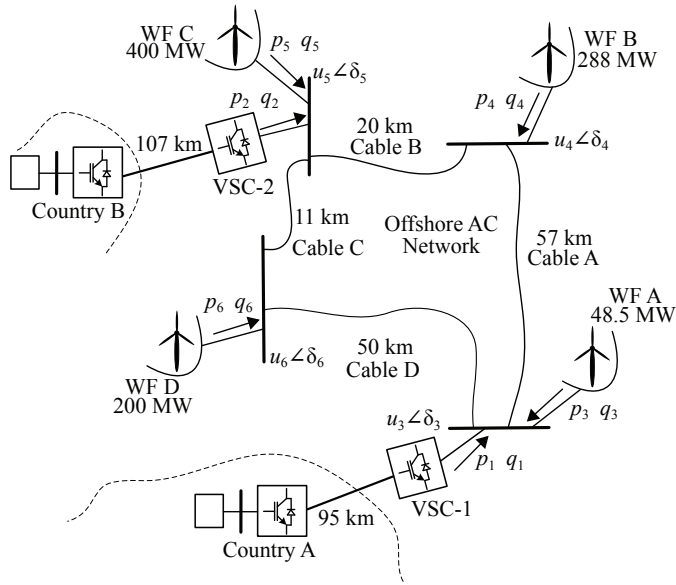
Figure 3.11: Configuration of an offshore AC network interconnecting two onshore grid using VSC HVDC transmission system.

factor of each VSC-HVDC transmission system according to the net wind power generation. The solution also provide the frequency and voltage droop gains value according to the sharing criteria.

3.3.1 System Configuration

An offshore AC network configuration having multiple grid forming VSC-HVDC system is presented in Figure 3.11. In the network, four wind power plants are connected together in a mesh configuration using AC cable at the voltage level of 150 kV. The net power from the AC network is supplied to two different onshore grids using point-to-point VSC-HVDC transmission system. The layout of the individual wind power plants is not the focus of this research as it is assumed that the wind power plant control system is able to provide reactive power support within its operating capability at the connection point. Further, it is also assumed that the internal layout of wind power plants is in radial or radial-ring configuration so that active power flows only from wind turbines to offshore AC network. The maximum

Table 3.3: Offshore AC network impedances for OPF algorithm

Name	Resistance	Inductance	Capacitance
AC Cable	0.0151 Ω/km	0.118 mH/km	0.24 μF/km
Transformer[a]	0.099 Ω	17.2 mH	-
Filter Capacitor[a]	-	-	6.85 μF
DC Cable	0.019 Ω/km	-	-

[a] refer to 150 kV level.

accumulated wind power into offshore AC network is 936.5 MW (1.873 p.u). The active power export capability of each transmission system is 655.55 MW (1.31 p.u). Thus, the maximum active power sharing factor that can be defined to one of the VSC-HVDC system is 0.7. The symmetrical monopolar HVDC transmission system is considered having voltage level of $\pm$150 kV. In Table 3.3, the impedance's of the network for the OPF algorithm are listed [102, 103]. The base power used in the results is 500 MVA.

The offshore side converters of both export transmission systems are in grid forming mode and they have the same control system as illustrated in Figure 3.2. The method of selecting the frequency and voltage droop gains explained in the previous section is applied to control the power sharing. The onshore side converter controls the DC voltage and its control system is given in Section 2.5. The steady-state voltage at the onshore converters DC busbars are controlled to 1.0 p.u ergo makes it as a slack bus in the DC network.

3.3.2 Optimization Problem

The management of the reactive power is an important factor for minimizing the losses of the network. The more the active elements that controls the voltage in the network more the flexibility in managing the reactive power. Apart from determining the optimum reactive power set-points of the wind power plants (as a tradition approach), an ability of a reactive power sharing among converters also contributes in minimization of the active losses. Normally, an optimization problem consists of the system constraints and the objective functions that are required to be satisfied to have the optimal solution. The power flow optimization is a nonlinear

non-convex problem and it has large number of local minima. A local minima can be designated as a global minima within the closed interval define by the constraints and boundaries. The system constraints and limits ensure that the same local minima is found at different initial values for the given predefined conditions and sets of inputs or get no solution at all. An optimization algorithm based on interior-point method is well suited to find the solution of nonlinear system. For the analysis, the optimization problem has been implemented using sets of nonlinear equations that are derived as follows:

Constraints: The network configuration and the control conditions are defined as a nonlinear equalities and inequalities constraints for the formulation of an optimization problem. In general, these constraints can be expressed as (3.26).

$$\text{System} \begin{cases} g(x) \leq 0 \\ h(x) = 0 \end{cases} \tag{3.26}$$

According to the problem, these constraints consists of AC and DC network topologies, VSCs droop control equations, power sharing criteria, and optimization variables boundary limit.

a) *Offshore AC and DC Network Topology*: The network topology is an equality constraint and it is usually defined by the power flow equation. The power flow equations for the AC network are defined using (3.12). In the DC network only the active power exists which can be defined for the OPF algorithm as (3.27).

$$P_i = U_i \sum_{j=1}^{k} U_j G_{ij} \tag{3.27}$$

The link between the AC and DC power flow is established by defining active power loss function as (3.28).

$$p_{vsc} + P_{dc} + P_{loss} = 0 \tag{3.28}$$

Here, p_{vsc} and P_{dc} are the AC and DC active power of the VSC respectively, and P_{loss} is the converter stations active power loss. The per unit converter station active power loss (P_{loss}) is calculated using quadratic function depending on the converter current (i_{vsc}) as expressed by (3.29).

$$P_{loss} = a + b \cdot i_{vsc} + c \cdot i_{vsc}^2$$
$$i_{vsc} = \frac{\sqrt{p_{vsc}^2 + q_{vsc}^2}}{u_{vsc}} \qquad (3.29)$$

Here, $a = 11.033 \times 10^{-3}$ p.u is no-load coefficient, $b = 3.464 \times 10^{-3}$ p.u is the voltage drop coefficient, and $c = 4.4 \times 10^{-3}$ p.u is the ohmic loss coefficient. The value of these power loss coefficients are derived from [59].

b) *Voltage and Frequency Droop Control of the VSC-HVDC*: The VSCs control the voltage at the filter bus, and this bus act as a slack bus in the AC network. In the OPF algorithm, the offshore converters are like the slack sources who must consume all power injected by the wind power plants. Without droop control, the active and reactive power through VSCs flows according to the impedance of the network. Using voltage and frequency droop schemes, the VSC-1 and VSC-2 control equation of grid forming mode operated in parallel can be written as (3.30). The power sharing will be achieved by determining the droop gains according to the assigned contribution factor.

$$u_1 = u_0 + k_{u1} \cdot q_1$$
$$u_2 = u_0 + k_{u2} \cdot q_2$$
$$\omega_1 = \omega_0 - k_{f1} \cdot p_1 \qquad (3.30)$$
$$\omega_2 = \omega_0 - k_{f2} \cdot p_2$$

Here, u_1 and u_2 are VSC-1 and VSC-2 filter bus voltages, ω_1 and ω_2 are the frequencies imposed by VSC-1 and VSC-2, p_1 and q_1 are the active and reactive power of VSC-1, and p_2 and q_2 are the active and reactive power of VSC-2.

The resultant steady-state frequency imposed by both VSCs on the offshore AC network is calculated using (3.31). These VSCs control equations are applied as equality constraint in the OPF algorithm.

$$\omega = \omega_0 - \frac{k_{f1}k_{f2}}{k_{f1} + k_{f2}} \cdot (p_1 + p_2) \qquad (3.31)$$

c) *Power Sharing Criteria*: The OPF algorithm provides the droop gains value by applying additional power sharing criteria. The power sharing factor could be a transmission system operator requirement which defines the percentage of the total wind power to be transferred through each VSC-HVDC transmission system. The power sharing criteria is defined as an equality constraint in the OPF algorithm. Consider, α as an active power contribution of VSC-2, thus using (3.18), the power sharing condition for VSC-2 is defined as (3.32).

$$\alpha \cdot (k_{f1} + k_{f2}) - k_{f1} = 0 \qquad (3.32)$$

The active power contribution factor of VSC-1 will then be $1 - \alpha$ and its relation with the power is defined using (3.17). The power sharing condition for VSC-1 can be written as (3.33).

$$\alpha \cdot p_1 + (1 - \alpha) \cdot p_2 = 0 \qquad (3.33)$$

Similarly, consider β as a reactive power contribution factor of VSC-2. By applying (3.21), the condition of reactive power sharing for VSC-2 can be written as (3.32).

$$(1 - \beta) \cdot q_2 - \beta \cdot q_1 = 0 \qquad (3.34)$$

By applying (3.25), the condition for VSC-1 reactive power sharing is defined as (3.35) in order to reduce the impact of droop gains on the network voltages.

$$u_3 \cdot b_{13} \cdot q_1 \cdot k_{u1} + u_5 \cdot b_{25} \cdot q_2 \cdot k_{u2} = 0 \qquad (3.35)$$

Here, b_{13}, and b_{25} are the susceptance of VSC-1, and VSC-2 transformers respectively. Note that the equation is approximated for small voltage angle.

d) *Operational Boundary Limits*: The operational limits are applied by defining inequality constraints. These boundaries limits are based on the general requirements of the TSOs define in the grid code [47]. The limits of frequency and voltage droop gains are required to be calculated by performing small signal analysis of an offshore AC network. The method of calculating droop gain stability boundary is explained in next chapter. The wind power plants reactive power limits are applied to enforce the power factor within the grid code limits and they are based on each wind power plants active power rating. The power factor of 0.97, 0.96, 0.93, and 0.92 are considered for WF-A, WF-B, WF-C, and WF-D respectively. The output vector is bounded between upper and lower limits as (3.36).

$$
\begin{aligned}
0.90 &\leq u \leq 1.10 \\
-\pi &\leq \delta \leq \pi \\
-1.31 &\leq p_{vsc} \leq 1.31 \\
-0.4 &\leq q_{vsc} \leq 0.4 \\
0.98 &\leq \omega \leq 1.004 \\
0 &\leq k_f \leq 0.01 \\
-0.1 &\leq k_u \leq 0.1 \\
0 &\leq \beta \leq 1.0 \\
-0.0243 &\leq q_3 \leq 0.0243 \\
-0.168 &\leq q_4 \leq 0.168 \\
-0.281 &\leq q_5 \leq 0.281 \\
-0.1561 &\leq q_6 \leq 0.1561
\end{aligned}
\qquad (3.36)
$$

In addition, the maximum frequency deviation limit is imposed by applying condition given in (3.10) at maximum power. It is a nonlinear inequality constraint defined as (3.37).

$$p_{max} \cdot k_{f1} \cdot k_{f2} - \Delta\omega_{max}\left(k_{f1} + k_{f2}\right) < 0 \tag{3.37}$$

Objective Functions: The objective function defines the criteria of finding the best solution from all feasible solution for an optimization problem. Multiple objective functions can also be applied for optimal solution. However, simultaneously optimizing each objective functions may not lead to a single solution for nontrivial multi-objective optimization problem. In that case, objective functions are said to be conflicting and the solution of the system cannot be found without degrading the objective values. A tradeoff is required between the functions in order to obtain a favorable solution. The simplest approach to achieve the trade-off among the objective functions is a weighted sum method [104]. In weighted sum method, a single function is formulated by multiplying each objective function with a predefined weighting factor as expressed by (3.38). The weighting factor defines the relative magnitude of each function in the overall solution. Pareto Front analysis of the objective functions can then be applied to choose the optimal operating points and the best solution.

$$\min\left\{F\left(x\right)\right\}$$
$$F\left(x\right) = \sum_{m=1}^{h} \gamma_m f_m\left(x\right) \quad \gamma_m \in [0, 1] \tag{3.38}$$

Here, γ_m is the weight of the mth objective function. In general, the weights are selected to satisfy (3.39).

$$\left(\sum_{m=1}^{h} \gamma_m\right) = 1 \tag{3.39}$$

An objective function can either be a loss function or profit function but all objectives must be converted into one type for weighted sum method. Two objective functions are selected for the optimization problem as expressed

by (3.40).

$$\min \{f(p, v, \gamma)\}$$
$$f(p, v, \gamma) = \gamma \cdot f_l(p) + (1 - \gamma) \cdot f_v(v) \tag{3.40}$$

Here, $f_l(p)$ is an objective function to minimize active loss, and $f_v(v)$ is an objective function for minimizing AC and DC voltages deviation from their nominal values.

a) *Minimizing Active Losses*: The active loss minimization objective function is given in (3.41). It is defined as the sum of total wind active power infeed into the offshore AC network and the net active power received at onshore grids. The function is expressed as least square error of the network active power losses.

$$f_l(p) = (p_3 + p_4 + p_5 + p_6 + p_{grid\_A} + p_{grid\_B})^2 \tag{3.41}$$

Here, p_3, p_4, p_5, and p_6 are the active power of wind power plants A, B, C, and D respectively. The active power received at onshore grid of country A and B are referred as p_{grid_A}, and p_{grid_B} respectively. The full weight to this objective function is given at $\gamma = 1$.

b) *Minimizing Voltage Deviation*: An objective function to minimize the least square voltage deviation is given in (3.42).

$$f_v(v) = \sum_{i=1}^{n} (u_i - 1.0)^2 \tag{3.42}$$

Here, u_i is the voltage magnitude of ith bus. The full weight to this objection function is given at $\gamma = 0$.

3.3.3 Optimization Result Analysis

The solution of the optimization algorithm provides the optimum operating values of the wind generation and VSC-HVDC systems which consists of
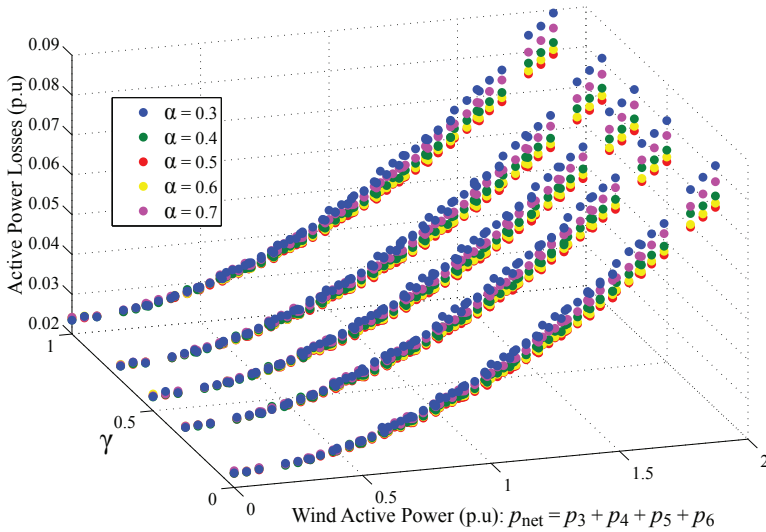
Figure 3.12: Total active power losses of the system.

the voltage and frequency droop gains, the reactive power support by each wind power plants, and the VSC-HVDC reactive power sharing factor. The optimum operating values are found with respect to the wind active power infeed and the VSC-HVDC active power sharing factor. The network is optimized with respect to the total active losses in the network and the bus voltage deviation from its rated value. The optimization variables for the network under study are given in (3.43).

$$
\begin{aligned}
x = [&u_1 \cdots u_z, \delta_1 \cdots \delta_z, U_1 \cdots U_k, P_1 \cdots P_k, p_1, q_1, p_2, q_2, p_{grid\_A} \\
&p_{grid\_B}, q_{grid\_A}, q_{grid\_B}, \omega, k_{u1}, k_{f1}, k_{u2}, k_{f2}, \beta, q_3, q_4, q_5, q_6]
\end{aligned}
\tag{3.43}
$$

Here, z is the total number of AC busbar, and k is total number of DC busbar. The optimization variable includes AC busbar voltage magnitude and phase angle, DC bubar voltage, DC active power, VSCs active and reactive power, onshore grid active and reactive power, offshore AC network frequency, VSCs frequency and voltage droop gains, VSCs reactive power sharing factor, and reactive power operating points of wind power plants. The optimization algorithm input parameters are wind power plants active
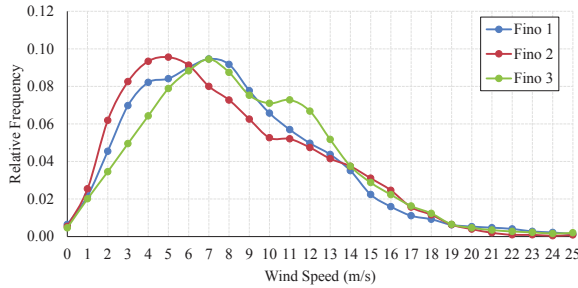
(a) FINO wind profile of the year 2016
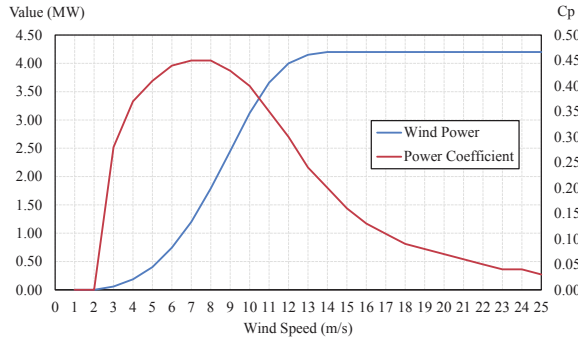
(b) Wind Turbine E-126-EP4

Figure 3.13: Wind profile according to the FINO 1, 2, and 3 database, and ENERCON wind turbine power curve.

power infeed, VSC active power sharing factor, and objective functions weighting factor as given in (3.44).

$$u = [p_3, p_4, p_5, p_6, \alpha, \gamma] \tag{3.44}$$

In Figure 3.12, the total active power losses of the AC and DC network are shown with respect to objective weighting factor and active power sharing factor. The plot illustrate the network losses over the range of wind active power from zero to maximum. The wind powers are the inputs of the OPF algorithm and it is executed over the range of wind power by first changing WF-A power from zero to maximum, and then increasing WF-B power up to maximum power while keeping WF-A power fixed to maximum value, and then increasing WF-C power and so on. In the results, the scale of wind power is defined as cumulative power refer as p_{net} at each step. According

(a) Pareto Front at $\alpha = 0.5$, and
$p_{net} = 0.688$ p.u

(b) Pareto Front at $\alpha = 0.5$, and
$p_{net} = 1.8753$ p.u
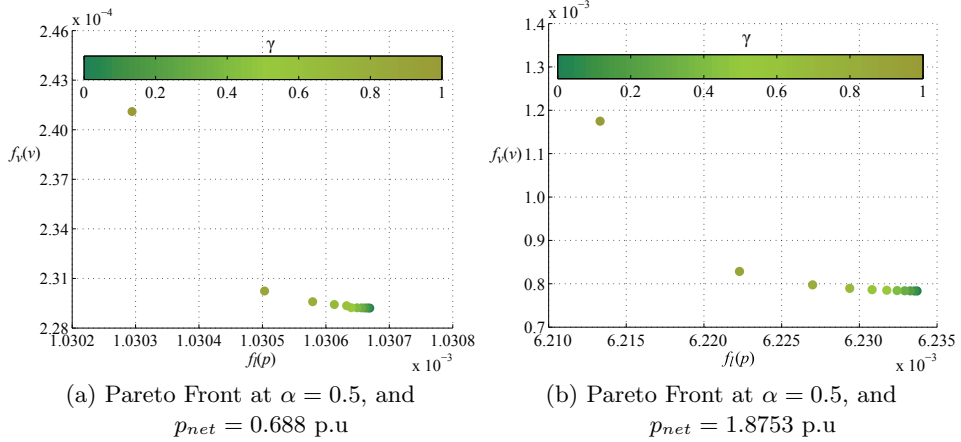
Figure 3.14: Pareto Front analysis of objective functions with respect to objective weighting factor (γ).

to the result, the active power loss variation is relatively low with respect to the objective function weighting factor. The variation of active power loss with respect to the power sharing factor can be observed at high wind infeed i.e the minimum losses in the network are at $\alpha = 0.5$. Large wind power is installed near country B therefore the network produces high active power losses at $\alpha = 0.3$.

The average power infeed by the wind power plants into the offshore AC network is calculated using wind profile of FINO database [105]. FINO is a research project started in 2002 having funding support by Federal Ministry for the Environment, Nature, Conservation, Building and Nuclear Safety (BMU) of Germany. The database provide meteorological and oceanographic measurement made at three research platforms in the North and Baltic Seas. The wind profile of FINO 1, 2 and 3 are shown in Figure 3.13a over the period of one year. By considering FINO 1 wind profile for WF-C and WF-D, the average wind speed of 8 m/s is considered for both wind power plants. FINO 2 wind profile is considered for WF-A which give the wind speed of 5 m/s. And, the wind speed of 7 m/s is assumed for WF-B by considering FINO 3 wind profile. By considering the power curve of ENERCON wind turbine E-126-EP4 given in Figure 3.13b for all wind power plants, the most
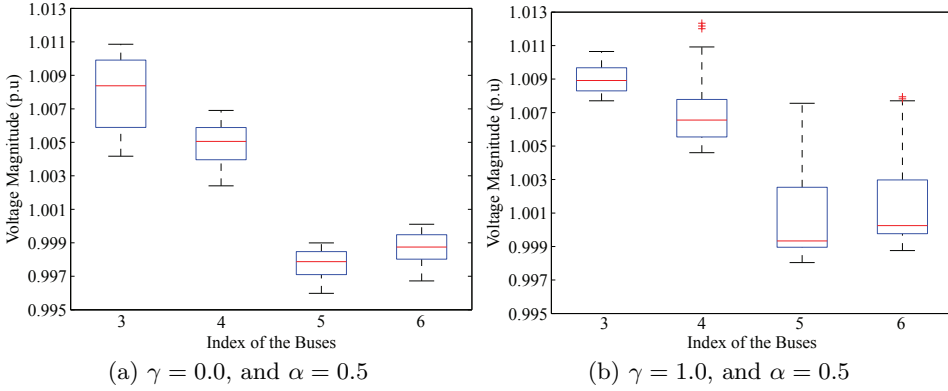
Figure 3.15: Offshore grid busbars voltage probability at the given γ and α.

frequent active power available in the offshore AC network is calculated as 0.688 p.u [106]. The profile is applied to compare the Pareto Front analysis at average and maximum wind production.

Pareto Front analysis has been shown in Figure 3.14a to illustrate the best optimum solution with respect to the objective functions weighted factor (γ). The weight factor apply the trade-off criteria between the active power losses and the network voltages deviations. Pareto Front has been generated at $\alpha = 0.5$ and $p_{net} = 0.688$ p.u. It is clear from the result that the minimum active losses are achieved at $\gamma = 1.0$, and the best optimum voltage level is achieved at $\gamma = 0.0$. However, the improvement in the active losses is low over the range of γ i.e the improvement factor is approximately $0.5\text{x}10^{-6}$, whereas the improvement factor in the voltage is approximately $13.0\text{x}10^{-6}$. In order to determine the optimum operating points, higher weighting can be given to voltage optimization objective function as a trade-off. Pareto Front at the maximum active power has been shown in Figure 3.14b. At high wind power penetration, relatively high reactive power is required to minimize the active losses which increases the voltage deviation in the network. At high power, the active power loss improvement factor is approx $21.0\text{x}10^{-6}$, and the voltage improvement factor is $0.4\text{x}10^{-3}$. The effect of objective weight on the improvement of the voltage and power loss is relatively more at high energy in the offshore network. The comparison conclude that the

(a) Optimum β at $\gamma = 0.0$ (b) Optimum β at $\alpha = 0.5$
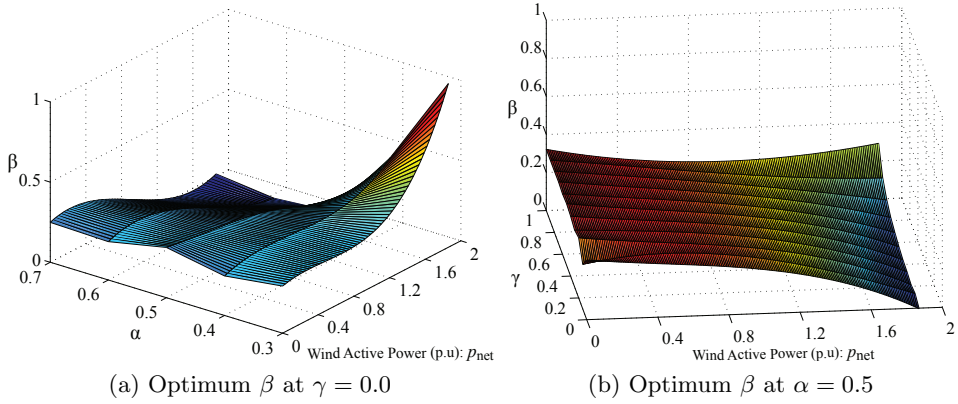
Figure 3.16: The response of reactive power sharing with respect to α and γ.

reasonable trade-off can be achieved between objective functions at $\gamma = 0.9$. Note that the optimum solution also depend on α which is the energy export factor defined by the transmission operator.

The probability of network voltages level at $\alpha = 0.5$ and $\gamma = 0.0$ is shown in Figure 3.15a. In this condition, the full weight is given to voltage minimization function in order to observe the least voltage deviation in the network. The probability plots can be analyzed for other conditions using similar method. In the result, the first quartile is set to 25th percentile and the third quartile is set to 75th percentile. According to the result, the maximum voltage deviation will occur at busbar 3 with 50 % probability of having voltages between 1.010 p.u and 1.006 p.u. The maximum voltage at the busbar 3 is 1.011 p.u. The minimum voltage deviation will occur at busbar 5 having 50 % probability to be in the voltage range of 0.998 p.u and 0.997 p.u. The minimum voltage at the busbar 5 is 0.996 p.u. Similarly, the network voltages probability at $\alpha = 0.5$ and $\gamma = 1.0$ is shown in Figure 3.15b. It can be observed from the result that the variation in the voltage level is slightly higher because of optimizing only active losses in the system. In this case, the busbar 5 voltage are in the range of 1.0025 p.u and 0.999 p.u with 50 % probability. The minimum voltage is at busbar 5 with the magnitude of 0.998 p.u. The maximum voltage will occur at busbar 4 with the magnitude
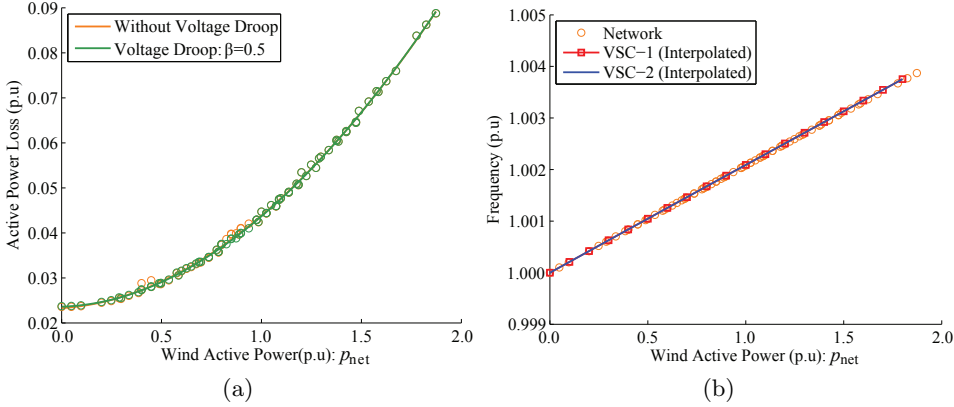
Figure 3.17: The responses of active power loss comparison with and without voltage droop control, and the frequencies at $\alpha = 0.3$ and $\gamma = 1.0$.

of 1.012 p.u. The results show that the voltages are within the required operating range.

To achieve the minimum loss, the reactive power sharing (β) between converters must also be optimally chosen. The response of β with respect to the wind power infeed and α is shown in Figure 3.16a. Here, the weighting factor is assigned to $\gamma = 0.0$. It is clear that more reactive power contribution is required by the VSC-2 when the large power is transferred to the country A at high wind penetration. Furthermore, the VSC-2 need to have more reactive power compared to VSC-1 for $\alpha < 0.5$ and almost all of the reactive power must be provided by VSC-1 at $\alpha = 0.7$, when the net wind power is greater than 1.0 p.u. On the other hand, the reactive power sharing factor is approximately 0.3 up to 1.0 p.u net wind power.

The influence of the weighting factor can be observed on the β from Figure 3.16b for $\alpha = 0.5$. It can be seen that β is relatively constant with respect of γ and changes mainly with respect of wind power. As the affect of γ is significant on the minimization of two objective functions at high power. It can be seen that more contribution is required from the VSC-1 at high wind power in order to minimize the voltage deviation.

The comparison of the active power losses with and without voltage droop
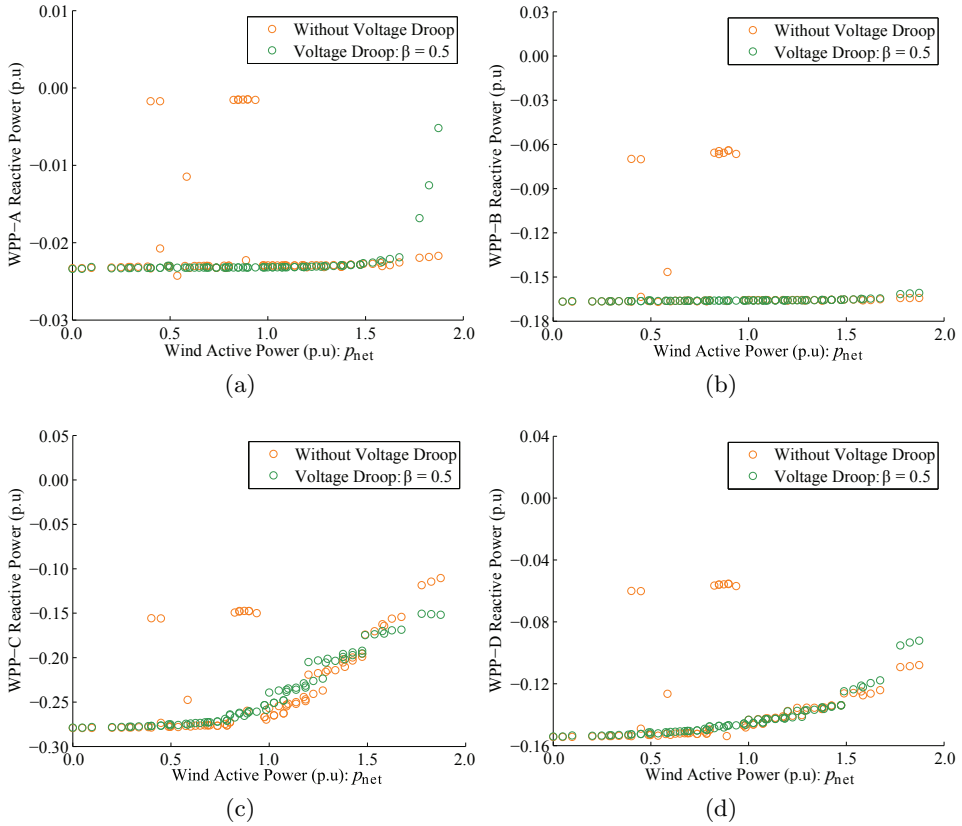
Figure 3.18: Comparison of the reactive power support by wind power plants at $\alpha = 0.3$, and $\gamma = 1.0$ with and without voltage droop control.

schemes is shown in Figure 3.17a. No voltage droop scheme means that both offshore converters of HVDC transmission system are controlling the bus voltages at the fixed set-points i.e 1.0 p.u. In this case, the reactive power flow depends on the network impedance and converter active power. Thus, it is not possible to control the contribution of each VSCs reactive power. The response shows that the active power loss is same in both cases however the application of the voltage droop provides additional degree to control the reactive power sharing of the VSCs. The transmission operator can additionally optimize the cost with the control over reactive power sharing. The steady-state frequencies respons are shown in Figure 3.17b. It is clear
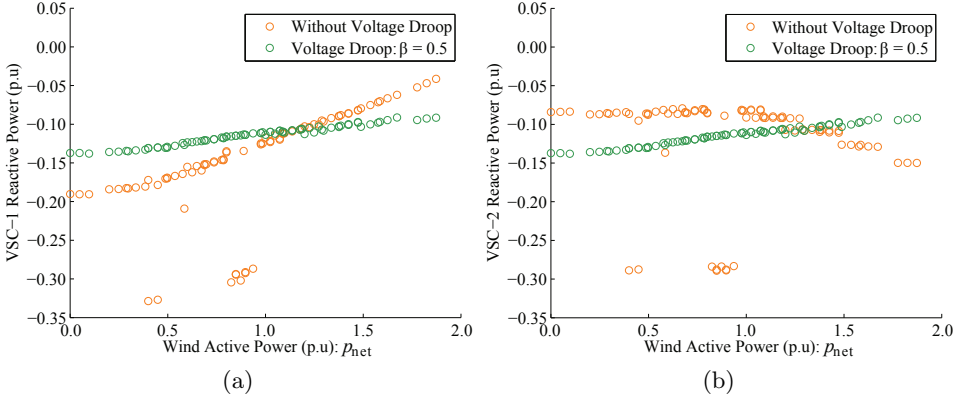
Figure 3.19: Comparison of the reactive power support by VSC-HVDC system at $\alpha = 0.3$, and $\gamma = 1.0$ with and without voltage droop control.

that the frequencies imposed by both VSCs are same and the maximum frequency deviation in the system does not exceed the limit i.e the maximum frequency deviation is 50.19 Hz at 1.873 p.u wind power. Note that here the active power sharing is 0.3 and objective weighting factor is 1.0. The calculated frequency droop gains of VSC-1 and VSC-2 are $k_{f1} = 0.0030$ p.u, and $k_{f2} = 0.0070$ p.u respectively.

Furthermore, the difference in with and without voltage droop schemes can be seen from the reactive power support provided by the wind power plants. The optimum reactive power points of the wind generation systems are shown in Figure 3.18 at $\alpha = 0.3$ and $\gamma = 1.0$. Offshore network has relatively high cable capacitance which require wind turbines to absorb this power to minimize the voltage deviation. Without voltage droop scheme, the reactive power operating point of the wind turbines are required to be set with respect to the variation of VSCs reactive power. The VSC reactive power variation is then mainly influenced by the impedance of the network and active power flow. This can be observed by the reactive power response of the VSC-1 and VSC-2 as shown in Figure 3.19. The reactive power of VSC-1 and VSC-2 are not equal, and their sharing is not controllable without voltage droop scheme. One converter flow more reactive power than other and some of

the reactive power operating points are near to their limits, consequently reactive power operating point of wind power plants are influenced. On the other hand, reactive power flow is consistent and equally shared by both VSC-HVDC transmission systems using voltage droop scheme. The voltage droop scheme provides better control of reactive power in the offshore AC network, and they are well within the limits. The desire reactive power contribution by each VSCs can be assigned by setting voltage and frequency droop gains value acquire through optimization algorithm. For the studied system, the voltage droop gains at $\alpha = 0.3$, $\beta = 0.5$, and $\gamma = 1.0$ are found as $k_{u1} = -0.0446$ p.u, and $k_{u2} = 0.0451$ p.u.

3.4 Summary

Large offshore wind power plants installed at North Sea will make future European energy efficient and affordable. The concept of offshore AC network enables the integration of such high wind energy generations with the onshore grids. In this chapter, the control scheme of grid forming voltage source converters is proposed for an offshore AC network that has multiple VSC-HVDC transmission systems. Frequency and voltage droop schemes are proposed to share active and reactive power among transmission systems. Later, a method to select these gains according to operational requirement is presented. The proposed method is analyzed both for steady-state and dynamic performance. It is concluded that the frequency and voltage droops are interlinked and required to be designed by considering both active and reactive power flows. Furthermore, it has been demonstrated that the VSCs can control the power flow using droop scheme which provides additional degree of freedom to manage power losses in the network. In the end, an optimization problem has been addressed to demonstrate the ability of VSCs to manage reactive power in the offshore AC network. An offshore AC network can be utilized as a mediator between two different countries electrical transmission systems hereby enables the trade. In comparison to an alternative MTDC HVDC transmission system topology, net active power in the offshore AC network can be higher than a single HVDC transmission system. In addition, it does not require DC circuit breaker and protection

can be done through conventional AC protection scheme. However, the addition of the droop scheme influences the network stability which is studied in the next chapter.

4 Dynamic and Stability Analysis of an Offshore AC Network

This chapter presents a methodology to perform a small-signal analysis of an offshore AC network which is formed by interconnecting several offshore wind power plants. The offshore AC network is connected with different onshore AC grids using point-to-point VSC-HVDC transmission systems. Each offshore HVDC converters are operated in grid forming mode to increase the reliability of the network operation. The offshore VSC grid forming control is enhanced by using frequency and voltage droop schemes in order to establish a coordinated grid control among the offshore converters as explained in the previous chapter. In this chapter, a small-signal model of an offshore AC network is developed which includes the HVAC cable model, the converters current and voltage control model, frequency droop scheme, and voltage droop scheme. Based on this model, an eigenvalue analysis is performed in order to study the influence of the frequency and voltage droop gains on the overall offshore AC network stability. Finally, the theoretical analysis is validated by performing a nonlinear dynamic simulation[4].

4.1 Introduction

The concept of an offshore grid has been introduced in Chapter 3. In that chapter, the offshore grid control principle, its dynamic, and the steady-state operation have been analyzed. In general, an offshore grid integrates several offshore wind power plants and onshore grids as illustrated in Figure 4.1.

---

[4]This chapter is based on the following publication:

M. Raza, E. Prieto-Araujo, and O. Gomis-Bellmunt, "Small signal stability analysis of offshore AC network having multiple voltage source converters", IEEE Transactions on Power Delivery, doi: 10.1109/TPWRD.2017.2725982.
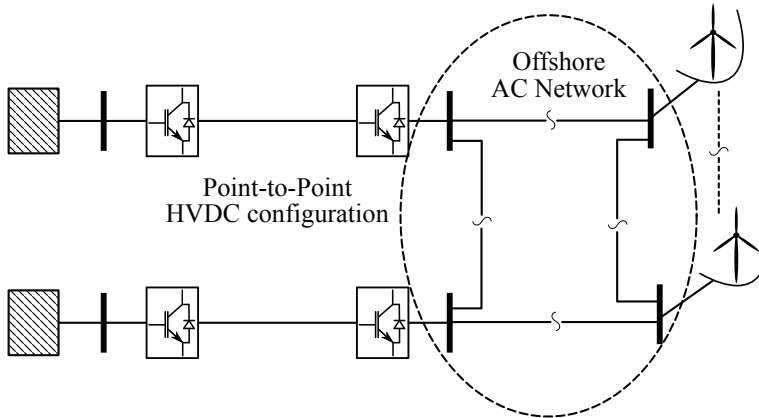
Figure 4.1: An overview of an offshore AC network interconnecting several offshore wind power plants with different onshore grids.

The offshore wind power plants are connected together using HVAC cables forming offshore AC hub or a network. This offshore AC network is connected with different onshore AC grids using point-to-point VSC-HVDC transmission system. To ensure an adequate operation of the offshore AC network, each offshore VSC-HVDC converter operates in grid forming mode. In grid forming mode, the offshore VSCs impose the frequency and voltage at their corresponding AC buses [67, 70].

The grid forming control of a VSC is shown in Figure 4.2. The VSC control consists of an inner current and outer voltage control loop in order to regulate the voltage at its corresponding AC filter bus. The VSC control system is designed in the $dq0$ synchronous rotating frame [107]. The set-points for the voltage control are defined as $u_{r\_d} = 1.0$ p.u, and $u_{r\_q} = 0.0$ p.u without including the voltage droop scheme. Also, the set-point of the imposed frequency is defined as $\omega_r = 1.0$ p.u without including the frequency droop scheme. Without the voltage and frequency droop scheme, the active and reactive power flow through each offshore VSC is established based on the offshore AC network impedance. The grid forming control of the VSC is enhanced by applying voltage and frequency droop schemes using (4.1) to establish a coordinated grid control [70]. The coordinated control establishes an active and reactive power sharing among
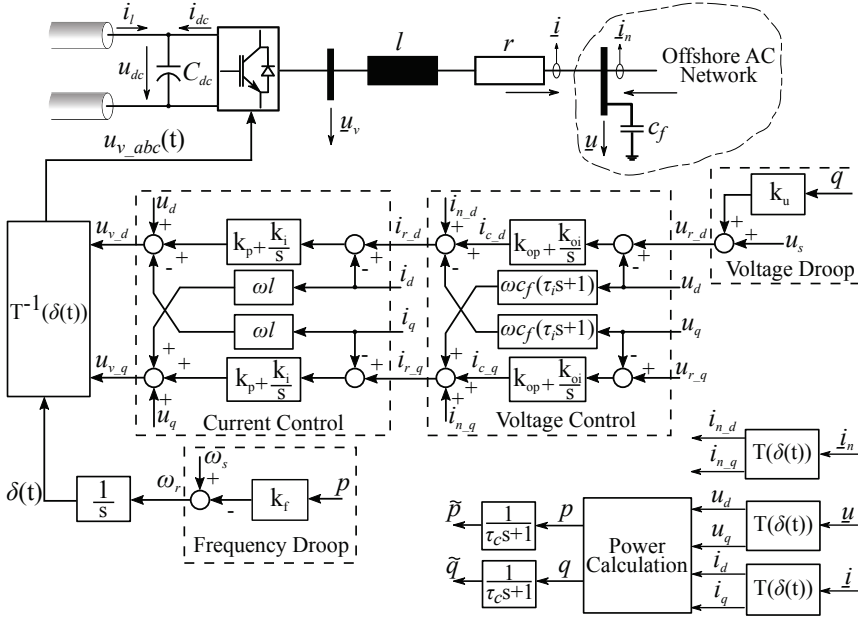
Figure 4.2: Grid forming voltage source converter control system for an offshore AC network.

the different VSC-HVDC transmission systems using locally implemented droop schemes without communications among them. This power sharing is usually defined according to the steady-state operational requirements by selecting appropriate droop values.

$$\omega_r = \omega_s - k_f \cdot p, \quad u_{r\_d} = u_s + k_u \cdot q \tag{4.1}$$

Here, ω_s and u_s are the nominal grid frequency and voltage, p and q are the VSC active and reactive power measured without a low-pass filter, k_f and k_u are the frequency and voltage droop gains, and ω_r and u_{r_d} are the frequency and voltage imposed by the VSC. A low-pass filter can be added on the active and reactive power measurement in order to increase the overall offshore AC grid damping. The impact of including this filter is later discussed in this chapter.

Nowadays, type IV wind turbines are very common to be installed in the offshore wind power plants. This type of wind generation units isolates the

offshore AC network from the turbine generator inertia. Also the offshore AC network is isolated from the onshore synchronous generators inertia due to the VSC-HVDC transmission systems. For such a network, the grid frequency would be the average of the imposed frequencies by the grid forming converters [108]. The frequency of the network (ω) can be calculated using (4.2).

$$\omega = \frac{1}{z} \sum_{i=1}^{z} \omega_{r\_i} \tag{4.2}$$

Here, ω_{r_i} is the frequency imposed by the ith VSC, and z is the total number of grid forming VSCs in the network.

In a stable system, all the frequencies of the grid forming converters converge at the same equilibrium value in steady-state, and the power is shared according to the droop values. Generally, the droop values are selected according to the steady-state operational requirements. These droop gains not only affect the steady-state power sharing but also the offshore AC network stability. Therefore, the selection of the droop values is crucial to ensure both the network stability and an adequate dynamic performance [109]. In Chapter 3, the method of selecting frequency and voltage droop gains have been presented from the prospective of the steady-state operation. However, the boundary of these droop gains are required to be determined in which an offshore AC network remain stable. This can be achieved by performing a small signal analysis on an offshore AC network.

4.2 Offshore AC Network Small-Signal Modeling

A linearized system model is best suitable to apply the linear control theory for small-signal analysis. For z grid forming converters in the offshore AC network, the complete network open loop small-signal model can be developed according to the block diagram shown in Figure 4.3. The small signal model of an offshore AC network is split into two sub-models. Firstly, a VSC model that includes the differential equations of the converter AC filter busbar voltage and the VSC control equations. Secondly, an offshore
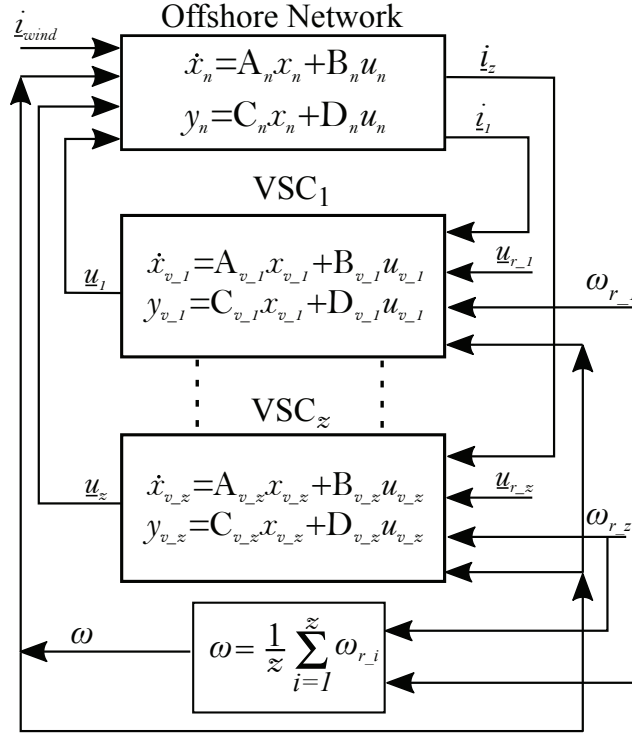
Figure 4.3: An open loop block diagram of an offshore AC network small signal model in the state space representation.

network model which consists of HVAC cables model and the wind power plants (WPPs) model. The frequency and voltage droop values are expressed in the form of state feedback gains which allows to analyze the location of the poles on the s-plane. Using (4.3), the closed loop small-signal model can be represented in the state-space.

$$
\begin{aligned}
\dot{x} &= (A - BK)\, x + B u_s \\
y &= (C - DK)\, x + D u_s
\end{aligned}
\tag{4.3}
$$

Here, K is the state feedback matrix, A, B, C and D are the state, input, output and feed-through matrices of the open loop system.

Note that in the block diagram, the VSC small-signal model does not include the droop equation. The droop equations are added as a state feedback matrix (K). The presented modeling approach can be applied

easily on the large network. The model of individual components such as converter, cable, and wind turbine can be modified and extended without affecting other component models. Further, the system closed loop poles trajectory can be analyzed with respect to only droop gains. The complete model is formulated in the state-space form so that the system stability can be determined using an eigenvalue analysis of the closed loop matrix $(A_{cl} = A - BK)$. A system is stable if the real part of all the eigenvalues of the closed loop state matrix lie on the left half of the s-plane.

4.2.1 VSC Small-Signal Model

The small-signal model of the VSC has been developed based on the control system shown in Figure 4.2. The analysis is mainly focused on the impact of frequency and voltage droop on the network stability. Therefore, the dynamics of the DC side of the HVDC system are not included in the small signal model. It is considered that the stability of the DC link is ensured by the DC voltage control of the onshore VSC and the voltages are within the operational limits. Thus, the small-signal model contains the dynamic equations of the controlled AC busbar, and the VSC current and voltage control equations.

Dynamics of VSC Controlled AC Busbar: In grid forming mode, the VSC controls the voltage at the point of common coupling (PCC) that connects the VSC substation with rest of the offshore network. The dynamics of the PCC bus voltage can be derived from the differential equations of the capacitor connected to it. This capacitor can be defined as an equivalent offshore network cable capacitance at the controlling busbar or as an added filter capacitance installed at the offshore substation [31]. The voltage differential equations of the VSC controlled busbar can be defined as (4.4).

$$\frac{du_d^n}{dt} = \frac{1}{c_f}(i_d^n + i_{n\_d}^n - u_{q0}c_f(\omega_0 - \omega) + \omega_0 c_f u_q^n)$$

$$\frac{du_q^n}{dt} = \frac{1}{c_f}(i_q^n + i_{n\_q}^n + u_{d0}c_f(\omega_0 - \omega) - \omega_0 c_f u_d^n)$$

$$(4.4)$$

Here, c_f is the equivalent capacitance at the VSC controlled bus, $i_{n\_d}^n$ is the network current d-component, $i_{n\_q}^n$ is the q-component of the network current, i_d^n is the VSC current d-component, i_q^n is the q-component of the VSC current, u_d^n is the VSC voltage d-component at the controlled busbar, and u_q^n is the q-component of the VSC voltage at the controlled busbar. The voltage equations are linearized at ω_0, u_{d0}, and u_{q0}. Note that the superscript n indicates that the state variables are in $dq0$ rotating frame synchronized with the network frequency.

Current Control: A vector control scheme using proportional-plus-integral (PI) regulator is applied for current control to ensure zero steady state error, and the poles are placed such that it has first order response. Further, the current control loop is designed to have fast response compared to outer voltage control loop. Thus, instead of using the PI control equations with the current decoupling scheme, an equivalent first order transfer function is sufficient for defining VSC current differential equations as expressed by (4.5).

$$\frac{di_d^v}{dt} = \frac{1}{\tau_i}\left(i_{r\_d}^v - i_d^v\right), \qquad \frac{di_q^v}{dt} = \frac{1}{\tau_i}\left(i_{r\_q}^v - i_q^v\right) \tag{4.5}$$

Here, τ_i is the time constant of the current response, i_d^v and i_q^v are the VSC currents, and $i_{r\_d}^v$ and $i_{r\_q}^v$ are the current references. The superscript v indicate that the variables are in $dq0$ rotating frame synchronized with the VSC frequency.

Voltage Control: The reference current signal is the output of the VSC voltage control as shown in Figure 4.2. The voltage control consists of a PI controller and the voltage d- and q- components decoupling scheme. The voltage control equations are given in (4.6).

$$
\begin{aligned}
i_{r\_d}^v &= i_{c\_d}^v - i_{n\_d}^v - \omega_0 c_f u_q^v - \omega_0 c_f \tau_i \frac{du_q^v}{dt} + u_{q0} c_f \left(\omega_0 - \omega\right) \\
i_{r\_q}^v &= i_{c\_q}^v - i_{n\_q}^v + \omega_0 c_f u_d^v + \omega_0 c_f \tau_i \frac{du_d^v}{dt} - u_{d0} c_f \left(\omega_0 - \omega\right)
\end{aligned}
\tag{4.6}
$$

Here, $i_{c\_d}^v$ and $i_{c\_q}^v$ are the outputs of the voltage PI controller which are
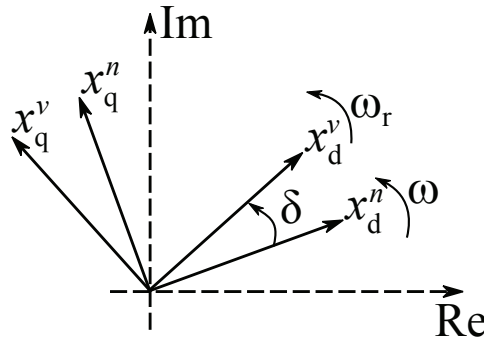
Figure 4.4: Illustration of VSC variables transformation into common reference frame.

given in (4.7).

$$\frac{de_d^v}{dt} = k_{oi}\left(u_{r\_d} - u_d^v\right), \qquad \frac{de_q^v}{dt} = k_{oi}\left(u_{r\_q} - u_q^v\right)$$
$$i_{c\_d}^v = k_{op}\left(u_{r\_d} - u_d^v\right) + e_d^v, \;\; i_{c\_q}^v = k_{op}\left(u_{r\_q} - u_q^v\right) + e_q^v \tag{4.7}$$

Here, k_{op} and k_{oi} are the proportional and the integral gains of the voltage controller, e_d^v is the integral output of voltage $d-$ component PI controller, and e_q^v is the integral output of the voltage $q-$ component PI controller. The VSC inner, outer, and network level control are connected in cascaded form and they are designed sequentially. Thus, the method of voltage and current PI controller are same as explained in Chapter 2 and they must be known for small signal analysis. Note that the droop control is implemented as a local network level control.

Common Reference Frame: In order to combine the VSC small-signal model and the offshore network small-signal model, the VSC control variables are converted into the common reference frame. Here, the common reference frame is defined by the offshore network frequency (ω). The axis transformation principle is illustrated in Figure 4.4. The network variables are rotating with the angular frequency of ω whereas the VSC variables are rotating with the angular frequency of ω_r. Any change in the difference of these frequencies will create a change in the phase angle which can be expressed using (4.8).

$$\frac{d\delta}{dt} = \omega_r - \omega \tag{4.8}$$

The transformation between these two frames can be done using (4.9). The rotation matrix $(R\,(\delta))$ is orthogonal. It is derived from Euler formula and posses the property of $R\,(\delta) \cdot R^{-1}\,(\delta) = I$.

$$x^v = R\,(\delta)\,x^n$$
$$\begin{bmatrix} x_d^v \\ x_q^v \end{bmatrix} = \begin{bmatrix} \cos(\delta) & \sin(\delta) \\ -\sin(\delta) & \cos(\delta) \end{bmatrix} \begin{bmatrix} x_d^n \\ x_q^n \end{bmatrix} \tag{4.9}$$

Here, x_d^n and x_q^n are variables rotating with the network frequency, x_d^v and x_q^v are variables rotating with the VSC imposed frequency, and δ is the phase angle between these two references. To be used in a linear small-signal model, the above transformation equation can be linearized at the equilibrium point of δ_0, x_{d0}, and x_{q0}. It is considered that both frames are initially aligned, thus the linearized VSCs variables in the common frame can be defined using (4.10).

$$x_d^v = x_d^n + x_{q0}\delta \qquad \because \delta_0 = 0$$
$$x_q^v = x_q^n - x_{d0}\delta \tag{4.10}$$

The voltage state variables in the VSC voltage control equation can be transformed into the common frame using above equation as (4.11). Here, the voltage equilibrium points are set as $x_{d0} = u_{d0} = 1.0$ p.u, and $x_{q0} = u_{q0} = 0.0$ p.u by considering a flat-start of the network.

$$u_d^v = u_d^n$$
$$u_q^v = u_q^n - u_{d0}\delta \tag{4.11}$$

Similarly, assuming that there is no current flowing at the equilibrium point (flat-start) i.e $x_{d0} = i_{d0} = 0.0$ p.u, and $x_{q0} = i_{q0} = 0.0$ p.u. Then, the current state variables in the VSC current and voltage control equation can be transformed in the common frame using (4.12).

$$i_d^v = i_d^n, \quad i_q^v = i_q^n$$
$$i_{d\_n}^v = i_{d\_n}^n, \quad i_{q\_n}^v = i_{q\_n}^n \tag{4.12}$$

Note that the constants are not required to be transformed into the common frame.

Complete VSC State-Space Model: In the common reference frame, a VSC small-signal model can be written using the equations given in previous sections. The VSC model state and input vectors are given in (4.13).

$$x_v = \begin{bmatrix} e_d^n & e_q^n & i_d^n & i_q^n & u_d^n & u_q^n & \delta \end{bmatrix}^T$$
$$u_v = \begin{bmatrix} u_{r\_d} & u_{r\_q} & i_{n\_d}^n & i_{n\_q}^n & \omega_r & \omega & \Delta\omega \end{bmatrix}^T \tag{4.13}$$

Here, the input variable $\Delta\omega$ is a deviation of the network angular frequency from its equilibrium point. It reflects a linear change in the network impedances due to a change in the network frequency. It is defined as (4.14).

$$\Delta\omega = \omega_0 - \omega \tag{4.14}$$

The inputs of the converter model are the voltage set-points (u_{r_d}, and u_{r_q}), the offshore network current ($i_{n\_d}^n$, and $i_{n\_q}^n$), the reference frequency (ω_r), and the network average frequency (ω). The state, input, and output matrices of the VSC model are given in (4.15), (4.16), and (4.17).

$$A_v = \begin{bmatrix}
0 & 0 & 0 & 0 & -k_i & 0 & 0 \\
0 & 0 & 0 & 0 & 0 & -k_i & k_i u_{d0} \\
\frac{1}{\tau_i} & 0 & -\frac{1}{\tau_i} & -\omega_0 & \frac{\omega_0^2 c_f \tau_i - k_p}{\tau_i} & -\frac{\omega_0 c_f}{\tau_i} & \frac{\omega_0 c_f u_{d0}}{\tau_i} \\
0 & \frac{1}{\tau_i} & \omega_0 & -\frac{1}{\tau_i} & \frac{\omega_0 c_f}{\tau_i} & \frac{\omega_0^2 c_f \tau_i - k_p}{\tau_i} & \frac{k_p u_{d0}}{\tau_i} \\
0 & 0 & \frac{1}{c_f} & 0 & 0 & \omega_0 & 0 \\
0 & 0 & 0 & \frac{1}{c_f} & -\omega_0 & 0 & 0 \\
0 & 0 & 0 & 0 & 0 & 0 & 0
\end{bmatrix} \tag{4.15}$$

$$B_v = \begin{bmatrix} k_i & 0 & 0 & 0 & 0 & 0 & 0 \\ 0 & k_i & 0 & 0 & 0 & 0 & 0 \\ \frac{k_p}{\tau_i} & 0 & -\frac{1}{\tau_i} & -\omega_0 & c_f u_{d0}\omega_0 & -c_f u_{d0}\omega_0 & \frac{-\tau_i c_f u_{d0}\omega_0 + c_f u_{q0}}{\tau_i} \\ 0 & \frac{k_p}{\tau_i} & \omega_0 & -\frac{1}{\tau_i} & 0 & 0 & \frac{-\tau_i c_f u_{q0}\omega_0 - c_f u_{d0}}{\tau_i} \\ 0 & 0 & \frac{1}{c_f} & 0 & 0 & 0 & -u_{q0} \\ 0 & 0 & 0 & \frac{1}{c_f} & 0 & 0 & u_{d0} \\ 0 & 0 & 0 & 0 & 1 & -1 & 0 \end{bmatrix} \quad (4.16)$$

$$C_v = \mathrm{I}(7\mathrm{x}7), \qquad D_v = 0 \quad (4.17)$$

4.2.2 Offshore Network Small-Signal Model

A small-signal model of the offshore AC network can be constructed by combining the branches current and voltage differential equations using (4.18) and (4.19).

$$\begin{bmatrix} \dot{i}^n_{d\_k} \\ \dot{i}^n_{q\_k} \end{bmatrix} = \begin{bmatrix} -\frac{r}{l} & \omega_0 \\ -\omega_0 & -\frac{r}{l} \end{bmatrix} \begin{bmatrix} i^n_{d\_k} \\ i^n_{q\_k} \end{bmatrix} + \begin{bmatrix} \frac{1}{l} & 0 & -i_{q0} \\ 0 & \frac{1}{l} & i_{d0} \end{bmatrix} \begin{bmatrix} \Delta u^n_{d\_k} \\ \Delta u^n_{q\_k} \\ \Delta\omega \end{bmatrix} \quad (4.18)$$

Here, $i^n_{d\_k}$ and $i^n_{q\_k}$ are the currents of the branch in the common reference frame. The voltages across the branch element are defined as $\Delta u^n_{d\_k} = u^n_{d\_m+1} - u^n_{d\_m}$ and $\Delta u^n_{q\_k} = u^n_{q\_m+1} - u^n_{q\_m}$. Also, $\Delta\omega$ is the frequency deviation from its equilibrium point and it can be calculated using (4.14).

$$\begin{bmatrix} \dot{u}^n_{d\_m} \\ \dot{u}^n_{q\_m} \end{bmatrix} = \begin{bmatrix} 0 & \omega_0 \\ -\omega_0 & 0 \end{bmatrix} \begin{bmatrix} u^n_{d\_m} \\ u^n_{q\_m} \end{bmatrix} + \begin{bmatrix} \frac{1}{c} & 0 & -u_{q0} \\ 0 & \frac{1}{c} & u_{d0} \end{bmatrix} \begin{bmatrix} \Delta i^n_{d\_m} \\ \Delta i^n_{q\_m} \\ \Delta\omega \end{bmatrix} \quad (4.19)$$

Here, $u^n_{d\_m}$ and $u^n_{q\_m}$ are the voltages of the branch in the common reference frame. The currents injected into the busbar are defined as $\Delta i^n_{d\_m} = i^n_{d\_k+1} + i^n_{d\_k} + i^n_{d\_wind}$, and $\Delta i^n_{q\_m} = i^n_{q\_k+1} + i^n_{q\_k} + i^n_{q\_wind}$.

It is assumed that type IV wind turbines are installed at the offshore wind power plants which can control the active and the reactive power independently. Since the focus of the study is on the droop effects and not
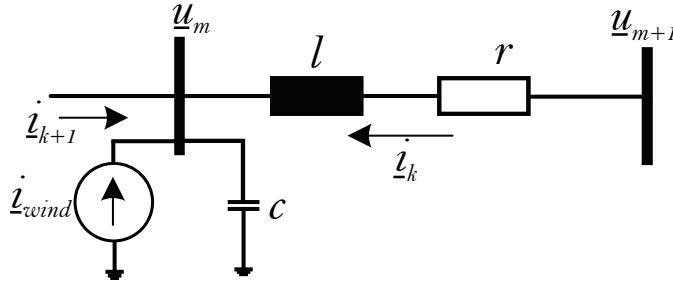
Figure 4.5: A simplified diagram for modeling offshore AC network branches and busbars.

on the wind turbine dynamics, the wind turbines are modeled as controlled current sources as it is shown in Figure 4.5, which is sufficient for a small-signal analysis. In the presented study, only the HVAC cables are considered as the branch elements, however other branch elements such as transformer can also be incorporated conveniently by using their linear small-signal model. Typically, a π-cable model is adequate for short distances and low frequencies. However, other cable models can also be applied by using their linear differential model [24].

4.2.3 State Feedback Matrix (K)

A small-signal analysis of the offshore AC network is carried out using a linear model in order to evaluate the droop scheme performance. In the linear model, the droop scheme (4.1) is applied in the form of state feedback matrix which simplifies the system analysis. In addition, these frequency and voltage droop equations must be linear. These droop equations include the active and reactive power measurements which are calculated using (4.20) which is a nonlinear function.

$$
\begin{aligned}
p &= u_d i_d + u_q i_q \\
q &= u_q i_d - u_d i_q
\end{aligned}
\tag{4.20}
$$

Thus, the above power equations must be linearized to include them in the linear model. Then, (4.20) are linearized at the equilibrium point u_{d0}, u_{q0}, i_{d0}, and i_{q0}. By considering flat start as the equilibrium state of the

offshore AC network, the linear droop equations for the small-signal model can be written as (4.21).

$$
\begin{aligned}
\omega_r &= \omega_s - k_f i_d^n, \quad &&\because p = i_d \\
u_{r\_d} &= u_s - k_u i_q^n, \quad &&\because q = -i_q
\end{aligned}
\tag{4.21}
$$

Here, i_d^n, and i_q^n are the VSC current dq- components in common reference frame. The state feedback matrix can be defined using (4.22) for z grid forming VSCs. The closed loop system is a multi-input multi-output (MIMO) system and K is not a full state feedback matrix.

$$
Kx =
\begin{bmatrix}
k_{f\_1} & 0 & \cdots & & 0 \\
0 & k_{u\_1} & & & \\
\vdots & & \ddots & & \vdots \\
& & & k_{f\_z} & 0 \\
0 & \cdots & & 0 & k_{u\_z}
\end{bmatrix}
\begin{bmatrix}
i_{d\_1}^n \\
i_{q\_1}^n \\
\vdots \\
i_{d\_z}^n \\
i_{q\_z}^n
\end{bmatrix}
\tag{4.22}
$$

Here, x is the state vector and K is the state feedback matrix. Note that the matrix K is defined without including a low-pass filter at the active and reactive power measurements. Without including the low-pass filter, the network voltage and frequency may have an oscillatory behavior due to the droop schemes. In order to increase damping in the system, a low-pass filter is included on the power measurements. The droop equations including the low-pass filter can be defined as:

$$
\begin{aligned}
\omega_r &= \omega_s - k_f \tilde{p}, \quad &&\because \tilde{p} = \frac{\omega_c}{s + \omega_c} p \\
u_{r\_d} &= u_s + k_u \tilde{q}, \quad &&\because \tilde{q} = \frac{\omega_c}{s + \omega_c} q
\end{aligned}
\tag{4.23}
$$

Here, $\omega_c = 1/\tau_c$ is the cutoff frequency of the low pass filters, and $\tilde{p}, \tilde{q}$ are the filtered active and reactive power outputs. Note that $\tilde{p} = \tilde{i}_d^n$, and $\tilde{q} = -\tilde{i}_q^n$ for the linearized small-signal model.
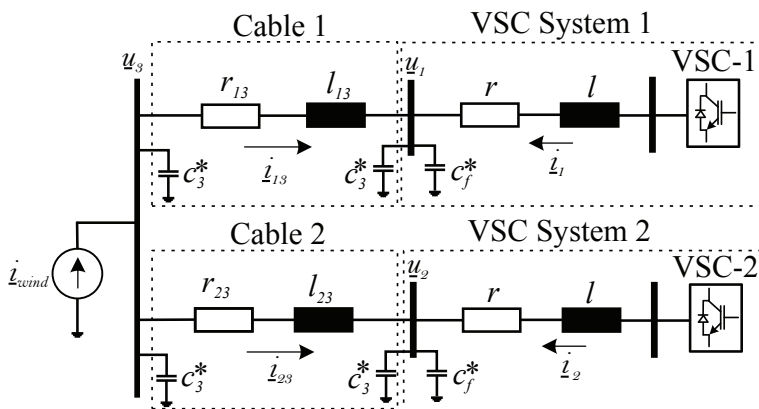
Figure 4.6: Offshore AC network having two frequency controlled voltage source converter.

4.3 Case Study

In this section, a small-signal analysis of the network shown in Figure 4.6 is performed using the proposed method. The offshore AC network has two VSCs and an equivalent wind power plant. In the presented case study, each VSC system is connected with the AC hub bus (u_3) using HVAC cables. The length of the cables are 10 km each [11]. The network and control parameters are given in Table 4.1. The cable parameters are taken from the manufacturer data sheet listed in [102, 110]. Note that the filter capacitance value in the VSC small-signal model is $c_f = c_f^* + c_3^*$, and the equivalent capacitance at the AC hub bus is $c = c_3^* + c_3^*$. Where, c_3^* is the half of the total cable capacitance, r_{13}, r_{23} are the total cable resistances, and l_{13}, l_{23} are the total cable inductances.

At first, a complete closed loop system small-signal model is obtained using the proposed method. The closed loop system is defined in a state-space form as given in (4.3). The eigenvalue analysis can then be performed using the state matrix. The small-signal analysis determines the frequency and voltage droop values at which the system becomes unstable. Finally, the dynamic performance of the system and the stability conditions are validated by performing a nonlinear simulation in Simulink SimPowerSystems.

Table 4.1: Offshore AC network and control parameters for stability analysis

Variables	Value	Unit
Rated voltage	220	kV
Rated apparent power	500	MVA
Nominal angular frequency (ω)	314.16	rad/s
Cable resistance	0.032	Ω/km
Cable inductance	0.4	mH/km
Cable capacitance	0.17	μF/km
Length of cables 1, and 2	10	km
Filter capacitance (c_f^*)	3.29	μF
VSC reactor resistance	0.5	mΩ
VSC reactor inductance	55.0	mH
VSC voltage control gain	$0.3 + \frac{0.15}{s}$	p.u
VSC current time constant (τ_i)	0.002	s
Cutoff frequency of low-pass filter (ω_c)	25	rad/s

4.3.1 Formation of Complete System Model

The analytic procedure of connecting offshore network and VSCs model is explained here to form the complete system model in the state-space representation. The complete model can also be formed by using computational tools such as a MATLAB function 'linmod'. The function obtains a linear model of the system expressed as Figure 4.3 described in the Simulink model. The input and output of the complete system must be assigned using Simulink input and output port blocks.

In order to formulate the system complete model analytically, the resultant state vector of the network can be written as (4.24). Note that the frame superscript label is removed since both VSCs and offshore network model are in common reference frame.

$$
\begin{aligned}
x &= \begin{bmatrix} x_1 & x_2 & x_3 \end{bmatrix} \\
x_1 &= \begin{bmatrix} e_{d\_1} & e_{q\_1} & i_{d\_1} & i_{q\_1} & u_{d\_1} & u_{q\_1} & \delta_1 \end{bmatrix}^T \\
x_2 &= \begin{bmatrix} e_{d\_2} & e_{q\_2} & i_{d\_2} & i_{q\_2} & u_{d\_2} & u_{q\_2} & \delta_2 \end{bmatrix}^T \\
x_3 &= \begin{bmatrix} i_{d\_13} & i_{q\_13} & u_{d\_3} & u_{q\_3} & i_{d\_23} & i_{q\_23} \end{bmatrix}^T
\end{aligned}
\tag{4.24}
$$

Here, the complete system state variables split into three sub-vectors according to the models i.e x_1 is the state vector of VSC-1 model, x_2 is the state vector of VSC-2 model, and x_3 is the state vector of the offshore network model. The offshore network state, input, and output matrices are given as follows.

$$A_n = \begin{bmatrix} -\frac{r_{13}}{l_{13}} & \omega_0 & \frac{1}{l_{13}} & 0 & 0 & 0 \\ -\omega_0 & -\frac{r_{13}}{l_{13}} & 0 & \frac{1}{l_{13}} & 0 & 0 \\ -\frac{1}{c_3} & 0 & 0 & \omega_0 & -\frac{1}{c_3} & 0 \\ 0 & -\frac{1}{c_3} & -\omega_0 & 0 & 0 & -\frac{1}{c_3} \\ 0 & 0 & \frac{1}{l_{23}} & 0 & -\frac{r_{23}}{l_{23}} & \omega_0 \\ 0 & 0 & 0 & \frac{1}{l_{23}} & -\omega_0 & -\frac{r_{23}}{l_{23}} \end{bmatrix} \tag{4.25}$$

$$B_n = \begin{bmatrix} -\frac{1}{l_{13}} & 0 & 0 & 0 & 0 & 0 & -i_{q0} \\ 0 & -\frac{1}{l_{13}} & 0 & 0 & 0 & 0 & i_{d0} \\ 0 & 0 & \frac{1}{c_3} & 0 & 0 & 0 & -u_{q0} \\ 0 & 0 & 0 & \frac{1}{c_3} & 0 & 0 & u_{d0} \\ 0 & 0 & 0 & 0 & -\frac{1}{l_{23}} & 0 & -i_{q0} \\ 0 & 0 & 0 & 0 & 0 & -\frac{1}{l_{23}} & i_{d0} \end{bmatrix} \tag{4.26}$$

$$C_n = \mathrm{I}(6x6), \qquad D_n = 0 \tag{4.27}$$

The input vector of the offshore network model is given in (4.28). The matrices of VSC model are given in (4.15), (4.16), and (4.17).

$$u_n = \begin{bmatrix} u_{d\_1} & u_{q\_1} & i_{d\_wind} & i_{q\_wind} & u_{d\_2} & u_{q\_2} & \Delta\omega \end{bmatrix}^T \tag{4.28}$$

The complete system state matrix A can also be written in the form of sub-matrices as expressed by (4.29). The diagonal sub-matrices A_{11} and A_{22} are the matrices of VSCs models, and they are defined using (4.15). The diagonal sub-matrix A_{33} is the self matrix of offshore network model which is defined by (4.25). Furthermore, the VSC-1 and VSC-2 converters are controlling different busbars and they are not directly connected, thus $A_{12} = A_{21} = 0$.

$$A = \begin{bmatrix} A_{11}\,(7\text{x}7) & A_{12}\,(7\text{x}7) & A_{13}\,(7\text{x}6) \\ A_{21}\,(7\text{x}7) & A_{22}\,(7\text{x}7) & A_{23}\,(7\text{x}6) \\ A_{31}\,(6\text{x}7) & A_{32}\,(6\text{x}7) & A_{33}\,(6\text{x}6) \end{bmatrix} \tag{4.29}$$

The matrix A_{13} connects the output of the network current with the input of VSC-1. The network currents i_{d_13} and i_{q_13} are the inputs to VSC-1 model. In order to link the offshore network model output with the VSC-1 model inputs, the corresponding columns of matrix C_n given in (4.27) are multiplied with the corresponding columns of matrix B_v given in (4.16) as:

$$A_{13} = \begin{bmatrix} B_{v\_1}(7\text{x}2) \times C_{n\_1}(2\text{x}2) & 0(7\text{x}4) \end{bmatrix}$$
$$B_{v\_1} = \begin{bmatrix} C_3 & C_4 \end{bmatrix}, \qquad C_{n\_1} = \begin{bmatrix} 1 & 0 \\ 0 & 1 \end{bmatrix} \tag{4.30}$$

The network current i_{d_23} and i_{q_23} are the inputs of VSC-2 model. The matrix A_{23} can be found in a similar manner as given by (4.31). The corresponding columns of matrix B_v for matrix B_{v_2} are the same as of B_{v_1}. The matrix C_{n_2} is also an identity matrix.

$$A_{23} = \begin{bmatrix} 0(7\text{x}4) & B_{v\_2}(7\text{x}2) \times C_{n\_2}(2\text{x}2) \end{bmatrix} \tag{4.31}$$

The matrix A_{31} connects the output voltage of the VSC-1 model with the input of the offshore network model, and it can be defined as (4.32). The state variables u_{d_1} and u_{q_1} of the VSC-1 model are the input of network model, thus the column 1 and 2 of matrix B_n are multiplied by the corresponding matrix of C_v.

$$A_{31} = \begin{bmatrix} 0(6\text{x}4) & B_{n\_1}(6\text{x}2) \times C_{v\_1}(2\text{x}3) \end{bmatrix}$$
$$B_{n\_1} = \begin{bmatrix} C_1 & C_2 \end{bmatrix}, \qquad C_{v\_1} = \begin{bmatrix} 1 & 0 & 0 \\ 0 & 1 & 0 \end{bmatrix} \tag{4.32}$$

Similarly, the matrix A_{32} links the output voltage of the VSC-2 with the network model, and its value is calculated using (4.33).

$$A_{32} = \begin{bmatrix} 0(6\text{x}4) & B_{n\_2}(6\text{x}2) \times C_{v\_2}(2\text{x}3) \end{bmatrix} \tag{4.33}$$

Here, the matrix column of C_v for C_{v_2} are same as of C_{v_1} and they are applied using VSC-2 parameters. The corresponding column indexes of B_n for VSC-2 are 5 and 6.

The input vector u for the whole system can be defined in a similar manner. The input vector can be split into two sub-vectors as (4.34).

$$u = \begin{bmatrix} u_{vi}(6\text{x}1) & u_\omega(3\text{x}1) \end{bmatrix}^T$$

$$u_{vi} = \begin{bmatrix} u_{r\_d1} & u_{r\_q1} & u_{r\_d2} & u_{r\_q2} & i_{d\_wind} & i_{q\_wind} \end{bmatrix} \qquad (4.34)$$

$$u_\omega = \begin{bmatrix} \omega_{r1} & \omega_{r2} & \omega_0 \end{bmatrix}$$

Here, u_{vi} is the input vector containing the voltage set-points of VSCs and the wind power plant current infeed. u_ω is the vector of input frequencies. Thus, the B matrix can be written in the form of sub-matrices as (4.35).

$$B = \begin{bmatrix} B_{11}(7\text{x}2) & 0 & 0 & B_{14}(7\text{x}3) \\ 0 & B_{22}(7\text{x}2) & 0 & B_{24}(7\text{x}3) \\ 0 & 0 & B_{33}(6\text{x}2) & B_{34}(6\text{x}3) \end{bmatrix} \qquad (4.35)$$

The set-points of the VSC-1 and VSC-2 voltage controller are defined by the matrices B_{11} and B_{22} respectively, and their respective columns 1 and 2 are extracted from (4.16). The matrix B_{33} corresponds to the input of offshore network model and its respective column indexes are 3 and 4 extracted from (4.26).

The matrix B_{14} is an input matrix of frequencies for VSC-1 i.e ω_{r1}, ω, and $\Delta\omega$. In order to link the VSC-1 frequency with the network frequency and VSC-2 frequency, input matrix can be rewritten by applying (4.2) and (4.14). The input frequencies transformation matrix for VSC-1 is given in (4.36).

$$\begin{bmatrix} \omega_{r1} \\ \omega \\ \Delta\omega \end{bmatrix} = \begin{bmatrix} 1 & 0 & 0 \\ 0.5 & 0.5 & 0 \\ -0.5 & -0.5 & 1 \end{bmatrix} \begin{bmatrix} \omega_{r1} \\ \omega_{r2} \\ \omega_0 \end{bmatrix} \qquad (4.36)$$

Thus, the B_{14} can be defined by extracting the corresponding columns from (4.16) and multiplying with the transformation matrix given in (4.36)

as

$$B_{14} = \begin{bmatrix} C_5 & C_6 & C_7 \end{bmatrix} \begin{bmatrix} 1 & 0 & 0 \\ 0.5 & 0.5 & 0 \\ -0.5 & -0.5 & 1 \end{bmatrix} \qquad (4.37)$$

The matrix B_{24} is defined in a similar manner. However, the input transformation matrix is modified according to VSC-2 input as (4.38).

$$B_{24} = \begin{bmatrix} C_5 & C_6 & C_7 \end{bmatrix} \begin{bmatrix} 0 & 1 & 0 \\ 0.5 & 0.5 & 0 \\ -0.5 & -0.5 & 1 \end{bmatrix} \qquad (4.38)$$

The influence of the change in network frequency on the network elements in term of frequencies set-points can be defined by multiplying the corresponding column from (4.26) with the input frequency transformation matrix. Thus, the matrix B_{34} is calculated using (4.39).

$$B_{34} = \begin{bmatrix} C_7 \end{bmatrix} \begin{bmatrix} -0.5 & -0.5 & 1 \end{bmatrix} \qquad (4.39)$$

The vector of output variables define in (4.40) contains state and input variables.

$$y = \begin{bmatrix} i_{d\_1} & i_{q\_1} & u_{d\_1} & u_{q\_1} & i_{d\_2} & i_{q\_2} & u_{d\_2} & u_{q\_2} & u_{d\_3} & u_{q\_3} \\ & & & & & \omega & \omega_1 & \omega_2 \end{bmatrix}^T \qquad (4.40)$$

The state output matrix C is a diagonal matrix whose values are calculated using (4.17) and (4.27).

$$Cx = \begin{bmatrix} y_{11}(4\text{x}7) & 0 & 0 \\ 0 & y_{22}(4\text{x}7) & 0 \\ 0 & 0 & y_{33}(5\text{x}6) \end{bmatrix} \begin{bmatrix} x_1 \\ x_2 \\ x_3 \end{bmatrix}$$

$$y_{11} = y_{22} = \begin{bmatrix} 0 & 0 & 1 & 0 & 0 & 0 & 0 \\ 0 & 0 & 0 & 1 & 0 & 0 & 0 \\ 0 & 0 & 0 & 0 & 1 & 0 & 0 \\ 0 & 0 & 0 & 0 & 0 & 1 & 0 \end{bmatrix}, \quad y_{33} = \begin{bmatrix} 0 & 0 & 1 & 0 & 0 & 0 \\ 0 & 0 & 0 & 1 & 0 & 0 \\ 0 & 0 & 0 & 0 & 0 & 0 \\ 0 & 0 & 0 & 0 & 0 & 0 \\ 0 & 0 & 0 & 0 & 0 & 0 \end{bmatrix} \tag{4.41}$$

Furthermore, the feed-forward matrix D can be defined as (4.42).

$$Du = \begin{bmatrix} D_{11}(10\text{x}6) & 0 \\ 0 & D_{22}(3\text{x}3) \end{bmatrix} \begin{bmatrix} u_{vi} \\ u_{\omega} \end{bmatrix}$$

$$D_{11} = 0, \qquad D_{22} = \begin{bmatrix} 0.5 & 0.5 & 0 \\ 1 & 0 & 0 \\ 0 & 1 & 0 \end{bmatrix} \tag{4.42}$$

The derived state, input and output matrices, according to the block diagram shown in Figure 4.3, do not include the frequency and voltage droop gains of VSCs. In the developed modeling approach, these droop gains are applied as a state feedback gains to evaluate the network closed-loop poles location on the s-plane. The poles location directly corresponds to the eigenvalues of the system which control the system response. According to (4.21), the state feedback signals are VSCs current d- and q- components. Thus, the feedback matrix K having frequency and voltage droop gains without low pass filter can be defined as (4.43). Here, the frequency and voltage droop gain for VSC-1 are designated as k_{f1} and k_{u1}. For VSC-2, k_{f2} and k_{u2} are the droop gains of frequency and voltage respectively.

$$
K = \begin{bmatrix}
0 & 0 & 0 & k_{u1} & 0 & 0 & 0 & 0 & 0 & 0 & 0 \\
0 & 0 & 0 & 0 & 0 & 0 & 0 & 0 & 0 & 0 & 0 \\
0 & 0 & k_{f1} & 0 & 0 & 0 & 0 & 0 & 0 & 0 & 0 \\
0 & 0 & 0 & 0 & 0 & 0 & 0 & 0 & 0 & 0 & k_{u2} \\
0 & 0 & 0 & 0 & 0 & 0 & 0 & 0 & 0 & 0 & 0 \;\Big|\; 0(9\text{x}9) \\
0 & 0 & 0 & 0 & 0 & 0 & 0 & 0 & 0 & k_{f2} & 0 \\
0 & 0 & 0 & 0 & 0 & 0 & 0 & 0 & 0 & 0 & 0 \\
0 & 0 & 0 & 0 & 0 & 0 & 0 & 0 & 0 & 0 & 0 \\
0 & 0 & 0 & 0 & 0 & 0 & 0 & 0 & 0 & 0 & 0
\end{bmatrix} \qquad (4.43)
$$

The closed loop state matrix given in (4.3) can now be computed to analyze the system dynamics and its stability.

4.3.2 Eigenvalue Analysis

Using an eigenvalue (λ) analysis, the closed loop system poles and zeros can be plotted on the s-plane as shown in Figure 4.7. In Figure 4.7, the poles and zeroes of the system are plotted using the following droop values: $k_{f1} = 0.00165$ p.u (VSC-1 frequency droop), $k_{u1} = 0.0020$ p.u (VSC-1 voltage droop), $k_{f2} = 0.00231$ p.u (VSC-2 frequency droop), and $k_{u2} = -0.0020$ p.u (VSC-2 voltage droop). As observed from the plot, the system is stable since the real parts of all eigenvalues are negative.

There are two sets of poles that are influenced by the droop gains. One set is mainly affected by the frequency droop gain and the other is influenced by the voltage droop gain. To observe the influence of the frequency droop gain on the system poles, the trajectories of the poles map are shown in Figure 4.8a. These trajectories are generated by varying only the VSC-1 frequency droop gain as $0.0 \leq k_{f1} \leq 0.01$ p.u while keeping the other parameters constant. In the plot, the poles move along the gradient from blue ($k_{f1} = 0.0$ p.u) to red ($k_{f1} = 0.01$ p.u). It can be observed that the poles located close to -0.5 and -50 of the real axis scale are dominant and lead the system into instability for $k_{f1} \geq 0.003$ p.u. The poles located close to -200 of the real axis scale are not importantly affected by the frequency
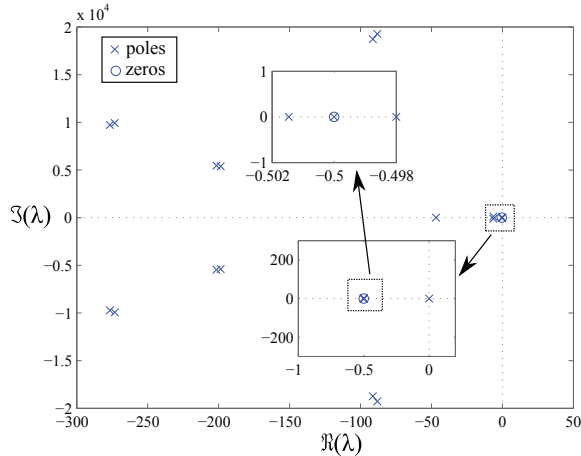
Figure 4.7: Poles-Zeros map of offshore AC network having multiple grid forming VSCs.

droop gain.

Similarly, the impact of the voltage droop gain on the system poles is shown in Figure 4.8b. In the plot, the poles move along the gradient from blue to red by varying VSC-1 voltage droop gain as $0.0 \leq k_{u1} \leq 0.04$ p.u. It can be observed that the poles located close to -200 of the real axis scale are now significantly affected. The poles located at -0.5 on the real axis are also importantly affected by the voltage droop and lead the system into instability for $k_{u1} > 0.027$ p.u. For $k_{u1} \leq 0.027$ p.u system remains stable. The poles map indicates which poles have a larger effect on the system response with respect to the droop gain.

In the previous analysis, the active and reactive power feedback signals are applied in the droop scheme without including low-pass filters. In case of a sudden power change in the offshore wind power generation, large voltage transient deviations might appear depending on the VSCs controller performance. This voltage transient has a direct impact on the power flow of the VSCs, consequently the droop closed loop feedback signals produce an oscillatory frequency and voltage set-points. Hereby, the whole offshore AC network becomes a low damped system. However, the damping in the system can be increased by applying low-pass filters at the power measurements.

(a) For $0 \leq k_{f1} \leq 0.01$ p.u without including low-pass filter

(b) For $0.0 \leq k_{u1} \leq 0.04$ p.u without including low-pass filter

(c) For $0 \leq k_{f1} \leq 0.02$ p.u including low-pass filter

(d) For $0 \leq k_{u1} \leq 0.04$ p.u including low pass filter
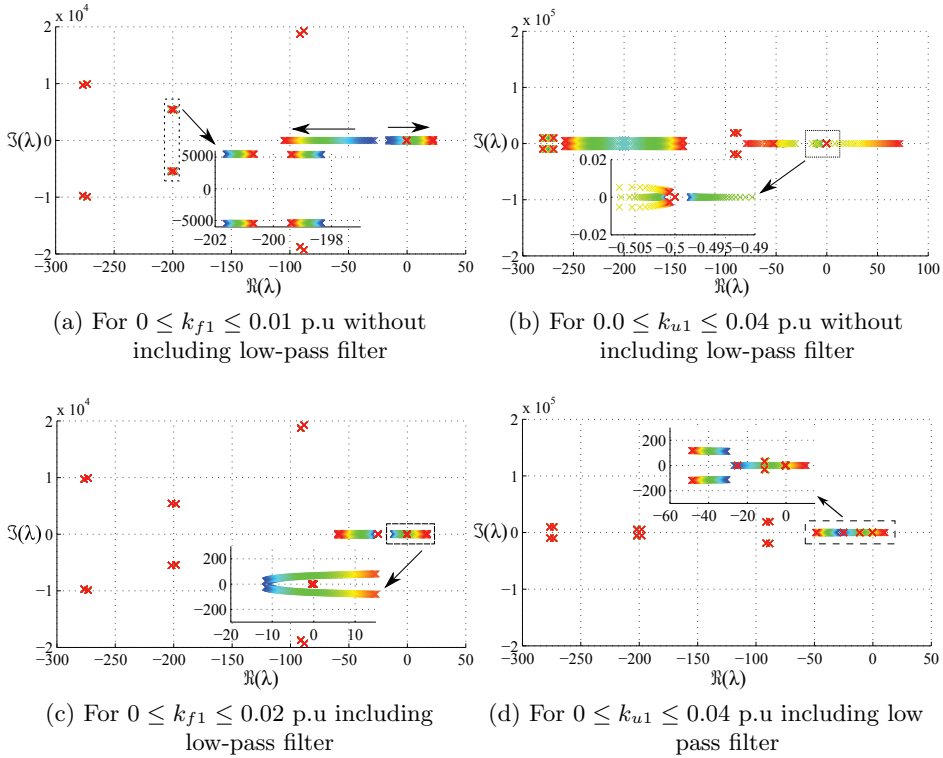
Figure 4.8: Poles maps of the offshore AC network with or without including low-pass filter on power measurements.

The system closed loop poles map for $0.0 \leq k_{f1} \leq 0.02$ p.u including low-pass filter is shown in Figure 4.8c. The low-pass cutoff frequency is 25 rad/s[68]. Note that this filter is only applied to the active and reactive power droop feedback signals. From Figure 4.8c, it can be observed that the poles are moving towards the right side of the s-plane for large k_{f1} values. In this case, the system becomes unstable for $k_{f1} > 0.01$ p.u. The low-pass filter is able to damp the oscillation that appears in the droop feedback signals increasing the stable operation range. The poles located closed to -0.5 of the real axis scale lead the system to instability as in the previous case.

Similarly, the effect of the reactive power measurement filter on the system poles can be observed in Figure 4.8d. As it has been observed previously, the

(a) VSC-1 voltage d-component (u_{d_1})   (b) VSC-2 voltage d-component (u_{d_2})
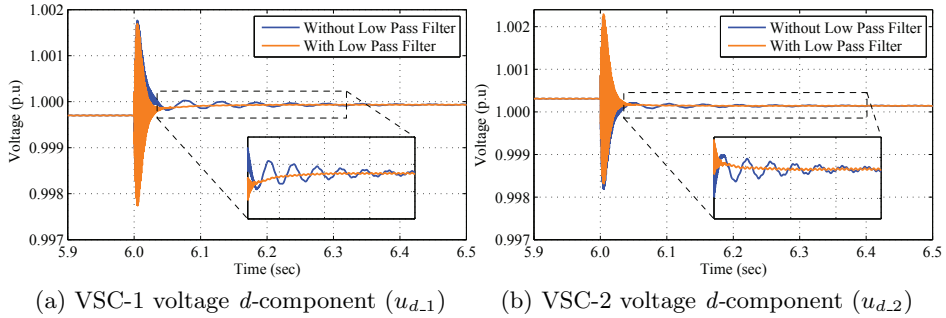
Figure 4.9: The nonlinear time domain simulation plots of converters controlling busbar.

voltage droop gains have an impact on both sets of poles. Although, the low-pass filter of the reactive power measurement reduces the poles movement located close to -200 of the real axis scale, but the poles located close to -0.5 of the real axis scale are influenced in the same manner. Therefore, the system becomes unstable at the same voltage droop gain i.e $k_{u1} > 0.027$ p.u.

The droop gains range for stable operation can be increased by decreasing the power measurement low-pass filter bandwidth. However, it is important to note that high droop values can lead the steady-state frequency and voltage operating points above the nominal range. By performing an eigenvalue analysis, the boundary of the frequency and voltage droop gains can be calculated for stable operation of the offshore AC network.

4.3.3 Nonlinear Dynamic Simulation Results

The propose method for determining the frequency and voltage droop gains for stable operation is validated by performing a nonlinear simulation of the network shown in Figure 4.6. The network is modeled in Simulink SimPowerSystems. Both VSCs are operating in grid forming mode. The grid forming control is shown in Figure 4.2. The HVAC cables are represented using a $\pi-$equivalent model. The WPP is modeled as equivalent three-phase current source synchronized with the network frequency. In all the simulations performed, the frequency and voltage droop gains are $k_{f1} = 0.00165$ p.u, $k_{f2} = 0.00231$ p.u, $k_{u1} = 0.0020$ p.u, and $k_{u2} = -0.0020$ p.u,

(a) Bode plot of voltage transfer function $T_{ui}^d(s)$ and $T_{ui}^q(s)$

(b) Bode plot of frequency transfer function $T_{\omega i}^d(s)$
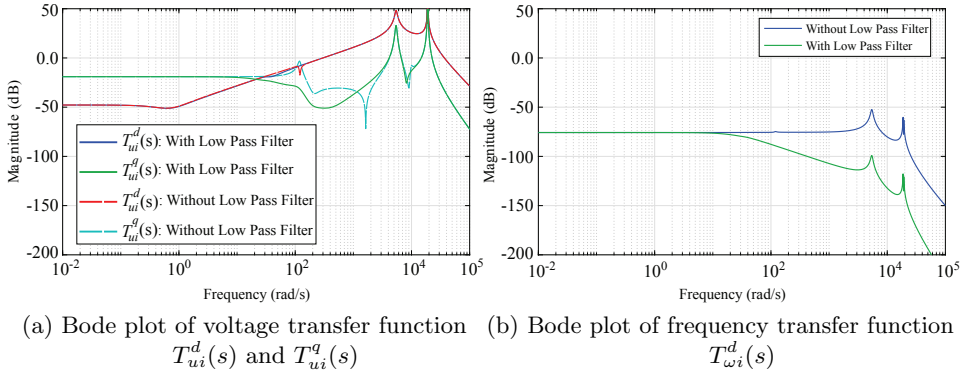
Figure 4.10: The frequency response analysis of the VSC-1 output voltage and the network frequency change with respect of wind active current.

unless stated explicitly in plots. These droop gains have been calculated based on a given active and reactive power sharing factor between both converters as explained in Chapter 3. According to the power sharing criteria, the percentage of active power distribution between VSC-1 and VSC-2 is 42.0 % and 58.0 % respectively.

The system dynamic response is analyzed by applying a step change in the WPP active current (i_{d_wind}) from 0.0 to 0.5 p.u at 4.0 s. Also, an inductive reactive current (i_{q_wind}) step change in the WPP is applied at 6.0 s from 0.0 to 0.2 p.u. According to the droop gains, the magnitude of active power through VSC-1 and VSC-2 should be 0.21 p.u and 0.29 p.u respectively. The reactive power sharing depends on both the voltage droop values and the amount of active power flow through each converters. According to the voltage droop gains setting, the magnitude of reactive power of VSC-1 and VSC-2 should be same after 6.0 s i.e 0.05 p.u. Note that the generator oriented sign convention is applied in the simulation results.

The voltage responses of both VSCs at the controlled busbar (u_{d_1}, u_{d_2}) are shown in Figure 4.9. During $6.0 - 6.02$ s, high frequency transients can be observed in the voltage response due to the reactive power change in the network. For a clear understanding of this transient behavior, the bode plot of the VSC-1 output voltage with respect to WPP current with or

(a) Reactive Power   (b) Active Power
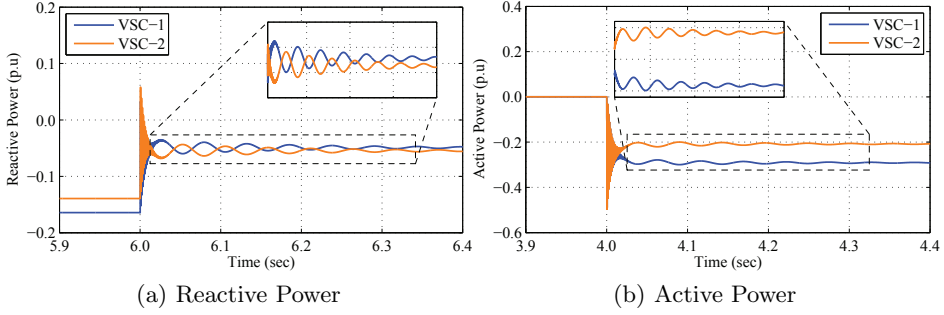
Figure 4.11: Power response of the VSCs without having low pass filters at the power measurements.

without including the low-pass filter is shown in Figure 4.10a. Here, $T_{ui}^d(s) = \Delta u_{d\_1}/i_{d\_wind}$ is the transfer function of VSC-1 output voltage d-component with respect to the WPP current d-component. And, $T_{ui}^q(s) = \Delta u_{d\_1}/i_{q\_wind}$ is the transfer function of the VSC-1 output voltage d-component with respect to the WPP current q-component. From the bode analysis, it is clear that the system has a resonance due to the submarine cables which can cause the oscillation in the voltages when the WPP current is suddenly varied. Moreover, it can be observed that the low-pass filters do not affect the system response at higher frequencies. In order to limit the output voltage oscillation at higher frequencies, the rise time of the wind power is recommended to be limited up to 10 ms. Note that there is no effect of the low-pass filter in the voltage response with respect to the wind active current $(T_{ui}^d(s))$. The transient in the voltage due to a change in the reactive power $(T_{ui}^q(s))$ improves for certain frequencies (10^2 to 10^3 rad/s) by applying a low-pass filter. The damping effect of the low-pass filter in the voltage response can be observed after 6.02 s in Figure 4.9. After 6.02 s, the VSCs droop control starts to establish the power sharing between VSCs. And during this period, the oscillation in the voltage signal are damped by having low-pass filter at the power measurement signals.

The VSCs reactive power response without including the low-pass filters is shown in Figure 4.11a. It is clear that the reactive power has oscillations during the power sharing period i.e after 6.02 s. Similarly, the VSCs active

(a) Reactive Power   (b) Active Power
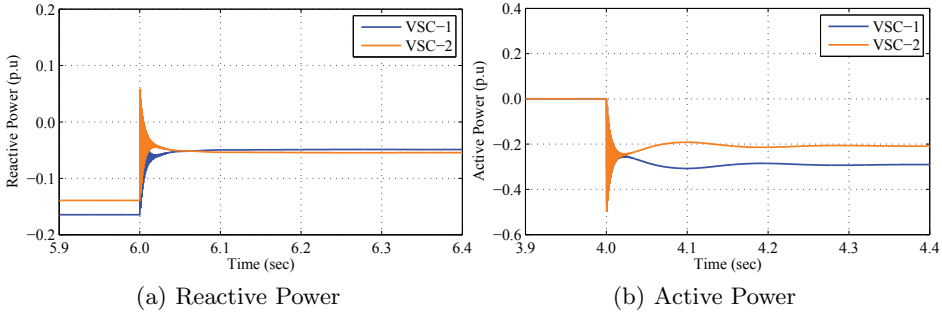
Figure 4.12: Power response of the VSCs having low pass filters at the power measurements.

power response without including the low-pass filters is shown in Figure 4.11b. Here, the active power sharing period starts at 4.02 s. Like the reactive power response, the active power also shows a low damping response during power sharing period. This oscillation can be damped using low-pass filter at the power measurements. The responses of the VSCs active and reactive power including the low pass filters are shown in Figure 4.12. It is clear that the damping in the system has been increased. Also, the power is distributed between the VSCs according to the sharing criteria.

The power-frequency relation in the VSCs is established by the frequency droop scheme. Furthermore, it has been observed that the active power has oscillations due to the offshore AC network dynamic behavior. These oscillations will appear in the VSCs imposed frequencies if the low-pass filters are not included as it is shown in Figure 4.13a. The bode plot of the network frequency with respect to the wind active current is shown in Figure 4.10b. The transfer function for the bode analysis is $T_{\omega i}^d(s) = \omega/i_{d\_wind}$. Note that the complete system is multi-input multi-output (MIMO) system and the frequency response is shown only with respect to wind power infeed. The cutoff frequency of the low-pass filter can be set such that it reduces the high frequency gain below its steady-state gain. Based on the frequency response, it is concluded that a low-pass filter bandwidth of 25 rad/s is sufficient to damp the frequency oscillation. The effect of this low-pass filter on the VSCs and the network frequencies can be seen from Figure 4.13b.

(a) Response without low pass filter

(b) Response with low pass filter
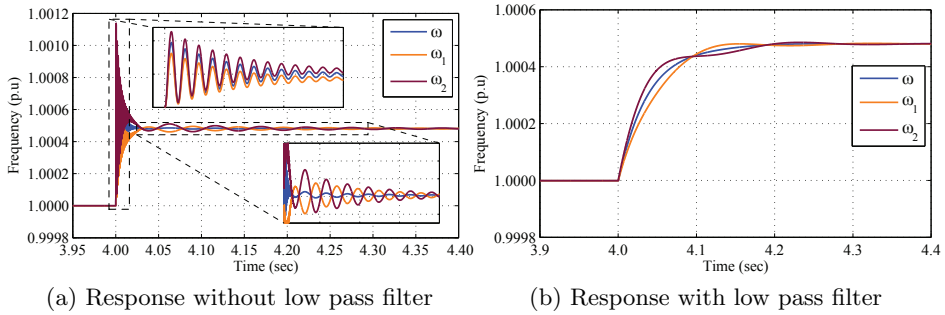
Figure 4.13: Nonlinear simulation response of VSCs frequencies.

The network frequency now has a first order response, and the damping has been increased in the VSCs imposed frequencies.

A demonstration of the system instability caused by the frequency droop gain is shown in Figure 4.14a. To perform the test, initially the frequency droop gain of VSC-1 (k_{f1}) is set to 0.0028 p.u, and it is changed to 0.0030 p.u at 14.0 s. All the other control parameters remain same. It is clear that any initial active and reactive power transients are damped before 14.0 s. After 14.0 s, the system becomes unstable due to the frequency droop value. At $k_{f1} = 0.0029$ p.u the system is marginally stable. The frequency gain value at which the system becomes unstable is the same as determined by the eigenvalue analysis. The nonlinear simulation of the offshore AC network validates the proposed small-signal modeling method for network stability analysis.

Furthermore, the robustness of the proposed method is tested at different cable lengths in order to evaluate the effects of the parametric uncertainty. The same simulation procedure has been performed by using different cables length. In the eigenvalue analysis, the droop gains stability limits are calculated with the cables length of 10 km. While in the nonlinear simulink model, the length of the cable-1 is changed to 9 km and the length of the cable-2 is changed to 11 km. It can be observed from Figure 4.14b that the power response has slightly more oscillations compared to the previous results. However, the system becomes unstable at the same frequency droop gain. This shows that the small-signal modeling method is robust, and it

(a) System instability at the cables length of 10 km each

(b) Sensitivity analysis by changing cables length to 9.0 km and 11.0 km
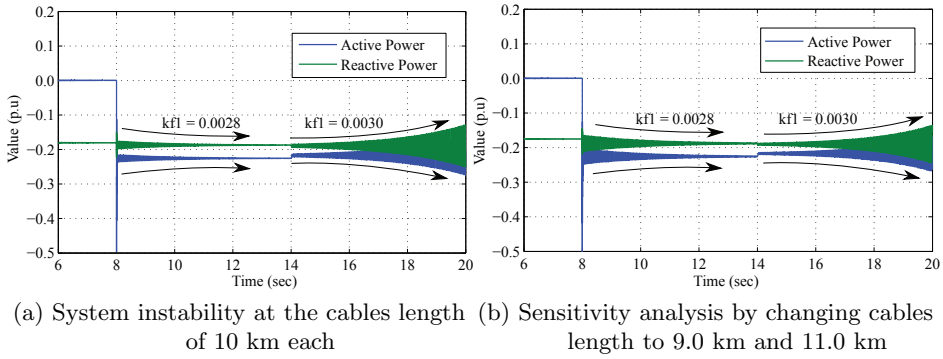
Figure 4.14: A nonlinear simulation test for the validation of stability range and sensitivity analysis.

can provide reliable offshore AC network stability margin.

4.4 Summary

In this chapter, a method of modeling offshore AC network has been proposed to perform a small-signal stability analysis. With the proposed method, a stable operational range of frequency and voltage droop gains can be found. It is recommended to include the dynamics of the VSC voltage and the current control in the small-signal model in conjunction with droop scheme in order to consider the complete performance of the VSCs in the overall system response. A comparison of the system performance with and without including a low-pass filter in the power measurements has been shown. It has been observed that the low-pass filters increase the damping in the overall system response. Further analysis indicate that all the oscillation in the system, caused by fast changed in wind energy, cannot be fully damped by the VSCs. The performance limitation of the VSCs have to be considered in the grid code for offshore wind power plants.

5 Short Circuit Analysis of an Offshore AC Network

This chapter presents the short circuit analysis of an offshore AC network that interconnects the offshore wind power plants with different onshore grids using VSC-HVDC transmission system. The short circuit control system is presented for the wind turbines, onshore and offshore VSCs. The chapter presents a method to calculate the control limits of VSCs considering operational capability. Furthermore, the short circuit analysis of a network has been performed to propose the suitable control scheme. In order to verify the proposed short circuit control scheme, three phase symmetric faults are applied on a wind turbine busbar, offshore HVAC busbar, at the offshore AC cable that interconnects the VSC-HVDC systems, and at the onshore grid. Additionally, a frequency coordination control scheme is proposed between wind power generation and offshore VSCs of HVDC systems without using communication signal. The methodology and control system are validated by performing a nonlinear simulation[5,6].

5.1 Introduction

An offshore grid has importance in the integration of the future large offshore wind power plants with the onshore grids [111]. The concept

---

[5]This chapter is based on the following publications:

M. Raza, M. Aragues-Penalba, and O. Gomis-Bellmunt, "Short circuit analysis of an offshore AC network having multiple VSCs imposing frequency" International Journal of Electrical Power and Energy Systems, Elseiver (peer-reviewed).

[6]M. Raza and O. Gomis-Bellmunt, "Control design strategy to enhance the fault ride through capability of VSC-HVDC transmission system interconnecting offshore wind power plant", in EWEA Annual Conference and Exhibition 2015, (Paris, France), nov 2015.

of the offshore grid control principle has been presented in the previous chapters. The control principle covers the operation of the network with respect of steady state behavior, dynamic response, and small signal stability. The complete successful operation of an offshore grid further requires that the wind generation units and offshore VSCs should continue operating during fault for short period of time, and they must continue to function after isolation of faulted area [112]. The grid integration requirements are usually provided by transmission operators in their grid codes [47]. The fault ride through (FRT) capability is required even at very low fault voltage. For the onshore grid connection, the grid code requirements are fulfilled by onshore converters of VSC-HVDC transmission system at the point of common coupling (PCC) [113]. During low voltage ride through or fault, it is recommended to inject the reactive current in order to support the onshore grid voltage. However during recovery period, this reactive current must be removed as fast as possible, and the rate of active power recovery should also be high to ensure system stability [83].

In the network such as illustrated in Figure 5.1, VSCs of HVDC transmission system decouple the offshore grid from the mainland grid which makes offshore grid vulnerable to dynamic voltage events due to low short circuit power in the network [114]. The short circuit power in the offshore network is limited by the maximum rated power of the HVDC transmission system and wind turbines. The offshore network formation by interconnecting several offshore wind power plants may increase the short circuit current level in the network compare to a single wind power plant connection with an onshore grid. However, it is important that the offshore VSCs of HVDC systems must ensure the voltage stability during fault and post fault states. In the event of fault, the VSC operation is switched from control voltage source to current source once current limit reaches. In this situation, the network complex voltage at the VSC controlling busbar appears according to the equivalent fault impedance and the VSC current [83]. Depending on the VSC current angle infeed, the fault voltage angle could deviate significantly from its pre-fault state. The large angle deviation can cause instability during recovery period [82]. This requires a suitable control scheme to improve the voltage phase angle during fault close to the level of pre-fault state. This
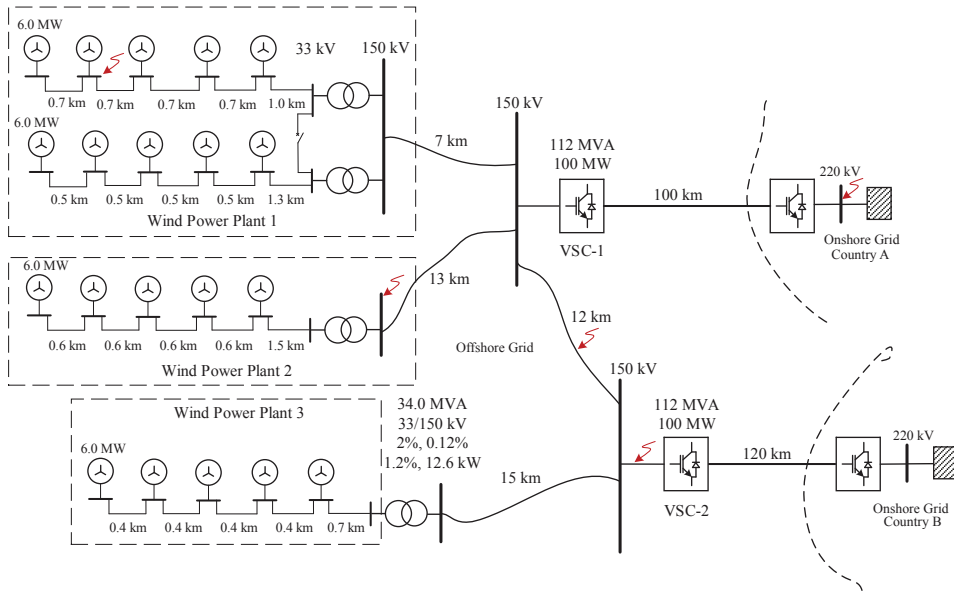
Figure 5.1: Configuration of offshore AC network integrating two onshore grids with three wind power plants using VSC HVDC transmission system in point to point configuration.

chapter presents the offshore AC network short circuit analysis to propose the suitable control scheme for the VSC-HVDC system.

As explained previously that the offshore AC network is formed by more than one VSC-HVDC transmission system i.e the network have multiple VSCs operating as reference machine. In the post fault state, the network should be able to operate normally after fault clearance, even the fault isolation creates multiple isolated networks. Such an operation requires a coordination between wind generation units and the VSC control system preferably without communication [77]. Typically, wind generation units are required to reduce their active power when the net power in the offshore AC network become greater than the rated power of the VSC-HVDC transmission system. In this regard, a coordination can be established between VSCs and the wind generation units using frequency [115]. In this chapter different aspects of short circuit events have been analyzed on the network shown in Figure 5.1, and the short circuit control system is proposed for wind generation units, offshore VSC, and onshore VSC.

5.2 Offshore Grid Configuration and VSC Control System

An offshore AC network interconnecting three wind power plants with two onshore grids using VSC-HVDC transmission systems is illustrated in Figure 5.1. The offshore network is formed by both offshore converters i.e VSC-1 and VSC-2. The interconnection is made between wind power plants using AC cables of 150 kV voltage level [102]. The wind power plants arrays are constructed in radial configuration with 33 kV AC cables [103]. The cables and 150/33 kV transformer parameters are given in Table 5.1. The power transmission capability of each VSC-HVDC system is 100 MW. All the wind generation units have active power rating of 6.0 MW. The rated active power of a WPP-1 is 60 MW, WPP-2 and WPP-3 have 30 MW each, making net active power in the offshore AC network equal to 120 MW. The combined power of all wind power plants is greater than a single VSC-HVDC transmission system. In this configuration, up to 83.3 % of net active power can be transferred through a signal VSC-HVDC transmission line. The distribution of the active power among the export system is controlled using frequency droop control.

5.2.1 Control of Wind Generation System

The wind generation units are based on permanent magnet synchronous generator with fully rated converter. Only the network side converter system is modeled for a wind generation unit as explained in Section 2.5. The wind generation unit parameters are given in Table 2.3. The control system of wind generation unit including short circuit scheme is given in Figure 5.2. The wind generation unit behaves as a controlled current source synchronized

Table 5.1: Cables and transformer parameters

	Voltage	Resistance	Inductance	Capacitance
Cable (MVAC)	33 kV	0.047 Ω/km	0.34 mH/km	0.3 μF/km
Cable (HVAC)	150 kV	0.06 Ω/km	0.44 mH/km	0.14 μF/km
Transformer (HV-MV)	150/33 kV	0.12%	2%	-

Figure 5.2: Control system of wind generation units including short circuit scheme.

with the network frequency. The reference output voltage signal is generated by the inner current controller. The bandwidth of the current closed loop control is adjusted to 1.0 ms. The reference current command is generated by the outer control loop which depend on the converter operational mode. The outer control system of wind generation unit is shown in Figure 5.3. The network side wind generation converter controls the DC voltage in the fully rated back-to-back converters in order to feed wind active power into the network as shown in Figure 5.3a. In order to support the voltage of the offshore AC network, the wind generation unit controls the reactive power at the given set-point. The reactive power control is shown in Figure 5.3b. Both DC voltage and reactive power control loops have proportional-plus-integral regulator for reference signal tracking. During over current period, the input

(a) DC Voltage Control   (b) Reactive Power Control

Figure 5.3: The outer voltage control of wind generation unit.

of the integral is tracked through the output signal of the current limiter in order to improve the dynamics response during fault and recovery periods.

The short circuit control scheme consists of two main parts. Firstly, an additional reactive current injection control to support the network voltages during short circuit or voltage sag. Secondly, frequency dependent active current reduction control to establish the coordination between wind turbine and VSC-HVDC transmission system during over frequency in the network. A chopper controlled resistor is also needed on the DC link to dissipate excess energy during fault.

5.2.2 Control of Offshore VSC-HVDC System

The offshore converter of HVDC transmission system imposes the frequency and provide reference voltage to the network as explained in Section 3.2. The offshore VSC substation parameters are given in Table 2.1. The control of VSC-HVDC offshore side converter including short circuit control is shown in Figure 5.4. In normal operation, the converter acts as a controlled voltage source, and it can be considered as DC voltage independent when the DC voltage variation is within the operating range at maximum power. In the VSC control scheme, there are two main control loops i.e a voltage control loop (outer controller) and current control loop (inner controller). The current controller improves the current dynamics as well as enable the current control during short circuit. Frequency and voltage droop control schemes are applied to operate the offshore network on the principle of multiple machine system and to control the power distribution among VSCs. Although the combined power of VSC-HVDC converters must be
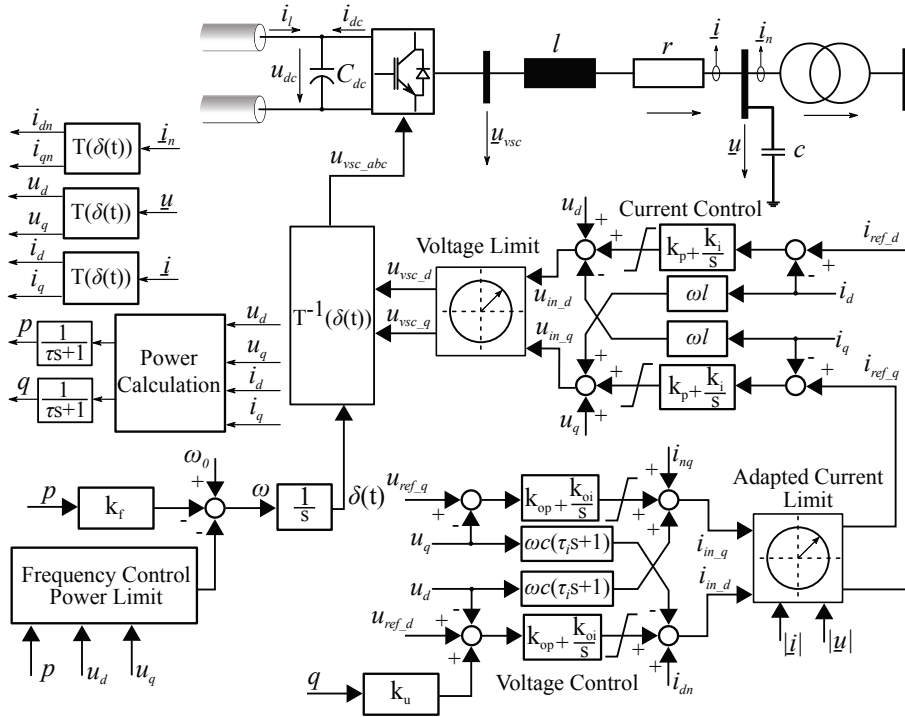
Figure 5.4: Offshore VSC control for HVDC system including short circuit scheme.

equal to the total wind power, it is not necessary for each VSC-HVDC converters to have equal or greater rated power than total wind power in the network. According to the droop gain setting, the steady state active power flows through VSC-1 and VSC-2 are 0.333 p.u and 0.667 p.u respectively. Furthermore, the reduction in the wind power generation is required up to the total remaining export capacity in the event of one transmission system disconnection. To achieve such operation, the in-service VSC-HVDC system increases the network frequency which is an indication to wind generation units to reduce the power generation.

5.2.3 Control of Onshore VSC-HVDC System

The onshore side VSC control system of HVDC transmission system is shown in Figure 5.5. The control system for both onshore converters are identical
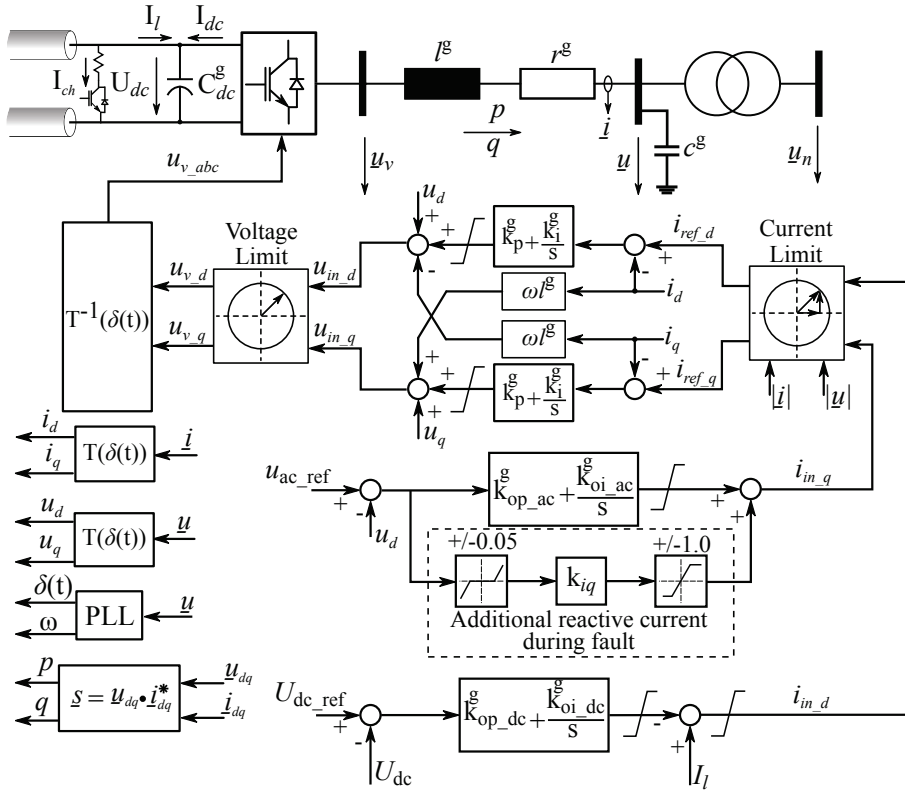
Figure 5.5: Onshore VSC control for HVDC system including short circuit scheme.

and their parameters are given in Table 2.2. In the point-to-point HVDC topology, onshore side VSC has responsibility to control the DC voltage. In this mode, the onshore VSC is synchronized with the onshore grid frequency and injects received power from the DC network into the onshore AC grid. Further, a DC chopper controlled resistor is installed to maintain the DC voltage during fault. The VSC is set into AC voltage control mode in order to support onshore grid voltage. Also on exceeding the voltage deviation limit of +/-5 %, additional reactive current is injected to support the onshore grid voltage. The PI control with anti windup scheme is implemented for both AC and DC voltage controls. These PI controller limits are based on the operational capability of the converter. The operational capability of the converter is calculated by performing PQ analysis.
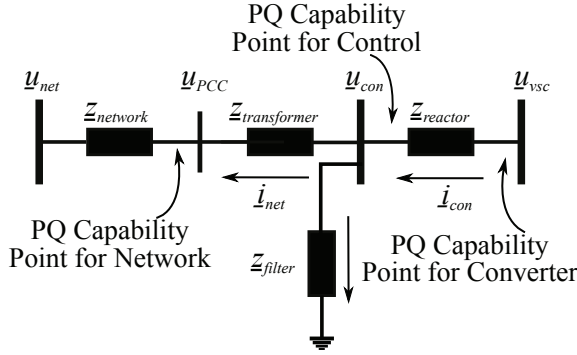
Figure 5.6: An equivalent impedance diagram of voltage source converter substation to analyze PQ characteristic.

5.3 Voltage and Current Operating Limits

The calculation method applied, in order to determine the converter voltage and current operational limits, is the same for both wind power plant and VSC-HVDC system. These limits are selected with respect to the PQ characteristics of the system. An equivalent diagram of converter substation for the PQ analysis is shown in Figure 5.6. Three connection points are important in the PQ analysis to determine the operational limits. Firstly, a PQ curve at the converter busbar that indicates the capability of the converter switching devices in term of current and voltage. Secondly, a PQ analysis after the series reactor where the actual current limit requires to be applied in the control system. Thirdly, a PQ curve at the point of common coupling (PCC) which defines the normal operating region for the network. Since, the ability of a converter to generate the AC output voltage peak depends on the DC voltage level, the minimum and maximum DC voltage needs to be considered in the analysis. For a point-to-point topology of the VSC-HVDC transmission system, the maximum and minimum DC voltage can be determined by calculating the voltage drop over the DC cable at maximum power using (5.1).

$$\Delta U_{dc\_dev} = \frac{R_{dc} \cdot P_{dc\_max}}{U_{dc\_rt}^2} \tag{5.1}$$

Here, ΔU_{dc_dev} is the per unit voltage deviation from the rated DC voltage,

(a) PQ characteristic at VSC busbar

(b) PQ characteristic at control busbar

(c) PQ characteristic at PCC considering operating limits

(d) $\underline{i}_{con}$ operational area considering PQ operating limits
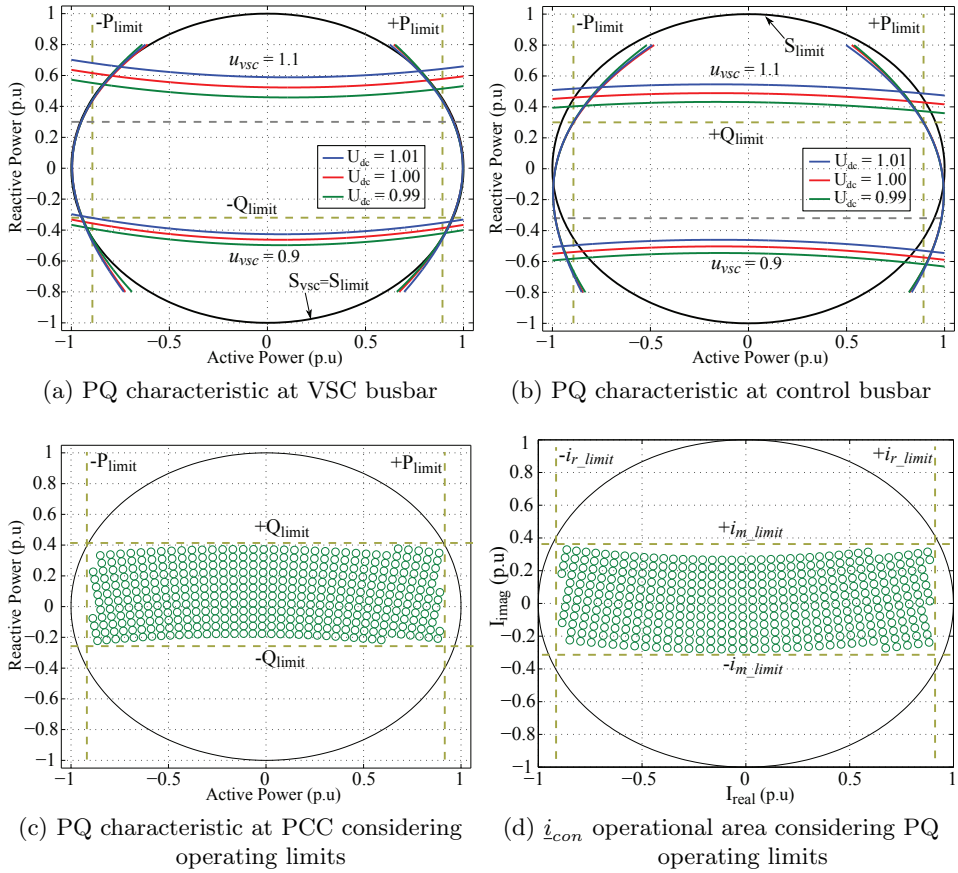
Figure 5.7: PQ characteristic analysis of VSC HVDC substation to determine voltage and current operational limits.

R_{dc} (Ω) is the total resistance of the DC cable, P_{dc_max} (MW) is the maximum active power, and U_{dc_rt} (kV) is the rated pole-to-pole DC voltage.

The PQ analysis results are shown in Figure 5.7. The unit circle is the rated power limit of the converter (S_{vsc}), and the power flow is considered positive in the direction of arrows as shown in Figure 5.6. Reactive power upper and lower limits are imposed according to the converter (u_{vsc}) maximum and minimum AC output voltage. It can be seen that the active power capability is not influenced significantly with respect to the DC voltage but reactive power capability varies. At the given active power limits, the

inductive reactive power $(-Q_{limit})$ is determined at minimum AC voltage and at maximum DC voltage, as illustrated in Figure 5.7a. Care must be taken while selecting reactive power limits to not to violate all limits on PQ capability curve at both converter and control busbar. The maximum capacitive reactive power limit (Q_{limit}) is set by PQ curves at control busbar at maximum AC and at minimum DC voltage as illustrated in Figure 5.7b. It can be noticed that capacitive reactive power limit is further reduced due to losses in the reactor. The operating region at the point of common coupling considering active and reactive power limits is shown in Figure 5.7c. Further, maximum steady state current limit can be determined from Figure 5.7d. Also, the maximum required modulation index can be calculated using (5.2).

$$m = \frac{u_{ac\_max}}{U_{dc\_min}} \cdot \frac{2u_{p\_rt}}{U_{dc\_rt}} \tag{5.2}$$

Here, u_{ac_max} (p.u) is the maximum AC output voltage, U_{dc_min} (p.u) is the minimum DC voltage for normal operation, u_{p_rt} (kV) is the rated AC output voltage, and U_{dc_rt} (kV) is the rated DC voltage.

5.4 Short Circuit Analysis of an Offshore Grid

The principle of VSC short circuit control can be understood by performing circuit theory analysis on a simplified network given in Figure 5.8. The wind power plants fault current is represented by the net current $(\underline{i}_7)$ injecting at the fault busbar $(\underline{u}_7)$. The VSCs behave as controlled voltage sources in the pre-fault state. However, these converters are required to be operated as control current sources during fault period and inject short circuit current up to their maximum capability. The impact of the short circuit current on the network voltages during fault can be analyzed by defining the net current infeed $(\underline{i}_{vsc})$ of the VSCs and the wind power plant current at the cable-1 ends as redrawn in Figure 5.8b. Here, $\underline{z}_{fault}$ is the parallel combination of the fault impedance and the cable capacitive impedance $(\underline{z}_{c1\_f})$. In parallel combination, the fault impedance is dominant due to smaller in value therefore only the fault impedance is shown in the equivalent network diagram. The bus voltages as a function of VSC and wind power
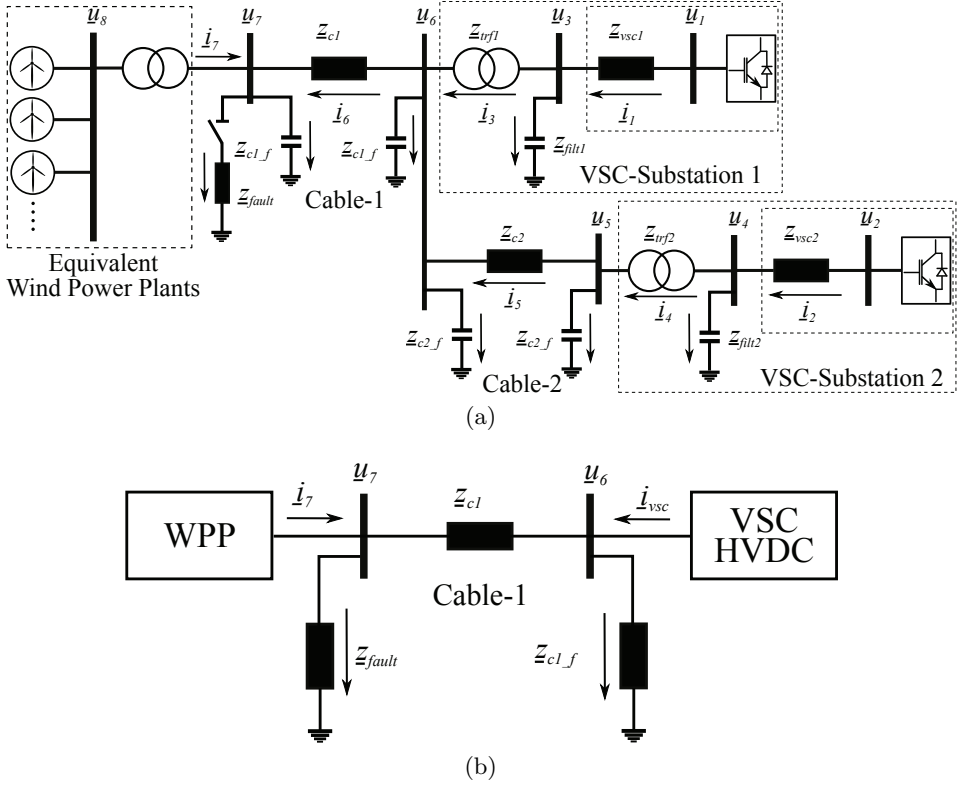
Figure 5.8: Simplified offshore AC network diagram for short circuit analysis.

plant currents are derived as (5.3). Using this equation, the behavior of the bus voltages can be analyzed. It is clear that the voltages magnitude during fault are proportional to the magnitude of the currents. However, the contribution of the currents from wind turbines and VSCs in the busbars voltage level depends on the equivalent Thévenin impedance.

$$
\begin{aligned}
\underline{u}_6 &= \frac{\underline{z}_{c1\_f}}{\underline{z}_{c1} + \underline{z}_{fault} + \underline{z}_{c1\_f}} \left\{ \left(\underline{z}_{c1} + \underline{z}_{fault} \right) \cdot \underline{i}_{vsc} + \underline{z}_{fault} \cdot \underline{i}_7 \right\} \\
\underline{u}_7 &= \frac{\underline{z}_{fault}}{\underline{z}_{c1} + \underline{z}_{fault} + \underline{z}_{c1\_f}} \left\{ \underline{z}_{c1\_f} \cdot \underline{i}_{vsc} + \left(\underline{z}_{c1} + \underline{z}_{c1\_f} \right) \cdot \underline{i}_7 \right\}
\end{aligned}
\tag{5.3}
$$

According to the above equation, the voltage level of $\underline{u}_6$ will have high current contribution from $\underline{i}_{vsc}$ since the cable series impedance is higher
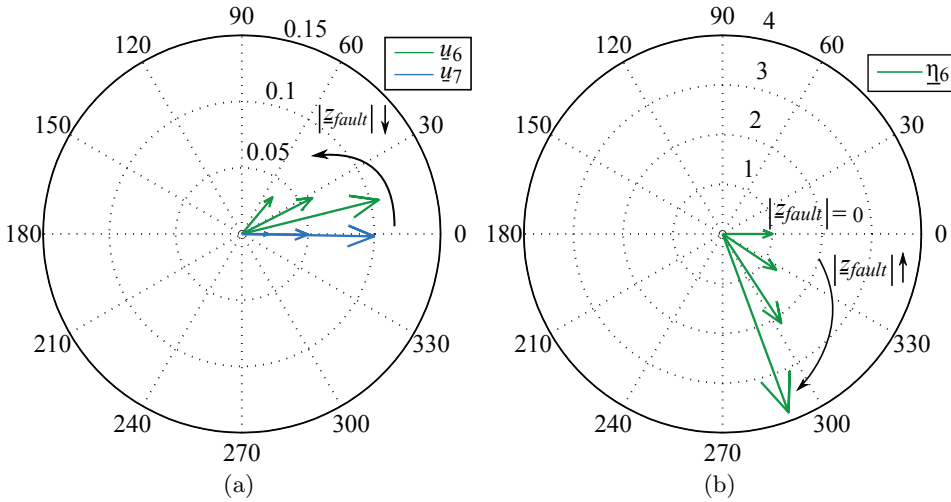
Figure 5.9: Effect of fault impedance magnitude on busbar voltages.

than the fault impedance i.e $\left(\underline{z}_{c1} + \underline{z}_{fault}\right) > \underline{z}_{fault}$. Similarly, the voltage level of $\underline{u}_7$ will be improved mainly by wind turbine current infeed. Apart of the current, the equivalent impedances also have high impact on the busbars voltage. The fault impedance introduces the voltage phase angle shift or phase angle jump due to difference in the equivalent impedance in fault and pre-fault states [116]. The power electronic devices are sensitive to phase angle jump which lead to their mal-operation and cause instability in the network. During fault, the busbar voltage phase angle difference needs to be analyzed with respect to its pre-fault value as well as from other voltage source bus phase angle. In order to do so, the effect of the fault impedance on the voltage phase angle is analyzed by phasor diagram as shown in Figure 5.9. The fault is considered as three phase resistive. In the results, the wind power plants are not injecting any current i.e $\underline{i}_7 = 0.0$, and the VSC injects rated current i.e $\underline{i}_{vsc} = 1.0\angle0.0$ deg. Note that the (5.3) represents the steady state voltage values during fault. Further, the converters are operating as controlled current sources during short circuit therefore its current can be taken as the reference vector on the complex plane. The voltage, current and impedance variables are expressed in polar coordinate to simply the notation as:

$$\underline{u}_6 = u_6 e^{j\delta_6}$$

$$\underline{u}_7 = u_7 e^{j\delta_7}$$

$$\underline{i}_7 = i_7 e^{j\psi_7}$$

$$\underline{i}_{vsc} = i_{vsc} e^{j\psi_{vsc}} \tag{5.4}$$

$$\underline{z}_{fault} = z_f e^{j\theta_f}$$

$$\underline{z}_{c1} = z_c e^{j\theta_c}$$

$$\underline{z}_{c1\_f} = z_{cf} e^{j\theta_{cf}}$$

Typically, pre-fault voltage phase angle is near 0.0 deg from the reference bus considering no phase shifting transformer included. Figure 5.9a illustrate that the phase angle of δ_6 changes significant with the reduction in the magnitude of the fault impedance. Also, the phase difference of both busbar i.e $\delta_6 - \delta_7$ increases proportionally. These large angle deviations can cause instability during fault and recovery period. Further, δ_7 is not changed from its pre-fault value since the wind turbines current is zero and the voltage level is due to converter current. Note that z_f only influences u_7 but not δ_7. To quantify the voltage angle deviation as function of equivalent impedance, a complex voltage ratio $\underline{\eta}_6$ is defined for busbar 6 as given by (5.5). Note that in the equation $\underline{i}_7 = 0.0$ p.u.

$$\underline{\eta}_6 = \frac{\underline{u}_6}{\underline{u}_6^0} = \frac{1 + \frac{z_f}{z_c} e^{j(\theta_f - \theta_c)}}{1 + \frac{z_f}{z_x} e^{j(\theta_f - \theta_x)}} \tag{5.5}$$

Here, $\underline{z}_x = \underline{z}_{c1} + \underline{z}_{c1\_f}$. Also, $\underline{u}_6^0$ refers to the voltage at the busbar 6 when the fault impedance is zero. Figure 5.9b illustrate the relative deviation in $\underline{\eta}_6$ with respect to voltage when the fault impedance is zero. On the complex plane, the reference vector is $\underline{u}_6^0$ i.e $1.0\angle 0.0$ deg. The impedance of the cable capacitance is high relative to the fault impedance therefore denominator in (5.5) is constant i.e $1 >> z_f/z_x$. Thus, the voltage angle deviation mainly occurs due to the cable series impedance angle which is inductive i.e $\theta_c \approx 90$ deg. With the increase in the z_f, the voltage at busbar 6 increases since the condition $1 < z_f/z_c$ is applied. In the plot, θ_f is constant at the value of 0.0 deg. This has demonstrated that the phase angle jump is the function of the equivalent fault impedance which varies according to the

(a) Pre-fault network voltages

(b) Fault response with $\underline{i}_1 = \underline{i}_2 = 1.0\angle0.0$, and $\underline{i}_7 = 0.0\angle0.0$
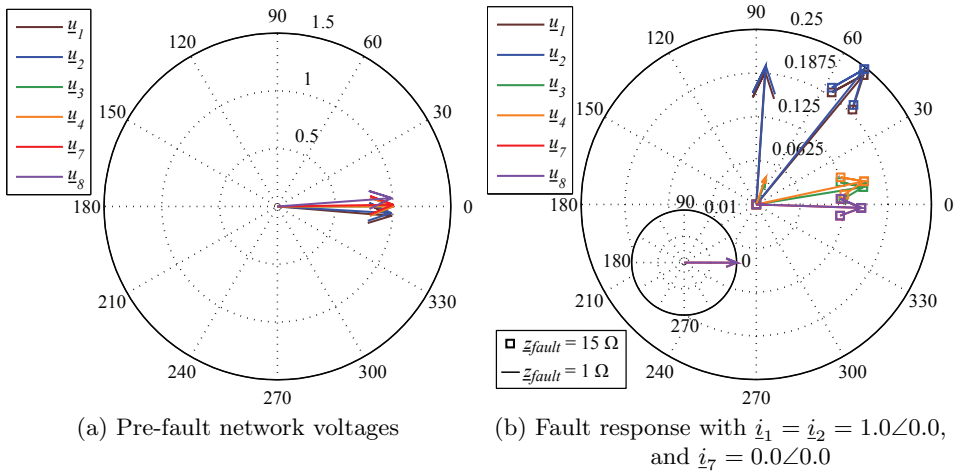
Figure 5.10: Offshore network voltages level in polar coordinates.

fault location.

The system equations can be extended in the similar manner to analyze remaining voltages of the network. The offshore network voltages response for pre-fault and fault states are shown in Figure 5.10. On the complex plane, the pre-fault voltage at the filter bus of the VSC substation is considered as reference phase angle i.e $\underline{u}_3 = \underline{u}_4 = 1.0\angle0.0$ deg. In the pre-fault state, the network voltage angles are closed to reference busbar voltage angle as illustrated in Figure 5.10a. It is well known that the voltage phase angle difference between busbars must be less than 90 deg to ensure stability in the network, and the phase difference is preferable to be within ±30 deg for practical reasons.

During fault, VSCs control the current injection thus the voltages in the network evolve according to the current infeed and short circuit impedance of the network. The network voltages during fault with VSCs current infeed of $1.0\angle0.0$ deg each is illustrated in Figure 5.10b. Note that wind power plants are not injecting any current in this case. The response has been analyzed for resistive faults at the value of $\underline{z}_{fault} = 15\ \Omega$ and $\underline{z}_{fault} = 1\ \Omega$. It can be seen that the VSC substation busbar voltages have large voltage angle deviation with respect of its pre-fault state for low impedance fault. This is due to the

(a) Fault response with
$\underline{i}_1 = \underline{i}_2 = 1.0\angle - 90$, and $\underline{i}_7 = 0.0\angle 0.0$

(b) Fault response with
$\underline{i}_1 = \underline{i}_2 = 1.0\angle - 90.0$, and
$\underline{i}_7 = 1.0\angle - 90.0$
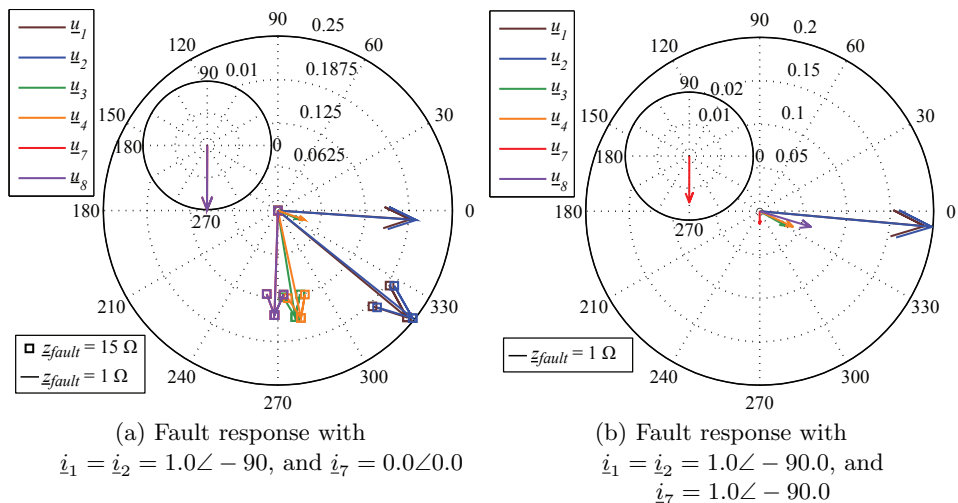
Figure 5.11: Offshore network voltages with and without wind power plant current infeed.

dominance of cable reactance in the equivalent impedance during fault. Note that the angle of $\underline{u}_7$ is in phase with $\underline{u}_8$. When $\underline{z}_{fault} = 1\ \Omega$, the voltage magnitude at the fault bus is 0.01 p.u, and 0.04 p.u at VSC controlling bus. At fault impedance of $\underline{z}_{fault} = 15\ \Omega$, the voltage phase angles will follow the difference of the cable series impedance and the equivalent fault impedance angle. The phase angle difference between both VSCs connected busbar is minimum since the affect of equivalent impedance change is same for both VSCs.

So far, the affects of fault magnitude on the voltage phase angle has been analyzed. Since the VSCs are controlling current during short circuit, the infeed current angle also influences the voltage phase angle which can be observed from Figure 5.11a. Here, the infeed current value is $1.0\angle - 90$ deg for both VSCs. The results shows that the voltage phase angle is shifted -90 deg for $\underline{z}_{fault} = 15\ \Omega$. In this case, the fault impedance is high compared to cable series impedance ergo voltage is aligned with VSCs infeed current. On the other hand, the voltage phase angle is closed to 0.0 deg for $\underline{z}_{fault} = 1\ \Omega$ since the series impedance angle is near 90 deg. The voltage phase angle at the VSC busbar is the sum of the equivalent impedance

angle and VSC current angle. It can be concluded that the VSC current is required to be controlled according to the equivalent impedance as seen from its controlling busbar (filter bus) in order to keep its busbar voltage angle near to pre-fault state. Further, the magnitude of the VSC substation voltages are not affected by the current angle rather they are proportional to the magnitude of the current. Thus, the VSCs must inject current of maximum magnitude in order to maximize the voltages during fault.

As it has been observed that the voltages at the wind power plants busbar ($\underline{u}_8$) mainly depends on the fault busbar voltages. The further improvement in the voltage at the busbar 8 can be done by wind power plant current injections as shown in Figure 5.11b. It is clear that the current injection with the angle -90 deg by the wind power plants improves both the magnitude and angle of $\underline{u}_8$. The fault bus voltage can be calculated using (5.6).

$$\underline{u}_7 = \underline{z}_{fault} \cdot (\underline{i}_7 + \underline{i}_6) \quad \text{where } \underline{i}_6 \approx \underline{i}_1 + \underline{i}_2 \tag{5.6}$$

5.5 Short Circuit and Frequency Coordinated Control System

There are two aspects of large signal disturbance that need to be considered in the control system for an offshore AC network. Firstly, a short circuit in the network leads to low voltages. In this case, converters behave as a controlled current source injecting maximum current. After fault isolation, the network must be restored as fast as possible and even create more than one isolated network if needed, such as in case of fault on interconnected cable (12 km) as shown in Figure 5.1. Secondly, the availability of more power in the offshore AC network than the export capacity. Such situation may appear when one VSC-HVDC transmission system is disconnected and the remaining in-operation transmission system has less export capacity than net power available in the network. In this case, the network frequency needs to be increased by the VSC-HVDC system to indicate wind generation systems to reduce their power generation up to the limit of export capacity. In this section, the control scheme is designed with respect of both scenarios.

5.5.1 Offshore VSC-HVDC Short Circuit Control

Usually, the operational limits in the voltage source converter are applied by limiting output voltage and current. The voltage limit can be applied by using (5.7) at the output command signal of the VSC to limit the output peak voltage. The minimum output voltage is set to zero. The saturation limit is not applied on δ_{vsc} since the current angle during fault depends on the fault impedance, and the maximum deviation in δ_{vsc} is limited by the current control. The anti-windup of current controller restricts the voltage angle within the stable region.

$$|u_{vsc}| = \begin{cases} |u_{in}| & \text{if } |u_{in}| < |u_{max\_limit}| \\ |u_{max\_limit}| & \text{if } |u_{in}| \geq |u_{max\_limit}| \end{cases}$$

$$\delta_{vsc} = \delta_{in} \tag{5.7}$$

$$u_{in} = \sqrt{u_{in\_d}^2 + u_{in\_q}^2}, \qquad \delta_{in} = \tan^{-1}\left(\frac{u_{in\_q}}{u_{in\_d}}\right)$$

$$u_{vsc\_d} = u_{vsc}\cos\left(\delta_{vsc}\right), \qquad u_{vsc\_q} = u_{vsc}\sin\left(\delta_{vsc}\right)$$

Further, the current controller integral limits correspond to the maximum voltage drop across the series reactor at rated current and it can be calculated by using (5.8).

$$\Delta u_{reactor} = z_{reactor} \cdot i_{p\_rt}$$

$$i_{p\_rt} = \frac{S_{rt}}{u_{p\_rt}}, \qquad z_{reactor} = \sqrt{r_{reactor}^2 + x_{reactor}^2} \tag{5.8}$$

The maximum current flow is limited by applying adaptive current limits on the current reference command as shown in Figure 5.12. The magnitude of the reference current is limited with respect to the actual current flowing through the series reactor, and it is activated when it exceeds the current operational limit i.e $i_{limit} = \sqrt{i_{r\_limit}^2 + i_{m\_limit}^2}$ (see Figure 5.7d). At the instant of the fault, the voltage d-component PI controller error will increase faster than q-component up to the saturation limit due to large error at the controller integral input. Consequently, the increase in current d-component sets the current angle near to zero. Once the voltage controller saturation
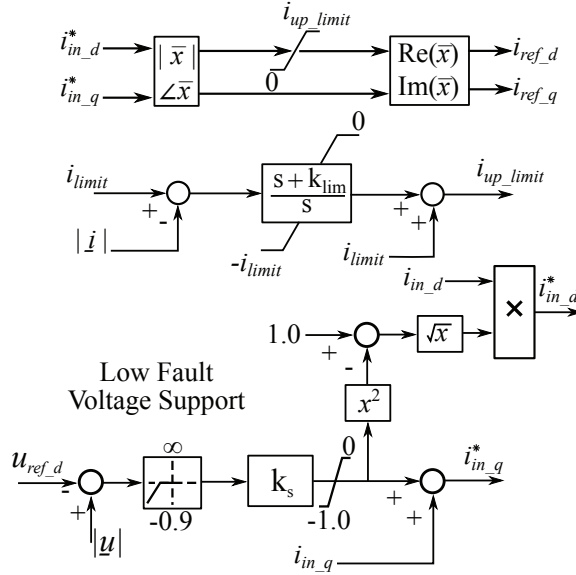
Figure 5.12: The over limit current control of HVDC transmission system offshore side voltage source converter.

limits reached, the positive feed-forward network current signal (i_{nd}, and i_{nq}) impose the reference current command during fault. As analyzed in Section 5.4, the VSCs current with angle 0.0 deg improves the voltage angles when the fault impedance is higher compare to the series cable impedance. In order to simplify the control scheme, the control of the VSC current angle is based on the voltage dip at the filter bus instead of equivalent impedance measurement. The analysis shows that the fault impedance can be considered higher than the cable series impedance up to the voltage drop of 0.1 p.u, thus in this case VSC must injects current with angle 0.0 deg. For voltage drop below 0.1 p.u, converter must injects current with -90 deg angle. The control scheme for low fault voltage is shown in Figure 5.12. The value of the k_s can be adjusted between 10 to 25 p.u depending on the amount of maximum reactive current demand at low voltage.

In normal operation, the output of the voltage PI controller is zero for successful reference signal tracking, however the integral output limits can be set such as to allow the margin for voltage control during transient period. These limits can be adjusted according to the reactive power in the system

Figure 5.13: Frequency control power limit with droop control for offshore VSC HVDC system.

e.g. ± 0.4 p.u.

5.5.2 Offshore VSC-HVDC Frequency Control

Typically, the low voltage level in the network is an indication of the short circuit. However in case of one transmission system disconnection (open circuit fault), network AC voltage will rise due to excess energy in the network. In this case, the VSC can communicate using frequency with the wind generation system to indicate the need of reducing power generation up to its maximum export capacity.

The VSC frequency control system in conjunction with droop control is shown in Figure 5.13. The power-frequency droop gain has two components. The first component (k_f) enables the power sharing among VSC-HVDC system during normal condition. The gain k_f is set such that the maximum change in network frequency does not exceed the threshold hold limit in the wind turbines, typically 50.2 Hz. The second gain k_{fs} produces change in the imposed frequency when the network voltage is higher than 0.8 p.u and the actual active power through the converter exceeds operational limits. The gain k_{fs} is set to increase the reference system frequency above the threshold limit of wind turbines. This rise in frequency triggers the active current reduction control in wind generation system, and the steady state

Figure 5.14: Voltage support control scheme of wind generation units.

in the system is achieved at the reduced wind power generation limited up to the export transmission capacity. According to the design setting, the maximum frequency rise is set up to 1.06 p.u.

5.5.3 Wind Generation Short Circuit Control

The wind generation converter output voltage limit is applied in a similar manner by using (5.7). The integral output of the current controller is also set by calculating maximum voltage drop across series reactor at rated power flow using (5.8). The wind generation converter system is operated in a grid synchronous mode and its behavior in the network is as a controlled current source. Therefore, a priority based current limit is applied as expressed by (5.9) and (5.10). The priority is given to the reactive current if the network voltage drop below 0.8 p.u otherwise active current has priority. As per requirement of the grid codes, additional reactive power is injected to support the grid voltage for the voltage deviation of ± 0.05 p.u from the rated voltage. The control scheme for additional reactive power infeed is shown in Figure 5.14.

$$
i_{ref\_d} = \begin{cases} \chi \cdot i^*_{in\_d} & \text{if } |\underline{u}| < 0.8 \wedge |\underline{i}| \geq 1.0 \\ i_{in\_d} & \text{otherwise} \end{cases}
$$

$$
i^*_{in\_d} = \min\left\{ \sqrt{1 - i^2_{in\_q}}, \ |i_{in\_d}| \right\}, \quad \chi = \begin{cases} 1 & \text{if } i_{in\_d} > 0 \\ -1 & \text{if } i_{in\_d} < 0 \end{cases}
$$

$$(5.9)$$
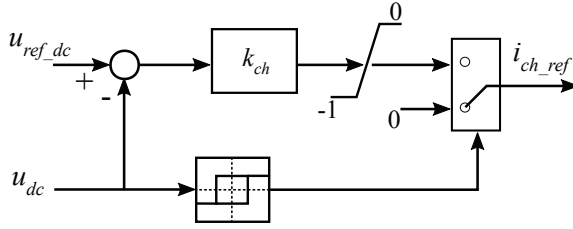
Figure 5.15: Chopper control scheme to control DC link of wind generation unit during fault.

$$
\begin{aligned}
i_{ref\_q} &= \begin{cases} \nu \cdot i_{in\_q}^* & \text{if } |\underline{u}| > 0.8 \wedge |\underline{i}| \geq 1.0 \\ i_{in\_q} & \text{otherwise} \end{cases} \\
i_{in\_q}^* &= \min \left\{ \sqrt{1 - i_{in\_d}^2}, \ |i_{in\_q}| \right\}, \quad \nu = \begin{cases} 1 & \text{if } i_{in\_q} > 0 \\ -1 & \text{if } i_{in\_q} < 0 \end{cases}
\end{aligned}
\tag{5.10}
$$

During fault, the VSC of wind generation unit no longer controls their corresponding DC link. The chopper control is then activated to maintain the DC voltage. The control scheme to activate the chopper control is shown in Figure 5.15.

Transient stability of the offshore network during fault is improved with the injection of reactive current by the wind turbine. However, active current must be reduced depending on the network voltage to avoid loss of synchronization [117]. The under-voltage dependent active current reduction scheme is shown in Figure 5.16. This scheme also enables the gradual rise in wind energy infeed during post fault state.

5.5.4 Wind Generation Frequency Control

Frequency dependent active current reduction scheme for the wind generation unit is shown in Figure 5.16. The reduction in the wind power generation is based on two quantities i.e the change in the frequency and the rise in the voltages. The offshore AC network that has only VSCs lacks in possessing inertia within it since the DC link in the back-to-back converter of wind
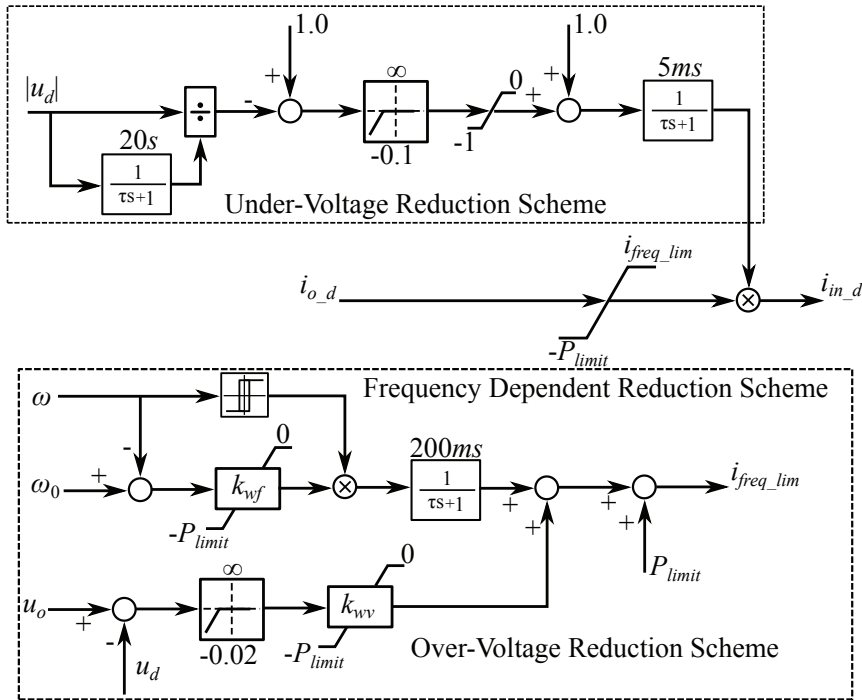
Figure 5.16: Voltage and frequency dependent active current reduction scheme of wind generation unit.

generation units isolate the wind turbine inertia, and the DC connection of VSC-HVDC transmission isolate the inertia of onshore synchronous machines. The abrupt power impacts the network voltages largely compare to the network frequency due to the fast response of converter voltage and current control. Consequently, the voltages in the network will rise faster than the frequency. The rate of change in network frequency depends on the gain of the frequency droop and its maximum value is limited by the stability condition. In the presence of excess active power in the network such as in the case of tripping one VSC-HVDC transmission line, the saturation of current limit in VSC-HVDC system raise the network voltage. In the active current reduction scheme shown in Figure 5.16, the voltage feed-forward path is added which reduces the active current if network voltage rise above 2%. Simultaneously, the active power limits in the VSCs increase the network frequency. The frequency feed-forward path will become dominant after

the network frequency upper limit exceeds i.e 1.004 p.u. Consequently, the current through VSC-HVDC system comes back within its operational limits and reinstates the reference voltage control which enforce the voltages in the network to be within the normal operational limits. The equilibrium in the system will be achieved at reduced wind power generation that would be equal to the export capacity of the transmission line. However, the steady-state network frequency will be higher than the nominal frequency. In case of over frequency in the network, the change in network frequency can be calculated using wind power frequency dependent reduction and the VSC frequency droop scheme. In the offshore AC network, the sum of all the wind turbine power is equal to the sum of the power received by the in-service VSC-HVDC transmission systems. Thus, the condition given in (5.11) must be satisfied.

$$\sum_{n=1}^{z} p_n + \sum_{m=1}^{y} p_m = 0 \tag{5.11}$$

Here, y is the total number of in-service VSC-HVDC system, z is the total number of wind generation system, p_n is the active power of nth wind generation unit, and p_m is the active power of mth VSC-HVDC system. The frequency droop control equation of mth VSC-HVDC system can be defined as (5.12) as illustrated in Figure 5.13.

$$\omega_m = \omega_0 - (k_{f\_m} + k_{fs\_m}) \, p_m \tag{5.12}$$

Note that all the impose frequencies by each VSC-HVDC system will be equal to network frequency at steady-state, then the active power for m^{th} VSC-HVDC system can be defined as (5.13).

$$\omega_1 = \omega_2 = \cdots = \omega_m = \omega$$
$$p_m = \frac{\Delta\omega}{k_{f\_m} + k_{fs\_m}} \qquad \because \Delta\omega = \omega_0 - \omega \tag{5.13}$$

The frequency dependent wind power reduction control equation of nth wind generation unit can be defined as (5.14).

$$p_n = P_{limit\_n} + k_{wf\_n}\Delta\omega \qquad \because \Delta\omega = \omega_0 - \omega \qquad (5.14)$$

By substituting (5.13) and (5.14) in (5.11), the per unit change in the network frequency can be calculated as

$$\Delta\omega = -\frac{a \cdot \left(\sum\limits_{m=1}^{y} \dfrac{1}{k_{f\_m} + k_{fs\_m}}\right)^{-1} \sum\limits_{n=1}^{z} P_{limit\_n}}{1 + a \left(\sum\limits_{m=1}^{y} \dfrac{1}{k_{f\_m} + k_{fs\_m}}\right)^{-1} \sum\limits_{n=1}^{z} k_{wf\_n}} \qquad (5.15)$$

Here, $a = S_b^{wind}/S_b^{vsc}$ and it is a ratio of base power of wind generation and VSC-HVDC system, k_{f_m} and k_{fs_m} are the frequency droop gains of VSC for normal and disturbance period in p.u respectively, k_{wf_n} (p.u) is a power reduction gain of wind generation system, P_{limit_n} (p.u) is the maximum active power limit of wind generation system. Furthermore, this rise in the network frequency can then be reduced through central command system using communication signal.

5.5.5 Onshore VSC Short Circuit Control

Onshore side converters are operated in grid synchronous mode synchronized with the onshore grid frequency. The onshore converter injects the received offshore power into the grid by controlling the DC voltage. Its short circuit control is mainly based on the principle of limiting the converter output voltage and current as shown in Figure 5.5. The maximum peak value of the VSC output voltage is determined using PQ analysis as explained in Section 5.3. The upper voltage limit is applied using (5.7) and the lower limit is set to zero. The output of the current PI regulator correspond to the voltage drop across the series reactor thus the output limits of the PI regulator is calculated using (5.8). The current control is the basic operational mode of the onshore VSC in both normal and short circuit condition therefore the limits on the reference current signals are applied based on the priority scheme. On exceeding the current operational limits, the priority is given to reactive current if voltage drop below 0.8 p.u otherwise

active current has priority. These current limits are applied by using (5.9) and (5.10).

The output of the DC voltage outer controller defines the reference current *d*-component and the AC voltage outer controller output defines reference current *q*-component. The saturation limit values on these controllers output are determined from Figure 5.7d. During fault, the outer control loop is isolated due to current limits consequently converter no longer controls the DC voltage. In this condition, the DC chopper is activated to dissipate the excess energy in the DC link.

5.6 Simulations and Results

The methodology and control system is validated by performing nonlinear simulation of the network shown in Figure 5.1. The network is modeled in Simulink environment using SimPower blockset. There are five locations within the network where faults have been applied for the analysis. First fault is applied at the MV busbar in the wind power plant. Second fault is applied at the HV busbar in the offshore AC network. Third fault is applied on the interconnecting cable that connect VSC-1 and VSC-2 at the voltage level of 150 kV. In fourth case, an open circuit fault is applied in the VSC-2. An onshore fault has been simulated as the fifth case study. A resistive three phase symmetrical fault of 1.0 Ω is applied for all fault analysis. In the case studies, different aspects of VSC control for offshore and onshore short circuit has been analyzed such as FRT capability, reduction in voltage phase angle jump during fault, ability to operate split network after fault, and frequency coordination scheme between VSC-HVDC transmission system and wind generation units.

Fault at MVAC Busbar: In this case, a fault is applied at wind power plant busbar at the voltage level of 33 kV. The fault is applied for 100 ms at 5.0 s. The response of the VSC voltage and current is shown in Figure 5.17. It can be observed that the voltage at the reference busbar of both VSCs drops up to 0.4 p.u. In this condition, the VSCs are directed to inject current with the rated peak. As the voltage drop at the reference busbar is above 0.1 p.u,

(a) VSC 1 Reference voltage

(b) VSC 2 Reference voltage

(c) VSC 1 Reference current

(d) VSC 2 Reference current
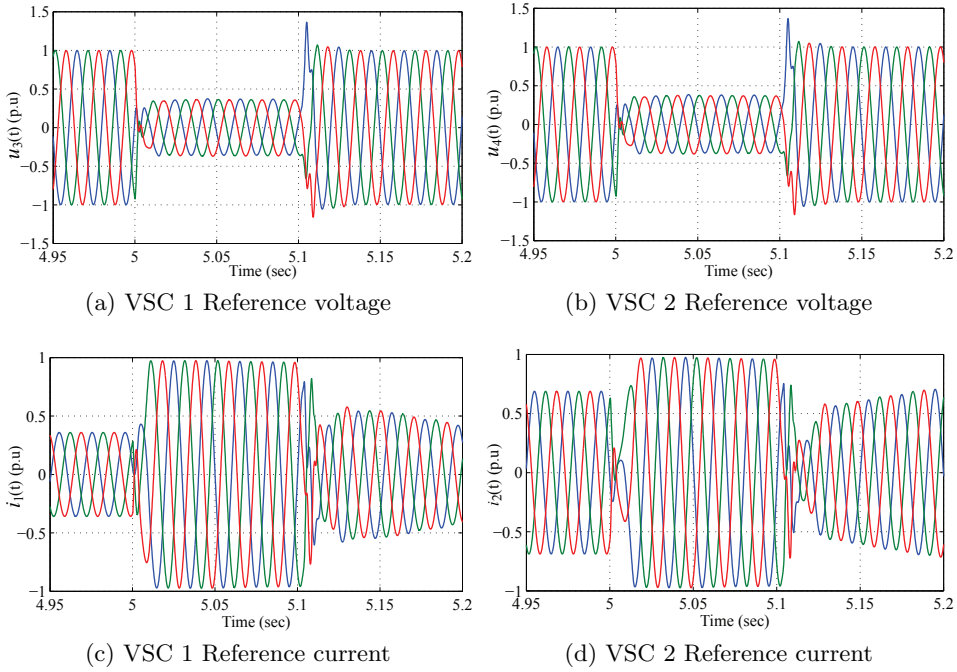
Figure 5.17: Short circuit response of VSC 1 and 2 substation currents and voltages for fault at 33kV wind turbine busbar.

the VSC infeed current angle is set to 0.0 rad. It is clear from the result that the voltage response is stable and the voltage recovery is achieved smoothly.

The fault location is considerable far from the VSC-HVDC system and the fault magnitude component in equivalent impedance at the VSC controlling bus is relatively low. In another word, the X/R ratio at the VSC controlling bus is same during pre-fault and fault state. This will produce less voltage phase jump. In Figure 5.18, the comparison of VSCs connecting busbar voltage angle has been made with respect to the VSC current infeed. The voltage angle during fault remains near to the pre-fault state with the infeed current angle of 0.0 rad, and the system remains stable in post fault state. The VSC-1 voltage angle is 0.45 rad during fault which is less than $\pi/6$ rad. On the other hand, the voltage angle deviates significantly from its pre-fault state with the infeed current of $-\pi/2$ rad. The VSC-1 voltage angle during fault is now near to -0.95 rad which is less than $-\pi/6$. This voltage angle

(a) VSC-1 connection bus voltage angle

(b) VSC-2 connection bus voltage angle
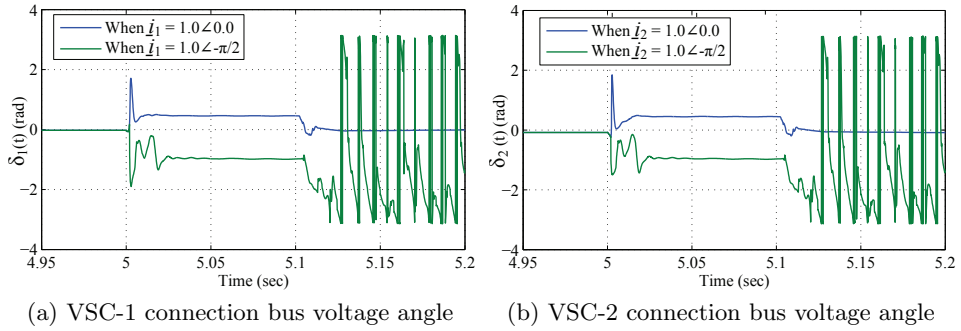
Figure 5.18: VSC 1 and 2 substation voltage phase angles for fault at 33kV wind turbine busbar.

rise above the limit of $\pm\pi/6$ rad has made system unstable in the post fault state.

Fault at HVAC Busbar: In this case, a fault is applied at the transformer busbar at 150 kV. The short circuit voltage response of the VSCs and the wind generation unit is shown in Figure 5.19. The VSC-1 reference bus voltage drop up to 0.05 p.u as shown in Figure 5.19a. In this condition, the VSCs injects current of rated peak with current angle of $-\pi/2$ rad. The voltage response shows a stable operation of the system during fault and post fault state. The wind generation units also inject reactive current during fault which supports the network voltages. The wind turbine busbar voltage is 0.1 p.u as shown in Figure 5.19b.

Furthermore, the comparison can be made in the response of the VSCs connection busbar voltage angle with respect of VSC current infeed angle as shown in Figure 5.19c, and Figure 5.19d. It is clear that the voltage angle increases significantly when the VSCs current angle is $-\pi/2$. In this case, the VSC-1 voltage angle is near 1.378 rad, and the VSC-2 voltage angle is 1.278 rad. On the other hand, the voltage angle is near to 0.0 rad with the current angle of $-\pi/2$. From the simulation results, it can be concluded that the network voltage level during fault is based on the amount of the current injected by the VSCs and the wind turbines. It is recommended that all the generation units must inject current up to their maximum capability.

(a) VSC 1 reference bus voltage

(b) Voltage at wind turbine busbar

(c) VSC 1 connection bus voltage angle

(d) VSC 2 connection bus voltage angle
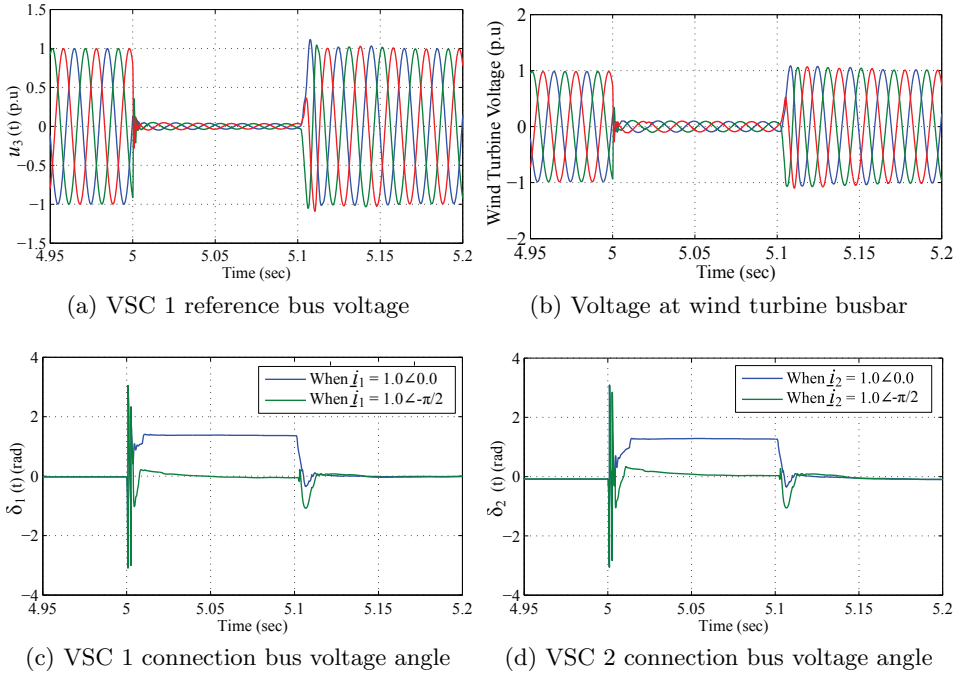
Figure 5.19: Voltage short circuit response of 150kV busbar fault.

Furthermore, the proposed short circuit scheme to mitigate the voltage phase angle jump ensure that the phase angle remains near to its pre-fault state. The analysis conclude that the VSC-HVDC transmission system offshore converters current angle must be controlled according to the voltage drop in order to ensure the network stability during fault and post fault state.

Fault at HVAC Cable: The reference frequency control of the offshore AC network through more than one VSC-HVDC transmission systems not only enable the trade between onshore grids but it can also operate two isolated networks as well. To demonstrate such ability, a fault has been applied on the cable that interconnects two VSC substations in the offshore network. The length of the cable is 12 km. A permanent fault is applied at 5.0 s and the AC circuit breaker at both ends of the cable is opened after 100 ms. After fault isolation, there are two isolated networks. After isolation, wind power plant 1 and 2 are connected with VSC-1 and the net power of these

(a) Frequency response

(b) VSC 1 current response

(c) VSC 2 current response

(d) Wind turbine current
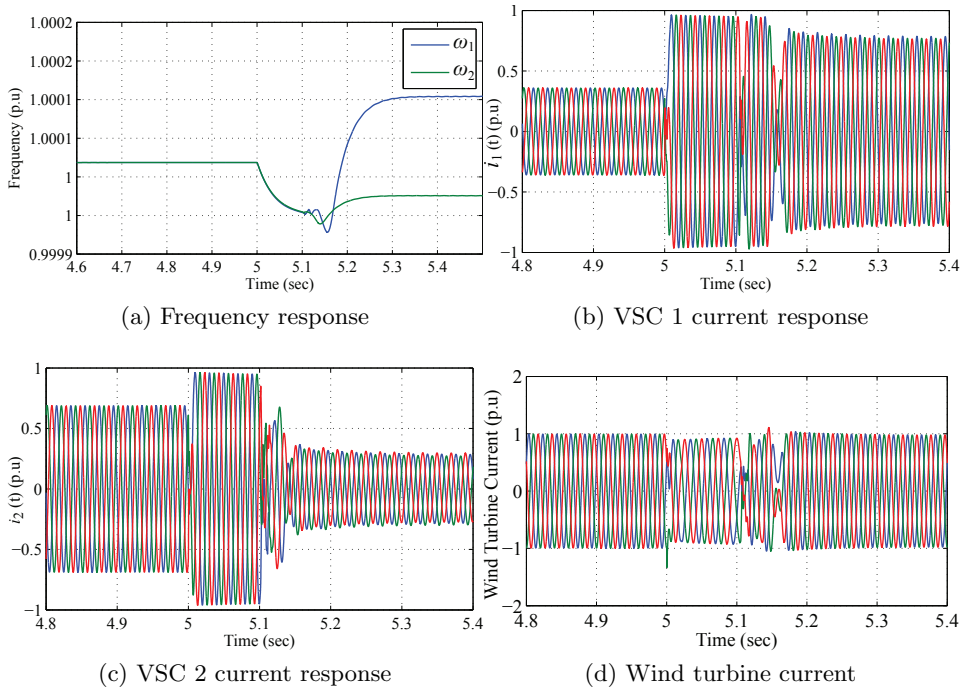
Figure 5.20: Frequency and current short circuit response of 150kV HVAC cable fault.

two wind power plants are transferred to country A. And VSC-2 is connected to only wind power plant 3 and country B now receives all the power from it. The short circuit response of this case study is shown in Figure 5.20.

The frequency response shown in Figure 5.20a demonstrates the ability of the converters to be operated individually and the network is restored to its normal condition. It can be noticed that the frequencies imposed by both VSCs converge at the same value in pre-fault state, and the VSCs are imposing different frequency in post fault state. The frequencies in post fault state depend on the frequency droop gain value and the amount of active power flow through each VSC. The network power balancing can be visualized through the current response of VSC-1 and VSC-2 as shown in Figure 5.20b and Figure 5.20c. In the pre-fault state, the VSC-1 is receiving 0.34 p.u active power and VSC-2 is receiving 0.69 p.u active power of the total wind power plants power. These sharing of active power is according to the

frequency droop gain values which is based on the steady-state operational requirements. Note that the combined wind active power is greater than one VSC-HVDC transmission system.

During fault, both VSCs inject current with rated peak. In the post fault state, the VSC-1 is now receiving 0.77 p.u active power, and the VSC-2 is transmitting up to 0.26 p.u active power to country B. This indicates that the network has been restored and it can still be operated after isolation between them. Furthermore, the fault-ride-through capability of the wind generation unit can be seen from the current response shown in Figure 5.20d. It is clear that the system has stable response and wind generation units continue to be operated in fault and post fault state without any interruption.

VSC-2 Open Circuit Fault: As stated before, the combined active power of wind power plants is greater than a single VSC-HVDC transmission system i.e 120 MW. Thus in case of fault in one VSC-HVDC transmission line, the wind generation unit needs to reduce their active power production according to the limits of in-operational VSC-HVDC transmission line. The control of such scenario has been validated by opening a circuit breaker connected at 150 kV side of VSC-2 substation transformer. The response of this case study has been shown in Figure 5.21. In the simulation, VSC-2 has been disconnected at 15.0 sec from the offshore AC network.

After the disconnection of the VSC-2 substation, the active power in the offshore network become greater than VSC-1 export capacity which exceed the VSC-1 power and current limits. The voltages in the network will rise due to the VSC current limitation and high active power in the network. The VSC-1 frequency droop scheme will also increase the network frequency, however the rate of change of frequency will be lower than the rate of change of voltage. This can be observed from the VSCs frequency response shown in Figure 5.21a and from the voltage response shown in Figure 5.21b. In order to activate the active current reduction control in the wind generation units, the threshold limit of the frequency is set to 1.004 p.u which is reached in 1.0 s and over-voltage limit is 1.02 p.u which reaches instantaneously. In first phase of power reduction scheme, the active power in the wind turbines are reduced through over-voltage active current reduction control.

(a) VSC 1 and 2 frequency response

(b) VSC 1 and 2 voltage response

(c) VSC 1 and 2 power response

(d) Wind turbine power response
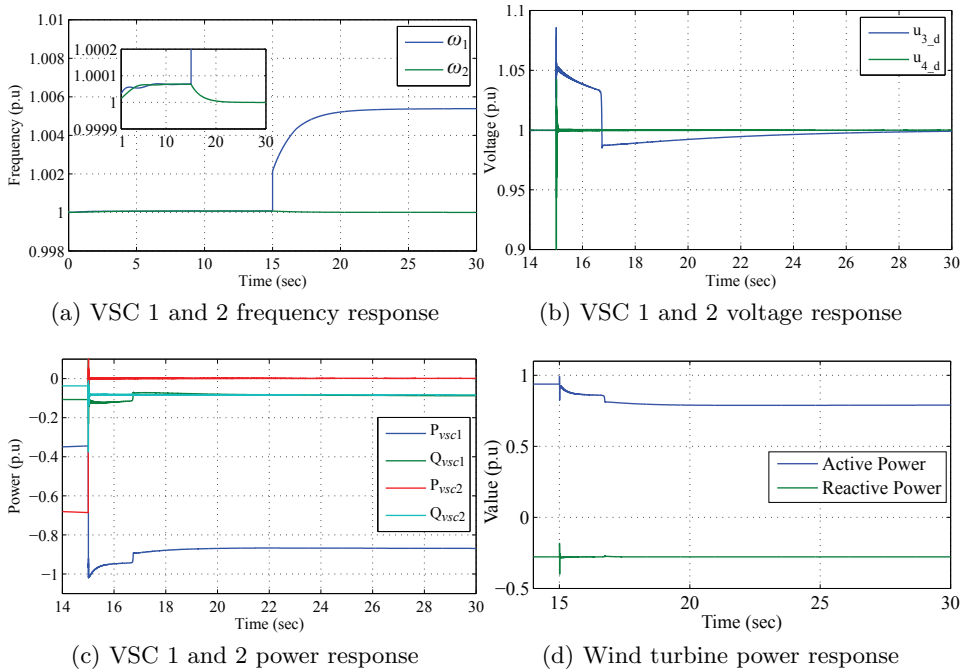
Figure 5.21: Response of the offshore AC network in the event of VSC 2 substation disconnection.

As the frequency threshold limit in the wind turbines reaches, the frequency dependent active current reduction control is activated and supersedes the over-voltage control. This can be seen from the power response of the VSCs shown in Figure 5.21c. Furthermore, once the active power flow through the VSC-1 drops below its limits, the voltage control is resumed and the network continues its operation at the reduced wind power generation. It can be observed from Figure 5.21d that the wind generation unit has reduced its generation according to the export capacity of the VSC-1 transmission line.

Onshore Fault: In this case study, an onshore fault has been simulated and the capability of the onshore converter of HVDC transmission system is evaluated. The short circuit response of the network is shown in Figure 5.22. In the event of the onshore voltage drop, the onshore VSCs provides the fault ride through capability and stays connected up to few milliseconds. The

(a) Onshore VSC filter bus voltages

(b) Current injected by onshore VSC

(c) DC voltage at onshore and offshore DC bubar

(d) Active and reactive power response of VSC-1 (offshore)
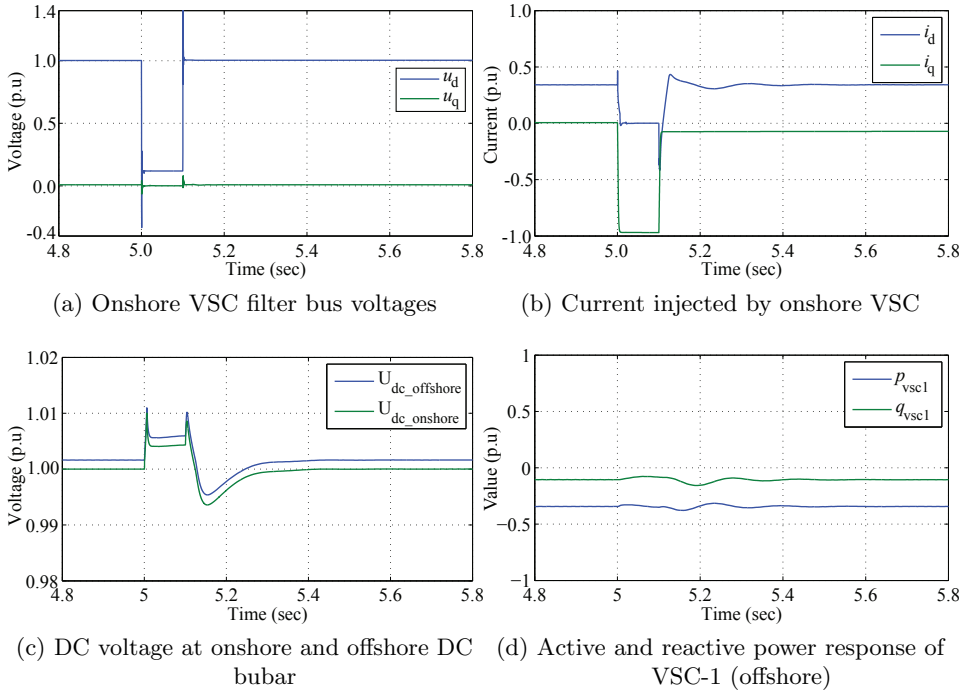
Figure 5.22: The network short circuit voltage and current response of the fault applied at country A onshore grid.

DC voltage of the HVDC transmission system is then controlled through a chopper that dissipate energy through the DC resistor.

To evaluate the onshore converter short circuit control system, the country-A onshore grid voltage is dropped to 0.1 p.u at 5.0 s for 100 ms. The response of the onshore VSC voltage in $dq0$ frame is shown in Figure 5.22a. Typically, it is defined in the transmission system grid code that the generation units must inject reactive current during fault to support the grid voltage. In this regard, the onshore VSC injects the reactive current which can be observed from Figure 5.22b. It can be seen that the current d-component reduces to zero and the q-component is increased for maximum reactive current injection. In the post fault state, both current components are restored as fast as possible in order to maintain the network stability. The DC voltage response at both ends of the DC cable is shown in Figure 5.22c. Since the PI

control of the onshore VSC DC voltage control is isolated during fault, the DC voltage is no longer controlled to 1.0 p.u. Instead the chopper control, which is like a proportional controller, maintain the DC voltage. It can be seen from the DC voltage response that the voltages remain with in the limit at both ends. Although, the offshore VSC has DC voltage independent control scheme but the ability of a converter to generate AC output voltage depends on the DC voltage. The variation in the DC voltage may appear on the AC output voltage consequently effect the power flow through the VSC. This can be observed through the power response of VSC-1 shown in Figure 5.22d. These variations can be minimized by increasing the stiffness of the offshore VSC voltage control.

5.7 Summary

This chapter presents the control system of the VSC-HVDC system for an offshore AC network for normal and short circuit operation. The offshore AC network is created by two VSCs using frequency and voltage droop control schemes. During short circuit, both VSCs inject current up to their maximum capability. It has been concluded that the VSCs must inject active current to ensure the system stability for the fault voltage above 0.1 p.u. Furthermore, the reactive current injection by the VSCs improves the network voltages for low voltage fault and keeps the network bus voltage angle near to pre-fault state. Through simulation, it has been proven that the control of the offshore AC network reference voltage and frequency via more than one VSC-HVDC system provides operational redundancy and the network can still be operated if isolation occurs between VSC-HVDC systems. Furthermore, the proposed coordinated control ensure the continuous operation of the network at reduced export capacity. The presented study and proposed control system can be a useful tool for establishing offshore grid codes.

6 Analysis of Hybrid AC/DC Offshore Grid

The focus of this chapter is on the application of integrating an offshore AC grid with an offshore DC grid. The future 'SuperGrid' may require the benefit of both offshore AC network and MTDC grid. To analyze the integrated AC and DC network, first the basic principle of the MTDC network control is discussed. Later, the aspects of the MTDC operation are addressed with respect to the VSCs ability to control the wind power distribution. The DC voltage droop control is applied for the distributed control of the MTDC network. The active power infeed into onshore grids has fluctuation according to the wind variation. In order to flow the constant power between onshore grids via offshore MTDC network, the dead-band droop control scheme is implemented in the onshore VSCs control system. The network operational principle has been demonstrated using nonlinear simulation. In the end, the operation of the combined offshore AC network and MTDC network is demonstrated.

6.1 Introduction

An efficient, economical, and reliable offshore wind power plant transmission system has utmost importance for the development of the future 'SuperGrid' [118]. The selection between the HVAC or HVDC transmission for the offshore wind power plant connection mainly depends on its distance from the shore and the installed capacity [119]. For the long distances, HVDC transmission system has preference over HVAC cables since the latter has higher losses and requires additional reactive power compensation. The offshore wind power plants located within the distance of 60 km from
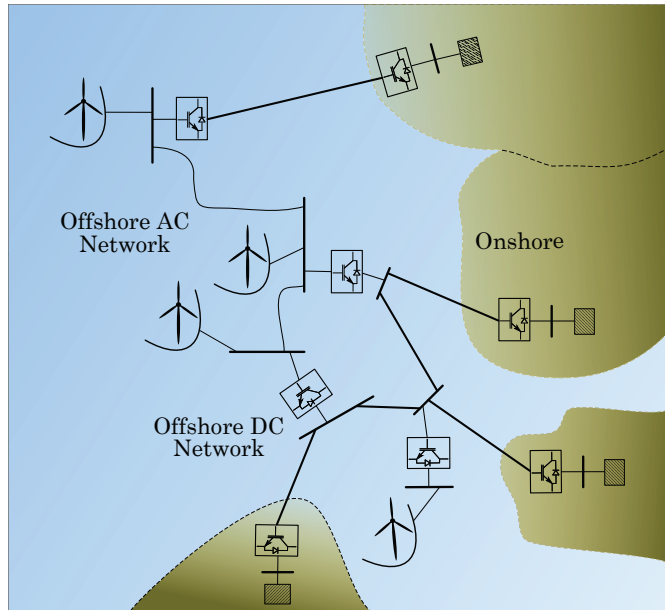
Figure 6.1: Offshore AC and DC grid interconnection with the onshore grids.

the shore are individually connected with the HVAC cables [21]. Longer connection also possible using HVAC cables by having multiple intermediate AC compensating stations [120, 121]. Wind power plants integration through AC hub is an alternative configuration instead of installing intermediate AC compensation. The offshore wind power plant integration with the offshore AC hub is economically suitable if it has distance less than 20 km. This benefit reduces as the distance increase, and it provides no economical advantage beyond 40 km [90]. The power from the offshore hub is transmitted to shore via VSC-HVDC transmission system either in point-to-point or multiterminal (MT) configuration [11, 100]. An example of offshore AC and DC grids integration is shown in Figure 6.1. Apart from integrating offshore AC hub with the grids, wind power plant far from both shore and AC hub can be connected through HVDC systems and an individual connected wind power plant with the grid can also be connected to AC hub using HVAC cable. Here, there are two main aspects: an integration of offshore wind energy with several onshore grids, and the energy trade between onshore grids. An integration via point-to-point VSC-HVDC system requires the

(a) Master-Slave Principle

(b) Voltage Margin Principle
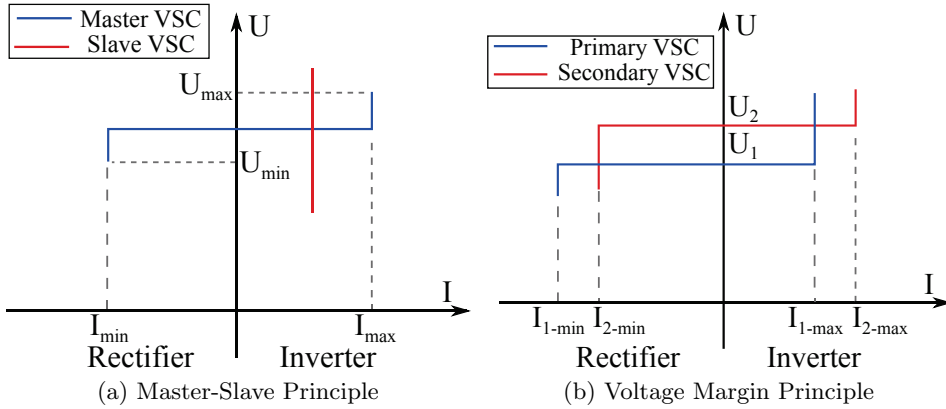
Figure 6.2: The characteristic curve of master-slave and voltage margin control principle.

wind power plant size equal or less than converter capacity and the power is only transfer to one onshore grid. These limitation are overcome by forming offshore AC network which transfer the power to different onshore grids from several offshore wind power plants. In such a network, although the sum of VSC-HVDC systems rated power should be equal or greater than the total power in the offshore AC network, the individual VSC-HVDC rated power is not necessary to be equal to the total power in order to make full use of the offshore wind generation. The control and operational principle of such network is explained in previous chapters. The energy can be traded between onshore grids via offshore AC network, however, it may produce unnecessary losses in the offshore converters and AC cables. To avoid these losses, a VSC based MT-HVDC transmission system is suitable for energy trade between countries [122].

The successful operation of the DC network requires that at least one of the converter must control the DC voltage. In the point-to-point configuration, the DC voltage is usually controlled by onshore converter [123]. The concept of DC voltage control by one converter and operating other converters in current or power control mode can be extended for MTDC system. The converter controlling DC voltage is typically referred as master and the remaining converters are called slaves [124]. The characteristic curve of

(a) Onshore VSC Control

(b) DC voltage control with proportional regulator

(c) Stability model of DC voltage with proportional regulator
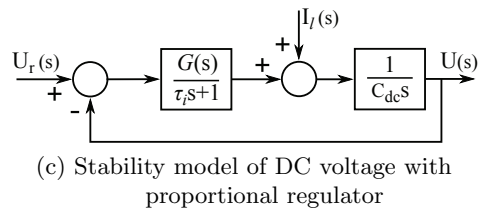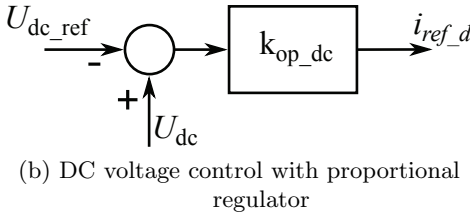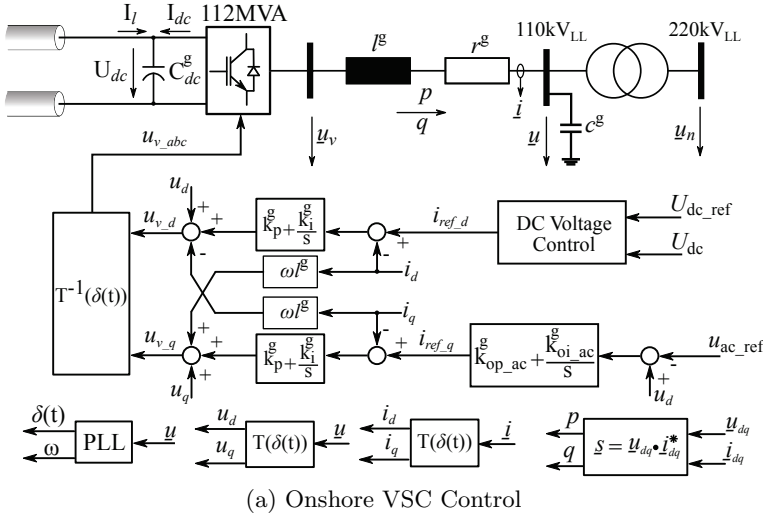
Figure 6.3: Onshore VSC substation and its control scheme for MTDC network.

master-slave control is shown in Figure 6.2a. This control principle has two main limitations. Firstly, the capacity of the master converter must be equal to the sum of the slave converters. Secondly, a communication system is required in order to make any slave converter to master in case the master converter become malfunction. The reliability of this control principle is very low and highly depends on the communication signal. In order to increase the reliability, more than one converter can be set to control the DC voltage with some voltage set-point margin [125]. Typically such scheme is known as margin voltage control [56]. The characteristic curve of the voltage margin control is shown in Figure 6.2b. In this scheme, master converter has main responsibility to control the DC voltage in normal condition and others are working in constant current mode. In case of exceeding master converter power limits, the voltages in the network start rising and reaches

voltage threshold limits at the slave converter busbar, hereby enforcing slave converter to regulate DC voltage instead of current [126]. In this control scheme, it is important that the master converter voltage set-point must be less than the slave converter threshold limit. As a disadvantage, the voltage margin control only allow fixed power sharing and it needs several control loops which make the voltage regulation slower [57].

Usually, any DC voltage regulation that requires communication at some extent are considered as centralized control system. A decentralized control system such as droop control increases the controllability and reliability in the system. The principle of the droop control is similar to the frequency regulation in the AC system. In this control scheme, all or selected onshore converters in the MTDC offshore network can have the droop control in order to control the DC voltages. In the droop control, the change in DC power received by the converter proportionally changes the DC voltage. For a stiff voltage control, the net power in the offshore DC grid can then be shared among onshore converters by adjusting the slope of the droop values. Furthermore, the network can be operated even if one or more onshore converters malfunction [127].

6.2 Multiterminal VSC-HVDC System

In the MTDC system for the offshore wind integration, all the onshore side VSCs can be set to control the DC voltage. A concept of the DC voltage control of VSC in point-to-point configuration is explained in Section 2.3. Usually, the DC resistance in the network is relatively small even for long cables (e.g 0.019 Ω/km). The DC voltage control using proportional-plus integral (PI) regulator in the MTDC system makes VSCs to react as voltage sources connecting in parallel at the common bus with very low equivalent resistance. This could cause large active power flow among them and lead system into instability. Thus, a proportional (P) control can be applied instead of PI regulator for DC voltage control. A proportional controller does not enforce the bus voltage at the given set-point rather the error in the voltage from the set-point enable the balancing of the network through multiple VSCs. The modified onshore substation and its control system is
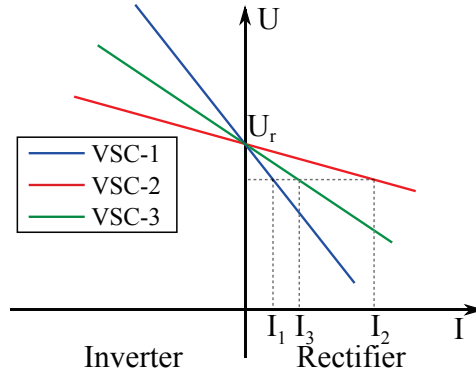
Figure 6.4: U-I characteristic of onshore VSCs DC voltage control to operate MTDC network.

shown in Figure 6.3 for MTDC network.

The feed-forward network current input (I_l) is removed to control with only voltage feedback signal to avoid conflict between VSCs in MTDC configuration. Note that the summation sign shown in Figure 6.3b are reversed to adjust the sign convention between DC and AC network. The closed loop transfer function can be derived from the stability model of the DC voltage control of a VSC given in Figure 6.3c.

$$U(s) = \frac{G(s)U_r(s) + (\tau_i s + 1)I_l(s)}{C_{dc}\tau_i s^2 + C_{dc}s + G(s)} \tag{6.1}$$

Here, τ_i is the time constant of the current closed loop, C_{dc} is the DC capacitance, $G(s)$ is the DC voltage controller, $U_r(s)$ is the voltage set-point, $I_l(s)$ is the network current, and $U(s)$ is the output voltage. Note that the closed loop transfer function given in (6.1) represents a single VSC DC voltage control dynamics. The stability conditions of only one VSC controlling DC voltage in the DC network are: $\tau_i > 0$ and $k_{op\_dc} > 0$. Using (6.1), the steady-state DC voltage equation of a VSC can be determined by setting all the derivatives to zero i.e $s \to 0$.

$$
\begin{aligned}
U(s) &= U_r(s) + \frac{1}{k_{op\_dc}}I_l(s) \quad \because G(s) = k_{op\_dc} \\
U(s) &= U_r(s) - \frac{1}{k_{op\_dc}}I_{dc}(s) \quad \because I_l(s) + I_{dc}(s) = 0
\end{aligned} \tag{6.2}
$$

It is clear from (6.2) that the DC voltage control now exhibit a droop characteristic. The U-I characteristic of the three onshore VSCs DC voltage control is shown in Figure 6.4. The proportional gain for the DC voltage control act as a slope (droop gain) of the U-I curve. By selecting the appropriate gains, the current or power distribution among VSCs can be controlled [128]. Note that the illustration of the U-I characteristic is ideal and the resistance of the DC network is neglected. The DC cable resistance also affects the power sharing criteria therefore an optimum power flow (OPF) algorithm is required to determine the steady-state operating point and the desire droop gains.

6.2.1 Droop Gain Selection

The droop gains can be selected within the stable operational range based on the DC network power flow solution and the steady-state power sharing criteria. The steady-state solution of the DC network can be found using current flow equation. Using (6.3), the load bus current injection can be defined.

$$I_i = \sum_{\substack{j=1 \\ j \neq i}}^{n} G_{ij} \left(U_i - U_j \right) \tag{6.3}$$

Here, I_i is the current injected at the ith DC bus, n is the total number of the DC busbar in the network, U_i is the voltage of ith DC bus, U_j is the voltage of jth DC bus, and G_{ij} is the conductance between DC bus node i and j.

The VSC controls the DC voltage therefore its busbar can be designated as slack or reference bus possessing the droop characteristics. The DC slack bus voltage equation can be defined by using VSC control equation i.e.

$$U_k = U_0 - m_k I_k \tag{6.4}$$

Here, k is the index of the DC bus connected to the onshore VSC, U_0 is the rated DC voltage, m_k is the slope of the U-I characteristic of kth VSC, and I_k is the kth VSC current.

The OPF algorithm can be implemented using MATLAB function 'fmincon' using interior-point method to solve the network equations. The network equations are applied as equality constraints. Further, the OPF algorithm provides the network voltages and currents as the results. The slope of the droop (m_k) can also be determined based on the current sharing criteria among onshore VSCs. The current of the kth VSC can be written as the sharing factor of the total current received by all the DC voltage control VSCs.

$$I_k = \alpha_k I_{tot} \tag{6.5}$$

Here, α_k is the current sharing factor of kth VSC, and I_{tot} is the sum of all the VSC current that has droop characteristic. For any z converters controlling DC voltage, I_{tot} can be calculated as

$$I_{tot} = \sum_{j=1}^{z} I_j \tag{6.6}$$

By substituting (6.6) in (6.5), the current sharing equation can be defined for any k^{th} DC voltage controlling VSC as given in (6.7). Furthermore, the sharing factor must satisfy the condition given in (6.8).

$$(1 - \alpha_k) I_k - \alpha_k \sum_{\substack{j=1 \\ j \neq k}}^{z} I_j = 0 \tag{6.7}$$

$$\sum_{j=1}^{z} \alpha_j = 1 \tag{6.8}$$

The state variables of the OPF algorithm can be defined as

$$x = \left[U_1 \cdots U_n, I_1 \cdots I_z, m_1 \cdots m_z \right] \quad \therefore k_{op\_dc\_z} = \frac{1}{m_z} \tag{6.9}$$

Note that the VSC voltage controller proportional gain is the reciprocal of the droop gain, and the OPF algorithm only provides the solution based on the steady-state requirements. Therefore, the upper and lower boundary of the state variables must be defined by considering their stable operational

Figure 6.5: Offshore multiterminal HVDC network.

range. The boundary limits of the droop slope can be determined by dynamic and stability analysis of the MTDC system [58]. Furthermore, the least square voltage deviation can be defined as the objective function for the optimization problem i.e.

$$\min \{f(x)\}$$
$$f(x) = \sum_{i=1}^{n} (U_i - 1.0)^2 \tag{6.10}$$

Case Study:

A MTDC network integrating three wind power plants with three onshore grids is shown in Figure 6.5. The control of the offshore VSCs of HVDC transmission systems are set to grid forming mode as explained in Section 2.4. The grid forming mode of VSC is usually the DC voltage independent control within the stable operating range. Also, these VSCs inject the active power received from the wind power plants into the DC network. Therefore, the DC

Table 6.1: MTDC network operational scenarios and voltage controller gains

Cases	α_1	α_2	α_3	I_{w1} (p.u)	I_{w2} (p.u)	I_{w3} (p.u)	k_{op_1} (p.u)	k_{op_2} (p.u)	k_{op_3} (p.u)
Case-I	0.33	0.33	0.34	0.88	0.88	0.88	427.36	783.91	575.05
Case-II	0.50	0.50	0.00	0.50	0.50	0.50	293.86	329.11	0.00
Case-III	0.10	0.30	0.60	0.50	0.50	0.50	19.74	86.17	385.45

buses connected to the offshore VSCs can be designated as load bus in the OPF algorithm. All the onshore VSCs have voltage droop characteristic and try to regulate the DC voltage as explained previously. In the DC network, the DC resistance per km of all cables are same i.e 0.019 Ω/km [102]. The DC voltage level is ±150 kV, and the active power transfer capability of each VSCs is 100 MW. The results are in the base power of VSC rated power i.e 112 MVA.

According to the network configuration, the net active power in the DC grid is three times than a single VSCs active power limits. Therefore, the current or power sharing factor among the onshore VSCs must be equal at the maximum power infeed by the wind power plants. The offshore substation parameters are given in Table 2.1, and the onshore substation parameter are given in Table 2.2 except the value of the DC voltage control proportional gain. The onshore converter DC voltage controller gains is calculated using OPF algorithm as explained in previous section. Three operational scenarios are analyzed to observe the power sharing principle in the MTDC system using droop scheme. The voltage controller gain values are given in Table 6.1 according to the cases. In first case, all the wind power plants are injecting rated power and the power sharing among onshore VSCs is equal. In second case, each of the wind power plants are injecting power half of their rated power. In this case, different power sharing factor can be defined among onshore VSCs. For the analysis, the VSC-1 and VSC-2 both are receiving 50 % of the total active power in the DC network, and VSC-3 is not exporting any power to onshore grid. In the third case, different power sharing factor is assigned to export the power to the onshore grids. The time domain simulation of the network shown in Figure 6.5 is carried out in Simulink using SimPowerSystems.

Figure 6.6: DC current and voltage responses of the MTDC system at $\alpha_1 = \alpha_2 = 0.33$, and $\alpha_3 = 0.34$.

To perform the time domain simulation, a step change in the active power generation of each wind power plants is applied from zero to maximum i.e 0.88 p.u. The power through VSC-4, VSC-5, and VSC-6 into the MTDC system are injected at 5.0 s, 6.0 s, and 7.0 s respectively. The net power in the DC network is 2.64 p.u which is equal to the combined power of onshore converters. For the successful operation, it is necessary that each onshore VSCs must contribute equally in balancing the power in the network. The voltage and current responses for Case-I are shown in Figure 6.6. Note that the generator oriented sign convention is adopted in the results. Here, VSC-1, VSC-2, and VSC-3 are the onshore converters and current sharing factors are defined for them. It can be observed from the current response after 7.0 s that all the onshore converters are sharing current equally according to the designed criteria. Note that the gain value is calculated using OPF at the maximum wind power infeed. Further, the simulation results show that the current sharing is not equal before 7.0 s. The voltages in the MTDC network are not only influenced by the voltage droop but the active power flow also affect them. The impact of the active power flow on the voltages depend on the network resistances, consequently it affect the current sharing among the onshore VSCs. The OPF algorithm provides the droop values by considering the network resistance, therefore the current sharing criteria is fulfilled only
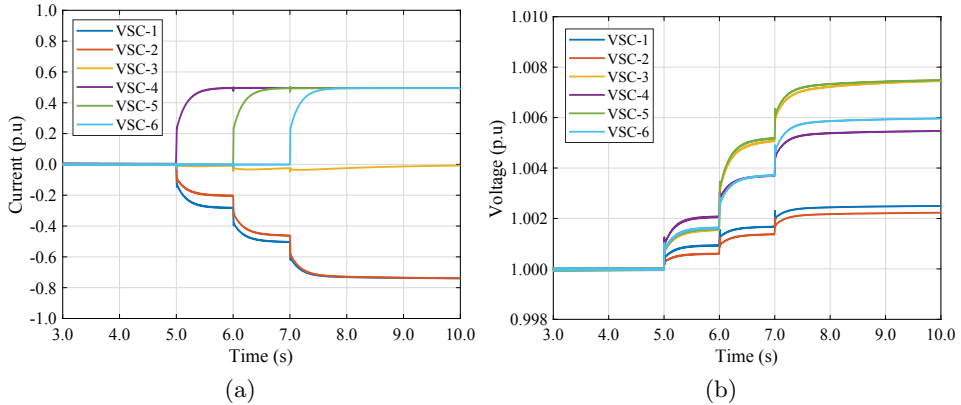
Figure 6.7: DC current and voltage responses of the MTDC network at $\alpha_1 = \alpha_2 = 0.5$, and $\alpha_3 = 0.0$.

at given wind current infeed set-points. As it has been explained before that the proportional gains of the DC voltage control is not only utilized for controlling the sharing of the current but also it must ensure the network stability. It is clear from Figure 6.6b that the voltages are well controlled and each onshore VSCs contribute in maintaining them.

In Case-II and Case-III, the ability of voltage control to share DC current at different factors is analyzed. In order to perform this test, the net active power in the DC network is reduced compared to the combined export capacity of onshore VSCs. In these cases, the step change in each wind power plants is applied from zero to 0.5 p.u. The net power in the DC network is now 1.5 p.u. In Case-II, the current sharing criteria is defined to flow 50 % of net current through VSC-1 and VSC-2 each, and VSC-3 does not contribute in sharing. The current and voltage responses for Case-II are shown in Figure 6.7. The results shows that the current sharing is equal after 7.0 s and the total current is distributed only between the VSC-1 and VSC-2. During transient period, a small current flow through VSC-3 can be observed. The ability of the VSC to generate AC output voltage depend on the DC voltage level. Since the VSC-3 is not controlling DC voltage due to zero proportional gain value, it act as a controlled current source. The DC busbar voltage connected to VSC-3 react as load bus and the voltage at
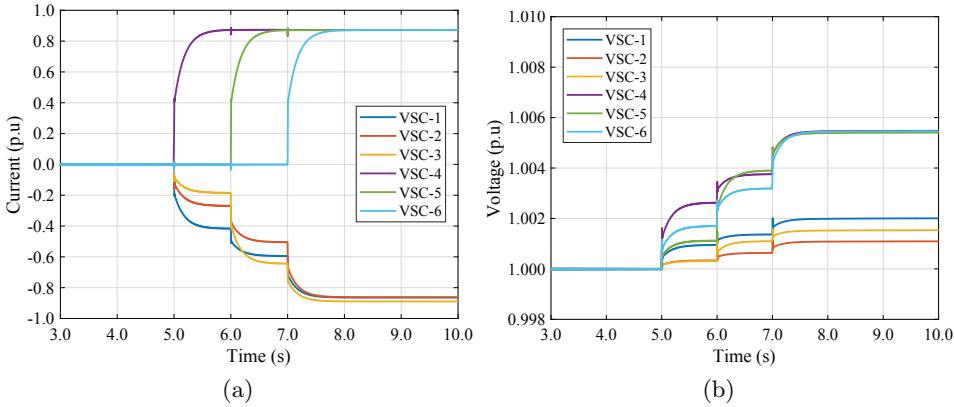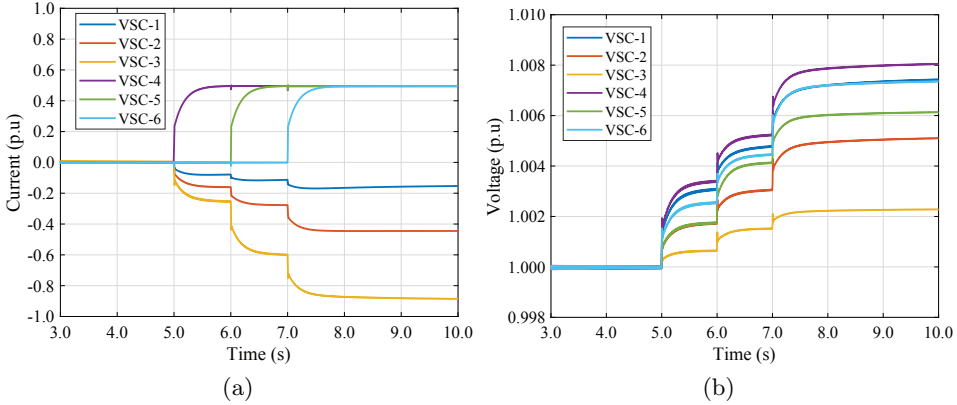
Figure 6.8: DC current and voltage response of the MTDC system at $\alpha_1 =$ 0.1, $\alpha_2 = 0.3$, and $\alpha_3 = 0.6$.

this busbar depends on the network power flow. Any transient in the DC voltage of the busbar connected to the VSC-3 produces change in the output voltage of the converter which generate AC current flow. This current is then consumed or supplied by DC network. Furthermore, the inner current controller will enforce the AC current to be zero due to zero proportional gain value which is achieved after 9.0 s as shown in Figure 6.7a. The response of the voltages for Case-II are shown in Figure 6.7b. It can be observed that the VSC-3 DC bus voltage rises compare to previous cases. Now, the stability in the DC network is ensured by only VSC-1 and VSC-2.

In Case-III, the same wind power infeed condition is applied but the current sharing factor is set differently. Now, the proportional gains are calculated such that the power through VSC-1 flow 10 % of total net power in the network. The VSC-2 and VSC-3 shared 30 % and 60 % respectively. The current and voltages response for Case-III are shown in Figure 6.8. From the current response shown in Figure 6.8a, it can be observed that the VSC-3 now reaches its maximum active current limit i.e 0.89 p.u. According to the network configuration, the sharing factor to VSC-3 cannot be assigned more than 60 % when the net wind power in the network is 1.5 p.u. After 7.0 s, the current flow through VSC-1 is -0.1561 p.u, and the VSC-2 has -0.4448 p.u. The sharing of the current among the onshore VSCs is due to the difference

(a) Droop principle with dead-band characteristics

(b) DC voltage control with dead-band characteristic
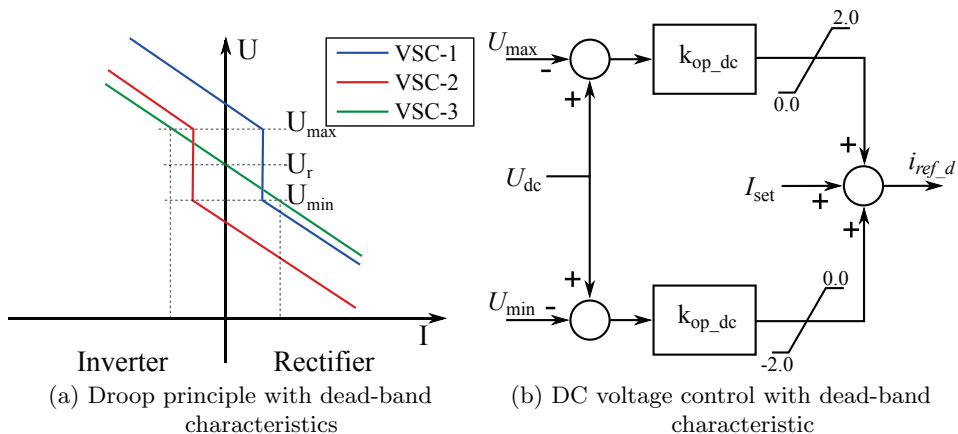
Figure 6.9: The dead-band droop characteristic and its control system.

in the busbar voltages of the VSCs. The change in the network voltages are mainly caused by droop characteristics of voltage controller. While selecting the proportional gain with respect of sharing criteria, it is also important to keep the network voltage within the operational limits. The voltages response shown in Figure 6.8b indicate that the change in network voltages are less than 1.0 %. The results show that the power or current distribution can be achieved through DC voltage controller while maintaining the DC network stability. Also, all the onshore VSCs are controlling DC voltage which provides the redundancy in the MTDC network.

6.2.2 Dead-Band Droop Control

The flow of DC current in the MTDC network can be controlled by adjusting the proportional gain of the DC voltage control as demonstrated in the previous section. Although, the distribution of the wind power infeed among onshore VSCs into the MTDC network is relatively easy but a constant power export is difficult between two onshore grids. A droop principle can be combined with constant current scheme in order to achieve export between onshore grids. This scheme is commonly known as dead-band droop control. The dead-band droop characteristic curve is illustrated in Figure 6.9a. In the MTDC network control principle, at least one of the VSC must have the
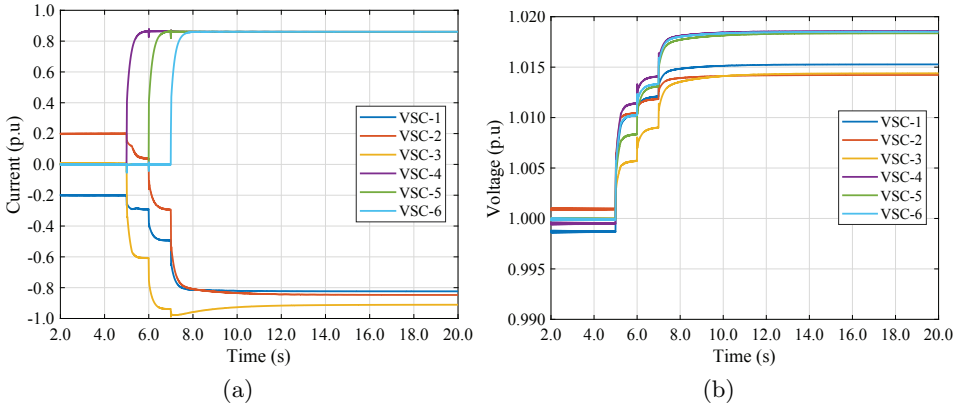
Figure 6.10: DC current and voltage response of the MTDC system with dead-band droop control.

droop control in order to balance the network, and one or more VSC can have dead-band droop characteristics. In the dead-band droop scheme, the VSC control the current or power at the set point within the DC voltage boundary i.e U_{max} and U_{min}. As soon as the DC voltage exceeds the voltage limits, the VSC start contributing in the control of DC voltage with droop characteristics. In the droop region, the contribution of each DC voltage control VSCs can be adjusted through droop gain.

The control implementation of dead-band droop characteristic is shown in Figure 6.9b. In normal condition, the VSC control the current at the pre-defined set-point (I_{set}). With rise in the DC voltage above the maximum limit (U_{max}), the output of the upper loop path is added up in the regulation of current loop reference set-point. Similarly, the output of the lower loop path is added up in the current regulation for DC voltage below the minimum limit (U_{min}). Both paths changes the VSC current set-point using proportional regulator.

The dead-band control operation is simulated on the MTDC network shown in Figure 6.5. The VSC-3 is controlling the DC voltage with droop control hereby acting as a main source to balance the DC network. The DC voltage control of VSC-1 and VSC-2 have dead-band droop characteristic. According to the setting, the upper limit of DC voltage is 1.01 p.u and

the lower limit is 0.99 p.u. The gain values of the DC voltage proportional control of VSC-1, VSC-2, and VSC-3 are 120 p.u, 250 p.u, and 100 p.u. The current and voltage responses of the system are shown in Figure 6.10. Initially, VSC-2 is set to export 0.2 p.u energy and VSC-1 is set to import 0.2 p.u. In the absence of wind power in the DC network, VSC-3 does not import or export power since the net power is balanced between VSC-1 and VSC-2. With the injection of the wind power, the VSC-3 start receiving this power to balance the network until the DC voltages at the VSC-1 and VSC-2 busbar reach the upper limit. Once the busbars voltage exceed the limits, all the onshore VSCs then import the wind power. The contribution of each VSCs in balancing the power in the DC network can be adjusted by the voltage limits and proportional gains.

6.3 Integration of Offshore AC and DC Grids

The realization of a 'SuperGrid' at the North and Baltic Sea may require the benefits of both offshore AC collector system and MTDC networks. An offshore AC network allows the centralized collection of offshore energies located at long distances, and the MTDC network can provide the mean of transferring this collected energy at different onshore grids and enable the trade between them. An example of an offshore grid formed by the combination of offshore AC network and MTDC network is shown in Figure 6.11. In the network, three wind power plants are connected together with HVAC cables to form offshore AC collector system. The fourth wind power plant is located far from both onshore grids and the collector system therefore it is interlinked with the HVDC system. Three onshore grids are connected with the offshore AC collector system via MT-VSC HVDC transmission system, and an onshore grid is interconnected with the AC collector system via VSC-HVDC system in the point-to-point configuration. All the VSCs have the same rated active power i.e 100 MW, and the rated apparent power is 112 MVA. The network voltages and cables parameters are given in Table 6.2.

The offshore VSCs 'Off-VSC-1', 'Off-VSC-2', and 'Off-VSC-3' are operating in the grid forming mode with frequency and voltage droop schemes
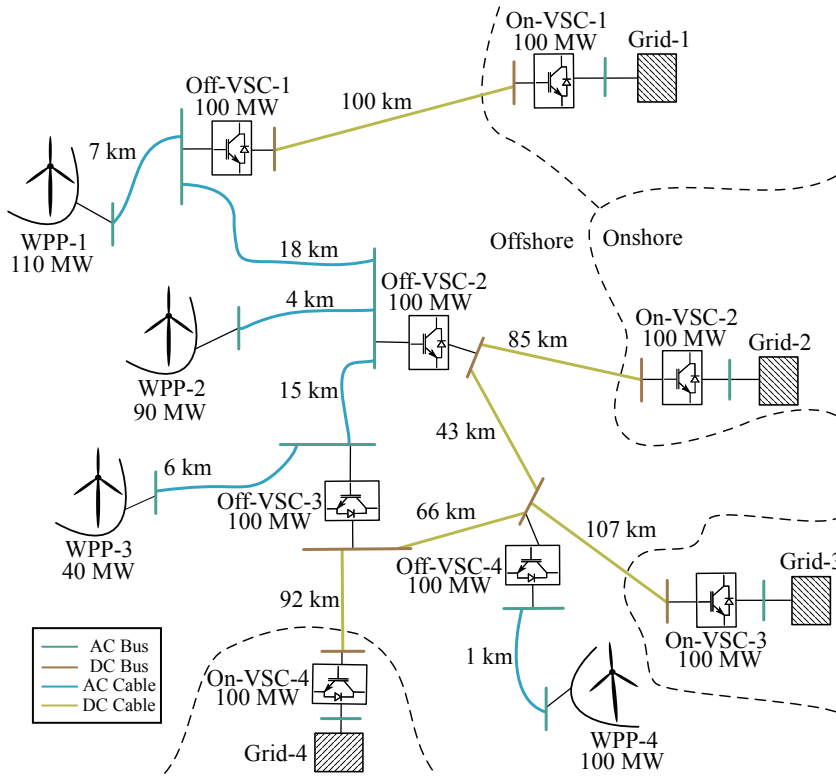
Figure 6.11: Integration of offshore AC and DC networks.

as explained in Chapter 3, and their substation configuration is based on Figure 5.4. This network is referred as offshore AC network in this chapter. The net maximum active power in the offshore AC network is 240 MW. The active power sharing is considered as equal among the offshore VSCs thus all of them have same frequency droop gains i.e $k_{f\_1} = k_{f\_2} = k_{f\_3} = 0.0002$ p.u. The voltage droop gain for 'Off-VSC-1', 'Off-VSC-2', and 'Off-VSC-3' are calculated as $k_{u\_1} = 0.001$, $k_{u\_2} = 0.001$ p.u and $k_{u\_3} = -0.001$ p.u respectively. The offshore VSC 'Off-VSC-4' is also operated in grid forming mode but without frequency and voltage droop scheme, and it substation configuration is same as shown in Figure 5.4 with $k_{f\_4} = k_{u\_4} = 0.0$ p.u.

The onshore VSC 'On-VSC-1' is controlling the DC voltage solely since it is connected in the point-to-point configuration. Its substation configuration is based on Figure 5.5. Furthermore, the onshore VSCs 'On-VSC-2', 'On-

Table 6.2: Network voltages and cables parameters for combined AC and DC grid

	Voltage kV	Resistance Ω/km	Inductance mH/km	Capacitance μ/km
AC Bus (offshore)	150.0	-	-	-
AC Bus (onshore)	220.0	-	-	-
AC Cable	150.0	0.06	0.44	0.14
DC Cable	150.0	0.019	0.0001	0.35

VSC-3', and 'On-VSC-4' are forming a MTDC network therefore they are controlling the DC voltage control with droop characteristics as explained in Section 6.2. With equal active power sharing criteria among the VSC in offshore AC collector network, the net maximum active power in the MTDC network is 260 MW. It is also considered that the onshore VSCs in MTDC networks are sharing active power equally at the rated power thus the proportional gains value of the DC voltage control is same as given for Case-I in Table 6.1. Furthermore, each wind power plants is an aggregate model having the same substation structure as shown in Figure 5.2 and their parameters are adapted according to the rated power [129].

The operation of the offshore grid is analyzed by applying step change in the wind power generations. All the wind power plants have 0.98 inductive power factor in order to support the network voltages. For analysis, WPP-1, WPP-2, WPP-3, and WPP-4 wind power generation are changed from zero to maximum at 3.0 s, 6.0 s, 9.0 s, and 12.0 s respectively. The responses of the active and reactive power flow of VSCs in the offshore AC network are shown in Figure 6.12. The results are in the per unit of rated apparent power i.e 112 MVA, and generator oriented sign convention is applied. The net active power in the offshore AC network formed by 'Off-VSC-1', 'Off-VSC-2', and 'Off-VSC-3' is greater than a single offshore VSCs active power transmission capacity. The frequency droop scheme enable the control over the active power distribution among them. The active power response shows that the power distribution among these VSCs is equal according to the power sharing criteria. After 10.0 s, each offshore VSCs in the AC collector network are receiving 0.7143 p.u active power. The WPP-4 is not connected

(a) Active Power Response (b) Reactive Power Response
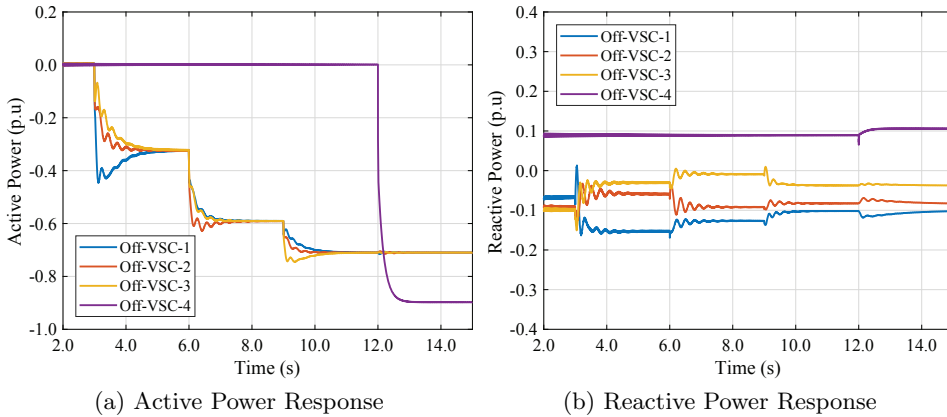
Figure 6.12: The power response of offshore VSCs.

with the AC collector network thus 'Off-VSC-4' is receiving the full wind power generation i.e 0.9 p.u. Although, wind power plants are absorbing the reactive power (inductive) from the network, the VSCs in the offshore AC network requires to flow inductive reactive power as shown in Figure 6.12b. This is due to the offshore AC cable capacitance which is comparatively higher than the onshore AC cables. On the other hand, the 'Off-VSC-4' is flowing capacitive reactive power since the AC cable connected with WPP-4 is not long. However, the reactive power can be managed in the offshore AC network by both offshore wind power plants and VSCs.

The offshore VSCs formed the AC collector network by imposing the frequencies and controlling the voltages. The response of the offshore VSCs frequencies and voltages are shown in Figure 6.13. It can be observed that the offshore AC network frequency is raised above the nominal value at steady-state. This change in the frequency enable the power distribution among the offshore VSCs. On the other hand, the frequency imposed by 'Off-VSC-4' is constant since there is no other VSC to share the active power. The energizing of the offshore network is mainly done by controlling the voltage through VSC outer voltage control. Note that there is lack of inertia in the offshore AC network since only static devices (only VSCs) exist in it. Any sudden change in the power imbalance in the network will directly impact the voltages, and VSCs voltage control has to ensure the network

(a) Frequencies Imposed by Offshore VSCs   (b) AC Voltages at VSCs Busbars
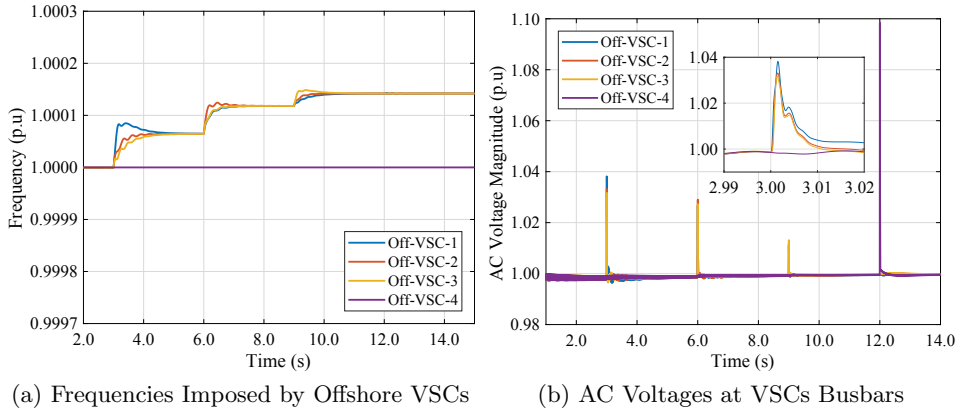
Figure 6.13: The response of offshore VSCs frequencies and their correspon-
ding busbar voltages.

stability. The response of the offshore network AC voltages are shown in
Figure 6.13b. It is clear that the VSC voltage control is robust and the
network voltage reaches to steady-state value fast to ensure network stability
i.e current response settling time is 20 ms. The maximum voltage rise in
the offshore AC network is 1.04 p.u, and the voltage rise due to change in
WPP-4 wind power is approximately 1.10 p.u.

The response of the active power flowing through the onshore VSCs and
the DC voltages at these converters busbars are shown in Figure 6.14. The
'On-VSC-1' is injecting approximately 0.7143 p.u active power into the
'Grid-1'. The active power supply into this grid can only be increased by
altering the power sharing factor of 'Off-VSC-1'. However, the supply of
active power into other onshore grids can be controlled either by the power
sharing factor within the MTDC network or with the increase in the MTDC
network net power through 'Off-VSC-2', and 'Off-VSC-3' converters. Note
that the frequency droop scheme in the offshore VSCs do not permit the
different active power flow directions with respect to each other. In other
words, all the offshore VSCs will supply the active power into the offshore
AC network to compensate the network losses when there is no wind power
generation. And, they all will receive the active power in case of wind energy
generation. This is evidence from the active power response of Figure 6.12a.

(a) Active Response

(b) DC Voltages at VSCs Busbars
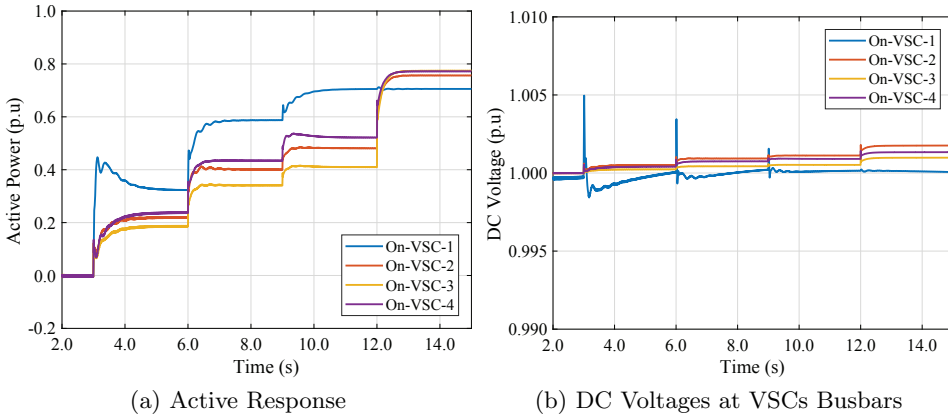
Figure 6.14: The active power and DC voltage response of the onshore converters.

The total active power losses in the offshore AC network is 2.21 MW which is equally shared by 'Off-VSC-1', 'Off-VSC-2', and 'Off-VSC-3' i.e 0.00659 p.u each. Such operational strategy avoid to flow the circulating active power in the loop that can be formed between MTDC and offshore AC network such as around 'Off-VSC-2' and 'Off-VSC-3'.

Furthermore, it can be observed from Figure 6.14a that the active power flow through 'On-VSC-2', 'On-VSC-3', and 'On-VSC-4' at the maximum wind power according to the designed power sharing criteria. Each of them are flowing 0.77 p.u of active power. As it has been explained before that the proportional gain of the DC voltage control of onshore VSCs not only enable the control over the power sharing but also they must ensure the DC network stability. The response of the DC voltages shown in Figure 6.14b indicates that the voltages are within the operational limits and the DC network is stable.

6.4 Summary

An offshore AC network formed by multiple VSCs make installation economically feasible for offshore wind power plant deep into the Sea. Also, multiterminal VSC based HVDC transmission systems is a better solution,

compare to point-to-point configuration, for the trade between the onshore grids via offshore grid. The DC voltage droop control is a simplest and effective control scheme to control the MTDC network with multiple onshore converters, which also enable the control over the power sharing. However, the trade between onshore grids become difficult using droop control. The enhancement of the simple droop scheme as a dead-band droop control can over come this limitation. Further, it is demonstrated that an offshore AC network formed by connecting several offshore wind power plants using AC cables interconnection can also be connected with MTDC network with ease.

7 Conclusions, Applications, and Future Works

The overall research findings are summarized in this chapter. The possible applications and future works have also been highlighted in this chapter.

7.1 Conclusions

The offshore grid has diverse benefits for the transnational electrical network and future offshore wind power integration. Future offshore grid at North and Baltic sea would be the combination of AC and DC network. To build such a network, a gradual approach have to be taken that must utilize the existing electrical grid infrastructure at offshore and reaches the stage of fully functional integrated network. In this regard, the aim of this thesis is to design the control of voltage source converter for high voltage direct current transmission system to cover the operational aspects of offshore grid. The different stages of offshore grid evolution have been analyzed started from point-to-point configuration up to the combined operation of offshore AC and multiterminal DC network.

In the first stage, the control of the VSC is designed from the prospective of the HVDC transmission system in point-to-point configuration. In this configuration, the control design establishes the fundamental control structure of the VSC which consists of inner and outer control system. The inner control loop is always a current closed loop while the outer control loop depends on the operational mode such as voltage or power control. The control loops are cascaded which imply that the reference of the inner control loop is set by the outer control loop. By this, the control loops can be designed sequentially as well as extended for network level control. The current closed loop inclusion

for both grid synchronous and grid forming mode enables the possibility of restraining the current flow by controller limits as well as react fast against any disturbances. This gives an advantage over other schemes of VSC grid forming control such as direct voltage control. The VSC controller design method for each operational mode, and the stability conditions for controller gains selection is addressed in Chapter 2. The chapter also established the fundamental control structure for offshore, onshore and wind generation unit substations which has been applied through out the research.

In the second stage of offshore grid development, interconnections of different wind power plants can be made using HVAC cables and the net energy can be exported to different onshore grids via VSC-HVDC transmission system in point-to-point configuration. Such a network is formed by multiple grid forming VSCs operating in parallel. Using frequency and voltage droop scheme as the VSC network level control, the offshore AC grid can be operated on the analogue principle of onshore grid with multiple synchronous machines. The droop gains provide the ability to control the power distribution among the offshore VSCs which can be set according to the energy export requirement of the onshore grids. The ability to control the power distribution is an additional degree of freedom to optimize network operation for minimizing losses and voltage deviation in the network. However, the application of voltage droop scheme could lead to long term voltage instability due to reactive power generation by changing VSC controlling busbar voltage. Thus, the criteria of selecting voltage droop gains has been developed for better control over reactive power in the offshore AC network which is presented in Chapter 3.

Apart from the steady-state operation requirement, the frequency and voltage droop gains must also be selected according to the offshore AC network stability conditions. By performing small-signal stability analysis, the stable boundary condition of droop gain can be determined. This study is presented in Chapter 4. The results suggest that the impact of the droop gains on the network stability are correlated with the performance of the VSC. Thus, in order to analyze the complete system stability, the VSC current and voltage control loops dynamics is essential to be included in the small-signal modeling of offshore AC network. By analyzing frequency

response using developed model, it has been concluded that the sufficient damping in the system cannot be achieved at all the high frequencies due to the performance limitation of the VSC. Although the VSC low-pass filter at the power measurement may increase damping in the voltage and frequency response, wind generation units also need to limit the rate of change of power injection for better system performance.

For long distance energy transmission especially from offshore wind power plant, the concept of offshore DC hub may have precedence over AC hub but the lack of DC circuit breaker availability for high DC voltage application restrains the development of multiterminal HVDC transmission system. On the other hand, the protection schemes in offshore AC network formed by multiple grid forming VSCs can be based on the conventional AC circuit breaker. Since the HVDC transmission system is in point-to-point configuration, the DC fault can be isolated by opening IGBTs and AC circuit breaker. In the offshore AC network, the selectivity can be ensured using AC circuit breaker. The fault-ride-through capability is needed in both offshore VSCs and wind generation units to allow sufficient time for protection devices to isolate the faulty cable. The short circuit analysis of an offshore AC network is presented in Chapter 5. The research concludes that the current control in the VSC grid forming mode enables the direct control over the current during short circuit to protect the IGBTs, and allow the continue operation in post fault state after network voltage restored. During fault, the transmission system VSC switches from voltage control to current control, the voltages in the network are generated based on the network impedance, and the current infeed by the VSCs and wind generation units. The magnitude of the voltage is directly proportional to the fault current, and it is recommended to inject current with maximum magnitude by VSCs and wind generation units. Since the voltage phase angle at the VSC controlling busbar is established according to the equivalent impedance of the network, the nature of current infeed either active or reactive depends on the magnitude of the fault resistance. In order to keep the network stable during fault and post fault state, it is desirable to keep the voltage phase angle as closed as possible to its pre-fault state. Usually, the voltage phase angle in the network remains with in $\pm\pi/6$ due to stability constraint. For low magnitude fault resistance,

the cable series impedance angle is dominant in the equivalent impedance, hereby requires VSCs to inject capacitive reactive power to keep voltage phase angle closed to its pre-fault state. On the other hand, it is required to inject active current for high magnitude fault resistance. The analysis presents fault behavior of the network at different locations in the offshore AC network.

Multiple grid forming VSCs provides redundancy in the offshore AC network and the network can continue to be operated in case of one VSC failure. In case of malfunction of one ore more grid forming VSCs, the sum of power infeed by the wind turbine could be greater than the sum of the combined export capacity of in-operation VSC-HVDC transmission system. The wind energy is then required to be reduced up to the remaining export capacity. A frequency coordination control system of VSCs and wind generation units is developed to reduce the wind generation units power production without communication signals. The analysis shows that large transient will appear in the network voltages at the instant of disturbance. This transient appears due to no inertia in the network and the impacts of large variation in the power on the network frequency is slower than on the voltages. The slow reaction of frequency change with respect of active power delays the process of reducing the wind power consequently the VSC operational limits is violated. To improve the system response, an over voltage active current reduction scheme in conjunction of frequency dependent active current reduction scheme for offshore wind generation units is proposed. In the proposed scheme, the wind power reduction is made during initial transient by voltage dependent power reduction scheme later frequency dependent power reduction scheme supersede and the network continues to be operated at reduce power with nominal voltages in the network. The proposed short circuit control scheme is robust and fulfills the grid code requirements such as FRT, operating split networks, improve voltage response during fault and post fault state etc.

A MTDC network is preferable solution for the trade between three or more onshore grids. The formation of offshore AC network can also be used for energy trade between onshore grids however extra power losses generated in the offshore converters and cables make the trade process less

efficient. In Chapter 6, the VSC control scheme is developed for MTDC network considering the network operational reliability and trade requirements. The analysis have shown that the active power distribution in the MTDC network is possible using DC voltage droop control, and it also introduced the redundancy of operating MTDC network through multiple onshore VSCs. The control scheme for onshore VSC for MTDC network operation is developed with simple modification in the DC voltage control. For MTDC network operation, all the onshore VSCs have the proportional control scheme for DC voltage control instead of proportional-plus-integral control scheme. This has modified the U-I characteristic of VSCs which now exhibit the principle of DC voltage droop control. A DC optimum power flow algorithm is developed to determine the DC voltage proportional controller gains according to the require distribution factor. The DC voltage control now have to ensure both the stability of the network and trade requirement. The setting of upper and lower boundary limits for droop gains in the OPF algorithm by considering the stability limits can provide the satisfactory solution. Although the DC droop control increase reliability in the MTDC network, it is difficult to steer power between onshore grids because of having only one variable (i.e voltage) to control the power both for balancing and trade. The trade between onshore grids can be improved by applying dead-band droop characteristics.

As the last stage of the offshore grid development, the thesis presents the combined operation of the integrated offshore AC and MTDC network.

7.2 Applications

This research can be applied to derive the information and recommendations for the future wind power plant projects. The results could be useful for developers, planners and operators as well as to national and international authorities. The analysis in this research could:

- Assess the information and recommendations for future HVDC transmission systems.

- Beneficial for pre-project planning and realization of offshore wind

power plants.

- Demonstrate the possibilities for reliable technical solution for offshore wind power integration.

- Provide the industry with the open source design tools of VSC based HVDC transmission system.

- Explore the possibilities for connecting the offshore wind power plants to the onshore grid, particularly options of an offshore grid extension.

- Provide the tools for optimal operational design of interconnected offshore and onshore electrical grid, and give insight of its transient behavior.

The findings of the presented research can be utilized in the definition of offshore grid codes, and in some of the ongoing European energy projects such as SuperGrid, MedGrid, Offshore Grid etc.

7.3 Future Works

The concept of an offshore grid is at its earlier state. The presented research consolidates the key aspects of offshore grids and open up the new ideas in the said field. Following is a list of ideas that can be considered for future work.

- In general, the average model of the voltage source converter is sufficient for power system dynamic and stability analysis. The average model is usually applied in order to speed up the simulation process. As a future work, the detailed MMC based VSCs model can be applied to evaluate the converter performance using proposed VSC control system design methodology.

- The Real Time Digital Simulator (RTDS) technology has revolutionized the power system modeling, analysis and control system design. The RTDS technology enables the testing and analysis of power system products under simulated condition close to actual system behavior

through 'Power-Hardware in the loop'. The RTDS can be utilized to model and analyze the hybrid AC/DC offshore grid presented in the thesis more specifically offshore AC and DC grids, wind farms generators, converter, and operational control schemes to evaluate the effectiveness of the proposed control strategies.

• In the thesis, the short circuit analysis and control system for an offshore grid is proposed for symmetrical three phase balance fault. The unbalance faults and disturbances in the offshore AC network can also be analyzed as the future extension of the proposed control scheme.

• DC fault analysis is another key issue that needs to be addressed for an offshore AC network that is connected either with MTDC network or point-to-point VSC-HVDC transmission system.

• Large offshore wind power plants are required to provide the frequency support to the onshore grids. In the presented control scheme, the offshore AC network is operated at variable frequency in order to control the distribution of active power among the transmission system. The frequency droop gain designing procedure consider that the maximum over frequency limit must not exceed for all normal operating points i.e 50.2 Hz. Thus, the provision of frequency support by the wind power plants can be designed above this limit. In this regard, the extension of the presented control scheme is to incorporate the onshore grid frequency control scheme with the control of active power distribution of offshore AC network. Also, the discussion and analysis needs to be done on; what would be the over frequency limit in the offshore grid code?

Appendix A

Author Publications

A.1 Publication in Journals

1. M. Raza, K. Schoenleber, and O. Gomis-Bellmunt, "Droop control design of multi-VSC system for offshore network to integrate wind energy" Energies (MDPI), 9(10):826, oct 2016, doi: 10.3390/en9100826.

2. M. Raza, E. Prieto-Araujo, and O. Gomis-Bellmunt, "Small signal stability analysis of offshore AC network having multiple voltage source converters" IEEE Transactions on Power Delivery, doi: 10.1109/TP-WRD.2017.2725982.

3. M. Raza, C. Collados, and O. Gomis-Bellmunt, "Reactive power management in an offshore AC network having multiple voltage source converters" Applied Energy (Elseiver), 206:793-803, nov 2017. ISSN 0306-2619. doi: 10.1016/j.apenergy.2017.08.182.

4. M. Raza, M. Aragues-Penalba, and O. Gomis-Bellmunt, "Short circuit analysis of an offshore AC network having multiple VSCs imposing frequency" International Journal of Electrical Power and Energy Systems, Elseiver (peer-reviewed).

A.2 Publication in Conferences

1. M. Raza, and O. Gomis-Bellmunt, "Dynamic modeling and implementation of VSC-HVDC system: A grid connected offshore wind farm application" in Proceedings of the 3rd International Conference on

Smart Grids and Green IT Systems, (Barcelona, Spain), pp. 53-62, apr 2014.

2. M. Raza, and O. Gomis-Bellmunt, "Multi infeed control of VSC HVDC transmission system for offshore wind power plant integration" in 13th International Workshop on Large-Scale Integration of Wind Power into Power Systems as well as on Transmission Networks for Offshore Wind Power Plants, (Berlin), pp. 376-381, nov 2014.

3. M. Raza and O. Gomis-Bellmunt, "Control design strategy to enhance the fault ride through capability of VSC-HVDC transmission system interconnecting offshore wind power plant" in EWEA Annual Conference and Exhibition 2015, (Paris, France), nov 2015.

4. M. Raza and O. Gomis-Bellmunt, "Control system of voltage source converter to interconnect offshore AC hub with multiple onshore grids" in 4th International Conference on Renewable Energy Research and Application, (Palermo, Italy), nov 2015.

5. M. Raza, C. Collados, and O. Gomis-Bellmunt, "Reactive power management in an offshore AC network having multiple voltage source converters" in 16th IEEE International Conference on Environment and Electrical Engineering, Florence, Italy, 7-10 jun 2016.

A.3 Publication in Book

1. M. Raza, "Load flow calculation and its application" in PowerFactory Applications for Power System Analysis SE - 1 (F. M. Gonzalez-Longatt and J. Luis Rueda, eds.), Power Systems, pp. 1-25, Springer International Publishing, 2014.

Appendix B

Mathematics for VSC System

B.1 Per Unit System for Network Parameters

Usually, it is convenient to design the control and perform the analysis in per unit (p.u) system. It simplify the computational process by eliminating the units. The base values for the principle variables are selected such that they are equal to one per unit under rated condition. For the network parameters, the base value of power and voltage are defined while current and impedance base values are calculated using ohm laws.

With the definition of the base power, frequency, and three phase AC voltage, the base of AC current can be calculated using (B.1). The subscript b is the notation of base variable.

$$s_b = p_b = q_b = \sqrt{3}u_b i_b$$
$$i_b = \frac{s_b}{\sqrt{3}u_b}$$

(B.1)

Here, u_b is the rated line-to-line RMS voltage, i_b is the rated line RMS current, s_b is the base apparent power, p_b is the base active power, and q_b is the base reactive power. The base values of the impedance and admittances can be calculated using (B.2).

$$z_b = \frac{u_b^2}{s_b}, \quad y_b = \frac{1}{z_b}$$

(B.2)

Also, the base values of inductance and capacitance are calculated using (B.3). The resistance base value is equal to the z_b.

$$l_b = \frac{z_b}{\omega_b}, \quad c_b = \frac{y_b}{\omega_b} \tag{B.3}$$

Here, $\omega_b = 2\pi f_b$ is the network angular frequency base value. Similarly, the base value for DC network variables can be calculated by defining DC active power and voltage base values. The DC quantities are notated using capitalized letter. The base value of current and resistance can then be calculated using (B.4). Usually, the DC base power is defined equal to the AC base power.

$$I_b = \frac{P_b}{U_b}, \quad R_b = \frac{U_b}{I_b} \tag{B.4}$$

B.2 Per Unit System for VSC Control

The three phase voltages and currents are the measurement quantities in the VSC control system. The Clark transformation matrix given in Chapter 2 preserve the peak of the measurement quantities, in another words it is called as voltage and current invariant transformation. In phasor notation, the measured three phase balanced voltage and current can be written as (B.5) in $\alpha\beta0$ frame.

$$\underline{u}_{\alpha\beta0\_pu}(t) = U_{m\_pu}e^{j(\omega t + \delta)}, \quad \underline{i}_{\alpha\beta0\_pu}(t) = I_{m\_pu}e^{j(\omega t + \psi)}, \tag{B.5}$$

Here, U_{m_pu} and I_{m_pu} are the peak voltages and current in per unit, δ is the voltage phase angle, ψ is the current phase angle, and ω is the network frequency. The complex power is calculated using (B.6) for analytical analysis. As explained in previous section, the base values are selected so that the measured signals are equal to 1.0 p.u at the rated values. Thus for the measurement signals, the base values are rated peak voltage of line-to-ground voltage ($u_b = \sqrt{2/3}U_{LL}$) and the rated peak line current ($i_b = \sqrt{2}I_{LL}$).

$$\begin{aligned} \underline{s}_{pu}(t) &= \underline{u}_{\alpha\beta0\_pu}(t) \cdot \underline{i}^*_{\alpha\beta0\_pu}(t) \\ \underline{s}_{pu} &= U_{m\_pu}I_{m\_pu}e^{j(\delta - \psi)} \end{aligned} \tag{B.6}$$

Let us compare the power calculation using per unit quantity with the actual value calculation. The matrices for signal transformation into $\alpha\beta0$ frame and its inverse is given in (B.7).

$$
T_{\alpha\beta0} = \frac{2}{3}
\begin{bmatrix}
1 & -\frac{1}{2} & -\frac{1}{2} \\
0 & \frac{\sqrt{3}}{2} & -\frac{\sqrt{3}}{2} \\
\frac{1}{2} & \frac{1}{2} & \frac{1}{2}
\end{bmatrix}, \quad
T_{\alpha\beta0}^{-1} =
\begin{bmatrix}
1 & 0 & 1 \\
-\frac{1}{2} & \frac{\sqrt{3}}{2} & 1 \\
-\frac{1}{2} & -\frac{\sqrt{3}}{2} & 1
\end{bmatrix}
\tag{B.7}
$$

The instantaneous three phase power can be calculated as (B.8) using three phase voltage and current measurement in matrix representation.

$$
s(t) = u_{abc}^T(t) i_{abc}(t) =
\begin{bmatrix} u_a(t) & u_b(t) & u_c(t) \end{bmatrix}
\begin{bmatrix} i_a(t) \\ i_b(t) \\ i_c(t) \end{bmatrix}
\tag{B.8}
$$

By applying the Clark transformation principle on the voltage and current, the power equation yield as (B.9).

$$
\begin{aligned}
s(t) &= \left(T_{\alpha\beta0}^{-1} \cdot u_{\alpha\beta0}(t) \right)^T \cdot T_{\alpha\beta0}^{-1} \cdot i_{\alpha\beta0}(t) \\
s(t) &= u_{\alpha\beta0}^T(t) \cdot \left(T_{\alpha\beta0}^{-1} \right)^T \cdot T_{\alpha\beta0}^{-1} \cdot i_{\alpha\beta0}(t) \\
\left(T_{\alpha\beta0}^{-1} \right)^T \cdot T_{\alpha\beta0}^{-1} &=
\begin{bmatrix}
\frac{3}{2} & 0 & 0 \\
0 & \frac{3}{2} & 0 \\
0 & 0 & 3
\end{bmatrix}
\end{aligned}
\tag{B.9}
$$

First two components are orthogonal in which α component is align with the a-phase and β components is lagging by $-\pi/2$. Third component of three phase voltage and current is zero in $\alpha\beta0$ frame for the balanced system, therefore the third component of power is also zero. Thus, power, voltage and current can be written in instantaneous vector form as expressed by (B.10). Note that the quantities are in actual values.

$$
\begin{aligned}
\underline{s} &= \frac{3}{2} \underline{u}_{\alpha\beta0}(t) \cdot \underline{i}_{\alpha\beta0}^*(t) \\
\underline{u}_{\alpha\beta0}(t) &= u_\alpha(t) + j u_\beta(t), \quad \underline{i}_{\alpha\beta0}(t) = i_\alpha(t) + j i_\beta(t)
\end{aligned}
\tag{B.10}
$$

Further, it can be observed from (B.6) that the calculation of power will

become the time invariant function after the product of voltage and current in $\alpha\beta 0$ frame. Thus, power equation can be written in Cartesian coordinate representation as

$$P = \frac{3}{2}\left(u_\alpha i_\alpha + u_\beta i_\beta\right)$$
$$Q = \frac{3}{2}\left(u_\beta i_\alpha - u_\alpha i_\beta\right) \tag{B.11}$$

Substitute the actual voltage and current values in (B.10) with the per unit variables and base values as given in (B.12). It can be observed that the factor of 3/2 is not required to calculate the power when using measurement signals in per unit.

$$\underline{s} = \frac{3\sqrt{2}\sqrt{2}}{2\sqrt{3}}U_{LL}\cdot I_{LL}\cdot\underline{u}_{\alpha\beta 0\_pu}(t)\cdot\underline{i}^*_{\alpha\beta 0\_pu}(t)$$
$$\underline{s} = \sqrt{3}U_{LL}\cdot I_{LL}\cdot\underline{u}_{\alpha\beta 0\_pu}(t)\cdot\underline{i}^*_{\alpha\beta 0\_pu}(t) \tag{B.12}$$
$$\underline{s}_{pu} = \underline{u}_{\alpha\beta 0\_pu}(t)\cdot\underline{i}^*_{\alpha\beta 0\_pu}(t)$$

Normally, the small signal analysis or control system design methods are performed using actual quantities of the variables. These analysis and methods provide the controller gains in units of actual quantities. For the control system implementation in per unit system, these controller gains need to be converted appropriately. In the presented thesis, the controller gains that are designed for VSC is belong to either one of the three main control systems i.e inner, outer, and network level controller.

The inner control is the current control loops in which input is current and output signal is voltage. Thus, the unit of inner current controller gains is V/A, and the actual controller gain value must be divided by the AC impedance base value for per unit control system.

The outer controller gains unit depends on the control loop. For active and reactive power control loop, the controller gains are unit less since the per unit absolute value of power and current are same in $dq0$ frame. For AC voltage control in both grid forming and grid synchronous mode, the output of the controller is the current and input is voltage ergo the controller gain unit is A/V and the gains must be multiplied by the AC impedance

base value for per unit control implementation. For DC voltage control, the input is DC voltage and output is the current which makes its unit as A/V therefore DC base resistance needs to be multiplied with the controller gains to set in per unit control system.

The network level control mainly consists of frequency and voltage droop control. The unit of voltage droop gain is V/Var and the factor that needs to multiply with the voltage droop value is s_b/u_b. Similarly, the unit of frequency droop gain is Hz/W and the gain is multiplied with the factor calculated as s_b/ω_b. Note that the droop gain value determined by the OPF algorithm is in per unit variables, and they are not required to be converted.

Bibliography

[1] Nathalie Girouard, Elianna Konialis, Cecilia Tam, and Peter Taylor. *Energy.* OECD Green Growth Studies. OECD Publishing, jan 2012. ISBN 9789264115101. doi: 10.1787/9789264115118-en.

[2] Mihai Tomescu, Ils Moorkens, Wouter Wetzels, Lukas Emele, Hannah Foerster, and Benjamin Greiner. Renewable energy in Europe 2016: Recent growth and knock-on effects. Technical report, European Envirnoment Agency, mar 2016. doi: 10.2800/6803.

[3] Daniel Fraile, Giorgio Corbetta, and Ivan Pineda. Making transition work. Technical report, Wind Europe, sep 2016. URL `https://windeurope.org/`.

[4] Ivan Pineda and Pierre Tardieu. Wind in power: 2016 European statistics. Technical report, Wind Europe, feb 2017. URL `https://windeurope.org/`.

[5] Ivan Pineda and Pierre Tardieu. The European offshore wind industry: key trends and statistics 2016. Technical report, Wind Europe, jan 2017. URL `https://windeurope.org/`.

[6] European council 23/24 october 2014 - conclusion: 2030 climate and energy policy framework, oct 2014. URL `https://ec.europa.eu/clima/policies/strategies/2030_en`.

[7] Ayla Uslu. Europe onshore and offshore wind energy potential. Technical report, European Environment Agency, jun 2009. doi: 10.2800/11373.

[8] Athanasia Arapogianni and Anne Benedicte Genachte. Deep water: The next step for offshore wind energy. Technical report,

WindEurope, jul 2013. URL `https://windeurope.org/about-wind/reports//deep-water/`.

[9] Nicolas Fichaux and Justin Wilkes. Oceans of opportunity. harnessing Europe's largest domestic energy resource. Technical report, European Wind Energy Association, sept 2009. URL `http://www.ewea.org/policy-issues/offshore/`.

[10] Stijn Cole, Karim Karoui, Til Kristian Vrana, Olav Bjarte Fosso, Jean Baptiste Curis, Anne Marie Denis, and Chen Ching Liu. A European supergrid: Present state and future challenges. In *Power Systems Computation Conference (PSCC)*. ETH Zurich, aug 2011.

[11] Jan De Decker, Paul Kreutzkamp, Achim Woyte, and Carlos Dierckxsens. The impact of large scale offshore electricity transmission: the European project offshore grid. In *2012 9th International Conference on the European Energy Market*. IEEE, may 2012. ISBN 978-1-4673-0833-5. doi: 10.1109/EEM.2012.6254680.

[12] WWF. Threats: Effects of climate change, 2017. URL `https://www.worldwildlife.org/threats/effects-of-climate-change`. Accessed on 30-05-2017.

[13] MEDOW. Multi terminal DC grid for offshore wind, 2017. URL `http://sites.cardiff.ac.uk/medow/`. Accessed on 30-05-2017.

[14] Nikolas Flourentzou, Vassilios Georgios Agelidis, and Georgios Demetriades. VSC-Based HVDC power transmission systems: An overview. *IEEE Transactions on Power Electronics*, 24(3):592–602, mar 2009. ISSN 0885-8993. doi: 10.1109/TPEL.2008.2008441.

[15] Fujin Deng and Zhe Chen. Design of protective inductors for HVDC transmission line within DC grid offshore wind farms. *IEEE Transactions on Power Delivery*, 28(1):75–83, jan 2013. ISSN 0885-8977. doi: 10.1109/TPWRD.2012.2224384.

[16] Ataollah Mokhberdoran, Helder Leite, Adriano Carvalho, and Nuno Silva. A review on HVDC circuit breakers. In *3rd Renewable Power*

Generation Conference (RPG 2014). IET, sep 2014. ISBN 978-1-84919-917-9. doi: 10.1049/cp.2014.0859.

[17] Robert Sellick and Markus Akerberg. Comparison of HVDC light (VSC) and HVDC classic (LCC) site aspects, for a 500MW 400kV HVDC transmission scheme. In *10th IET International Conference on AC and DC Power Transmission (ACDC 2012)*. IET, dec 2012. ISBN 978-1-84919-700-7. doi: 10.1049/cp.2012.1945.

[18] Mike Barnes. VSC-HVDC Newsletter. *University of Manchester, UK*, 5(4), apr 2017.

[19] Jeroen Brouwers. Tennet News: TenneT presents Hub and Spoke concept for large scale wind energy on the North Sea, jun 2016. URL `https://www.tennet.eu/news/detail/tennet-presents-hub-and-spoke-concept-for-large-scale-wind-energy-on-the-north-sea/`. Accessed on 23-06-2017.

[20] Jeroen Brouwers. Tennet News: Three TSOs sign agreement on North Sea wind power hub, mar 2017. URL `https://www.tennet.eu/news/detail/three-tsos-sign-agreement-on-north-sea-wind-power-hub/`. Accessed on 23-06-2017.

[21] Paola Bresesti, Wil Kling, Ralph Hendriks, and Riccardo Vailati. HVDC connection of offshore wind farms to the transmission system. *IEEE Transactions on Energy Conversion*, 22(1):37–43, mar 2007. ISSN 0885-8969. doi: 10.1109/TEC.2006.889624.

[22] Peter Sandeberg, Paul Moran, Alessio Lomardi, Alvaro Hernandez Manchola, Christian Feltes, and Douglas Ramsay. Special considerations for AC collector systems and substations associated with HVDC connected wind power plants. Technical Report WG SC B3.36, CIGRE International Council on Large Electric Systems, mar 2015.

[23] Christof Humpert. Long distance transmission systems for the future electricity supply: Analysis of possibilities and restrictions. *Energy,*

48(1):278–283, dec 2012. ISSN 03605442. doi: 10.1016/j.energy.2012. 06.018.

[24] Joseph Song Manguelle, Maja Harfman Todorovic, Song Chi, Satish Gunturi, and Rajib Datta. Power transfer capability of HVAC cables for subsea transmission and distribution systems. *IEEE Transactions on Industry Applications*, 50(4):2382–2391, jul 2014. ISSN 0093-9994. doi: 10.1109/TIA.2013.2291934.

[25] Wang Xifan, Cao Chengjun, and Zhou Zhichao. Experiment on fractional frequency transmission system. *IEEE Transactions on Power Systems*, 21(1):372–377, feb 2006. ISSN 0885-8950. doi: 10.1109/TPWRS.2005.860923.

[26] Nan Qin, Shi You, Zhao Xu, and Vladislav Akhmatov. Offshore wind farm connection with low frequency AC transmission technology. In *2009 IEEE Power and Energy Society General Meeting*. IEEE, jul 2009. ISBN 978-1-4244-4241-6. doi: 10.1109/PES.2009.5275262.

[27] Jose Luis Dominguez Garcia, Daniel Rogers, Carlos Ernesto Ugalde Loo, Jun Liang, and Oriol Gomis Bellmunt. Effect of non-standard operating frequencies on the economic cost of offshore AC networks. *Renewable Energy*, 44:267–280, aug 2012. ISSN 09601481. doi: 10.1016/j.renene.2012.01.093.

[28] Qingrui Tu, Zheng Xu, and Lie Xu. Reduced switching frequency modulation and circulating current suppression for modular multilevel converters. *IEEE Transactions on Power Delivery*, 26(3):2009–2017, jul 2011. ISSN 0885-8977. doi: 10.1109/TPWRD.2011.2115258.

[29] Weixing Lin, Dragan Jovcic, Samuel Nguefeu, and Hani Saad. Full bridge MMC converter optimal design to HVDC operational requirements. *IEEE Transactions on Power Delivery*, 31(3):1342–1350, jun 2016. ISSN 0885-8977. doi: 10.1109/TPWRD.2015.2475130.

[30] Jakob Glasdam, Jesper Hjerrild, Lukasz Hubert Kocewiak, and Claus Leth Bak. Review on multi-level voltage source converter based

HVDC technologies for grid connection of large offshore wind farms. In *2012 IEEE International Conference on Power System Technology (POWERCON)*. IEEE, oct 2012. ISBN 978-1-4673-2868-5. doi: 10.1109/PowerCon.2012.6401377.

[31] Michal Sztykiel, Rodrigo da Silva, Remus Teodorescu, Lorenzo Zeni, Lars Helle, and Philip Carne Kjaer. Modular multilevel converter modelling, control and analysis under grid frequency deviations. In *2013 15th European Conference on Power Electronics and Applications (EPE)*. IEEE, sep 2013. ISBN 978-1-4799-0116-6. doi: 10.1109/EPE. 2013.6634747.

[32] Lidong Zhang, Hans Peter Nee, and Lennart Harnefors. Analysis of stability limitations of a VSC HVDC link using power synchronization control. *IEEE Transactions on Power Systems*, 26(3):1326–1337, aug 2011. ISSN 0885-8950. doi: 10.1109/TPWRS.2010.2085052.

[33] Wenyuan Wang, Antony Beddard, Mike Barnes, and Ognjen Marjanovic. Analysis of active power control for VSC HVDC. *IEEE Transactions on Power Delivery*, 29(4):1978–1988, aug 2014. ISSN 0885-8977. doi: 10.1109/TPWRD.2014.2322498.

[34] Manuel Reyes, Pedro Rodriguez, Sergio Vazquez, Alvaro Luna, Remus Teodorescu, and Juan Manuel Carrasco. Enhanced decoupled double synchronous reference frame current controller for unbalanced grid voltage conditions. *IEEE Transactions on Power Electronics*, 27(9): 3934–3943, sep 2012. ISSN 0885-8993. doi: 10.1109/TPEL.2012. 2190147.

[35] Jiabing Hu and Ziqiang Zhu. Improved voltage vector sequences on dead beat predictive direct power control of reversible three phase grid connected voltage source converters. *IEEE Transactions on Power Electronics*, 28(1):254–267, jan 2013. ISSN 0885-8993. doi: 10.1109/TPEL.2012.2194512.

[36] Mehrdad Yazdanian and Ali Mehrizi Sani. Internal model based current control of the RL filter based voltage sourced converter. *IEEE*

Transactions on Energy Conversion, 29(4):873–881, dec 2014. ISSN 0885-8969. doi: 10.1109/TEC.2014.2353035.

[37] Salvatore D'Arco, Jon Are Suul, and Olav Bjarte Fosso. Small signal modeling and parametric sensitivity of a virtual synchronous machine in islanded operation. *International Journal of Electrical Power and Energy Systems*, 72:3–15, mar 2015. ISSN 01420615. doi: 10.1016/j. ijepes.2015.02.005.

[38] Michael Bierhoff and Friedrich Wilhelm Fuchs. Active damping for three phase PWM rectifiers with high order line side filters. *IEEE Transactions on Industrial Electronics*, 56(2):371–379, feb 2009. ISSN 0278-0046. doi: 10.1109/TIE.2008.2007950.

[39] Aleksandr Reznik, Marcelo Godoy Simoes, and Ahmed Al-Durra. LCL filter design and performance analysis for grid interconnected systems. *IEEE Transactions on Industry Applications*, 50(2):1225–1232, mar 2014. ISSN 0093-9994. doi: 10.1109/TIA.2013.2274612.

[40] Fei Li, Xing Zhang, Hong Zhu, Haoyuan Li, and Changzhou Yu. An LCL-LC filter for grid connected converter: Topology, parameter and analysis. *IEEE Transactions on Power Electronics*, 30(9):5067–5077, sep 2014. ISSN 0885-8993. doi: 10.1109/TPEL.2014.2367135.

[41] Dragan Jovcic, Lu Zhang, and Masood Hajian. LCL VSC Converter for high power applications. *IEEE Transactions on Power Delivery*, 28(1):137–144, jan 2013. ISSN 0885-8977. doi: 10.1109/TPWRD.2012. 2219560.

[42] Remus Beres, Xiongfei Wang, Frede Blaabjerg, Claus Leth Bak, and Marco Liserre. A review of passive filters for grid connected voltage source converters. In *2014 IEEE Applied Power Electronics Conference and Exposition*, pages 2208–2215. IEEE, mar 2014. ISBN 978-1-4799-2325-0. doi: 10.1109/APEC.2014.6803611.

[43] Bozo Terzic, Goran Majic, and Alojz Slutej. Stability analysis of three phase PWM converter with LCL filter by means of nonlinear

model. *Journal for Control, Measurement, Electronics, Computing and Communications (AUTOMATIKA)*, 51(3):221–232, sep 2010. ISSN 00051144.

[44] Antony Beddard and Mike Barnes. AC fault ride through of MMC VSC HVDC systems. In *7th IET International Conference on Power Electronics, Machines and Drives (PEMD 2014)*. IET, apr 2014. ISBN 978-1-84919-815-8. doi: 10.1049/cp.2014.0382.

[45] Yan Liu and Zhe Chen. A flexible power control method of VSC HVDC link for the enhancement of effective short circuit ratio in a hybrid multi infeed HVDC system. *IEEE Transactions on Power Systems*, 28(2):1568–1581, may 2013. ISSN 0885-8950. doi: 10.1109/TPWRS. 2012.2222057.

[46] Osman Addalan Kalcon Giddani, Abdelaziz Yousif Mohamed Abbas, Grain P. Adam, Olimpo Anaya Lara, and Kwok Lun Lo. Multi task control for VSC HVDC power and frequency control. *International Journal of Electrical Power and Energy Systems*, 53:684–690, dec 2013. ISSN 01420615. doi: 10.1016/j.ijepes.2013.05.002.

[47] Tennet TSO GmbH. Requirements for offshore grid connections in the grid of TenneT TSO GmbH, dec 2012. URL `http://www.tennet.eu/de/en/customers/grid-customers/grid-connection-regulations.html`.

[48] Tennet TSO GmbH. Grid code, high and extra high voltage, dec 2012. URL `http://www.tennet.eu/de/en/customers/grid-customers/grid-connection-regulations.html`.

[49] Arjen van der Meer, Mario Ndreko, Madeleine Gibescu, and Mart van der Meijden. The effect of FRT behavior of VSC HVDC connected offshore wind power plants on AC/DC system dynamics. *IEEE Transactions on Power Delivery*, 31(2):878–887, apr 2016. ISSN 0885-8977. doi: 10.1109/TPWRD.2015.2442512.

[50] Agusti Egea Alvarez, Jef Beerten, Dirk Van Hertem, and Oriol Go-
mis Bellmunt. Primary and secondary power control of multiterminal
HVDC grids. In *10th IET International Conference on AC and DC
Power Transmission (ACDC 2012)*. Institution of Engineering and
Technology, dec 2012. doi: 10.1049/cp.2012.1989.

[51] Christian Feltes, Holger Wrede, Friedrich Koch, and Istvan Erlich.
Enhanced fault ride through method for wind farms connected to the
grid through VSC based HVDC transmission. *IEEE Transactions
on Power Systems*, 24(3):1537–1546, aug 2009. ISSN 0885-8950. doi:
10.1109/TPWRS.2009.2023264.

[52] Francisco Gonzalez Longatt. Optimal steady state operation of a
MTDC system based on DC independent system operator objectives. In
11th IET International Conference on AC and DC Power Transmission.
IET, feb 2015. ISBN 978-1-84919-982-7. doi: 10.1049/cp.2015.0031.

[53] Eduardo Prieto Araujo, Agusti Egea Alvarez, Sajjad Fekri, and Oriol
Gomis Bellmunt. DC voltage droop control design for multi-terminal
HVDC systems considering AC and DC grid dynamics. *IEEE Tran-
sactions on Power Delivery*, 31(2):575–585, apr 2016. ISSN 0885-8977.
doi: 10.1109/TPWRD.2015.2451531.

[54] Giddani Kalcon, Grain Philip Adam, Olimpo Anaya Lara, Stephen
Lo, and Kjetil Uhlen. Small signal stability analysis of multi-terminal
VSC-based DC transmission systems. *IEEE Transactions on Power
Systems*, 27(4):1818–1830, nov 2012. ISSN 08858950. doi: 10.1109/
TPWRS.2012.2190531.

[55] Lie Xu and Liangzhong Yao. DC voltage control and power dispatch
of a multi terminal HVDC system for integrating large offshore wind
farms. *IET Renewable Power Generation*, 5(3):223, may 2011. ISSN
17521416. doi: 10.1049/iet-rpg.2010.0118.

[56] Zhuo di Wang, Ke Jun Li, Jing guo Ren, Li Jun Sun, Jian Guo Zhao,
Yong Liang Liang, Wei Jen Lee, Zhao hao Ding, and Ying Sun. A
coordination control strategy of voltage source converter based MTDC

for offshore wind farms. *IEEE Transactions on Industry Applications*, 51(4):2743–2752, jul 2015. ISSN 0093-9994. doi: 10.1109/TIA.2015. 2407325.

[57] Wenyuan Wang and Mike Barnes. Power flow algorithms for multi terminal VSC HVDC with droop control. *IEEE Transactions on Power Systems*, 29(4):1721–1730, jul 2014. ISSN 0885-8950. doi: 10.1109/TPWRS.2013.2294198.

[58] Rodrigo Teixeira-pinto. *Multi-terminal DC network: System integration, dynamics and control*. PhD thesis, Delft University of Technology, 2014.

[59] Jef Beerten, Stijn Cole, and Ronnie Belmans. Generalized steady state VSC MTDC model for sequential AC/DC power flow algorithms. *IEEE Transactions on Power Systems*, 27(2):821–829, may 2012. ISSN 0885-8950. doi: 10.1109/TPWRS.2011.2177867.

[60] Monica Aragues-Penalba, Agusti Egea-Alvarez, Samuel Galceran Arellano, and Oriol Gomis Bellmunt. Droop control for loss minimization in HVDC multi-terminal transmission systems for large offshore wind farms. *Electric Power Systems Research*, 112:48–55, jul 2014. ISSN 03787796. doi: 10.1016/j.epsr.2014.03.013.

[61] Wang Feng, Anh Le Tuan, Lina Bertling Tjernberg, Anders Mannikoff, and Anders Bergman. A new approach for benefit evaluation of multi-terminal VSC HVDC using a proposed mixed AC and DC optimal power flow. *IEEE Transactions on Power Delivery*, 29(1):432–443, feb 2014. ISSN 0885-8977. doi: 10.1109/TPWRD.2013.2267056.

[62] Roger Wiget and Goeran Andersson. Optimal power flow for combined AC and multi-terminal HVDC grids based on VSC converters. In *2012 IEEE Power and Energy Society General Meeting*. IEEE, jul 2012. ISBN 978-1-4673-2729-9. doi: 10.1109/PESGM.2012.6345448.

[63] Lianxiang Tang and Boon Teck Ooi. Locating and isolating DC faults in multi-terminal DC systems. *IEEE Transactions on Power Delivery*,

22(3):1877–1884, jul 2007. ISSN 0885-8977. doi: 10.1109/TPWRD. 2007.899276.

[64] Bernardo Silva, Carlos Leal Moreira, Helder Leite, and Joao Pecas Lopes. Control strategies for AC fault ride through in multi-terminal HVDC grids. *IEEE Transactions on Power Delivery*, 29(1):395–405, feb 2014. ISSN 0885-8977. doi: 10.1109/TPWRD.2013.2281331.

[65] Oriol Gomis Bellmunt, Jun Liang, Janaka Ekanayake, Rosemary King, and Nicholas Jenkins. Topologies of multiterminal HVDC VSC transmission for large offshore wind farms. *Electric Power Systems Research*, 81:271–281, feb 2011. ISSN 03787796. doi: 10.1016/j.epsr.2010.09.006.

[66] Hanchao Liu and Jian Sun. Voltage stability and control of offshore wind farms with AC collection and HVDC transmission. *IEEE Journal of Emerging and Selected Topics in Power Electronics*, 2(4):1181–1189, dec 2014. ISSN 2168-6777. doi: 10.1109/JESTPE.2014.2361290.

[67] Telles Brunelli Lazzarin, Guilherme Bauer, and Ivo Barbi. A control strategy for parallel operation of single phase voltage source inverters: analysis, design, and experimental results. *IEEE Transactions on Industrial Electronics*, 60(6):2194–2204, jun 2013. ISSN 0278-0046. doi: 10.1109/TIE.2012.2193856.

[68] Wanderley Alves Parreira, Henrique Jose Avelar, Joao Batista Vieira, Luiz Carlos Freitas, Luiz Carlos Gomes de Freitas, and Ernane Antonio Alves Coelho. Small signal analysis of parallel connected voltage source inverters using a frequency and voltage droop control including an additional phase shift. *Journal of Control, Automation and Electrical Systems*, 25(5):597–607, oct 2014. ISSN 2195-3880. doi: 10.1007/s40313-014-0143-5.

[69] Ernane Antonio Alves Coelho, Porfirio Cabaleiro Cortizo, and Pedro Francisco Donoso Garcia. Small signal stability for parallel connected inverters in stand alone AC supply systems. *IEEE Transactions on Industry Applications*, 38(2):533–542, mar 2002. ISSN 00939994. doi: 10.1109/28.993176.

[70] Charles Sao and Peter Lehn. Autonomous load sharing of voltage source converters. *IEEE Transactions on Power Delivery*, 20(2):1009–1016, apr 2005. ISSN 0885-8977. doi: 10.1109/TPWRD.2004.838638.

[71] Karel De Brabandere, Bruno Bolsens, Jeroen Van den Keybus, Achim Woyte, Johan Driesen, and Ronnie Belmans. A voltage and frequency droop control method for parallel inverters. *IEEE Transactions on Power Electronics*, 22(4):1107–1115, jul 2007. ISSN 0885-8993. doi: 10.1109/TPEL.2007.900456.

[72] Hisham Mahmood, Dennis Michaelson, and Jin Jiang. Accurate reactive power sharing in an islanded microgrid using adaptive virtual impedances. *IEEE Transactions on Power Electronics*, 30(3):1605–1617, mar 2015. ISSN 0885-8993. doi: 10.1109/TPEL.2014.2314721.

[73] Yixin Zhu, Fang Zhuo, Feng Wang, Baoquan Liu, and Yangjie Zhao. A wireless load sharing strategy for islanded microgrid based on feeder current sensing. *IEEE Transactions on Power Electronics*, 30(12):6706–6719, dec 2015. ISSN 0885-8993. doi: 10.1109/TPEL.2014.2386851.

[74] Martin Andreasson, Roger Wiget, Dimos Dimarogonas, Karl Johansson, and Goran Andersson. Distributed primary frequency control through multi-terminal HVDC transmission systems. In *2015 American Control Conference (ACC)*, pages 5029–5034. IEEE, jul 2015. ISBN 978-1-4799-8684-2. doi: 10.1109/ACC.2015.7172122.

[75] Samy Akkari, Marc Petit, Jing Dai, and Xavier Guillaud. Interaction between the voltage droop and the frequency droop control for multi-terminal HVDC systems. *IET Generation, Transmission and Distribution*, 10(6):1345–1352, apr 2016. ISSN 1751-8687. doi: 10.1049/iet-gtd.2015.0814.

[76] Jiebei Zhu, Campbell Booth, Grain Philip Adam, and Andrew Roscoe. Inertia emulation control of VSC-HVDC transmission system. In *2011 International Conference on Advanced Power System Automation and Protection*, volume 1. IEEE, oct 2011. ISBN 978-1-4244-9621-1. doi: 10.1109/APAP.2011.6180514.

[77] Xiaobo Hu, Jun Liang, Daniel Rogers, and Yalou Li. Power flow and power reduction control using variable frequency of offshore AC grids. *IEEE Transactions on Power Systems*, 28(4):3897–3905, nov 2013. ISSN 0885-8950. doi: 10.1109/TPWRS.2013.2257884.

[78] Ahmed Moawwad, Mohamed Shawky El Moursi, and Weidong Xiao. A novel transient control strategy for VSC-HVDC connecting offshore wind power plant. *IEEE Transactions on Sustainable Energy*, 5(4):1056–1069, oct 2014. ISSN 1949-3029. doi: 10.1109/TSTE.2014.2325951.

[79] Istvan Erlich, Fekadu Shewarega, Christian Feltes, Friedrich Koch, and Jens Fortmann. Offshore wind power generation technologies. *Proceedings of the IEEE*, 101(4):891–905, apr 2013. ISSN 0018-9219. doi: 10.1109/JPROC.2012.2225591.

[80] Zhe Chen and Hui Li. Overview of different wind generator systems and their comparisons. *IET Renewable Power Generation*, 2(2):123–138, jun 2008. ISSN 1752-1416. doi: 10.1049/iet-rpg:20070044.

[81] Mario Ndreko, Marjan Popov, and Mart van der Meijden. Study on FRT compliance of VSC-HVDC connected offshore wind plants during AC faults including requirements for the negative sequence current control. *International Journal of Electrical Power and Energy Systems*, 85:97–116, feb 2017. ISSN 01420615. doi: 10.1016/j.ijepes.2016.08.009.

[82] Omer Goksu, Remus Teodorescu, Claus Leth Bak, Florin Iov, and Philip Carne Kjaer. Instability of wind turbine converters during current injection to low voltage grid faults and PLL frequency based stability solution. *IEEE Transactions on Power Systems*, 29(4):1683–1691, jul 2014. ISSN 0885-8950. doi: 10.1109/TPWRS.2013.2295261.

[83] Bernd Weise. Impact of K-factor and active current reduction during fault ride through of generating units connected via voltage sourced converters on power system stability. *IET Renewable Power Generation*, 9(1):25–36, jan 2015. ISSN 1752-1416. doi: 10.1049/iet-rpg.2014.0116.

[84] Reigh Walling, Ekrem Gursoy, and Bruce English. Current contributions from Type 3 and Type 4 wind turbine generators during faults. In *2011 IEEE Power and Energy Society General Meeting*. IEEE, jul 2011. ISBN 978-1-4577-1000-1. doi: 10.1109/PES.2011.6039740.

[85] Tobias Neumann, Thomas Wijnhoven, Geert Deconinck, and Istvan Erlich. Enhanced dynamic voltage control of Type 4 wind turbines during unbalanced grid faults. *IEEE Transactions on Energy Conversion*, 30 (4):1650–1659, 2015. ISSN 0885-8969. doi: 10.1109/TEC.2015.2470126.

[86] Istvan Erlich, Worawat Nakawiro, and Marcela Martinez Rojas. Optimal dispatch of reactive sources in wind farms. In *2011 IEEE Power and Energy Society General Meeting*. IEEE, jul 2011. ISBN 978-1-4577-1000-1. doi: 10.1109/PES.2011.6039534.

[87] Monica Alonso, Hortensia Amaris, and Carlos Alvarez Ortega. A multiobjective approach for reactive power planning in networks with wind power generation. *Renewable Energy*, 37(1):180–191, jan 2012. ISSN 09601481. doi: 10.1016/j.renene.2011.06.021.

[88] Marcela Martinez Rojas, Andreas Sumper, Oriol Gomis Bellmunt, and Antoni Sudria Andreu. Reactive power dispatch in wind farms using particle swarm optimization technique and feasible solutions search. *Applied Energy*, 88(12):4678–4686, dec 2011. ISSN 03062619. doi: 10.1016/j.apenergy.2011.06.010.

[89] Hoan Van Pham, Jose Luis Rueda, and Istvan Erlich. Online optimal control of reactive sources in wind power plants. *IEEE Transactions on Sustainable Energy*, 5(2):608–616, apr 2014. ISSN 1949-3029. doi: 10.1109/TSTE.2013.2272586.

[90] Jan De Deckar and Paul Kreutzkamp. Offshore electricity grid infrastructure in Europe: A techno-economic assessment. Technical report, OffshoreGrid (3E Coordinator), oct 2011. URL http://www.offshoregrid.eu/.

[91] Ebrahim Rokrok and Mohamad Esmail Hamedani Golshan. Adaptive voltage droop scheme for voltage source converters in an islanded multibus microgrid. *IET Generation, Transmission and Distribution*, 4(5):562–578(16), may 2010. ISSN 17518687. doi: 10.1049/iet-gtd. 2009.0146.

[92] Donghwan Kim, Kyosun Jung, Kyungbae Lim, and Jaeho Choi. A droop method for high capacity parallel inverters considering accurate real power sharing. *Journal of Power Electronics*, 16(1):38–47, jan 2016. ISSN 1598-2092. doi: 10.6113/JPE.2016.16.1.38.

[93] Ngoc Tuan Trinh, Marcus Zeller, Klaus Wuerflinger, and Istvan Erlich. Generic model of MMC VSC HVDC for interaction study with AC power system. *IEEE Transactions on Power Systems*, 31(1):27–34, jan 2016. ISSN 0885-8950. doi: 10.1109/TPWRS.2015.2390416.

[94] Se Kyo Chung. A phase tracking system for three phase utility interface inverters. *IEEE Transactions on Power Electronics*, 15(3):431–438, may 2000. ISSN 08858993. doi: 10.1109/63.844502.

[95] Lus Guilherme Barbosa Rolim, Diogo Rodrigues da Costa, and Maurcio Aredes. Analysis and software implementation of a robust synchronizing PLL circuit based on the PQ theory. *IEEE Transactions on Industrial Electronics*, 53(6):1919–1926, dec 2006. ISSN 0278-0046. doi: 10.1109/TIE.2006.885483.

[96] XiaoQiang Guo, WeiYang Wu, and HeRong Gu. Phase locked loop and synchronization methods for grid-interfaced converters: a review. *Przeglad Elektrotechniczny*, 87(4), jan 2011. ISSN 0033-2097.

[97] Dunstan Graham and R. C. Lathrop. The synthesis of optimum transient response: Criteria and standard forms. *Transactions of the American Institute of Electrical Engineers, Part II: Applications and Industry*, 72(5):273–288, nov 1953. ISSN 0097-2185. doi: 10.1109/TAI. 1953.6371346.

[98] Ivan Pineda, Kristian Ruby, Andrew Ho, Ariola Mbistrova, and Giorgio Corbetta. The European offshore wind inductry: key trends and statistics 1st half 2016. Technical report, European Wind Energy Association, jul 2016. URL `http://www.ewea.org/statistics/offshore/`.

[99] Sascha Thorsten Schroder, Peter Meibom, Stephan Spiecker, and Christoph Weber. Market impact of an offshore grid: A case study. In *2010 IEEE Power and Energy Society General Meeting*. IEEE, jul 2010. ISBN 978-1-4244-6549-1. doi: 10.1109/PES.2010.5590044.

[100] Jan De Decker, Jens Tambke, Jakob Voelker, and Katarzyna Michalowska Knap. An offshore transmission grid for wind power integration: The European techno-economic study offshore grid. In *IEEE Power and Energy Society General Meeting*. IEEE, jul 2010. ISBN 978-1-4244-6549-1. doi: 10.1109/PES.2010.5589887.

[101] Abbas Rabiee, Maziar Vanouni, and Mostafa Parniani. Optimal reactive power dispatch for improving voltage stability margin using a local voltage stability index. *Energy Conversion and Management*, 59: 66–73, jul 2012. ISSN 01968904. doi: 10.1016/j.enconman.2012.02.017.

[102] ABB. Product Catalog: XLPE submarine cable systems, 2017. URL `http://new.abb.com/cables/cables/hvac-extruded-cables/hvac-submarine-cables`.

[103] Nexans. Product catalog: Nexans submarine power cables, 2013. URL `http://www.nexans.de`.

[104] Giorgio Chiandussi, Marco Codegone, Simone Ferrero, and Federico Erminio Varesio. Comparison of multi objective optimization methodologies for engineering applications. *Computers and Mathematics with Applications*, 63(5):912–942, mar 2012. ISSN 08981221. doi: 10.1016/j.camwa.2011.11.057.

[105] Federal Ministry for Economic Affairs, Energy (BMWi), and Project Executing Organization (PTJ). Wind speed data: FINO databank, 2017. URL `http://fino.bsh.de/`. Accessed on 23-03-2017.

[106] ENERCON. Product catalog: ENERCON product overview, 2017. URL http://www.enercon.de/en/home/. Accessed on 23-03-2017.

[107] Amirnaser Yazdani and Iravani Reza. Voltage Control. In *Voltage sourced converters in power systems: Modeling, control, and applications*, chapter Controlled frequency VSC system. A John Wiley and Son, 2010. ISBN 9780470521564.

[108] Luis Fernando Costa Alberto and Newton Geraldo Bretas. Estimating the frequencies of load buses and their effects on the critical clearing time. In *1998 International Conference on Power System Technology (POWERCON 98)*, volume 2, pages 1310–1314. IEEE, aug 1998. ISBN 0-7803-4754-4. doi: 10.1109/ICPST.1998.729298.

[109] Mohammad Hassanzahraee and Alireza Bakhshai. Transient droop control strategy for parallel operation of voltage source converters in an islanded mode microgrid. In *2011 IEEE 33rd International Telecommunications Energy Conference (INTELEC)*. IEEE, oct 2011. ISBN 9781457712494. doi: 10.1109/INTLEC.2011.6099827.

[110] Nkt-Cables. Product Catalog: High voltage cable system- cables and accessories up to 550 kV, 2017. URL www2.nktcables.com.

[111] Janusz Bialek. European offshore power grid demonstration projects. In *2012 IEEE Power and Energy Society General Meeting*. IEEE, jul 2012. ISBN 978-1-4673-2729-9. doi: 10.1109/PESGM.2012.6345283.

[112] Mario Ndreko, Ana-Maria Bucurenciu, Marjan Popov, and Mart van der Meijden. On grid code compliance of offshore MTDC grids: modeling and analysis. In *2015 IEEE Eindhoven PowerTech*. IEEE, jun 2015. ISBN 978-1-4799-7693-5. doi: 10.1109/PTC.2015.7232398.

[113] Istvan Erlich, Christian Feltes, and Fekadu Shewarega. Enhanced voltage drop control by VSC HVDC systems for improving wind farm fault ride through capability. *IEEE Transactions on Power Delivery*, 29(1):378–385, feb 2014. ISSN 0885-8977. doi: 10.1109/TPWRD.2013. 2285236.

[114] Jorun Irene Marvik and Harald Georg Svendsen. Analysis of grid faults in offshore wind farm with HVDC connection. *Energy Procedia*, 35:81–90, jan 2013. ISSN 18766102. doi: 10.1016/j.egypro.2013.07.161.

[115] Monica Aragues Penalba, Oriol Gomis Bellmunt, and Marcia Martins. Coordinated control for an offshore wind power plant to provide fault ride through capability. *IEEE Transactions on Sustainable Energy*, 5 (4):1253–1261, oct 2014. ISSN 1949-3029. doi: 10.1109/TSTE.2014. 2344172.

[116] Sungduck Kim, Medhat Morcos, and Juan Carlos Gomez. Voltage sag magnitude and phase jump due to short circuits in distribution systems with variable fault resistance. *Electric Power Components and Systems*, 33(5):493–512, aug 2005. doi: 10.1080/15325000590504984.

[117] Istvan Erlich, Fekadu Shewarega, Stephan Engelhardt, Jorg Kretschmann, Jens Fortmann, and Friedrich Koch. Effect of wind turbine output current during faults on grid voltage and the transient stability of wind parks. In *2009 IEEE Power and Energy Society General Meeting*. IEEE, jul 2009. ISBN 978-1-4244-4241-6. doi: 10.1109/PES.2009.5275626.

[118] Peter Fairley. Germany jump-starts the Supergrid: New developements in high voltage DC electronics could herald an epic shift energy delivery. *IEEE spectrum*, may 2013. ISSN 0018-9235.

[119] Hakan Ergun, Dirk Van Hertem, and Ronnie Belmans. Transmission system topology optimization for large scale offshore wind integration. *IEEE transactions on sustainable energy*, 3(4):908–917, oct 2012. ISSN 1949-3037. doi: 10.1109/TSTE.2012.2199341.

[120] Stefano Lauria, Marco Maccioni, Francesco Palone, and Maddalena Schembari. Very long distance connection of gigawatt size offshore wind farms: Extra high voltage AC versus high voltage DC cost comparison. *IET Renewable Power Generation*, 10(5):713–720, may 2016. ISSN 1752-1416. doi: 10.1049/iet-rpg.2015.0348.

[121] Bjorn Gustavsen and Olve Mo. Variable transmission voltage for loss minimization in long offshore wind farm AC export cables. *IEEE Transactions on Power Delivery*, 32(3):1422–1431, jun 2017. ISSN 0885-8977. doi: 10.1109/TPWRD.2016.2581879.

[122] Rodrigo Teixeira Pinto, Christian Alejandro, Monica Aragues Penalba, Andreas Sumper, and Elmer Sorrentino. A fast methodology for solving power flows in hybrid AC/DC networks: The European North Sea Supergrid case study. In *PCIM Europe 2016; International Exhibition and Conference for Power Electronics, Intelligent Motion, Renewable Energy and Energy Management*, pages 2211–2218. VDE, may 2016. ISBN 9783800741861.

[123] Yunhui Huang, Xiaoming Yuan, Jiabing Hu, Pian Zhou, and Dong Wang. DC bus voltage control stability affected by AC bus voltage control in VSCs connected to weak AC grids. *IEEE Journal of Emerging and Selected Topics in Power Electronics*, 4(2):445–458, jun 2016. ISSN 2168-6777. doi: 10.1109/JESTPE.2015.2480859.

[124] Roberto Sandano, Michael Farrell, and Malabika Basu. Enhanced master slave control strategy enabling grid support services and offshore wind power dispatch in a multi terminal VSC HVDC transmission system. *Renewable Energy*, 113:1580–1588, dec 2017. ISSN 0960-1481. doi: 10.1016/J.RENENE.2017.07.028.

[125] Haifeng Li, Chongru Liu, Gengyin Li, and Reza Iravani. An enhanced DC voltage droop control for the VSC HVDC grid. *IEEE Transactions on Power Systems*, 32(2):1520–1527, mar 2017. ISSN 0885-8950. doi: 10.1109/TPWRS.2016.2576901.

[126] Pierre Rault, Frederic Colas, Xavier Guillaud, and Samuel Nguefeu. Method for small signal stability analysis of VSC-MTDC grids. In *2012 IEEE Power and Energy Society General Meeting*. IEEE, jul 2012. ISBN 978-1-4673-2729-9. doi: 10.1109/PESGM.2012.6345318.

[127] Catalin Gavriluta, Ignacio Candela, Alvaro Luna, Antonio Gomez-Exposito, and Pedro Rodriguez. Hierarchical control of HV MTDC

systems with droop based primary and OPF based secondary. *IEEE Transactions on Smart Grid*, 6(3):1502–1510, may 2015. ISSN 1949-3053. doi: 10.1109/TSG.2014.2365854.

[128] Florian Thams, Robert Eriksson, and Marta Molinas. Interaction of droop control structures and its inherent effect on the power transfer limits in multiterminal VSC HVDC. *IEEE Transactions on Power Delivery*, 32(1):182–192, feb 2017. ISSN 0885-8977. doi: 10.1109/ TPWRD.2016.2600028.

[129] James Conroy and Ronald William Watson. Aggregate modelling of wind farms containing full-converter wind turbine generators with permanent magnet synchronous machines: transient stability studies. *IET Renewable Power Generation*, 3(1):39–52, mar 2009. ISSN 17521416. doi: 10.1049/iet-rpg:20070091.